



THE UNIVERSITY *of* EDINBURGH

This thesis has been submitted in fulfilment of the requirements for a postgraduate degree (e.g. PhD, MPhil, DClinPsychol) at the University of Edinburgh. Please note the following terms and conditions of use:

- This work is protected by copyright and other intellectual property rights, which are retained by the thesis author, unless otherwise stated.
- A copy can be downloaded for personal non-commercial research or study, without prior permission or charge.
- This thesis cannot be reproduced or quoted extensively from without first obtaining permission in writing from the author.
- The content must not be changed in any way or sold commercially in any format or medium without the formal permission of the author.
- When referring to this work, full bibliographic details including the author, title, awarding institution and date of the thesis must be given.

HYDRODYNAMIC PERFORMANCE OF FREE SURFACE SEMICIRCULAR BREAKWATERS



Hee Min Teh

A thesis submitted for the
degree of Doctor of Philosophy
The University of Edinburgh
2012

Abstract

Different types of breakwaters have been developed in the past for the protection of valuable coastal property, commercial activity and beach morphology. Among these, gravity-type breakwaters are the most common and provide good surface wave attenuation. However, these breakwaters are not always suitable due to their adverse impact on the coastal environment. To alleviate the problem, free surface breakwaters with a variety of caisson designs have been proposed and developed. The main advantages of such breakwaters are low capital cost, freedom from silting and scouring, short construction period, circulation of water beneath the breakwater and exertion of relatively low hydrodynamic forces on the structure as compared to conventional breakwaters. However, complete tranquillity on the lee side is not likely to occur due to wave energy transfer through the permeable parts of the breakwater. The degree of wave attenuation primarily depends on the configuration of the breakwater, the water depth and the incident wave conditions. The hydrodynamic performance of such free surface breakwaters is the subject of this thesis.

Semicircular breakwaters mounted on a low-crested rubble mound structure were successfully built for harbour protection in Japan and China. However, the concept of having semicircular structures as free surface breakwaters has not yet been explored by the research community. As a result, this research is initiated with the aim of developing a free surface semicircular breakwater (SCB) that would serve as an anti-reflection barrier and provide reasonably good wave protection to coastal and marine infrastructures. To meet this research goal, a free surface SCB models were constructed and tested in a wave flume under various wave conditions. The experiments were conducted in three stages. For the first stage, the SCB model was initially tested without any perforations on the curved surface (*i.e.* a solid SCB) for different depths of immersion from the still water level in the wave flume. For the second stage, the front curved wall of the model was subsequently perforated with rectangular openings of different dimensions, producing front wall porosity of 9, 18 and 27%. Following this, two rows of rectangular openings near the crest of the rear curved wall were provided so as to facilitate water infiltration and escape of the run-up waves. For the third stage, additional effort was made to extend the draft of the breakwater by adding a wave screen at the front or/and rear. The screen porosity was 25, 40 and 50%.

The hydrodynamic characteristics of the SCB models were investigated in both regular and irregular seas through a series of systematic experimental programme. The water surface elevations were measured at different locations upstream and downstream of the models to determine the coefficients of wave transmission (C_T), reflection (C_R) and energy dissipation (C_L) as well as the wave climate coefficients in front and inside the breakwater chamber. The horizontal wave forces exerted on the SCB models and the wave screen(s) were also measured and subsequently normalised to yield the force coefficients in the analysis. These hydrodynamic coefficients for the respective test cases are presented and discussed in this thesis.

The experimental results revealed that even though the solid SCB was a better wave attenuator than the perforated ones, it produced a considerable amount of wave reflection. The perforated SCB with 9% porosity of the front wall (denoted as SCB9) outperformed the other perforated breakwater models; however, it produced high wave transmission when the draft was limited and subjected to longer period waves. Hence, wave screens were added to further enhance the performance of the SCB9. The SCB9 with double screens of 25% porosity was found to provide the highest hydraulic performance.

Empirical equations were developed using a multiple regression technique to provide design formulae for wave transmission, wave reflection and horizontal wave forces. The proposed empirical equations showed good agreement with the experimental data. These equations are intended to be of direct use to engineers in predicting the hydrodynamic performance of free surface SCBs. However, sensible engineering judgement must be taken while using these equations as they are based on small scale laboratory tests.

Declaration

I hereby declare that this thesis has been composed by myself and that except where stated, the work contained is my own. I also declare that the work contained in this thesis has not been submitted for any other degree or professional qualification except as specified.



Hee Min Teh

November 2012

Acknowledgments

First of all, I would like to thank the Lord for making me able to undertake this research work.

My deepest gratitude must go to my supervisors, Dr. Vengatesan Venugopal and Dr. Tom Bruce, for nurturing my academic development and mentoring me throughout the study. This PhD research would not have been possible without their support and guidance. I am also indebted to Professor William Allsop of HR Wallingford for engaging in some enlightening discussion with me, and to Dr. William Scott of the School of Mathematics, the University of Edinburgh for help in solving the statistical problems. Special thanks are due to Mr. Neil Wood and Mr. Bill Leslie for their contribution in model fabrication and set-up, and to Dr. Thomas Davey and Mr. Brian Sellar for providing repair to the wave generating system whenever needed.

This research study was made possible by financial support from the *Universiti Teknologi PETRONAS* (UTP) under the Staff Development Programme and I am particularly grateful to the management of UTP for enabling me to further my study abroad. The contribution of the Institute for Energy Systems (IES) to success of this project must also be acknowledged, especially Professor Robin Wallace for approving several rewarding trips within the UK and abroad for attending conferences. I found my time at the IES to be both enjoyable and stimulating and would therefore like to thank all the people there for making it so. Particular gratitude is due to Dr. David Forehand, Dr. Ally Price, Dr. Alexandros Makridis, Dr. Gregory Payne and Dr. Remy Pascal, Mr. Bin Li and Mr. Zhe Ma for their invaluable help, encouragement and, most of all, friendship. I am also grateful to my cousin, Dr. Nathan Cheah for spending his Christmas break in proof-reading my thesis.

I would like to thank Paul Meiklejohn and Alan Scorbie of Rock Elim for being a first-rate landlord. Away from home, my time in Edinburgh was perpetually enlivened by a group of Malaysian friends whom I met in Edinburgh – Sau, Jimmy, Evelyn, David, Kiddo, Tham, CK, Yan Chiew and Eddie – for which I thank them. I will never forget the good time we had together. To all the brothers and sisters in the Chinese Evangelical Church in Edinburgh, I owe thanks for showing agape love and supporting me in prayers. Also, my sincere gratitude goes to my UTP colleagues – Prof. Malay, Zahiraniza, Koh, Niraku and Mubarak – for their unfailing support and care.

I would like to express enormous gratitude to my mum and the rest of my family members for their continuous moral support and encouragement. Finally and most importantly, I would like to thank my loving wife – Esther Ng – for her unceasing love, unreserved support and patience over the course of this research, and to my gorgeous son – Jonathan Teh – for being a great inspiration and motivation in the final stage of thesis writing. I hope I can repay their encouragement and love.

CONTENTS

	Page
Abstract.....	i
Declaration.....	iii
Acknowledgments.....	iv
List of Contents.....	v
Table of Figures.....	ix
Table of Tables.....	xii
List of Nomenclature.....	xiii
1 Introduction	
1.1 Overview on Breakwaters.....	1
1.2 Gravity Breakwaters.....	1
1.2.1 Classification of Gravity Breakwaters.....	2
1.2.2 Drawbacks of Gravity Breakwaters.....	3
1.3 Free surface Breakwaters.....	4
1.3.1 Classifications of Free Surface Breakwaters.....	6
1.3.2 Drawbacks of Free Surface Breakwaters.....	6
1.4 Semicircular Breakwater.....	7
1.4.1 Development and Construction.....	7
1.4.2 Advantages.....	11
1.5 Problem Statement.....	12
1.6 Research Objectives.....	12
1.7 Publications.....	14
2 Literature Review	
2.1 General.....	15
2.2 Fixed Free Surface Breakwaters.....	15
2.2.1 Solid-type.....	17
2.2.1.1 Box.....	17
2.2.1.2 Cylinder.....	18
2.2.1.3 Quadrant Front Face Barrier	20
2.2.1.4 Trapezoidal Barrier	20
2.2.2 Plate-type.....	21
2.2.2.1 Horizontal Plate.....	21
2.2.2.2 Complex Plate Formations.....	22
2.2.3 Caisson-type.....	24
2.2.3.1 Single-Chamber Caisson.....	24
2.2.3.2 Multiple-Chamber Caisson.....	27
2.2.4 Multipart-type.....	27
2.3 Wave Absorbing Caissons.....	29
2.3.1 Wall Configuration.....	29
2.3.2 Caisson Perforation.....	30
2.3.2.1 Perforated Wall Type.....	30
2.3.2.2 Wall Porosity.....	30

2.3.3	Interference Chamber.....	32
2.3.3.1	Wave Reflection.....	33
2.3.3.2	Energy Dissipation.....	33
2.3.3.3	Horizontal Wave Loadings.....	34
2.4	Wave Screens.....	34
2.4.1	Horizontally Slotted Screens.....	35
2.4.2	Pile Breakwaters.....	36
2.5	Skirt Breakwaters.....	36
2.6	Bottom Seated Semicircular Breakwaters.....	37
2.6.1	Classification.....	38
2.6.2	Research Development.....	38
2.6.2.1	Emerged Breakwaters.....	38
2.6.2.2	Submerged Breakwater.....	42
2.7	Summary.....	44
3	Theoretical Considerations	
3.1	General.....	45
3.2	Linear Wave Theory.....	45
3.3	Evaluation Criteria for the Hydraulic Performance of Breakwaters.....	48
3.4	Wave Characterisation and Measurement.....	51
3.4.1	Laboratory Waves.....	51
3.4.2	Measurement of Incident and Reflected Waves.....	53
3.5	Horizontal Loadings under Wave Crests on a Free Surface Semicircular Breakwater.....	56
3.6	Dimensional Analysis.....	61
3.6.1	For SCB: Hydraulic Coefficients.....	61
3.6.2	For SCB: Horizontal Loadings.....	64
3.6.3	For SCB with Wave Screen: Hydrodynamic Coefficients.....	67
4	Experimental System	
4.1	General.....	68
4.2	Free Surface Semicircular Breakwater Model.....	70
4.3	SCB with Wave Screen.....	72
4.4	Model Scale.....	74
4.5	Flume Facilities.....	76
4.5.1	Wave Flume.....	76
4.5.2	Wave Generator.....	78
4.5.3	Wave Absorber.....	83
4.6	Model Installations.....	85
4.6.1	SCB.....	85
4.6.2	Wave Screens.....	87
4.7	Wave Probes.....	89
4.8	Load Cells.....	91
4.9	Data Acquisition System.....	94
4.9.1	Data Logging Hardware.....	94
4.9.2	Data Acquisition and Processing Software.....	96
4.10	Test Programme.....	97
4.10.1	Experimental Set-up.....	97
4.10.2	Test Series.....	98
4.10.2.1	Experiment <i>Series A</i> : SCB Models of Various Porosities.....	100
4.10.2.2	Experiment <i>Series B</i> : SCB9 model with Wave Screen.....	102

4.11	Summary.....	105
5	Solid and Perforated Semicircular Breakwaters: Results and Discussions	
5.1	General.....	106
5.2	Hydraulic Characteristics of the SCB.....	107
5.2.1	Wave Transmission Coefficients.....	107
5.2.2	Wave Reflection Coefficient.....	112
5.2.3	Energy Dissipation Coefficient.....	115
5.2.4	Wave Disturbance Coefficient in Front of the Breakwater.....	121
5.2.5	Wave Disturbance Coefficient in the Interference Chamber.....	124
5.2.6	Effect of Breakwater Placement Ratio.....	127
5.2.7	Effect of the Rear Wall Perforation.....	132
5.2.8	Effect of Wave Spectra.....	135
5.2.9	Results Comparison.....	136
5.3	Horizontal Loadings on the Free Surface SCB models.....	142
5.3.1	Horizontal Force Coefficient.....	142
5.3.2	Effect of Breakwater Placement Ratio.....	145
5.3.3	Effect of the Rear Wall Perforation.....	147
5.3.4	Effect of Wave Spectra.....	148
5.3.5	Statistical Distributions of Forces.....	148
5.4	Selection of the Optimum Breakwater Design.....	154
5.5	Summary.....	155
6	Perforated Semicircular Breakwater with Wave Screens: Results and Discussions	
6.1	General.....	156
6.2	Efficiency of a Wave Screen.....	157
6.3	Hydraulic Characteristics of the SCB9 model with a Wave Screen(s).....	160
6.3.1	Wave Transmission Coefficient.....	162
6.3.2	Wave Reflection Coefficient.....	164
6.3.3	Energy Dissipation Coefficient.....	167
6.3.4	Wave Climate in Front of the Breakwater.....	174
6.3.5	Wave Climate in the Breakwater Chamber.....	177
6.4	Optimisation of the Hydraulic Efficiency of the Breakwater: Evaluation.....	180
6.5	Horizontal Wave Loadings on the SCB9 model with Wave Screens.....	183
6.5.1	SCB9-FS models.....	183
6.5.2	SCB9-RS models.....	185
6.5.3	SCB9-DS models.....	187
6.5.4	Evaluation.....	187
6.6	Summary.....	189
7	Perforated Semicircular Breakwater with Optimum Screen Configurations: Results and Discussions	
7.1	General.....	191
7.2	Hydraulic Performance of the SCB9-RS25 and SCB9-DS25 Models.....	192
7.2.1	Wave Transmission Coefficient.....	195
7.2.2	Wave Reflection Coefficient.....	197
7.2.3	Energy Dissipation Coefficient.....	199

7.2.4	Wave Disturbance Coefficient in Front of the Breakwater.....	202
7.2.5	Wave Disturbance Coefficient in the Breakwater Chamber.....	204
7.3	Horizontal Loadings on the SCB9-RS25 and SCB9-DS25 Models.....	207
7.3.1	Statistical Distribution.....	207
7.3.2	Parametric Analysis.....	210
7.3.3	SCB9-RS25 Model	211
7.3.4	SCB9-DS25 Model	213
7.4	Summary.....	215
8	Engineering Design Tools and Validations	
8.1	General.....	220
8.2	Multiple Regression Analysis.....	220
8.2.1	Multiple Linear Regression.....	221
8.2.2	Multiple Polynomial Regressions	222
8.2.3	Results.....	223
8.2.4	Model Validation	230
	8.2.4.1 Validation Tools.....	230
	8.2.4.2 Results	242
8.3	Prediction of the Horizontal Wave Forces Using Modified Goda's Equations.....	246
8.4	Summary.....	246
9	Conclusions and Recommendations	
9.1	General Conclusions.....	248
9.1.1	Free Surface Semicircular Breakwater (SCB)	249
9.1.2	Effect of Wave Screens.....	251
9.1.3	Optimum Design of SCB	252
9.1.4	Prediction Models	253
9.1.5	Summary.....	253
9.2	Recommendations for Future Work.....	254
	Appendices.....	255
	References.....	274

List of Figures

1.1: Cross section of the semicircular caisson breakwater at Miyazaki Port.....	8
1.2: Construction of the semicircular caisson breakwater at Miyazaki Port.....	9
1.3: Cross section of the semicircular caisson breakwater at the Yangtze River estuary jetty.....	10
1.4: Semicircular caisson breakwater at Yangtze River Estuary.....	10
2.1: Vorticity around the box-type barrier – $T = 1.3$ s, $H_i = 2.8$ cm.....	18
2.2: Vorticity around the trapezoidal-type barrier – $T = 1.3$ s, $H_i = 2.8$ cm.....	21
2.3: Normalised turbulent kinetic energy field, k/U_{max}^2	26
2.4: C_R of the perforated wall caissons.....	31
2.5: Velocity and turbulent fields in the vicinity of a perforated caisson breakwater.....	32
2.6: Types of semicircular caisson breakwaters.....	38
2.7: Transmission coefficients of the bottom-seated semicircular breakwater.....	39
2.8: Reflection coefficients of the bottom-seated semicircular breakwater.....	39
2.9: Energy dissipation coefficients of the bottom-seated semicircular breakwater.....	40
3.1: Wave pressure distributions.....	58
4.1: SCB models – (a) solid type; and (b) front wave-dissipating type.....	71
4.2: Completed SCB27 model.....	71
4.3: A conceptual diagram of the front view of the free surface semicircular breakwater.....	72
4.4: A conceptual diagram of the front view of the SCB with a front screen.....	73
4.5: Modelling of a wave screen.....	74
4.6: Plan view of the wave flume.....	77
4.7: Command signal for regular wave generation.....	79
4.8: Comparison between measured and targeted wave heights for regular waves.....	79
4.9: Command signal for a JONSWAP spectrum.....	80
4.10: Calibration chart for irregular seas as described by the JONSWAP spectra.....	80
4.11: Water elevation time histories measured from three repeat tests for regular seas.....	81
4.12: Water elevation time histories measured from three repeat tests for irregular waves.....	82
4.13: Wave spectra measured from three repeat tests.....	82
4.14: Variation of H_{m0} for different run times.....	83
4.15: Wave reflection in regular seas.....	84
4.16: Wave reflection in irregular seas.....	85
4.17: Mounting frame designed for fitting a SCB model.....	86
4.18: Natural frequencies of the SCB9 model at $D = 0.05$ m and 0.15 m.....	86
4.19: Installation of wave screen.....	87
4.20: Compete installation of test models – SCB9 model and wave screens.....	88
4.21: Natural frequencies of RS40 and RS25 at $D = 0.05$ m.....	88
4.22: Calibration chart for WP1.....	91
4.23: Load cells and amplifier.....	92
4.24: Load cell calibration.....	93
4.25: Load cell calibration charts at $D = 0.05$ m.....	93
4.26: Load cell response to variation of the immersion depth of the test models.....	94
4.27: Laboratory set-up.....	98
5.1: C_T for the SCB models in regular waves.....	109
5.2: C_T for the SCB models in irregular waves.....	109
5.3: The effect of wave period on wave transmission past the SCB0 model of $D = 0.10$ m when exposed to regular waves of $H_i = 0.16$ m – (a) $T = 1$ s; and (b) $T = 1.8$ s.....	110
5.4: The effect of breakwater porosity on wave transmission past the test models of $D = 0.10$ m when exposed to regular waves of $T = 1$ s and $H_i = 0.16$ m – (a) SCB0; and (b) SCB27..	110
5.5: The effect of immersion depth on wave transmission past the SCB27 model when exposed to regular waves of $T = 1.1$ s and $H_i = 0.12$ m – (a) $D = 0.05$ m; and (b) $D = 0.15$ m.....	111
5.6: C_R for the SCB models in regular waves.....	113
5.7: C_R for the SCB models in irregular waves.....	113

5.8:	Hydraulic processes observed in the experiment	115
5.9:	C_L for the SCB models in regular waves.....	117
5.10:	C_L for the SCB models in irregular waves	117
5.11:	Hydraulic processes induced by the SCB0 and SCB9 models immersed at $D = 0.05$ m and subjected to a train of regular waves of $T = 1.6$ s and $H_i = 0.10$ m.....	118
5.12:	Hydraulic processes induced by the SCB0 and SCB9 models immersed at $D = 0.10$ m and subjected to a train of regular waves of $T = 0.8$ s and $H_i = 0.17$ m.....	118
5.13:	Hydraulic processes induced by the SCB0 and SCB9 models immersed at $D = 0.05$ m and subjected to a train of regular waves of $T = 1.8$ s and $H_i = 0.16$ m.....	120
5.14:	Hydraulic processes induced by the SCB0 and SCB9 models immersed at $D = 0.15$ m and subjected to a train of regular waves of $T = 1.8$ s and $H_i = 0.16$ m.....	120
5.15:	C_F for the SCB models in regular waves.....	122
5.16:	C_F for the SCB models in irregular waves	122
5.17:	C_C for the SCB models in regular waves	125
5.18:	C_C for the SCB models in irregular waves	125
5.19:	The effect of the breakwater placement ratio on the hydraulic coefficients for the SCB9 model in regular waves and irregular waves	129
5.20:	Box plots of the hydraulic coefficients for the SCB9 model corresponding to the breakwater placement ratios in regular waves.....	130
5.21:	Box plots of the hydraulic coefficients for the SCB9 model corresponding to the breakwater placement ratios in irregular waves.....	131
5.22:	Effect of the rear wall openings on the hydraulic coefficients in regular waves.....	133
5.23:	Effect of the rear wall openings on the hydraulic coefficients in irregular waves	134
5.24:	Effect of spectral types on hydraulic coefficients of the SCB27 model.....	135
5.25:	Comparison of C_T for $0.015 < H_i/L < 0.044$ in regular waves.....	138
5.26:	Comparison of C_R for $0.015 < H_i/L < 0.044$ in regular waves.....	139
5.27:	Comparison of C_L for $0.015 < H_i/L < 0.044$ in regular waves.....	139
5.28:	Comparison of energy coefficients for $0.02 < H_i/L < 0.04$ and $B/L = 0.32$ in regular waves...	140
5.29:	Comparison of energy coefficients for $0.02 < H_i/L < 0.042$ in irregular waves	141
5.30:	Force coefficients of the SCB models in regular waves.....	143
5.31:	Force coefficients of the SCB model in irregular waves.....	143
5.32:	Design diagram for positive and negative forces developed by Goda and Kakizaki (1967).....	144
5.33:	Effect of B/d on the force coefficients of the SCB9 model in regular waves.....	146
5.34:	Effect of B/d on the force coefficients of the SCB9 model in irregular waves	146
5.35:	Effect of the rear wall openings on the force coefficients in regular waves.....	147
5.36:	Effect of the rear wall openings on the force coefficients in irregular waves	148
5.37:	Effect of wave spectral types on the force coefficients of the SCB27 model	149
5.38:	Weibull probability plots of the horizontal wave forces for the SCB9 model corresponding to $T_p = 1.0$ s, 1.3 s and 1.8 s, and $H_{m0} \approx 0.06$ m.....	151
5.39:	Force spectra for the SCB9 model of $T_p = 1.0$ s, 1.3 s and 1.8 s, and $H_{m0} \approx 0.06$ m	152
5.40:	Weibull probability plots of the peak wave crests and troughs for $T_p = 1.0$ s, 1.3 s and 1.8 s, and $H_{m0} \approx 0.06$ m.....	153
6.1:	Energy coefficients of the SCB9, SS25 and SCB9-FS25 models in regular waves.....	158
6.2:	Energy coefficients of the SCB9, SS25 and SCB9-FS25 models in irregular waves.....	158
6.3:	Wave interaction with the SS25 model	159
6.4:	Measured horizontal wave force on the SS25 model in regular and irregular seas.....	160
6.5:	C_T and ΔC_T of the SCB9-FS models in regular and irregular waves.....	162
6.6:	C_T and ΔC_T of the SCB9-RS models in regular and irregular waves	163
6.7:	C_T and ΔC_T of the SCB9-DS models in regular and irregular waves	164
6.8:	C_R and ΔC_R of the SCB9-FS models in regular and irregular waves.....	165
6.9:	C_R and ΔC_R of the SCB9-RS models in regular and irregular waves	166
6.10:	C_R and ΔC_R of the SCB9-DS models in regular and irregular waves.....	167
6.11:	C_L and ΔC_L of the SCB9-DS models in regular and irregular waves.....	168
6.12:	C_L and ΔC_L of the SCB9-RS models in regular and irregular waves.....	169
6.13:	C_L and ΔC_L of the SCB9-DS models in regular and irregular waves.....	170
6.14:	Wave interaction with SCB9-FS25 and SCB9-FS50 models.....	171

6.15: Wave interaction with SCB9-RS25 and SCB9-RS50 models.....	172
6.16: Wave interaction with SCB9-DS25 and SCB9-DS50 models	173
6.17: C_F and ΔC_F of the SCB9-FS models in regular and irregular waves.....	174
6.18: C_F and ΔC_F of the SCB9-RS models in regular and irregular waves	175
6.19: C_F and ΔC_F of the SCB9-DS models in regular and irregular waves.....	176
6.20: C_C and ΔC_C of the SCB9-FS models in regular and irregular waves	177
6.21: C_C and ΔC_C of the SCB9-RS models in regular and irregular waves	178
6.22: C_C and ΔC_C of the SCB9-DS models in regular and irregular waves	179
6.23: Mean variations of the hydraulic coefficients for the SCB9-FS, SCB9-RS and SCB9-DS models of different screen porosities in regular and irregular waves	182
6.24: Measured horizontal wave forces on the SCB9-FS models in regular and irregular waves.....	184
6.25: Measured horizontal wave forces on the SCB9-RS models in regular and irregular waves	186
6.26: Measured horizontal wave forces on the SCB9-DS models in regular and irregular waves	188
6.27: Total horizontal wave forces by the SCB9-FS, SCB9-RS and SCB9-DS models of different screen porosities in regular and irregular waves.....	189
7.1: Wave interaction with the SCB9-RS25 model at $D_T/d = 0.571$ and 0.643	193
7.2: Wave interaction with the SCB9-DS25 model at $D_T/d = 0.571$ and 0.643	194
7.3: C_T and ΔC_T of the SCB9-RS25 model in regular and irregular waves.....	196
7.4: C_T and ΔC_T of the SCB9-DS25 model in regular and irregular waves.....	196
7.5: C_R and ΔC_R of the SCB9-RS25 model in regular and irregular waves.....	198
7.6: C_R and ΔC_R of the SCB9-DS25 model in regular and irregular waves	198
7.7: C_L and ΔC_L of the SCB9-RS25 model in regular and irregular waves.....	201
7.8: C_L and ΔC_L of the SCB9-DS25 model in regular and irregular waves.....	201
7.9: C_F and ΔC_F of the SCB9-RS25 model in regular and irregular waves.....	203
7.10: C_F and ΔC_F of the SCB9-DS25 model in regular and irregular waves	203
7.11: C_C and ΔC_C of the SCB9-RS25 model in regular and irregular waves.....	206
7.12: C_C and ΔC_C of the SCB9-DS25 model in regular and irregular waves	206
7.13: Water wave and horizontal wave force spectra for the SCB9-DS25 models	208
7.14: Weibull probability plots for the horizontal peak forces acting on the SCB9-DS25 model.....	209
7.15: Weibull probability plots for the incident peak wave crests and troughs.....	210
7.16: Force coefficients for the SCB9-RS25 model at different D_T/d ratios in regular waves	212
7.17: Force coefficients for the SCB9-RS25 model at different D_T/d ratios in irregular waves.....	212
7.18: Force coefficients for the SCB9-D5 model at different D_T/d ratios in regular waves.....	214
7.19: Force coefficients for the SCB9-D25 model at different D_T/d ratios in irregular waves.....	215
7.20: Design diagram for horizontal wave forces acting on the SCB9-RS25 in regular waves.....	216
7.21: Design diagram for horizontal wave forces acting on the SCB9-RS25 in irregular waves.....	217
7.22: Design diagram for horizontal wave forces acting on the SCB9-DS25 in regular waves.....	218
7.23: Design diagram for horizontal wave forces acting on the SCB9-DS25 in irregular waves.....	219
8.1: Validation of empirical models for SCB0 (CASE I) in regular waves.....	231
8.2: Validation of empirical models for SCB0 (CASE I) in irregular waves.....	232
8.3: Validation of empirical models for the perforated SCB's (CASE II) in regular waves.....	233
8.4: Validation of empirical models for the perforated SCB's (CASE II) in irregular waves.....	234
8.5: Validation of empirical models for the SCB9 with different B/d ratios (CASE III) in regular waves.....	235
8.6: Validation of empirical models for the SCB9 with different B/d ratios (CASE III) in irregular waves.....	236
8.7: Validation of empirical models for SCB9-RS25 (CASE IV) in regular waves.....	237
8.8: Validation of empirical models for SCB9-RS25 (CASE IV) in irregular waves.....	238
8.9: Validation of empirical models for SCB9-DS25 (CASE V) in regular waves.....	239
8.10: Validation of empirical models for SCB9-DS25 (CASE V) in irregular waves.....	240
8.11: Comparison between the measured and predicted horizontal wave forces using the modified Goda's equations.....	247

List of Tables

1.1: Characteristics of the free surface breakwaters	6
1.2: Properties of the Chinese and Japanese semicircular breakwaters.....	8
2.1: Types of fixed free surface breakwater	16
2.2: Summary of the investigations of the solid-type free surface breakwaters	19
2.3: Summary of the investigation of the plate-type free surface breakwaters.....	23
2.4: Summary of the investigation of the caisson-type free surface breakwaters.....	25
2.5: Energy coefficients equations for U-type and Π -type breakwaters.....	26
2.6: Summary of the investigation of the multipart-type free surface breakwaters.....	28
4.1: Properties of the SCB models	71
4.2: Properties of the wave screen(s).....	74
4.3: Calibration constants for Equation (4.4)	80
4.4: Sea parameters from three nominally identical repeat tests for regular seas.....	82
4.5: Sea parameters from three nominally identical repeat tests for irregular seas.....	82
4.6: Summary of natural frequencies and damping ratios of the SCB models.....	86
4.7: Summary of natural frequency for the SCB test models.....	89
4.8: Test matrices for experiment <i>Series A</i> and <i>Series B</i> – wave types and water depths	99
4.9: Test parameters for Experiment <i>Series A</i>	101
4.10: Ranges of the dimensionless parameters.....	102
4.11: Test parameters for Experiment <i>Series B</i>	104
5.1: Ranges of C_T for the SCB models	111
5.2: Ranges of C_R for the SCB models.....	115
5.3: Ranges of C_L for the SCB models.....	121
5.4: Ranges of C_F for the SCB models.....	123
5.5: Ranges of C_C for the SCB models.....	127
5.6: The ranges of B/L for respective water depths	132
5.7: Details of the breakwaters selected for comparison.....	137
6.1: Abbreviations for test model.....	157
6.2: Effect of ΔC_i on the hydraulic performance of wave screens.....	161
6.3: Variations of hydraulic coefficients for the SCB9-FS, SCB9-RS and SCB9-DS models in regular and irregular waves.....	181
7.1: Ranges of C_T for the SCB9-RS25 and SCB9-DS25 models	197
7.2: Ranges of C_R for the SCB9-RS25 and SCB9-DS25 models	199
7.3: Ranges of C_L for the SCB9-RS25 and SCB9-DS25 models	200
7.4: Ranges of C_F for the SCB9-RS25 and SCB9-DS25 models	204
7.5: Ranges of C_C for the SCB9-RS25 and SCB9-DS25 models	205
8.1: Summary of notation for the empirical models for the SCB breakwaters.....	224
8.2: Regression coefficients of the SCB0 model (CASE I).....	225
8.3: Regression coefficients of the SCB 9, SCB18 and SCB27 models (CASE II)	226
8.4: Regression coefficients of the SCB9 model for different B/d ratios (CASE III)	227
8.5: Regression coefficients of the SCB9-RS25 model (CASE IV).....	228
8.6: Regression coefficients of the SCB9-DS25 model (CASE V).....	229
8.7: Model validation for SCB0 (CASE I)	243
8.8: Model validation for the perforated SCB's (CASE II).....	243
8.9: Model validation for the SCB9 with different B/d ratios (CASE III).....	244
8.10: Model validation for SCB9-RS25 (CASE IV)	244
8.11: Model validation for SCB9-DS25 (CASE V)	245
8.12: Model validation for the measured and predicted horizontal wave forces using the modified Goda's equations.....	247

List of Nomenclature

a_i	=	wave amplitude
B	=	width of the breakwater
b	=	length of the breakwater
C_C	=	wave climate coefficient at the breakwater's chamber
C_F	=	wave climate coefficient at the front of the breakwater
C_L	=	energy dissipation coefficient
C_R	=	wave reflection coefficient
C_T	=	wave transmission coefficient
c	=	wave celerity
D	=	immersion depth of the breakwater
D'	=	submergence depth of the breakwater
D_T	=	immersion depth of the semicircular caisson with a wave screen
d	=	water depth
E_i	=	incident wave energy
E_l	=	loss energy
E_r	=	Reflected wave energy
E_t	=	Transmitted wave energy
F_t	=	the measured negative peak horizontal forces under wave troughs
F_c	=	the measured positive peak horizontal forces under wave crests
$F_{n,t}$	=	the negative peak force coefficients under wave troughs
$F_{n,c}$	=	the positive peak force coefficients under wave crests
F_x	=	total horizontal wave force
F_r	=	Froude number
f	=	frequency
f_n	=	natural frequency
f_p	=	peak frequency
G	=	Gain value
g	=	acceleration due to gravity
H_c	=	Mean wave height at the breakwater chamber
H_D	=	design wave height
H_f	=	Mean wave height at the front of the breakwater
H_i	=	Mean incident wave height
H_r	=	Mean reflected wave height
H_t	=	Mean transmitted wave height
$H_{m0,c}$	=	significant wave height at the breakwater chamber in frequency domain
$H_{m0,f}$	=	significant wave height at the front of the breakwater in frequency domain
$H_{m0,i}$	=	significant incident wave height in frequency domain
$H_{m0,r}$	=	significant reflected wave height in frequency domain
$H_{m0,t}$	=	significant transmitted wave height in frequency domain
$H_{1/3}$	=	significant incident wave height in time domain
h_c	=	breakwater freeboard
k	=	wave number
L	=	wavelength corresponding to the mean peak period, T
L_p	=	wavelength corresponding to the peak period, T_p
L_s	=	wavelength corresponding to the significant wave period, T_s
l	=	screen spacing
m_0	=	spectral moment of zero order
N	=	sample size
n	=	integer
p	=	pressure force

p_G	=	pressure force estimated using Goda's method
R	=	radius of a semicircular breakwater
R^2	=	coefficient of determination
R_a^2	=	adjusted R squared
R_e	=	Reynolds number
$S(f)$	=	spectral energy density
s	=	horizontal distance between two plates
T	=	mean wave period
T_D	=	design wave period
T_p	=	peak wave period
T_s	=	significant wave period
t	=	time
u	=	horizontal water particle velocity
V	=	flow velocity
v	=	vertical water particle velocity
W	=	measured loads from the load cell
X	=	interval between wave probes
x	=	horizontal distance from the reference
Y_m	=	the measured value
Y_p	=	the predicted value
y	=	lateral distance from the reference
z	=	vertical distance from the reference
α	=	modification coefficients for pressure estimation of a semicircular caisson
ρ	=	density of the water
β	=	phase angle difference
γ	=	peak enhancement factor for JONSWAP spectrum
ϕ	=	velocity potential
ν	=	kinematic velocity
η	=	vertical water particle displacement
η^*	=	maximum wave run up
σ	=	wave angular frequency
σ_F	=	standard deviation of wave forces
λ_p	=	phase modification coefficient for a semicircular breakwater
ϵ_b	=	porosity of the base of the semicircular breakwater
ϵ_f	=	porosity of the front wall of the semicircular breakwater
ϵ_r	=	porosity of the rear wall of the semicircular breakwater
ϵ_{SCB9}	=	porosity of the front curve wall of the semicircular caisson
ϵ_{screen}	=	porosity of the wave screen

1

Introduction

1.1 Overview on Breakwaters

The enormous power of sea waves has been one of the most challenging tasks for coastal and offshore engineers to combat for many reasons; one of which is to protect coastal infrastructures, amenities and communities from destructive waves. A reasonably good tranquillity condition is expected in ports, harbours and marinas for the safety of navigation and berthing within the perimeter of the basin. Another purpose is to bring restoration to the eroded beaches by 'realigning' the profile and shape of the beach. Coastal protection by breakwaters is particularly relevant for beaches of high commercial and recreational values as the defence structures may save lives, valuable resources and properties, as well as commercial activities in coastal areas.

In this study, an emphasis has been given to sea defence breakwaters that are mainly used to provide protection against wave attack. In general, the size of such breakwaters depends on the level of wave protection required. For instance, port and harbour breakwaters are usually larger than marina and recreational breakwaters.

1.2 Gravity Breakwaters

Gravity-type breakwaters are the most common type of breakwaters. They rest on the sea bottom and the crests of these structures can be either emerged or submerged. They are generally massive in size and have enormous weight so as to provide structural strength and stability against waves.

1.2.1 Classification of Gravity Breakwaters

Allsop (1996) outlined three general forms of gravity-type breakwaters, *i.e.* permeable rubble mound breakwaters, impermeable vertical or steep-face breakwaters, and composite breakwaters incorporating a caisson or wall section.

(a) *Rubble Mound Breakwaters*

The best-known and universally used method of wave energy suppression has been a rubble mound breakwater that has a broad base and a narrow crest. The breakwater is typically constructed with a core of quarry-run stone, sand, or slag, and is protected from wave action by one or more stone under-layers and a cover layer composed of armour rocks or concrete armour units. The breakwater configuration is well designed to resist wave and geotechnical forces largely by their own weight and by friction with the underlying materials. These breakwaters are also designed to efficiently transfer the structure and dynamic loads to the sea floor. Functionally, rubble mound breakwaters mainly dissipate energy of the incoming waves by forcing them to break on a slope. As a result, no significant wave reflection is observed.

(b) *Vertical Breakwaters*

The vertical breakwaters are mainly composed of a battered wall section formed by stones or concrete blocks, built on a firm foundation. Modern vertical breakwaters are often constructed of concrete caissons in which the internal bodies are filled with concrete or sand. Functionally, vertical breakwaters reflect incident waves without dissipating much of the energy. Vertical breakwaters gain their merits by having shorter length of wall compared to the rubble mound breakwaters, which in turn requires less material, space and construction time (Tanimoto and Takahashi, 1994a).

(c) *Composite Breakwaters*

Composite breakwaters are virtually a mix of the rubble mound and the vertical breakwaters, *i.e.* a wall section erected on a low-crested rubble mound structure. Very often, concrete caissons of various configurations are used to substitute the wall section so as to reduce the effect of reflection. Such breakwaters are particularly helpful when used in deeper waters or at sites where tidal variation is large. These composite structures serve as mound breakwaters during low tides and vertical breakwaters during high tides (Goda, 1985).

1.2.2 Drawbacks of Gravity Breakwaters

Although the gravity-type breakwaters offer advantages in the form of effective storm protection, several drawbacks are associated with their use which may be detrimental to the environment. The impervious breakwaters can be a total barrier to close off significant portion of a waterway or entrance channel, and to completely stop the seawater exchange beneath the structure which is essential for fish migration and maintaining the water quality within the basin. At sites where strong littoral drift exists, the presence of the breakwater may interrupt alongshore sediment transport and cause erosion to the neighbouring beaches down-coast of the breakwater. In addition, construction of the gravity-type breakwaters is very much dependent on the bottom soil condition. They have to be laid on a firm foundation with good quality soils to prevent settlement problems. Careful consideration must be given to the design and alignment of these breakwaters, as well as their potential impact to the surroundings because they are difficult to remove once constructed. They become a permanent feature of the coastal landscape and any environmental damage caused must be tolerated with or else the breakwaters may be removed for sensitive construction sites.

Rubble mound breakwaters are the most economical when built at sites with limited water depths, preferably less than 4 m (McCartney, 1985). Beyond that the construction cost could be substantial as it increases exponentially with the increase of water depth due to the increase of materials used (Sorensen, 1978). Some other major concerns of these breakwaters are their large footprints that pose restrictions to entrance width and basin space, and the potential depressing impacts they may cause to the nearby environment, ecology and social-economy.

The increased wave activity in front of the breakwaters due to reflection often causes navigation problems in the vicinity of the harbour and the adjoining areas (Allsop, 1995). The severity of the problem is particularly marked when the breakwaters have impervious vertical or steep seaward faces. Substantial wave activity in front of the breakwaters may also lead to scour formation at the toes if they are built in relatively shallow waters. For vertical structures, the horizontal wave forces acting on the wall are considerable and strong impulsive breaking wave pressure on the upright section of the breakwater may also be present during storm events.

1.3 Free surface Breakwaters

In an environmentally sensitive site where complete wave tranquillity is not needed, free surface breakwaters may be a viable alternative to the gravity-type breakwaters. Free surface breakwaters, also known as open breakwaters, have generated a great deal of interest in coastal and ocean engineering industry in recent years. They are essentially barriers located near free surface where the energy flux is the greatest. They are built to distort orbital motion of the water particles near sea surface, where the particle amplitudes and velocities are maximal. The total height of such caissons is smaller than the water depth; thus permitting water circulation beneath the structures. The breakwater barriers could be installed on a group of piles or jacket structures, or even held floating by mooring cables. These structures, which control the height of the incident waves mainly by reflection and energy loss, are most effective when used at locations that are exposed to waves with period up to 5 s and with height up to 1 m (Isaacson *et al.*, 1995).

Free surface breakwaters offer a number of desirable characteristics that allow them to be potentially used as sea defence structures in harbours and marinas:

- a. *Low construction cost:* Free surface breakwater barriers require less concrete per unit run as compared to the conventional breakwaters especially when constructed at sites with relatively large water depths (Neelamani and Reddy, 1992);
- b. *Ease of construction:* Free surface breakwater barriers can be mass fabricated and assembled on land, and then towed to the site by floating barges for installation;
- c. *Applicability in poor soil foundation and complex bathymetry:* Construction of free surface breakwaters is less subjected to the bottom soil condition, particularly for the floating ones. The pile-supported breakwaters can be constructed at steep slope foreshore where the nature of the bathymetry makes the construction of the conventional breakwater to be less feasible;
- d. *Less interference to the ecosystem:* The methods used for breakwater installation reduce environmental impacts, *e.g.* noise and dust pollutions on site, at the quarry, and in transport to the site. The breakwaters permit adequate flow exchange between the partially enclosed water body and the open sea, enabling fish migration, preservation of water quality and sediment transport activity;
- e. *Relocation and recyclability:* The free surface breakwater barrier can be dismantled and relocated with minimum effort and without leaving permanent damage to the environment; and

- f. Reduced visual impact:* The breakwaters have low profile and are particularly favourable to the beach users. They can sustain and preserve natural beauty of the beach.

It is stressed that the use of free surface breakwaters as sea defence structures is only restricted to semi-sheltered sites that are exposed to short period waves such as bays, estuaries, reservoirs, marinas, lakes and rivers. During extreme wave conditions, an under-designed breakwater may be unable to provide adequate protection to the sheltered regions or suffers from functional failures despite surviving structurally. The excessive wave loadings and overtopping may also pose a threat to both stability and integrity of the structures. Therefore, it has been proposed that the free surface breakwaters be built together with the main structures such as seawalls, jetties, or even fixed breakwaters, so as to reduce the pressures and forces exerted on the main structures and to maximise their overall hydraulic efficiency (Hsu and Wu, 1999; Hu *et al.*, 2002).

Despite their limitations, free surface breakwaters are still being widely studied by a number of researchers worldwide due to their application potentials in various sectors. Currently, the interest in free surface breakwaters mainly comes from the pleasure boat market, from the expansion of commercial harbours, from the creation of safe recreational zones and from the military for constructing deployable ports. Most of these sites will need some forms of perimeter protection from wind waves as well as waves generated by boat traffic. Even a sheltered site will likely require some separation between the berthing area and the river or outlet in order to reduce the impact of short period waves and to keep out floating debris. They can be useful even in the most unusual applications such as installation in sewage ponds by simply helping to moderate the wave or providing access from one place to another. Most of these facilities do not require a high level of wave attenuation. For recreational harbours, coastal swimmers and surfers prefer to have acceptable wave conditions to suit their sporting activities; and for fishing harbours, creation of still water conditions is not a necessity. Therefore, free surface breakwaters may be a viable and economical solution for such applications.

1.3.1 Classifications of Free Surface Breakwaters

In this study, emphasis has been given to the fixed free surface breakwaters. Numerous ingenious designs of fixed free surface breakwaters have been proposed, tested, reported, and even constructed with mixed success in the past. Based on their configurations, four classifications of fixed free surface breakwater can be made (Teh *et al.*, 2010), namely solid-type, plate-type, caisson-type and multipart-type. Detailed descriptions of each type of the breakwater is given in Section 2.2 and the summary of the overall characteristics of the breakwaters is presented in Table 1.1.

Table 1.1: Characteristics of the free surface breakwaters

	<i>Solid-type</i>	<i>Plate-type</i>	<i>Caisson-type</i>	<i>Multipart-type</i>
Wave attenuation	High	Moderate	Moderate/High	Moderate
Wave reflection	High	Low/Moderate	Moderate/High	Low
Energy loss	Low	Moderate	Moderate/High	High
Effective mass	High	Low	Low/Moderate	Moderate
Installation cost	High	Low	Low/Moderate	High

1.3.2 Drawbacks of Free Surface Breakwaters

The hydrodynamics exhibited by the free surface breakwaters closely correspond to the physical configuration of the breakwaters. The primary concerns of the respective free surface breakwaters as classified by Teh *et al.*(2010):

- Although the solid-type barriers are efficient wave attenuators; they are also strong wave reflector, resulting in considerable standing waves in front of the structures.
- The submerged plate-type breakwaters may be difficult to construct in sea environment and may pose navigation risk to the marine vessels.
- The caisson-type barriers may be highly reflective to the incident waves if wave energy absorbing features are not inherited in the structures.
- The perforation of the multi-part-type barriers is created to enhance the energy dissipation ability of the breakwater; nonetheless, the installation of multiple parts of the structure in the sea domain could be laborious and time consuming.

The limitations of the free surface breakwaters have brought about the various research efforts made to improve the existing breakwater design so as to meet the functional and economical requirements.

1.4 Semicircular Breakwater

Ever since the construction of the first semicircular breakwater in Japan in the early 90's, the use of the arched structures for coastal protection has received a great deal of interest among the researchers and engineers. Development of a curved barrier as a free surface breakwater is a new research venture in recent years; however, the literature to-date on such breakwater designs is rather scarce. In the present study, attempt is made to explore the feasibility of using the semicircular structure as a free surface breakwater. Prior to the investigation, it is worth understanding the development history and the advantages of the bottom-seated semicircular breakwaters.

1.4.1 Development and Construction

The study of semicircular caisson breakwater was first initiated by a joint research group formed by the Port and Harbour Research Institute of the Ministry of Transport of Japan, Coastal Development Institute of Technology and several other corporations in the early 1990s. The development of the breakwater was aimed at meeting the diverse design requirements such as excellent wave attenuation performance, superb structural stability, low reflectivity, water permeability and scenery enhancement. The prototype semicircular caisson breakwater was first erected at Miyazaki Port in Kyushu Island, Japan during 1992 to 1993 to withstand severe wave conditions during storms. This 36-m long structure consists of a pre-cast semi-cylindrical caisson made of pre-stressed concrete and a bottom slab placed onto a low-crested rubble-mound foundation. The breakwater is perforated on the rear of the arch, and the opening ratios are 25% and 10% for the rear wall and bottom slab, respectively. In addition, as a response to requests by local community to consider the water exchange through the caisson, some pores were added close to the bottom of the front wall. The cross section and design properties of the semicircular breakwater are presented in Figure 1.1 and Table 1.2, respectively, and the manufacturing process is shown in Figure 1.2.

The success of the Japanese semicircular caisson breakwaters in operation has inspired a number of interests from the port and harbour industry in Asia, particularly in China. In 1997, another semicircular breakwater (front-wave dissipative type), 527 m in length, was successfully constructed for protecting the south harbour area of Tianjin Port, China (see Table 1.2). Subsequent in year 2000, an 18-km-long semicircular estuary jetty was completed for the first-phase works of the Deep Channel Improvement Project of the Yangtze River Estuary in Shanghai, China. This estuary jetty is essentially a submerged

breakwater at high water level. Figures 1.3 and 1.4 present the cross section as well as the construction of the semicircular breakwater at the Yangtze River Estuary.

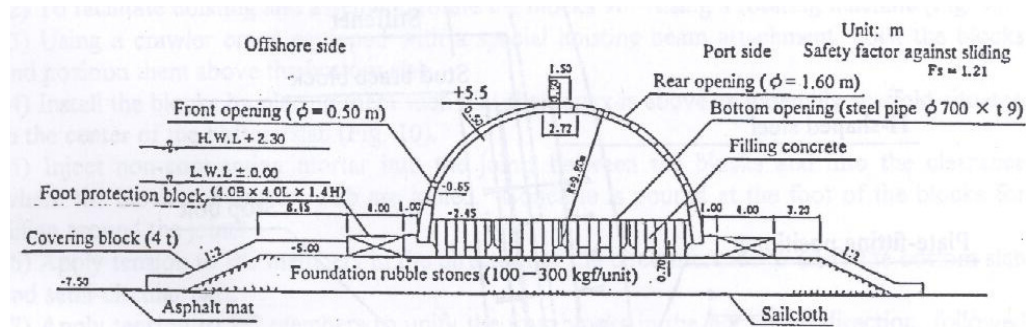
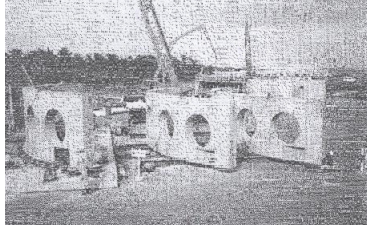


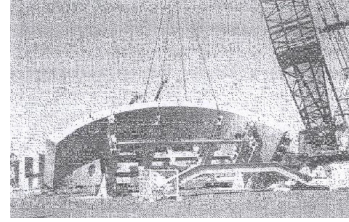
Figure 1.1: Cross section of the semicircular caisson breakwater at Miyazaki Port
(Source: Sasajima *et al.*, 1994)

Table 1.2: Properties of the Chinese and Japanese semicircular breakwaters

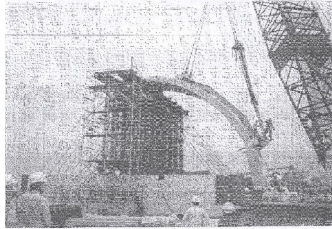
Construction Site & Country	Miyazaki Port, Japan	Tianjin Port, China	Yangtze River Estuary, China
Construction period	1992 – 1993	1995 - 1997	1998 - 2000
Breakwater type	Permeable-type, emerged	Front wave-dissipative, emerged	Front wave-dissipative, emerged/submerged
Total breakwater length	36 m	527 m	18 000 m
<u>Semicircular caisson:</u>			
(a) Length	12 m	2.5 m	4.5 m
(b) Radius	9.8 m	4.5 m	4.0 m
(c) Arch thickness	0.50 m	0.55 m	0.75 m
<u>Front wall perforation:</u>			
(a) Opening diameter	0.5 m	0.5 m	0.5 m
(b) Porosity	1%	± 5%	± 5%
<u>Rear wall perforation:</u>			
(a) Opening diameter	1.6 m		
(b) Porosity	25%		
<u>Bottom Slab:</u>			
(a) Opening diameter	0.7 m	<i>n.a.</i>	0.5 m
(b) Porosity	10%	<i>n.a.</i>	± 11%
(c) Slab thickness	0.70 m	0.80 m	1.25 m
<u>Height of structure:</u>			
Rubble	2.5 m	1 m	3 m
Breakwater	13 m	7 m	10 m
<u>Design water depths:</u>			
Minimum depth	7.5 m	2.3 m	8.2 m
Maximum depth	9.5 m	6.1 m	16.3 m



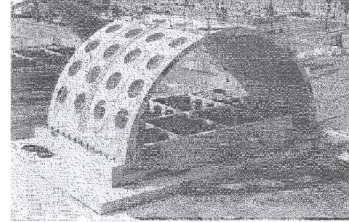
(a) Manufactured of $\frac{1}{4}$ -circular precast blocks using steel molds



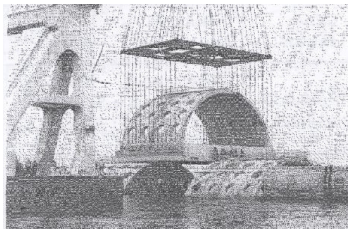
(b) Lifting and rotating of a precast block by the rotating machine



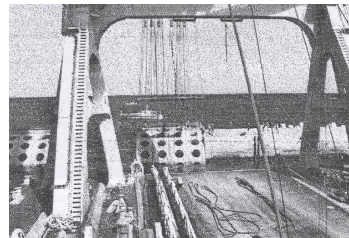
(c) Installation of a precast block



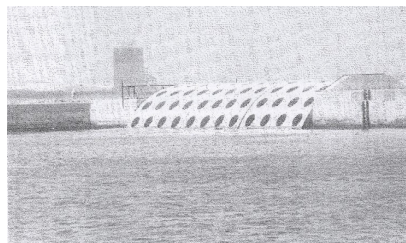
(d) Assembled semicircular caisson



(e) Semicircular caissons was towed to the construction site by a floating crane



(f) Lowering of semicircular caissons from a floating crane



(g) Installation of the standard caissons was completed by poring concrete onto their bases

Figure 1.2: Construction of the semicircular caisson breakwater at Miyazaki Port (Source: Sasajima *et al.*, 1994; Tanimoto and Takahashi, 1994a)

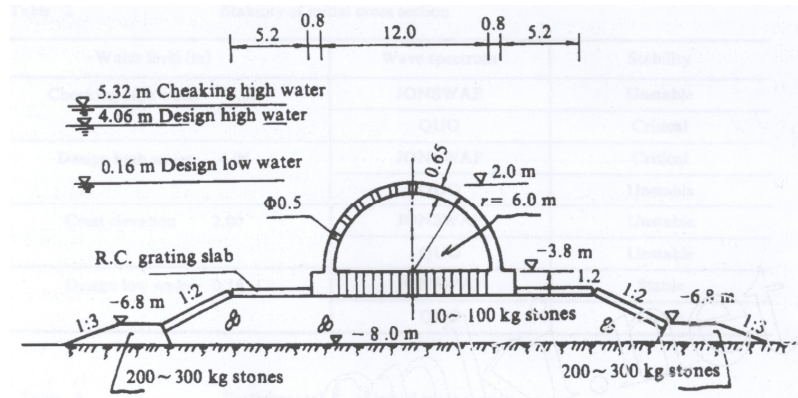


Figure 1.3: Cross section of the semicircular caisson breakwater at the Yangtze River estuary jetty (Source: Xie, 1999)



(a) Handling of the semicircular caisson unit



(b) Installation of the standard caisson on a mound structure



(c) Completion of construction project

Figure 1.4: Semicircular caisson breakwater at Yangtze River Estuary

(Source: <http://images.google.cn/images?hl=zhCN&q=%E5%8D%8A%E5%9C%86%E5%BD%A2%E9%98%B2%E6%B3%A2%E5%A0%A4&gbv=2&aq=f&oq=>)

1.4.2 Advantages

Semicircular breakwater has been proven to be an excellent coastal defence structure in a broad range of water depths (Tanimoto and Takashashi, 1994b), particularly when the seaside wall is perforated (Dhinakaran *et al.*, 2001a). Apart from its good wave attenuation performance, there are other distinguished merits that worth to be highlighted:

- a. *Enhanced structural stability:* The arch feature of the semicircular caisson reduces the risk of overturning (Graw *et al.*, 1998). The stability of the structure is further enhanced with the use of a porous bottom slab due to the absence of dominant uplift pressure (Sasajima *et al.* 1994);
- b. *High stability against wave action:* The semicircular caisson has greater sliding stability against waves in comparison with the vertical breakwaters. The vertical component of the wave force is applied downward along the curved wall and eventually transmitted to the foundation soil; hence, the caisson is adequately stable against waves and is not subjected to impulsive breaking wave force (Aburatani *et al.*, 1996);
- c. *Applicability in poor soil foundation:* The wave force exerted on the curved surface is always directed to the centre of the semicircle, leading to uniform distribution of sub-grade reaction across the bottom slab (Tanimoto and Goda, 1992). As a result, the sub-grade reaction per unit area is comparatively small;
- d. *Low construction costs:* The engineering cost of a semicircular breakwater is about 20% lower than that of a conventional rubble mound structure (Xie, 2001);
- e. *Ease of construction:* The modular semicircular caissons can be manufactured either by the solid body method or the pre-cast block assembly method. The caissons can be towed and installed at the construction sites with minimum efforts. Only the bottom slabs of the semicircular caisson are filled with concrete to provide adequate stability to the caisson;
- f. *Relocation and reuse:* It is relatively easy to re-lift and relocate the semicircular caissons to another site for wave protection; and
- g. *Good scenery enhancement:* The arch configuration of the breakwaters generally fits into the landscape very well and provides high aesthetic value.

1.5 Problem Statement

The gravity-type breakwaters, which have long been perceived as a security feature to many coastal communities, generally provide high resistance to wave action. However, this option may be undesirable and controversial in the perspective of conservation of coastal environment and marine ecosystem due to the environmental impacts it might cause. These include interruption to seawater exchange and fish migration, water contamination and drastic change of shoreline in the vicinity of the breakwaters (Further concerns have been highlighted in Section 1.2.2). To alleviate these problems, various forms of free surface breakwater have been developed. They are generally more space-and-cost efficient than the gravity type breakwaters.

In reviewing of the drawbacks of the free surface breakwaters in Section 1.3.2, a number of limitations of these structures have been identified that warrant further attention by researchers. One of which is the problem of standing waves due to reflection in front of the breakwater. The majority of the free surface breakwaters are designed to provide protection for a narrow range of wave climates, (*i.e.* wave height less than 1 m and wave period less than 4 s) in limited water depths. This has, however, confined the applications of the breakwaters to milder seas in the coastal regions. As a result, numerous efforts have been made to improve the existing breakwaters so that they can operate in more robust wave conditions.

The merits of the free surface breakwaters and the semicircular breakwaters have been outlined in Sections 1.3 and 1.4.2, respectively. A free surface breakwater with a semicircular caisson combines the advantages offered by the respective structures, and may produce a promising hydrodynamic performance. To the knowledge of the author, there was no study on such breakwater reported so far. Therefore, this has become the main motivation for the present work.

1.6 Research Objectives

This research seeks to develop a free surface semicircular breakwater which will provide good wave attenuation performance with low reflectivity and will be suitable for a broad range of water depths. It is the central objective of this thesis to provide insight into how the configuration of the breakwater affects its hydrodynamic performance and strategies to improve the breakwater efficiency, through a series of laboratory tests. Note that numerical

modelling for such breakwater is not attainable in this study due to the depth of complexity of the problem involved and the time constraint of this course of research study.

The primary objectives of the research are:

1. to construct laboratory scale physical models of semicircular breakwaters with various porosity levels and evaluate their performance under waves generated in controlled conditions;
2. to understand the hydrodynamic interactions of the breakwaters and identify the factors that influence the nature of this interference under regular and irregular seas of varying wave condition;
3. to propose an optimum breakwater configuration and justify its creditability and limitations;
4. to provide strategies in improving the limitations of selected breakwater models and understand their impact on the overall behaviour of the structures;
5. to understand and interpret the hydrodynamic characteristics of selected breakwater configurations in different immersion depths; and
6. to develop empirical models for the estimation of the overall hydrodynamic performance of the breakwater and validate them with the measurements.

Structure of the thesis:

A review of available literature is provided in Chapter 2. The theoretical considerations associated with the hydrodynamic performance evaluation of the free surface breakwaters and measurement of laboratory waves are presented in Chapter 3. Chapter 4 introduces a new design concept of the free surface breakwater and laboratory apparatus used in the experimental studies. A complete experimental test structure for the study is also given in this chapter. Chapters 5 – 7 contain results and discussions of the experimental tests and their evaluations. Chapter 8 provides a number of design formulae for the prediction of the hydrodynamic performance of the breakwater models, including verification of the results. Finally, a summary of the study and conclusions of the research are presented in Chapter 9 with recommendations for future research.

1.7 Publications

In the course of this research, the author has published the following journal and conference papers:

1. Teh, H. M. and Venugopal, V. (2010). Experimental investigation on a perforated semicircular breakwater in irregular waves. In *Proceedings of the 2nd United Kingdom-Malaysia Engineering Conference*, London, April 2010.
2. Teh, H. M., Venugopal, V. and Bruce, T. (2010). Hydrodynamic performance of a free surface semicircular perforated breakwater. In *Proceedings of the 32nd International Conference on Coastal Engineering*, Shanghai, China, July 2010.
[Online version: http://journals.tdl.org/ICCE/article/view/1112/pdf_200]
3. Teh, H. M. and Venugopal, V. (2011). Hydrodynamic characteristics of free surface, semicircular breakwater. *The 7th UK Young Coastal Scientists and Engineers Conference (YCSEC)*, Liverpool, March 2011.
4. Teh, H. M., Venugopal, V. and Bruce, T. (2011). Performance analysis of a semicircular free surface breakwater. In *Proceedings of the 30th International Conference on Ocean, Offshore and Arctic Engineering*, Rotterdam, The Netherlands, June 2011.
5. Teh, H. M., Venugopal, V. and Bruce, T. (2012). Hydrodynamic characteristics of a free surface semicircular breakwater exposed to irregular waves. *Journal of Waterway, Port, Coastal and Ocean Engineering*, 138(2), ASCE, 149-163.
6. Teh, H. M., Venugopal, V. and Bruce, T. (2012). Hydrodynamic performance analysis of semicircular breakwaters with truncated wave screens. *The 33rd International Conference on Coastal Engineering*, Santander, Spain, July 2012.
7. Teh, H. M. and Venugopal, V. and Bruce, T. (2012). Wave transformation by a perforated free surface semicircular breakwater in irregular waves. *The 2nd International Conference on Civil Engineering and Building Materials*, Hong Kong, November 2012.

2

Literature Review















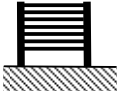
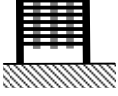
2.1 General

This chapter describes the types of free surface breakwaters developed in the past and the associated wave suppression features. It subsequently highlights the hydrodynamic performance of the perforated breakwaters, such as perforated breakwater caissons, wave screens and skirt breakwaters, as the design requirement of these breakwaters are referred in this study. This chapter also covers some of the relevant literature on the bottom seated semicircular breakwaters which is the main motivation for this study. It is also worthwhile to mention that the intention of this chapter is not to provide a detailed description of the respective subjects, but rather to provide the necessary background of the relevant field which will enable the understanding of the work carried out in this research.

2.2 Fixed Free Surface Breakwaters

In the past, various forms of free surface breakwaters were proposed and developed to suit different purposes in coastal and marine applications. Some breakwaters are simple in design, whilst the others are structurally complex. Based on their configurations, Teh *et al.* (2010) classified the free surface breakwaters into four types: (a) solid-type; (b) plate-type; (c) caisson-type; and (d) multipart-type. The wave barriers under each breakwater type are given in Table 2.1.

Table 2.1: Types of fixed free surface breakwater

Breakwater Types	Geometry & Cross Sectional View	References
Solid-type	Box 	Koutandos & Prinos (2005) Koutandos (2007) Koutandos & Prinos (2011)
	Cylinder 	Li <i>et al.</i> (2005)
	Quadrant front face 	Sundar & Subba Rao (2002; 2003)
	Trapezoid 	Koftis & Prinos (2005a)
Plate-type	Horizontal plate 	Hsu & Wu (1999) Hu <i>et al.</i> (2002)
	Inclined plate 	Rao <i>et al.</i> (2009)
	Twin-plate 	Neelamani & Gayathri (2006) Liu <i>et al.</i> (2008)
	T- type 	Neelamani & Rajendran (2002a)
	⊥- type 	Neelamani & Rajendran (2002b)
	H - type 	Neelamani & Vedagiri(2002)
Caisson-type	U - type 	Günaydın & Kebdaşlı (2004)
	Π - type 	Günaydın & Kebdaşlı (2006)
	Ш - type 	Brossard <i>et al.</i> (2003)
	⊂- type 	Teh <i>et al.</i> (2010; 2011; 2012)
Multipart-type	Multiple-layer 	Wang <i>et al.</i> (2006)
	Porous-piles 	Hsiao <i>et al.</i> (2008)

There are different approaches used to investigate the hydraulic characteristics of the free surface breakwaters. Analytical and numerical analyses are mostly used to study the breakwaters with simple configurations and are confined to simplified boundary conditions under a set of controlled test environments. However, mathematical and computer solutions may not be capable of providing realistic solutions if the problem becomes more complicated. In that case, physical modelling is found to be more appropriate. The following sections address some typical findings of each type of free surface breakwater. Note that the breakwater models discussed herein were tested in fixed state unless it is further specified.

2.2.1 Solid-type

The solid-type barriers are generally simple in design and have high effective mass for stability. The typical designs for solid-type barriers include box, cylinder, quadrant front face and trapezoidal structures, as shown in Table 2.1. The majority of the solid-type barriers suppress wave energy mainly by reflection.

2.2.1.1 Box

Box-type breakwater is the most classic and simplest form of design in the development of free surface breakwaters. It has a rectangular section typically made of reinforced concrete. Koutandos and Prinos (2005) conducted large-scale physical tests to study the hydraulic characteristics of a fixed box-type wave barrier in shallow and intermediate waters for both regular and irregular waves. They found that the breakwater of deeper immersion induced greater wave reflection and the effect intensified as the barrier was exposed to shorter-period waves. With wave steepness, H_i/L ranging from 0.0015 – 0.0480, the wave reflection coefficient, C_R , which is a ratio of the reflected wave height-to-the incident wave height (see Equation (3.19)), increased from 0.4 – 0.9 as the relative breakwater width, B/L increased from 0.045 – 0.312. (Note that H_i = incident wave height, L = wavelength, and B = breakwater width). The corresponding wave transmission coefficient, C_T , which is a ratio of the transmitted wave height-to-the incident wave height (see Equation (3.17)), decreased from 0.90 – 0.25. The effect of double box barriers parted by a distance was further explored by Koutandos (2007). The detailed experiments and results are summarised in Table 2.2a.

Apart from wave reflection, the box barrier also induces some amount of energy dissipation when interacting with waves. In the numerical simulation of vorticity around the fixed box-type barrier using Reynolds Average Navier-Stokes equations (RANS) solver, Duclos *et al.* (2004) noticed a pair of eddies formed around the two sharp bottom edges of the body, at which the upstream vortices were more developed than the downstream ones as shown in

Figure 2.1. The formation of eddies around the barrier is believed to be the key mechanism that governs the energy dissipation. However, the amount of energy dissipated by the barrier is relatively small even with an addition of a solid or porous front plate to the bottom of the barrier (Koutandos and Prinos, 2011).

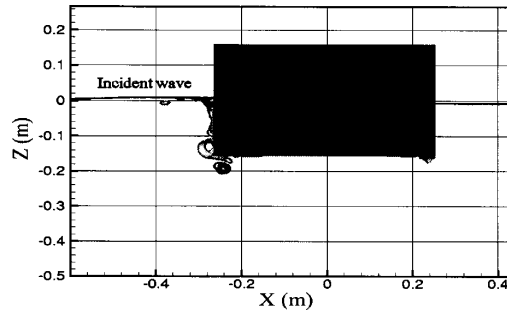


Figure 2.1: Vorticity around the box-type barrier – $T = 1.3$ s, $H_i = 2.8$ cm
(Source: Duclos *et al.*, 2004)

2.2.1.2 Cylinder

The use of a circular section as a breakwater has the advantage of preventing significant torsional moments and corner stress concentrations that are induced by wave action on the box-type breakwaters. Significant cost savings may be attainable by using circular concrete pipe due to the low manufacturing cost (Isaacson *et al.*, 1995). Isaacson *et al.* (1995) experimentally studied wave transmission of a circular cross-section floating breakwater with moorings in regular waves. They reported that the B/L had more influence on the C_T of the cylindrical barrier compared to H/L . The C_T decreased noticeably from 1.15 – 0.3 as B/L increased from 0.08 – 0.52. They also compared the experimental results with the corresponding results for a rectangular-section breakwater. Both sections were reported to perform similarly, exhibiting a decrease in the C_T as B/L was increased, and both geometries became ineffective for $B/L < 0.2$. At larger range of B/L , the rectangular cross section performed slightly better than the circular one.

Li *et al.* (2005) modelled the characteristics of wave transmission past an infinitely long cylinder in fixed position in shallow, transitional and deep waters using the modified Tsay and Liu's (1983) approximation. The numerical results showed a decrement in C_T with the increase of the relative breakwater width and relative breakwater immersion depth. The range of C_T with respect to different relative immersion depth, D/d (where D = breakwater immersion depth and d = water depth) are presented in Table 2.2b.

Table 2.2: Summary of the investigations of the solid-type free surface breakwaters

No	Breakwater Types	Ref.	Types of Analysis	Model Dimension	Test Parameters				Dimensionless Parameters				Energy Coefficients			
					Wave d (m)	D (m)	H _t (m)	T (s)	d/L	D/d	H/L	B/L	C _r	C _d	C _t	C _i
SOLID-TYPE BARRIER																
(a) Box																
1	Single box	Koulardos & Pinos, 2005a	Experimental	B = 2 m H = 1.5 m L = 2.8 m	Reg Irr	2	0.40 0.50 0.65	0.2 & 0.3	2.04 - 9.17	0.04 - 0.35	0.2 0.25 0.33	0.002 - 0.048	0.05 - 0.31	0.25 - 0.90	0.4 - 0.9	0.17 - 0.23
2	Double box	Koulardos, 2007	Experimental Numerical (RANSE & VOF)	B = 2 m H = 1.5 m L = 2.8 m Δs = 9.5 m	Reg JONS	2	0.5	0.2 & 0.3 0.3	2.04 - 9.17 2.15 - 5.04	0.04 - 0.32 0.08 - 0.29	0.25	0.002 - 0.048 0.014 - 0.044	0.04 - 0.32 0.08 - 0.29	0.12 - 0.82 0.42 - 0.76	0.33 - 0.90 0.43 - 0.76	0.02 - 0.53 0.48 - 0.64
3	Single box with a front plate (solid & perforated)	Koulardos & Pinos, 2011	Experimental Numerical (RANSE & VOF)	B = 2 m H = 1.5 m L = 2.8 m H _{plate} = 0.2 m S _{plate} = 0 - 0.6	Reg	2	0.2	0.3	2.04 - 9.17	0.04 - 0.24	0.2	0.002 - 0.048	0.04 - 0.24	0.53 - 0.92 0.32 - 0.88 0.52 - 0.87	0.32 - 0.82 0.31 - 0.80 0.33 - 0.82	0.04 - 0.17 0.20 - 0.34 0.02 - 0.22
4	Single box	Duclos et al., 2004	Numerical (Potential flow) (1:60)	Top width = 0.14 m Base width = 0.51 m Model height = 0.26 m Front face = Elliptical Rear face = inclined 55°	Reg	0.8	0.162	n.a.	0.78 - 1.56					0.05 - 0.75	0.67 - 0.98	n.a.
5	Single box	Koitis & Pinos, 2005	Numerical (RANSE & VOF)	B = 2 m	Reg	2	0.4 - 1.2	0.26	2.04 2.67 3.16	0.17 - 0.32	0.2 - 0.6	0.02 - 0.04	0.16 - 0.32	0.20 - 0.58	0.68 - 0.85	n.a.
(b) Cylinder																
1	Floating cylinder	Isaacson et al., 1995	Experimental (1:10)	R = 0.16 m	Reg	0.6	0.186	0.5 - 1.5	2.0 - 5.0	0.15 - 0.97	0.31	n.a.	0.08 - 0.52	0.31 - 1.05 0.34 - 1.14	n.a. n.a.	n.a. n.a.
2	Cylinder	Li et al., 2005	Numerical (Modified Tsay-Liu approx.)	n.a.	Reg	n.a.	n.a.	n.a.	n.a.	n.a.	0.25 0.50 0.75	n.a.	0.01 - 0.64	0.10 - 1.0 0.02 - 1.0 0.03 - 1.0	n.a. n.a. n.a.	n.a. n.a. n.a.
(c) Quadrant Front Face																
1	Pile supported quadrant front face	Sundar & Subba Rao, 2002	Experimental	R = 0.5 m Pile dia. = 0.59 m Pile height = 0.55 m Deck height = 0.1 m Total height = 1.15 m Δs_pile/D = 5	Reg	0.8 0.9 1.0	0.25 0.35 0.45	0.08 - 0.32	1.0 - 2.4	n.a.	0.31 0.39 0.45	n.a.	0.15 - 0.65	0.04 - 0.66 0.06 - 0.49 0.08 - 0.58	0.26 - 0.58 0.30 - 0.75 0.38 - 0.89	0.51 - 0.89 0.49 - 0.85 0.41 - 0.82
2	Pile supported quadrant front face	Sundar & Subba Rao, 2003	Experimental (1:25)	R = 0.5 m Pile dia. = 0.59 m Pile height = 0.55 m Deck height = 0.1 m Total height = 1.15 m Δs_pile/D = 5	PM	0.8 0.9 1.0	0.25 0.35 0.45	0.03 - 0.19	1.0 - 2.0	n.a.	0.31 0.39 0.45	n.a.	0.15 - 0.65	0.11 - 0.45 0.14 - 0.42 0.12 - 0.38	0.41 - 0.54 0.42 - 0.67 0.54 - 0.78	n.a. n.a. n.a.
(d) Trapezoid																
1	Trapezoid	Duclos et al., 2004	Numerical (Potential flow & RANSE) (1:60)	Top width = 0.14 m Base width = 0.51 m Model height = 0.26 m Front face = Elliptical Rear face = inclined 55°	Reg	0.8	0.162	n.a.	0.78 - 1.56	n.a.	n.a.	n.a.	n.a.	0.00 - 0.55 0.02 - 0.38	0.76 - 0.98 0.56 - 0.80	n.a. n.a.
2	Trapezoid	Koitis & Pinos, 2005a	Numerical (RANSE & VOF)	Base = 2 m Front face = inclined 45° Rear face = inclined 45°	Reg	2	0.4 - 1.2	0.26	2.04 2.67 3.16	0.17 - 0.32	0.2 - 0.6	0.02 - 0.04	0.16 - 0.32	0.12 - 0.40	0.51 - 0.76	n.a.

2.2.1.3 Quadrant Front Face Barrier

A quadrant front face barrier comprises a rectangular section and a quadrant of a circular section in which the radius is equivalent to the width of the rectangular section. Sundar and Sabbarao (2002 and 2003) investigated a quadrant front face barrier that was supported by a group of closely spaced piles. The structure was designed to reduce the excessive wave energy by reflection from the quadrant front face during high tides, and to dissipate the wave energy with its closely spaced piles when water level stayed below the barrier. The test results in regular waves obtained by Sundar and Sabbarao (2002) showed a rapid improvement in wave attenuation as the relative breakwater width was increased. The wave suppression of the barrier was mainly prompted by energy dissipation at the structure and some amount of reflection. The reflection was found to be stronger ($C_R > 0.5$) when the breakwater was subjected to shorter period waves. The model was also tested in irregular seas (Sundar and Subbarao, 2003). The C_R and C_T due to irregular waves were found to be greater than those due to regular waves by 10% – 15% and about 5%, respectively. Whereas, the energy dissipated by irregular waves was reported to be about 5% – 10% less than that by regular waves. A summary of the results derived from the Sundar and Subbarao's experiments is given in Table 2.2c.

2.2.1.4 Trapezoidal Barrier

A trapezoidal-section barrier has a pair of upper and lower surfaces of unequal length, and the front and rear surfaces can be inclined or curved. The trapezoidal barriers offer advantages by providing increased surface areas for wave interaction and energy dissipation. Duclos *et al.* (2004) numerically simulated vorticity around a trapezoidal barrier with a concave front face (see Figure 2.2). The geometry of the barrier generated multiple higher harmonic components in the reflected waves resulting in energy dispersion over a large range of angular frequency. In comparison with the box-type barrier shown in Figure 2.1, the vortices generated in front of the trapezoidal barrier are more developed than those generated in front of the box-type barrier under identical test conditions. This subsequently leads to the conclusion that the trapezoidal barrier is a better energy dissipater than the box-type barrier. This finding agrees with the numerical results obtained by Koftis and Prinos (2005a) who compared the hydraulic efficiency between the trapezoidal barrier with inclined faces of 45° and the rectangular barrier. A summary of their results is given in Table 2.2d.

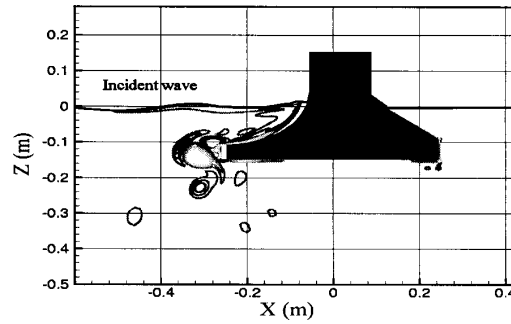


Figure 2.2: Vorticity around the trapezoidal-type barrier – $T = 1.3$ s, $H_i = 2.8$ cm
(Source: Duclos *et al.*, 2004)

2.2.2 Plate-type

A plate-type barrier consists of a single or a combination of multiple plates with different alignments located at various submergence depths in the water domain. The typical plate-type breakwaters include a single horizontal plate, twin horizontal plates, inclined plate, T-type barrier, \perp -type barrier and H-type barrier, as outlined in Table 2.1.

2.2.2.1 Horizontal Plate

Pile supported horizontal submerged plates have been proposed as offshore breakwaters for coastal protection since the 1970s. They are generally more economical in the use of construction materials. The presence of a horizontal plate near the free surface tends to steepen the waves over the plate due to shoaling and part of the incident wave energy gets dissipated by wave breaking, turbulence and friction on the plate surface. The hydraulic efficiency of the breakwater often relates to its submergence from the still water level D' . In an early study, Hattori (1975) investigated wave transmission and reflection of a single horizontal plate fixed at different relative submergence, $D'/d = 0, 0.25$ and 0.50 , in regular waves. They found that both wave attenuation and reflection were high at smaller value of D'/d , signifying that the surface plate was a better wave attenuator and a stronger reflector than the submerged plate. These findings somehow contradicted with the results obtained by Dattatri *et al.* (1977) whereby the maximum reflection was found to occur at $D'/d = 0.07$. Dattatri *et al.* (1977) suggested that for maximum wave reflection the optimum plate width B should be about $0.3 - 0.4$ times the incident wavelength, L , *i.e.* $0.3 < B/L < 0.4$.

Patarapanich (1984) provided numerical solutions of wave reflection and transmission for a horizontal plate subjected to a large range of water conditions covering from shallow to deep water limits using the finite element method. It was found that the C_T generally increased as

D'/d and d/L were decreased, and the minimum C_T occurred at $B/L \approx 0.7$. The drawback of this model is that it does not account for energy loss at the structure. This aspect was later addressed by Patarapanich and Cheong (1989) through experimental studies of a horizontal plate. They recommended that for a plate of $0.05 < D'/d < 0.15$ in regular waves the optimum width should be about 0.5 – 0.7 times the wavelength above the plate.

To enhance the hydraulic performance of the breakwater, an additional plate is introduced at a distance below the surface plate, forming a double-plate system. The wave interactions with double-plate breakwaters were studied by Usha and Gayathri (2005), Neelamani and Gayathri (2006) and Liu *et al.* (2008). Alternatively, it was also suggested that the single horizontal plate be used as a secondary structure placed in front of a primary wave defence structure so as to boost the overall hydraulic performance. The optimisation of performance by the horizontal plate was investigated by Hsu and Wu (1999) and Hu *et al.* (2002). A summary of the studies on horizontal plates is illustrated in Table 2.3.

2.2.2.2 Complex Plate Formations

Rao *et al.* (2009) experimentally explored wave transmission of a plate at varying inclinations and submergence in regular waves. They found that wave transmission of the breakwater was not affected by the forward and reverse inclinations of any plate configuration. The plate inclined at 60° performed efficiently ($C_T < 0.6$) at $H_i > D'$, where D' is the submergence depth between still water level and the upper hinge of the plate. Although the upright plate outperformed ($C_T < 0.4$) the other incline plates, it induced excessive reflection in front of the breakwater.

On the other hand, Neelamani and Rajendran (2002a and 2002b) experimentally investigated the T-type and \perp -type breakwaters at varying submergence under regular and irregular seas. The experimental results showed an improvement of wave attenuation with an increase in wave steepness, H/L and relative water depth, d/L . They reported that the T-type breakwater was superior to the \perp -type breakwater by about 20-30% in wave attenuation under identical testing conditions. The H-shape barrier, which consists of a pair of vertical plates of varying length, is another unique plate-type breakwater. Neelamani and Vedagiri (2002) experimentally explored the geometrical effect of the partially immersed twin vertical barrier under different wave conditions. The breakwater with longer rear plate was recommended as it suppressed waves more effectively particularly under deeper immersion. The twin plate

breakwater was also found to be highly dissipative to the energy of the larger waves. A comparative study of these breakwaters is presented in Table 2.3c.

Table 2.3: Summary of the investigation of the plate-type free surface breakwaters

No	Breakwater Types	Ref.	Types of Analysis	Model Dimension	Wave d (m)	Test Parameters		Dimensionless Parameters			Energy Coefficients					
						D (m)	H ₁ (m)	T (s)	d/L	D/d	H/L	B/L	Test Condition	C _t	C _r	C _i
PLATE-TYPE BARRIER																
(a) Single Plate																
1	Horizontal plate	Patarapanich & Cheong, 1989	Experimental	B = 1 m	Reg	n.a.	n.a.	0.33-2.00	0.3	0.0-0.5	<0.075	0.2-0.8	D/d = 0.2-0.3	0.41-0.96	0.08-0.74	0.01-0.45
					PM	n.a.	n.a.	0.71-2.00	0.027-0.023	0.0-0.5	0.003-0.006	n.a.	D/d = 0.0-0.5	0.36-0.86	0.24-0.49	0.16-0.64
2	Hor. plate in front of a trapezoidal breakwater	Hsu & Wu, 1999	Numerical (BEM)	B = 0 - 1.5 m	Reg	0.3	n.a.	n.a.	0.2	0.2	n.a.	0.1-1.0	D/d = 0.2	0.52-1.0	n.a.	n.a.
3	Hor. plate in front of a vertical wall	Hu et al., 2002	Numerical (Linear potential wave theory & Eigen expansions)	n.a.	Reg	n.a.	n.a.	n.a.	0.25	0.3	n.a.	0.1-1.5	L ₁ /L = 1.5, p = 0.5	0.27-0.56	0.38-0.87	n.a.
4	Submerged inclined plate	Sabba Rao et al., 2009	Experimental	B = 0.50 m Thickness = 0.003 m	Reg	0.3 0.4 0.5	0 0.05 0.1 0.15	1.0 1.6 2.2	0.11-0.33	0.0-0.3	0.001-0.014	n.a.	d/L = 0.33, θ = 60°	0.32-0.50	n.a.	n.a.
(b) Twin Plate																
1	Twin hor. plate	Usha & Gayathri 2005	Analytical (Linear potential wave theory)	n.a.	Reg	n.a.	n.a.	n.a.	0.08-0.42	0.12-0.40	n.a.	n.a.	D/d = 0.12 D/d = 0.23 D/d = 0.40	0.08-0.83 0.34-0.87 0.26-0.83	0.15-0.90 0.27-1.0 0.22-0.95	n.a. n.a. n.a.
2	Twin hor. plate (with supports)	Neelamani & Gayathri 2006	Experimental (1:10)	B = 1.3 m	Reg	0.64	0.025-0.250	1.0-3.0	0.089-0.414	0.04-0.4	0.007-0.103	0.18-0.84	D/d = 0.04 D/d = 0.16 D/d = 0.40	0.25-0.79 0.22-0.60 0.18-0.75	0.32-0.68 0.35-0.65 0.43-0.77	n.a. n.a. n.a.
(c) Complex Plate Configurations																
1	T-type	Neelamani & Rajendran 2002a	Experimental (1:25)	Top width = 1 m Keel height = 0.25 m	Reg	0.7	0.05-0.20 (submerged)	1.0-3.0	0.09-0.45	0.01-0.29	0.004-0.133	n.a.	D/d = 0.0, d/L = 0.22 H/d = 0.29, d/L = 0.22 H/d = 0.10-0.21, d/L = 0.15	0.27-0.36 0.34-0.57 0.30-0.46	0.42-0.70 0.45-0.61 0.46-0.67	0.38-0.71 0.29-0.66 0.45-0.58
2	I-type	Neelamani & Rajendran 2002b	Experimental (1:25)	Vertical beam = 0.25 m Base width = 1 m	Reg	0.7	-0.10 to +0.10 -ve = submerg +ve = emerg	1.0-3.0	0.09-0.45	-0.14 to +0.14	0.004-0.133	n.a.	D/d = 0.0, d/L = 0.22 D/d = -0.14, d/L = 0.22 H/d = 0.05-0.07, d/L = 0.15 H/d = 0.10-0.18, d/L = 0.15	0.16-0.24 0.37-0.65 0.43-0.60 0.11-0.46	0.29-0.65 0.56-0.77 0.37-0.65 0.49-0.76	0.52-0.69 0.61-0.71 0.25-0.50 0.71-0.73
3	H-type	Neelamani & Vedagiri 2002	Experimental (1:25)	Front barrier = 0.55 m Rear barrier = 0.65 m Length = 1.95 m Spacing = 0.7 m	Reg	0.7	Front barrier = 0.1 - 0.2 m Rear barrier = 0.1 - 0.3 m	1.0-3.0	0.09-0.45	0.01-0.43	0.003-0.129	n.a.	D/d = (0, 0.14), d/L = 0.22 D/d = (0, 0.14), d/L = 0.45 D/d = (0.14, 0.14), H/d = 0.12-0.18 D/d = (0.28, 0.43), H/d = 0.12-0.18	0.38-0.62 0.13-0.37 0.30-0.62 0.08-0.47	0.24-0.30 0.42-0.61 0.28-0.40 0.36-0.75	0.52-0.79 0.49-0.77 0.53-0.72 0.41-0.67

2.2.3 Caisson-type

The key feature in distinguishing a caisson-type barrier from a solid-type barrier is that the caisson-type barrier is usually equipped with an open interference chamber that permits wave interaction taking place from within. The chamber is also used to ‘tune’ waves to be out of phase so as to minimise the wave activity in the vicinity of the breakwater; thus, it is often termed ‘absorbing caisson’. In some cases, multiple-chamber caissons are used to optimise the overall performance of the breakwater.

2.2.3.1 Single-Chamber Caisson

Günaydın and Kebdaşlı (2004; 2007) experimentally studied the hydraulic performance of the U-type and Π-type barriers under regular and irregular waves. These caissons were also perforated to enhance the energy dissipation performance. The settings of their experiments are presented in Table 2.4a. They discovered that the Π-type barrier was a better wave attenuator compared to the U-type barrier, and both impervious barriers were shown to be slightly more effective when compared to the perforated ones. They proposed several generic design formulae for both types of barriers as tabulated in Table 2.5.

The Π-type barrier was further investigated by Koftis and Prinos (2005b) using the unsteady Reynolds Averaged Navier-Stokes equations. They concluded that maximum wave reflection for this structure occurs at $B/L = n/2$ (where $n = 1, 2, 3\dots$) due to resonant excitation. They also found that the turbulent kinetic energy^a (TKE) field near the front wall was consistently higher than that of the rear wall (see Figure 2.3), and wave activity in the chamber was relatively small at higher immersion depths.

^a The full form of the TKE equation is

$$\underbrace{\frac{\partial K}{\partial t}}_{\text{Local derivative}} + \underbrace{u_j \frac{\partial K}{\partial x_j}}_{\text{Advection}} = \underbrace{-\frac{1}{\rho} \frac{\partial \overline{u_i' p'}}{\partial x_i}}_{\text{Pressure diffusion}} - \underbrace{\frac{\partial \overline{K u_i}}{\partial x_j}}_{\text{Turbulent transport}} + \underbrace{\nu \frac{\partial^2 K}{\partial x_j^2}}_{\text{Molecular viscous transport}} - \underbrace{\overline{u_i' u_j'} \frac{\partial \overline{u_i}}{\partial x_j}}_{\text{Production}} - \underbrace{\nu \frac{\partial \overline{u_i' \partial u_i'}}{\partial x_j \partial x_j}}_{\text{Dissipation}} - \underbrace{\frac{g}{\rho} \overline{\rho u_i'} \delta_i}_{\text{Buoyancy flux}}$$

The total mean kinetic energy is the sum of the kinetic energy of the mean velocity and the mean kinetic energy of the turbulence, K :

$$\left\langle \frac{1}{2} \rho |\bar{u}|^2 \right\rangle = \left\langle \frac{1}{2} \rho u_i u_i \right\rangle = \frac{1}{2} \rho U_i U_i + \left\langle \frac{1}{2} \rho u_i' u_i' \right\rangle = \frac{1}{2} \rho |\bar{U}|^2 + \rho K$$

where K can be quantified by the mean of the turbulence normal stress

$$K = \frac{1}{2} \langle u_i' u_i' \rangle = \frac{1}{2} [\langle u'^2 \rangle + \langle v'^2 \rangle + \langle w'^2 \rangle]; \text{ and}$$

the fluctuating part of the velocity is defined by:

$$u_i = U_i + u_i'$$

In computational fluid dynamics (CFD), the mean kinetic energy per unit mass associated with eddies is a fundamental flow property which must be computed in order for fluid turbulence to be modelled.

Table 2.4: Summary of the investigation of the caisson-type free surface breakwaters

CAISSON-TYPE BARRIER																	
No	Breakwater Types	Ref.	Types of Analysis	Model Dimension	Wave	Test Parameters			Dimensionless Parameters				Energy Coefficients				
						d (m)	D (m)	H ₁ (m)	T (s)	d/L	D/d	H/L	B/L	Test Condition	C _T	C _R	C _L
(a) Single-chamber Caisson																	
1	U-type (solid & perforated)	Günaydın & Keleşli 2004	Experimental	Hor plate = 0.25 x 0.1 m ² Ver plate = 0.125 x 0.1 m ² Holes = 1.8-cm diameter 10 holes on ver. plate 20 holes on hor. plate	Reg PM	0.6	0.075 0.125 0.175 0.230	0.08 - 0.20 0.08 - 0.16	0.8 - 1.5 0.9 - 1.7	n.a.	0.13 0.21 0.29 0.36	n.a.	n.a.	See Table 2.5			
2	T1-type (solid & perforated)	Günaydın & Keleşli 2007	Experimental	Hor plate = 0.25 x 0.1 m ² Ver plate = 0.125 x 0.1 m ² Holes = 1.8-cm diameter 10 holes on ver. plate 20 holes on hor. plate	Reg PM	0.6	0.075 0.125 0.175 0.230	0.11 - 0.23 0.08 - 0.16	0.8 - 1.5 1.0 - 1.7	n.a.	0.13 0.21 0.29 0.36	n.a.	n.a.	See Table 2.5			
3	T1-type (solid)	Kořitka & Prinos 2005b	Numerical (RANSE & VOF)	Base = 2 m Height = 0.90 m	Reg	2	0.4 - 1.2	0.25	2.04	n.a.	0.2 - 0.6	n.a.	n.a.	B/L = 0.32	0.02 - 0.62	0.35 - 0.79	n.a.
(b) Multi-chamber Caisson																	
1	W-type (perforated)	Brossard et al. 2003	Experimental	B = 0.36; 0.45; 0.54	Reg	0.25	0.08 0.12 0.16	n.a.	0.56 - 1.23	0.14 - 0.47	0.32 0.48 0.66	n.a.	n.a.	B = 0.36 m; D/d = 0.48 B = 0.54 m; D/d = 0.48 B = 0.54 m; D/d = 0.64	0.05 - 0.28 0.02 - 0.24 0.01 - 0.14	0.07 - 0.49 0.09 - 0.52 0.05 - 0.41	n.a. n.a. n.a.

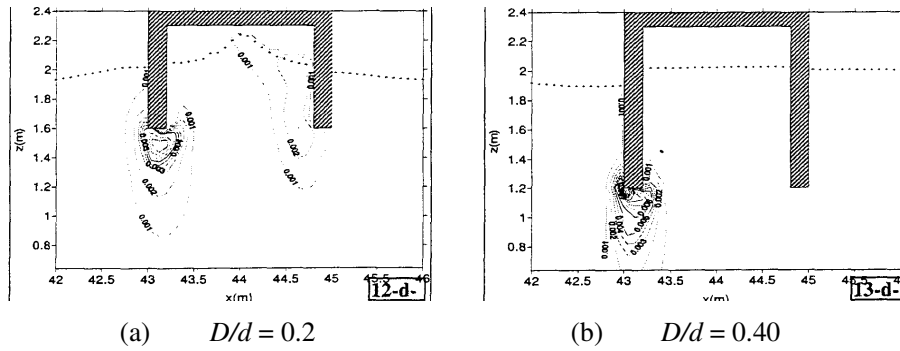


Figure 2.3: Normalised turbulent kinetic energy field, k/U_{max}^2
 (Source: Koftis and Prinos, 2005b)

Table 2.5: Energy coefficients equations for U-type and Π-type breakwaters
 (Source: Günaydın and Kebdaşlı, 2004; 2007)

	U-type breakwater		Π-type breakwater	
	Solid model	Perforated model	Solid model	Perforated model
Transmission: $C_T = \left[m(par1)^n \frac{L}{d-D} \right]^2$	$m = 1.1004$ $n = 0.2635$ $R^2 = 0.76$	$m = 0.8300$ $n = 0.2249$ $R^2 = 0.88$	$m = 0.6685$ $n = 0.2067$ $R^2 = 0.85$	$m = 0.8975$ $n = 0.2305$ $R^2 = 0.87$
Reflection: $C_R = \left[m(par1)^n \frac{L}{d-D} \right]^2$	<i>n.a.</i>	$m = 0.3573$ $n = 0.2224$ $R^2 = 0.56$	$m = 0.3789$ $n = 0.2267$ $R^2 = 0.59$	$m = 0.3742$ $n = 0.2170$ $R^2 = 0.50$

Note: $par1 = \frac{H_i^2(d-D)}{L^3}$, H_i = incident wave height, d = water depth, D = immersion depth, L = wavelength

2.2.3.2 Multiple-Chamber Caisson

Brossard *et al.* (2003) developed a \mathbb{H} -type barrier comprising two chambers – a solid chamber and an absorbing caisson with perforation at the seaside wall. The effectiveness of the absorbing caisson was experimentally compared with a non-absorbing caisson. The C_R of the non-absorbing caisson was about 0.9 over a broad range of wave period; whereas the C_R of the absorbing caisson ranged from 0.05 – 0.60. This implies that the absorbing caisson is indeed a good anti-reflection structure. They further mentioned that wave energy was suppressed much effectively by increasing the immersion depth of the caisson than by increasing the width. The details of the experimental results are presented in Table 2.4b. More discussion on the absorbing caisson is provided in Section 2.3.

2.2.4 Multipart-type

A multipart-type barrier is formed by an assembly of multiple structural elements, *e.g.* planks, rods, pipes, *etc.* These barriers are highly porous to the incoming waves, thus limiting wave reflection and the horizontal wave forces acting on the breakwaters. Wang *et al.* (2006) proposed a barrier that was made of a large number of closely-spaced horizontal plates (see Table 2.1) to retard the fluid particle motions in the vertical direction. The experimental results revealed that the breakwater exhibited a maximum C_R of about 0.6, and C_T values of less than 0.5 at $B/L > 0.25$. The influence of the relative gap interval of the plates on C_T and C_R was found to be marginal. The details of the experiments are outlined in Table 2.6.

Hsiao *et al.* (2008) developed a multipart-type breakwater that was an assembly of a number of closely-spaced bars placed in lateral and transverse manners interchangeably as shown in Table 2.1. The double barriers were arranged in pair with a gap spacing, s . The experimental results showed increased wave transmission, and reduced reflection and dissipation performance with the increase in the porosity of the structure with a fixed gap distance. The C_R displayed a series of peak values (this phenomenon is termed ‘Bragging effect’) when the $s/L = 0.5$ and 1.0.

Table 2.6: Summary of the investigation of the multipart-type free surface breakwaters

No	Breakwater Types	Ref. & Year	Types of Analysis	Model Dimension	Test Parameters			Dimensionless Parameters				Energy Coefficients				
					Wave d (m)	D (m)	H _i (m)	T (s)	d/L	D/d	H _i /L	BL	Test Condition	C _T	C _a	C _L
1	Multiple-layer Breakwater	Wang et al. 2006	Experimental	0.1 m < Height < 0.5 m Δgap = 0.04 (11 layers) B = 0.2, 0.4 and 0.6 m	0.4 (Freeboard = 0.10 m)	0.3	0.04 - 0.16	0.07 - 1.46	n.a.	0.75	0.04 - 0.09	0.08 - 0.75	B = 0.2 m Δgap = 0.04 (11 layers)	0.14 - 0.37	0.08 - 0.58	n.a.
2	Porous-pled Breakwater	Hsiao et al. 2008	Experimental (1.64)	B = 0.038 m H = 0.025 m (single and double units) Porosity = 0.4, 0.6, 0.8	0.5	n.a.	0.03 - 0.08	0.7 - 1.8	0.015 - 0.051	n.a.	0.02 - 0.08	n.a.	Double units, ε = 0.4 Double units, ε = 0.6 Double units, ε = 0.8	0.10 - 0.85 0.49 - 0.92 0.48 - 0.93	0.10 - 0.52 0.08 - 0.40 0.05 - 0.24	0.13 - 0.62 0.05 - 0.63 0.03 - 0.58

2.3 Wave Absorbing Caissons

The use of prefabricated concrete caisson becomes prevalent in the design of ports and harbours over the last 50 – 60 years because it strikes a balance of advantages and disadvantages between rubble and vertical breakwaters. The most common form of caisson is rectangular or square in plan. Caissons may typically be 15 – 30 m long, divided internally into cells and seated on a rubble mound structure (Allsop *et al.*, 1996). They are designed to be floated out, ballasted with water to sink them into position at the construction site, and then filled with heavy materials (*e.g.* rock, sand, or concrete ballast) to ensure adequate weight to resist sliding or overturning.

A perforated caisson breakwater employing a perforated front wall and an interference chamber was first proposed by Jarlan (1961) and subsequently constructed in Comeau Bay, Canada in 1966. The Jarlan's breakwater has a perforated wall through which waves can enter and leave the chamber freely, and the energy is dissipated by the generation of eddies. Since then, the perforated caissons are increasingly being adopted worldwide as seawalls and breakwaters due to their high wave-absorbing ability. The application of the perforated caissons, which was initially intended for use in relatively calm seas, has gradually been adopted in heavier, open seas (Takahashi *et al.*, 2002). Even though a vast research has been conducted to study the bottom-seated perforated caisson breakwaters, the design concepts and some of the physical principles have been found to be particularly applicable to the free surface perforated caisson breakwaters. These aspects of the study are further addressed in the following sections.

2.3.1 Wall Configuration

There are four types of walls incorporated in breakwater caissons, *i.e.* vertical wall, sloped wall, concave wall and convex wall (Tanimoto and Goda, 1992). The caissons of vertical wall caisson are the simplest in design; however, the horizontal wave forces acting on the wall are almost in the same phase from the top to the bottom, thus posing a considerable force on the caisson. Some of the possible modes of major failures of the vertical caissons due to excessive wave action are sliding and overturning of the upright sections (Goda, 1985). On the other hand, breakwaters of other wall configurations, *i.e.* sloped, concave and convex, intercept waves at varying phases and the wave impact effect is thus limited. A caisson with a sloped wall is the most stable under the action of wave crests if the slope is selected appropriately; it is, however, difficult to be built for the whole height (Tanimoto and Goda, 1992). The concaved-wall caissons prevent wave overtopping by directing the

excessive waves to seaward. They help to bring down the width requirement and therefore suitable to be built in relatively deep water regions. For caissons with convex walls which also appear as quadrant-circles, the downward components of the wave pressures exerted on the curved surfaces act towards the centre of the breakwater; hence no rotational moment is yielded. As a result, a uniform distribution of the reaction at the bottom slab would be expected. See Section 1.4.2 for further benefits of the semicircular caisson.

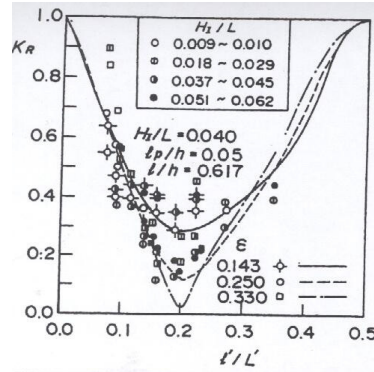
2.3.2 Caisson Perforation

2.3.2.1 Perforated Wall Type

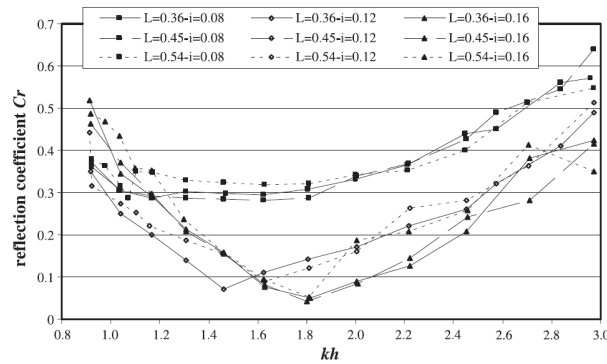
There are various types of perforated wall for a caisson breakwater. The most common ones are horizontal- and vertical-slit walls, while circular- and rectangular-hole walls are also popular. There is some evidence that the shape of the wall elements is the primary influence on the hydraulic performance of the breakwater (Gruene and Kohlhase, 1974) but this argument was later challenged by Gardner and Townend (1988), Allsop (1995) and Takahashi *et al.* (2002) who were in consensus that the influence was relatively weak. Further, Gruene and Kohlhase (1974) and Allsop (1995) realised from their experimental studies that wave transmission and reflection by the vertical slotted wall were not affected by the wall thickness.

2.3.2.2 Wall Porosity

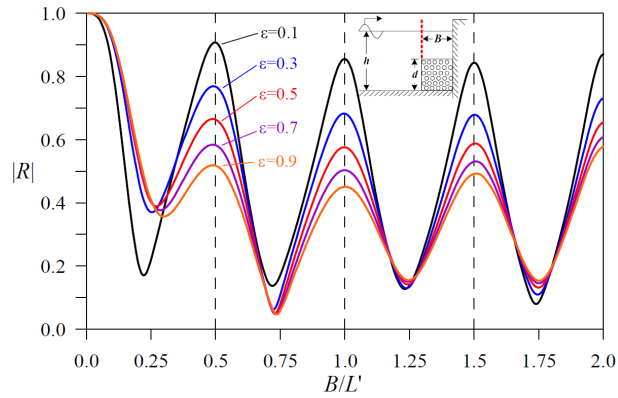
The influence of wall porosity on the reflective performance of the bottom seated caisson breakwaters was studied by Allsop and McBride (1993), Takahashi *et al.* (2002), Liu *et al.* (2007) and Yueh *et al.* (2008); and that of the free surface caisson breakwater was studied by Brossard *et al.* (2003). These literatures confirmed that the wall porosity is a major parameter affecting the C_R of the perforated caisson breakwaters, for which higher wall porosity induces lesser reflection regardless of the water depth. The C_R of these perforated structures displayed a 'U'-shape trend when plotted with respect to a relative wave period term as shown in Figures 2.4a and 2.4b. If the relative term is increased to a higher value, one should observe the C_R fluctuates like the one seen in Figure 2.4c. This is called the 'Bragging effect' (Jeon and Cho, 2006) that is due to wave resonance within the interference chamber (see Section 2.3.3).



(a) Annotations: K_R = wave reflection coefficient; l = breakwater chamber width; L' = local wavelength, ϵ = front wall porosity, h = water depth, H_I = incident wave height, L = offshore wave length



(b) Annotations: C_r = wave reflection coefficient; k = wave number; h = water depth; L = local wavelength in meter, i = breakwater immersion depth in meter



(c) Annotations: $|R|$ = wave reflection coefficient; B = width of the breakwater chamber; L' = local wavelength; ϵ = front wall porosity; h = water depth

Figure 2.4: C_R of the perforated wall caissons – (a) Bottom-seated perforated wall caisson [Takahashi *et al.*, 2002]; (b) Free surface Π -type breakwater [Brossard *et al.*, 2003]; (c) Absorbing-type breakwater [Yueh *et al.*, 2008]

Another purpose of the perforated walls of the breakwater caisson is to dampen the wave energy by dissipation as water flows through the orifices. A Particle Image Velocimetry (PIV) study by Michel *et al.* (2003) showed that the vortices developed beneath the jet-like flow at the rear wall, as illustrated in Figure 2.5a, was the primary cause of the energy dissipation. Strong annular vortices were also observed at the seaward wall of the free surface U-type breakwater during flow exchange (Brossard *et al.*, 2003).

The criteria for selection of the ‘optimum’ porosity for a perforated caisson vary with respect to applications. In fact, a perforated caisson breakwater with a specific porosity may fail in one situation but do very well in others. Some of the major concerns that would affect the choice of the ‘optimum’ caisson porosity are the tolerance to wave reflection in the vicinity of the breakwater, the sensitivity of the construction sites, the stability of the breakwater against external forces, the restrictions of policies and regulations by the local authorities, and most importantly the preference of the designers.

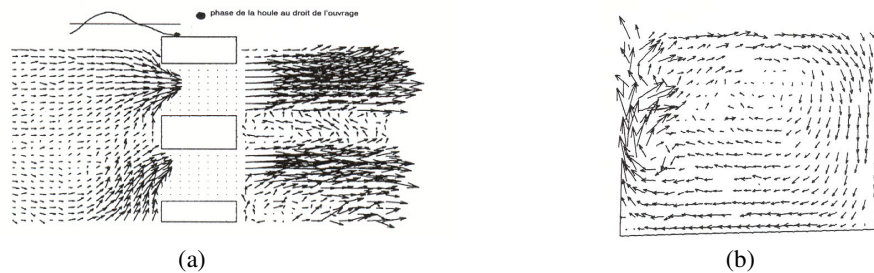


Figure 2.5: Velocity and turbulent fields in the vicinity of a perforated caisson breakwater – (a) Perforated wall of 28% porosity; (b) Interference chamber
(Source: Michel *et al.*, 2003)

2.3.3 Interference Chamber

The interference chamber of a perforated caisson is constructed to maximise energy dissipation, to reduce reflection and run-up of waves, and to prevent impulsive wave forces acting on the caissons (Takahashi *et al.*, 1994; Takahashi and Shimosako, 1994; Allsop and Kortenhaus, 2001). The presence of the interference chambers renders the caisson breakwaters particularly suitable for use not only as quay walls inside shelter harbours but also as external caisson breakwaters for wave protection.

2.3.3.1 Wave Reflection

As mentioned earlier, the typical interference chamber consists of a perforated front screen separated from a solid rear screen by a spacing distance. The chamber can be open, or covered by a slab at the top with a venting system to reduce the air pressure within the chamber. The response of the chamber is often ‘tuned’ with response to the period of the incident wave by varying the resonant mode (Takahashi *et al.*, 2002; Liu *et al.*, 2007) and by varying pressure (Ikeno *et al.*, 1998).

The resonant behaviour within the chamber, as shown in Figure 2.4, is due to the interaction between the incident and reflected progressive waves in the open seas and in the chambers. At resonance, the C_R is at its maximum and the reflected wave is approximately in phase with the incident wave. The numerical modelling obtained by Fugazza and Natale (1992) showed that the resonant condition for a single-chamber breakwater is given by $B/L = (2n+1)/4$, where $n = 0, 1, 2, \dots$, $B =$ width of the interference chamber; and $L =$ local wave length. It is stressed that the resonant mode of practical interest is the fundamental mode where $n = 0$, *i.e.* $B/L = 0.25$ due to the width limit of the breakwater. At this optimum spacing, wave transmitted through the front screen is reflected off the solid rear screen to return towards the front screen out of phase with the next wave. The resulting interaction between wave crest and trough close to the perforated wall leads to considerable energy dissipation and low reflection. For wavelengths outside the optimum range, the reflections become greater.

Earlier numerical studies showed that the fundamental mode of resonance occurred at $B/L = 0.25$ for a single chamber caisson. Nevertheless, from the laboratory testing conducted by Allsop (1995) the minimum C_R was reported to occur at $0.15 \leq B/L \leq 0.25$. This might be attributed to the delay of wave advance due to wave interception at the perforated wall.

2.3.3.2 Energy Dissipation

Some amount of wave energy is dissipated as flow interacts with the interference chamber. For instance, the annular flow formed in the chamber, as shown in Figure 2.5b, sets the water in turbulent and reduces the energy through frictional dissipation (Michel *et al.*, 2003). Further, energy dissipation would be anticipated when the water level difference is large between the inside and outside of the wave chamber (Allsop and Kortenhuis, 2001; Takahashi *et al.*, 2002). The amount of energy dissipation depends on several factors, *e.g.* chamber dimensions, wetted area in the chamber, wall roughness, *etc.*

2.3.3.3 Horizontal Wave Loadings

Subsequent to the reduction of wave height in front of the breakwater, the resulting horizontal loadings exerted on the structure are reduced accordingly. This is mainly due to the phase lag between the horizontal wave forces acting on the front and rear walls, and the effect of the negative forces acting on the shoreward of the perforated wall (Michel, *et al.*, 2003; Allsop and Kortenhaus, 2001). Phase difference between the peaks of the horizontal forces on both walls becomes an advantage of the perforated caisson as it prevents the occurrence of the simultaneous wave impact corresponding to those maximum forces.

Liu *et al.* (2008) reported that the phase difference between the horizontal force on the front wall F_f and that on the rear wall F_r increased with the increasing B/L , and the phase difference between the total horizontal force F_x and the shoreward force F_f increased with the porosity of the front wall. They also found that the peaks of F_x emerged between the maximum values of F_f and F_r , implying that the highest total horizontal force occurred after the wave crests entered into the chamber and before attacking the rear wall.

To the knowledge of the author, there are yet to be similar studies or literatures on the free surface rectangular caisson-type breakwater; however, it is believed that the horizontal loading characteristics of both types of the breakwaters are almost analogous.

2.4 Wave Screens

Wave screens are inexpensive and easily constructible breakwaters in comparison to the caisson breakwaters. The basic structure is a screen with a series of slots or holes that allow energy dissipation in the viscous eddies formed by the flow through the perforations. The porosity of the wave screens is the key design parameter in controlling the hydraulic performance of the breakwaters. Due to the relatively large transmission of waves through the screens, the efficiency of the breakwaters is therefore restricted. Even so, wave screens have a number of desirable features that have encouraged their use within harbours, *i.e.* easy navigation within the harbour due to reduced wave activity, permission of water exchange and maintenance of water quality within the basin, and reduced wave loads on the barrier. In general, there are two types of wave screens commonly used in harbours, *i.e.* the horizontally slotted screens and the closely spaced piles.

2.4.1 Horizontally Slotted Screens

A typical slotted screen comprises a series of closely spaced components (*e.g.* precast concrete or timber planks, and pipes) mounted on a supporting frame extending from the seabed to well above the water surface. These structures generally have lower construction cost; however, the screen components may need to be heavily maintained due to shorter design life. These slotted breakwaters find their applications in many recreation and fishing ports where partial transmission of waves is permissible.

The influence of screen porosity on the hydraulic performance of the slotted breakwaters has been surveyed by some researchers. Bennett *et al.* (1992) proposed a theory in calculating the reflection properties for screens both with and without a solid backing wall. For a single wave screen, the C_R was found to increase with increasing wave height, and the C_R variation became smaller as the porosity of the screen was reduced. Adding a solid back wall to the screen with an interval gap in between, standing waves formed within the space and the CR displayed the braggging effect resembled to that shown in Figure 2.4c.

Allsop and Hettiarachchi (1988) studied wave screens of 14% – 28% porosities with respect to a broad range of relative screen spacing, l/L ranging from 0 – 1.2. They found that the lowest C_R occurred at $B/L \approx 0.25$ and 0.75, and the highest values occurred at $B/L \approx 0.5$ and 1.0; and the influence of screen porosity was only apparent when the wave reflection was small. Note that the test range of B/L is much wider than the range used in practice. Due to the restriction of harbour space, the screen spacing is normally confined to $0.1 < B/L < 0.5$. In another study, Allsop (1995) recommended that the porosity of the screen ranging from 5% – 15% should be provided for reasonably good wave suppression. McBride *et al.* (1994) proposed several simple design formulae to predict the reflection performance of single and double wave screens.

Attention was also devoted to studying the performance of wave screens that were formed by circular pipes, in which the details were discussed by Balaji and Sundar (2002) and Krishnakumar *et al.* (2010).

2.4.2 Pile Breakwaters

A pile breakwater is typically formed by a row or multiple rows of closely spaced piles extending from the seabed to some distance above water surface. In practice, construction of these breakwaters is difficult and expensive to drive single piles closely together (Allsop, 1995). Nonetheless, these breakwaters are successfully employed in many ports and harbours that are exposed to mild to moderate wave fields (Heikal *et al.*, 2007).

The functional performance of the pile breakwaters is often evaluated by examining the C_T and C_R with respect to the geometry of the piles, the pile dimensions, the pile spacing and their distributions. The most typical pile shapes have been rectangular and circular. The study of wave interaction on the screens with rectangular piles was studied by Huang (2007a), Heikal *et al.* (2007) and Koraim (2007); whilst those with circular piles was investigated by Subba Rao *et al.* (1999), Yagci *et al.* (2006), Koraim (2007) and Heikal *et al.* (2007). Overall, these investigations showed an increase in wave attenuation with decreasing pile spacing and increasing pile size. The square pile breakwater was found to be more efficient than the circular ones in wave attenuation by 5% – 15%; however, the breakwater performance was less affected by the pile arrangement (Koraim, 2007).

2.5 Skirt Breakwaters

A typical skirt breakwater or curtainwall pile breakwater consists of a row of solid wall projecting from an arbitrary depth of water to above water surface but does not reach down to the sea bottom leaving a significant gap below it. The vertical wall attached to the supporting piles offers wave protection mainly by reflection. If closely-spaced piles are adopted, the efficiency of the barriers would be greatly improved due to additional energy dissipation induced by the piles (Suh *et al.* 2006). Skirt breakwaters are particularly suitable to be built in water depth up to 20 m and are capable of protecting harbours in moderate to severe wave climates with significant wave height of up to 3 m or more and peak periods up to 6 seconds (Gilman and Kriebel, 2000). Prototype examples of these structures that have been successfully completed are mainly in the USA, *e.g.* Alaska, Washington and Oregon.

Numerous literatures published in the past provided description of the hydrodynamic characteristics of a skirt breakwater (without a supporting structure) using theoretical and empirical approaches. Wiegel (1960) developed a theory based on wave power transmission past a rigid vertical thin barrier extending from above the water surface to some distance

below the surface. The theoretical results were in agreement with the laboratory measurements in wave transmission decreased with an increase of wave steepness. The Wiegel's method was further validated by the experimental results of Reddy and Neelamani (1992) and Kriebel and Bollman (1996). They commented that the Wiegel's method generally over-predicted wave transmission because it did not account for wave reflection. Other theories developed for determination of the interaction of waves with such wave barriers are the boundary integral equation method (Liu and Abbaspour, 1982), volume of fluid method (Koutandos, 2009), and the eigenfunction expansion method (Losada *et al.*, 1994; Isaacson *et al.*, 1999; Kriebel, 2000; Sahoo *et al.*, 2000; Suh *et al.* 2007; Rageh and Koraim; 2010).

The study of skirt breakwaters was further extended to the use of the perforated truncated wall in limiting reflection of waves. Koutandos (2009) found that the skirt breakwater with solid wall induced greater energy dissipation than those with perforated walls. The numerical models showed strong vortices circulating beneath the lower tip of the solid wall and extending to a certain distance downward; on the other hand, the turbulence kinetic energy field, which was observed along the main body of the perforated wall, exhibited higher intensity at the upper part of the wall near the free surface where wave action was more pronounced.

Other strategies to improve the hydraulic efficiency of the skirt breakwaters are: (1) applying a closely-spaced piles of various shapes (Suh *et al.*, 2006; Suh *et al.*, 2007); (2) attaching a horizontal slotted screen underneath the vertical solid wall (Rageh and Koraim, 2009; Rageh and Koraim, 2010); and (3) adopting the double skirt breakwaters in which the solid walls have different length (Suh and Ji, 2006; Ji and Suh, 2008).

2.6 Bottom Seated Semicircular Breakwaters

Ever since the world's first semicircular breakwater was constructed at Miyazaki Port in Japan in 1993, the concept of semicircular breakwater receives considerable attention by researchers worldwide, particularly those from Japan, India and China. A review of these breakwaters is vital in this study because it provides some useful reference for the development of the free surface semicircular breakwater in this study.

2.6.1 Classification

There are various designs of semicircular breakwaters that have been proposed and tested in Japan. Sasajima *et al.* (1994) classified the breakwater designs into four types:

- (i) the ‘solid type’ having impermeable front and rear walls;
- (ii) the ‘front wave-dissipating type’ having only a perforated front wall;
- (iii) the ‘permeable type’ having perforated front and rear walls; and
- (iv) the ‘rear wave-dissipating type’ having only a perforated rear wall.

The schematic views of these breakwater types are presented in Figure 2.6. Each type of the breakwater has unique hydraulic characteristics. The ‘solid-type’ is highly reflective and has low resistance to wave overtopping. This drawback can be offset by using the ‘rear wave-dissipating-type’ because the openings on the rear walls allow the overtopping water to infiltrate the interference chamber. These openings on the rear wall also reduce the wave reflection within the harbour. The ‘front wave-dissipative-type’ reduces the seaward reflected waves by energy dissipation, while the ‘permeable-type’ enables seawater exchange between the harbour and open seas when driven by tidal currents and waves.

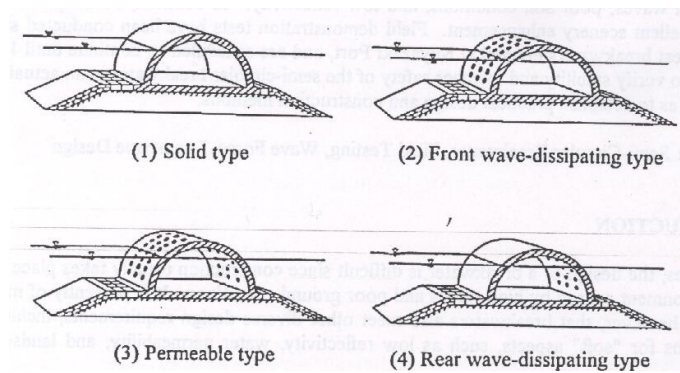


Figure 2.6: Types of semicircular caisson breakwaters (Source: Sasajima *et al.*, 1994)

2.6.2 Research Development

2.6.2.1 Emerged Breakwaters

The study of semicircular breakwaters was first initiated by Tanimoto and his research team dated in the 1980s. Extensive tests on various types of semicircular breakwater were conducted in a 2D wave flume. They reported their findings in a series of publications, *e.g.* Tanimoto *et al.* (1987; 1988 and 1989). Figures 2.7 – 2.9 display some of their experimental results presented in the forms of the coefficients of transmission K_T , reflection K_R and energy

dissipation K_L^2 (refer to Equation (3.21)) plotted against the breakwater freeboard-to-incident wave height ratios $h_c/H_{1/3}$, the incident wave height-to-water depth ratios, $H_{1/3}/d$ and the chamber width-to-wavelength ratio, $B_c/L_{1/3}$. The effects of porosity at the front wall, ϵ_f , at the rear wall, ϵ_r and at the bottom, ϵ_b are also illustrated in the figures. It can be seen from the figures that the ‘rear wave-dissipating type’ breakwater is a better wave attenuator than the ‘solid type’ breakwater due to infiltration of the overtopping waves allowed by the rear perforated wall (Figure 2.7a); whereas the ‘front wave-dissipating type’ outperforms the ‘permeable type’ significantly (Figure 2.7b). In Figure 2.8, the ‘solid type’ breakwater is shown to be more reflective than the ‘front wave-dissipating type’. In terms of energy dissipation, both the ‘front wave-dissipating type’ and the ‘permeable type’ breakwaters dissipate a significant amount of wave energy with their perforated walls and interference chambers (Figure 2.9). It is also learnt from the figures that the porosity of the structure is a major influence on the hydraulic performance of the bottom-seated semicircular breakwaters.

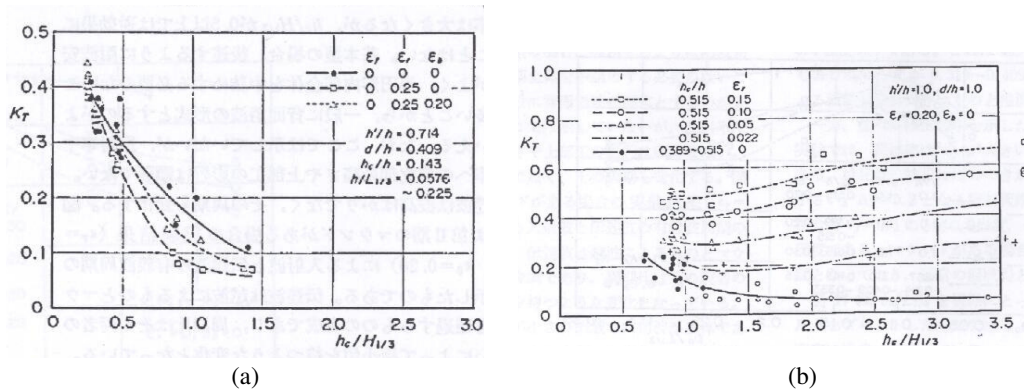


Figure 2.7: Transmission coefficients of the bottom-seated semicircular breakwater; (a) the solid and rear wave dissipating type; and (b) the front wave-dissipating and the permeable types (Source: Tanimoto *et al.*, 1989)

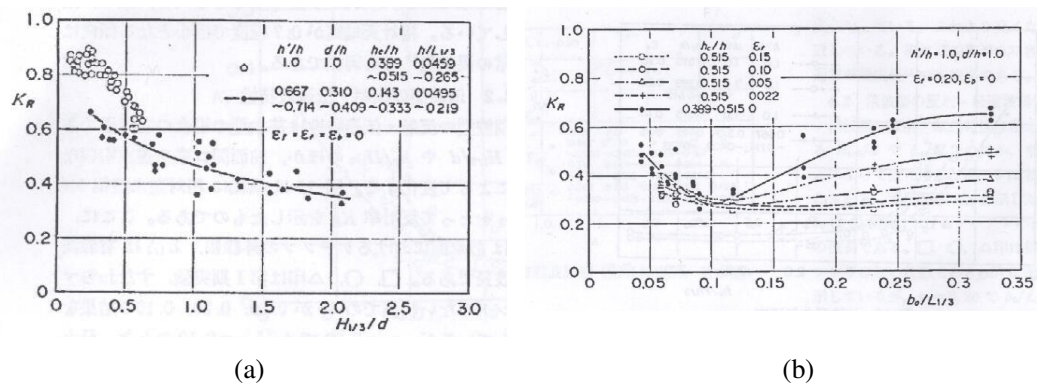


Figure 2.8: Reflection coefficients of the bottom-seated semicircular breakwater; (a) the solid type; and (b) the front wave-dissipating and permeable types (Source: Tanimoto *et al.*, 1989)

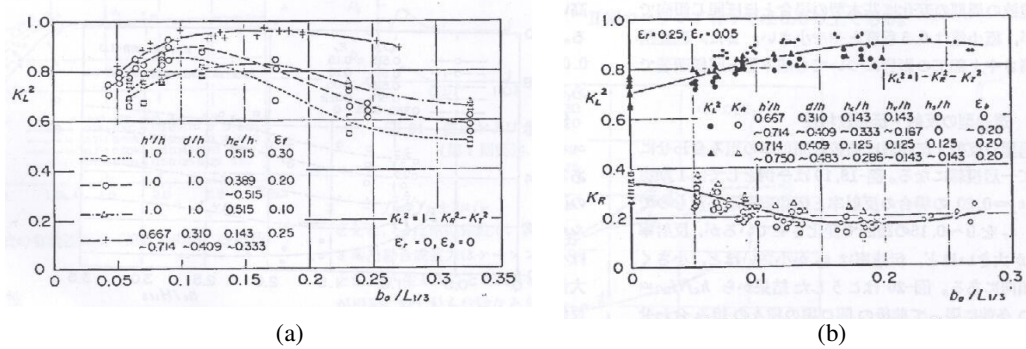


Figure 2.9: Energy dissipation coefficients of the bottom-seated semicircular breakwater; (a) the front wave-dissipating type; and (b) the permeable type (Source: Tanimoto et al., 1989)

Tanimoto and his team also investigated the wave loadings behaviours of the ‘solid type’ semicircular breakwaters. Tanimoto *et al.* (1987; 1988; 1989) found that the horizontal component of the wave forces applied to a semicircular surface was smaller than that applied to an upright wall, and the vertical force component applied downward along the wall provided additional stability against the waves. They nullified the uplift wave pressure acting on the bottom slab when (i) the porosity of the bottom slab was more than 10%; and (ii) the wave chamber was not airtight. Tanimoto and Takahashi (1994a) calculated the wave forces acting on the emerged semicircular breakwater using Goda’s formulae (1974) designed for vertical wall structures. They introduced a phase-modification coefficient and an angle-modification coefficient to address the geometry of the semicircular structures. A brief discussion of Goda’s model is presented in Section 3.5.

Sasajima *et al.* (1994) conducted field measurements at the prototype semicircular breakwater (see Figure 1.1) installed at the Miyazaki Port from 1993 to 1994 with the aim of verifying the structural stability and safety of the structure under the attack of severe storm waves. The results confirmed the findings of Tanimoto (1989) that (i) a reduction in the horizontal wave force component due to phase difference in the wave pressure are applied to the curved surface of the breakwater; and (ii) almost equal amount of uplift and inner wave pressure applied to the bottom slab of 10% porosity in which they offset each other by being in the opposite directions. They also found an increase of the sliding resistance and stability of the structure due to simultaneity of the peak occurrence between the horizontal wave component and the vertical downward wave force component. Sasajima *et al.* (1994) compared the measured and calculated horizontal wave pressures using the modified Goda’s method and a good agreement was attained for smaller waves with a height up to 3 m; the measured values were comparatively less for greater wave heights due to the effects of wave

breaking and overtopping. Similar conclusions were also drawn by Aburatani *et al.* (1996) based on a large field data set taken during typhoons occurring from 1993 to 1995.

The study of the bottom-seated semicircular breakwater was extended by a group of devoted Indian researchers who conducted the works using the 2D wave flume of the Department of Ocean Engineering, Indian Institute of Technology in Madras from 1997 to 2002. Their studies mainly emphasised on the evaluation of the hydrodynamic characteristics of the solid and perforated semicircular breakwaters under various wave conditions and water depths.

Sundar and Raghu (1997a and 1997b) re-confirmed by experimental approaches that the ‘solid type’ breakwater was highly reflective in both regular and irregular seas with $0.5 < C_R < 0.95$; however, the C_R variation was insensitive to the change of wave steepness. Sri Krishna Priya *et al.* (2000a) measured the wave pressures along the seaward circumference of the solid breakwater immersed at different levels under regular waves. They noticed an exponential dynamic pressure decay from water surface towards the bed, with larger pressure on the structure from longer period waves and smaller immersion depth. They further commented that the modified Goda’s method over-predicted the pressure, particularly closer to still water level. Similar study was undertaken by Graw *et al.* (1998), who reported that the modified Goda’s method under-predicted the pressure exerted on the impermeable structure at the relative water depth, $d/L < 0.35$, and an over-prediction of pressure at $d/L > 0.58$.

For the ‘front wave-dissipating type’ breakwater, Dhinakaran and his research team conducted a detailed study on the effect of the front wall porosity and the effect of water depth on the hydrodynamic behaviours of the structure through laboratory tests. They reported their progressive findings through a number of publications, *e.g.* Dhinakaran *et al.* (2001a), Dhinakaran *et al.* (2001b), Dhinakaran *et al.* (2002a) and Dhinakaran *et al.* (2008). They selected three front wall porosities in their studies, *i.e.* 7%, 11% and 17%, and they found that the C_R and the normalised forces decreased with the increasing breakwater porosity. They also observed that the normalised vertical forces (acting downward) were 2 – 5 times greater than the normalised horizontal forces, which would increase the stability of the structure. Dhinakaran *et al.* (2008) presented a number of criteria that would optimise the design of the ‘front wave-dissipating type’ breakwater: (i) the front wall porosity was 11%; (ii) the total height of the breakwater was 1.25 times the water depth; and (iii) the height of the rubble mound was 0.29 times the total height of the breakwater.

2.6.2.2 Submerged Breakwater

The submersible semicircular breakwater was first built at the Yangtze River Estuary, China from 1998 to 2000. The details of which are presented in Table 1.2. These breakwaters are designed to accommodate a large tidal range at the estuary. They emerge in low waters and are submerged in high waters. The Chinese and Indian researchers have provided major contribution in investigating the hydrodynamics of the alternatively submerged and submerged semicircular breakwaters.

Sri Krishna Priya *et al.* (2000b) experimentally explored the ‘solid type’ breakwater with different submergence ratios $d/h = 1.0, 1.2$ and 1.4 , where h and d are the height of the breakwater and the water depth, respectively. In comparison with the emerged breakwater, the transmission of waves above the breakwater reduced the C_R values from $0.50 - 0.90$ to $0.15 - 0.54$, with higher C_R at smaller d/h ratios. The breakwater offered higher wave attenuation ability at $d/h = 1.0$. They also found that the horizontal and vertical forces on the breakwater increased with the increasing wave period, and the vertical forces (acting downward) was almost twice the horizontal force during submergence.

In the prediction of wave pressures, the use of the modified Goda’s method was proven to be inappropriate by Yu *et al.* (1999). Subsequently, Xie (1999; 2001) accounted for the effect of the wave force acting on the inner circumference of the semicircular arch and introduced a new phase modification coefficient in the Goda’s method. This intergrated model was later adopted in the design of the south jetty of the first stage project of the Deep Channel Improvement Project of Yangtze River Estuary, China.

The numerical simulations of wave forces on the submerged impermeable semicircular breakwaters were explored by a number of Chinese researchers. Jia (1999) first used the boundary element method of potential flow theory to resolve the problem; however, the model neglected water viscosity and the energy dissipation mechanisms such as wave breaking, vortex generation and diffusion during wave-structure interactions could not be simulated. Yuan and Tao (2002; 2003) addressed this problem in their hybrid model incorporating both the boundary element method and the finite difference method. Liu and Tao (2004) further improved the Yuan and Tao’s model using the Reynolds Averaged Navier Stokes equations to simulate solitary wave interaction with the breakwaters. The model is capable of predicting the velocity and pressure fields, vorticity and diffusion, wave surface deformation near the breakwaters, and wave forces on the structure. It is worthwhile

to highlighting some interesting observations of the three typical hydrodynamic states of the semicircular structure:

- (a) *Emerged breakwater with no wave overtopping*: High peak wave run-up and agitating water surface in front of the breakwater.
- (b) *Breakwater with its crest at free surface*: Only very steep waves managed to pass through the breakwater. Large vortices were generated near the free surface at the lee of the breakwater due to the effect of wave impact. The velocity near the bottom of the structure was relatively small.
- (c) *Submerged breakwater*: After wave crests flow past the submerged breakwater, a large clockwise vortex was generated close to the bottom rear of the structure and gradually diffused near the water surface. The resulting bottom vortex may cause local scour at the leeside of the breakwater.

Zhang *et al.* (2005) experimentally studied the wave loadings on a ‘solid-type’ semicircular breakwater subjected to oblique waves in both regular and irregular seas. They found that the maximum horizontal wave forces under both wave crests, F_c and troughs, F_t were almost identical when the structure was either largely emerged or submerged, *i.e.* $|d'/H_i| > 1$ (where d' is the vertical distance between the water level and the crest of the breakwater, and H_i is the incident wave height); however, F_t were much larger than F_c when the breakwater was at the alternately submerged situation, *i.e.* $|d'/H_i| < 1$. This phenomenon was also observed by Yu *et al.* (1999). Zhang *et al.* (2005) further explained the distortion phenomenon of the elliptical tracking of the water particles as waves ran down the semicircular breakwater, whereby the water particle velocity in the opposite direction in turn became larger. The effect of angle of wave incidence on the horizontal loadings is complicated; therefore the findings are not discussed here. More details of the experimental works are provided by Wang *et al.* (2005) and Wang (2006).

2.7 Summary

The use of various types of free surface breakwater as alternatives to the conventional breakwaters has been thoroughly discussed in this chapter. These breakwaters, however, are subjected to a number of drawbacks, *e.g.* insufficient wave protection, high reflection, and survivability during storms. The aim of this study is to propose a free surface semicircular breakwater that is functionally viable and is able to serve as an effective energy dissipater rather than a good wave reflector. Breakwaters of a semi-cylindrical configuration seated on rubble mound structures have been widely studied; however, literatures pertaining to the free surface semicircular breakwater are particularly scarce. The emphasis of this chapter has been given to the bottom seated semicircular breakwaters whereby it is believed that some of the hydrodynamic interactions of the breakwater are somewhat similar to those of the free surface ones. Some strategies in optimising the breakwater performance have also been discussed. These include the perforated breakwater caissons, wave screens and skirt breakwaters. The design principles of these structures form a good reference to the development of the breakwater for this study.

3

Theoretical Considerations

3.1 General

This chapter describes some of the theoretical considerations associated with the performance evaluation of the breakwater design, the generation and measurement of the laboratory waves, the hydrodynamic loadings on the semicircular structures and the dimensionless analysis for result interpretation in the subsequent chapters.

3.2 Linear Wave Theory

Linear wave theory, also often referred to as Airy wave theory or small amplitude wave theory, gives a linearised description of the propagation of two-dimensional periodic gravity waves on the surface of a homogeneous fluid domain with a uniform mean depth. This linear theory is often used to get an estimate of wave characteristics and their effects associated to coastal and ocean engineering applications. The theory is developed based on the following assumptions:

1. the fluid is homogeneous, incompressible and inviscid;
2. no surface tension, *i.e.* wavelength is greater than about 3 cm;
3. constant and uniform pressure at the free surface;
4. the water is of constant depth, d and wavelength, L (or period, T);
5. wave amplitude, a is small compared to the wavelength and water depth;
6. the wave motion is two dimensional which leads to long crested waves;
7. the wave height, H is constant along the crests; and
8. the waves are of constant form and they do not change with time.

The derivation of the Airy wave equations starts from the Laplace equation for two-dimensional flow. The Laplace equation is an expression of the velocity potential $\phi(x, z)$ in horizontal and vertical directions:

$$\frac{\partial^2 \phi}{\partial x^2} + \frac{\partial^2 \phi}{\partial z^2} = 0 \quad (3.1)$$

At the bottom, the vertical component of the water particle velocity w must be zero:

$$w = \frac{\partial \phi}{\partial z} = 0 \quad \text{at } z = -d \quad (3.2)$$

At the free surface, there is a kinematic boundary condition that relates the vertical velocity at the surface to the mean water position ($z = \eta = 0$):

$$w = \frac{\partial \eta}{\partial t} + u \frac{\partial \eta}{\partial x} \quad \text{at } z = \eta \quad (3.3)$$

The dynamic boundary condition using Bernoulli equation for unsteady irrotational flow must be satisfied:

$$\frac{p}{\rho} + \frac{1}{2}(u^2 + w^2) + g\eta + \frac{\partial \phi}{\partial t} = 0 \quad (3.4)$$

where p is the pressure, ρ is the fluid density and g is the acceleration of gravity. At the surface where the pressure is zero, Equation (3.4) becomes

$$\frac{1}{2}(u^2 + w^2) + g\eta + \frac{\partial \phi}{\partial t} = 0 \quad \text{at } z = \eta \quad (3.5)$$

Both kinematic and dynamic boundary conditions have to be linearised by the assumption that the wave amplitude is small compared to the wavelength and water depth. At still water level, the resulting kinematic and dynamic boundary equations yield

$$w = \frac{\partial \eta}{\partial t} \quad \text{at } z = 0 \quad (3.6)$$

and

$$g\eta + \frac{\partial \phi}{\partial t} = 0 \quad \text{at } z = 0 \quad (3.7)$$

The resulting solution of velocity potential is

$$\phi = \frac{gH}{2\sigma} \frac{\cosh k(d+z)}{\cosh kd} \sin(kx - \sigma t) \quad (3.8)$$

where $k = \text{wave number} = 2\pi/L$, $\sigma = \text{wave angular frequency} = 2\pi/T$, $L = \text{wave length}$ and $T = \text{wave period}$. Substituting Equation (3.8) into Equations (3.6) and (3.7), differentiating and rearranging them result in the equation for the wave surface profile:

$$\eta = \frac{H}{2} \cos(kx - \sigma t) \quad (3.9)$$

and the equation for the wave celerity, c

$$c = \left(\frac{g}{\sigma} \right) \tanh(kd) \quad (3.10)$$

or

$$\sigma^2 = gk \tanh kd \quad (3.11)$$

Equation (3.11) is known as the wave dispersion equation. For a spectrum of waves having different wave periods, the larger period waves propagate at a higher celerity and move ahead of the shorter period ones. The equation is used to calculate the wavelength, L iteratively when wave period, T and water depth, d are given:

$$L = \frac{gT^2}{2\pi} \tanh \frac{2\pi d}{L} \quad (3.12)$$

Note that Equation (3.12) was used to estimate the wavelengths generated in the wave flume in this experimental study. Other wave properties, such as water particle displacements and velocity, were also estimated by using the Airy wave equations.

There are three basic physical parameters that control water surface elevation, η as shown in Equation (3.9), namely the incident wave height, H , wavelength, L and wave period, T . The properties of the wave can be controlled by varying one or more of these physical quantities. Since wave energy is proportional to the square of the wave height, it is more realistic to reduce the wave energy by suppressing their heights. Other mechanisms for energy transformation are by reflection and energy loss, which are presented in Section 3.3.

3.3 Evaluation Criteria for the Hydraulic Performance of Breakwaters

When waves interact with breakwaters of any shape, some of the energy is reflected seaward of the structures; some are dissipated through energy transformation by the structures; and the remainder is transmitted to the lee side of the structures. Theoretically, this hydrodynamic problem complies with the law of conservation of energy and can be mathematically expressed in the form of energy equilibrium (Tanimoto *et al.*, 1989; Sundar and Sabbarao, 2002; Burcharth and Hughes, 2003; Koutandos and Prinos, 2011):

$$E_i = E_t + E_r + E_\ell \quad (3.13)$$

where E_i , E_t , E_r , and E_ℓ are incident, transmitted, reflected and dissipated energy, respectively. Equation (3.13) is further expressed in the form of wave height giving:

$$E_i = \frac{\rho g H_i^2}{8} = \frac{\rho g H_t^2}{8} + \frac{\rho g H_r^2}{8} + E_\ell \quad (3.14)$$

where H_i , H_t and H_r are the wave heights for incident, transmitted and reflected wave heights respectively; ρ is the fluid density and g is the acceleration of gravity. Rearranging Equation (3.14) yields

$$1 = \left(\frac{H_t}{H_i}\right)^2 + \left(\frac{H_r}{H_i}\right)^2 + \frac{E_\ell}{E_i} \quad (3.15)$$

and
$$1 = C_T^2 + C_R^2 + C_L \quad (3.16)$$

where C_T , C_R , and C_L are the energy coefficients for wave transmission, reflection and energy dissipation, respectively.

The transmission coefficient C_T , which relates the size of the transmitted wave to the incident wave, is the key indicator of the wave attenuation ability of a breakwater:

$$C_T = \frac{H_t}{H_i} \quad (3.17)$$

Alternatively, C_T can also be expressed in term of energy:

$$C_T = \sqrt{\frac{E_t}{E_i}} \quad (3.18)$$

Wave energy increases with the square of the wave height; therefore, a general rule of thumb as suggested by Tabiasson and Kollmeyer (1991) is that to reduce one-half of the wave energy the wave height has to be reduced by about one-quarter. The selection of allowable C_T in the design of breakwaters largely depends on the applications and the clients' requirements. For instance, a C_T value of 0.6 may be an ideal level of wave attenuation for coastal recreational and sporting activities; however, it may not be acceptable for ports and harbours that require excessive filtering of the wave energy. Briggs (2001) suggested a benchmark for the transmission coefficient that a value of C_T equal or less than 0.5 (*i.e.* the transmitted waves have less than 25% of its incident energy) is indicative of very good breakwater performance.

Similarly, wave reflection is quantified by the reflection coefficient, C_R :

$$C_R = \frac{H_r}{H_i} \quad (3.19)$$

or
$$C_R = \sqrt{\frac{E_r}{E_i}} \quad (3.20)$$

At $C_R = 0$, wave reflection does not exist at all. Partial wave reflection occurs at $0 < C_R < 1$; and total reflection at $C_R \approx 1$. The measurement technique for the reflected wave height used in this study is discussed in Section 3.4.2.

The physics underlying the energy dissipation processes taking place at a breakwater during wave-structure interaction are complex and are difficult to measure. Hence, the amount of energy dissipation induced by a breakwater is often estimated by the energy dissipation coefficient, C_L :

$$C_L = \frac{E_\ell}{E_i} = 1 - C_T^2 - C_R^2 \quad (3.21)$$

The energy dissipation coefficient C_L indicates the portion of the incident wave energy that is dissipated by the breakwater. For instance, a C_L value of 0.5 is an indication of energy loss by 50% of the incident wave energy. This form of expression is widely used to quantify the amount of energy loss in breakwaters (Tanimoto *et al.*, 1989; Isaacson *et al.*, 1998; Suh *et al.*, 2006; Koutandos and Prinos, 2011). In some cases, the energy dissipation coefficient is expressed in term of wave heights by energy loss H_ℓ (Neelamani and Rajendran 2002a; Koutandos, 2007; Günaydın and Kebdaşlı, 2007):

$$C_L = \frac{H_\ell}{H_i} \quad (3.22)$$

and

$$C_L = \sqrt{\frac{E_\ell}{E_i}} = \sqrt{1 - C_T^2 - C_R^2} \quad (3.23)$$

Note that H_ℓ is an imaginary wave that is physically inexistent in nature and immeasurable. For energy loss estimation, Equation (3.21) is adopted in this study because the C_L value obtained is equivalent to the percentage of energy loss with reference to the incident wave energy. It is, therefore, believed that the output values are to be more indicative and meaningful.

It is also an intention of this study in quantifying the wave climate in the proximity of the free surface semicircular breakwater developed in this study. Wave activity around the

breakwater models can be quantified by the wave climate or disturbance coefficients, which are the ratios of the local wave height relative to the incident wave heights. The wave behaviour in front of the breakwater is represented by C_F :

$$C_F = \frac{H_f}{H_i} \quad (3.24)$$

and that in the interference chamber is represented by C_C :

$$C_C = \frac{H_c}{H_i} \quad (3.25)$$

where H_f and H_c are the wave heights at the front and inside of the interference chamber, respectively. A value of C_F or C_C of more than unity indicates an amplification of wave activity at the front or inside of the interference chamber, and vice versa.

3.4 Wave Characterisation and Measurement

3.4.1 Laboratory Waves

The experiments in this study were conducted in both regular and irregular waves in a wave flume (refer to Section 4.5.1). For regular waves, the wave trace records were evaluated using time domain analysis. The mean wave height, $\overline{H_i}$ was used to represent the average height of a number of waves past a measuring point, n :

$$\overline{H_i} = \frac{\sum H_i}{n} \quad (3.26)$$

For irregular waves, the spectral zeroth moment wave height, H_{m0} was obtained from the wave spectrum that exhibits the distribution of wave energy over frequency:

$$H_{m0} = 4\sqrt{m_0} \quad (3.27)$$

where m_0 is the moment of zero-order which represents the area under the spectral energy density curve, $S(f)$ over a range of frequencies, Δf .

$$m_0 = \sum S(f)\Delta f \quad (3.28)$$

For narrow-banded spectra in deeper waters, H_{m0} is approximately equal to the significant wave height $H_{1/3}$; therefore, H_{m0} is often referred to as “significant wave height” (Hughes, 1993). The World Meteorological Organization (1998) related H_{m0} to $H_{1/3}$ by

$$H_{m0} = 1.05H_{1/3} \quad (3.29)$$

The concept of wave spectrum, which is expressed as a function of frequency, $S(f)$, is commonly employed in modelling the sea state. These spectra may be obtained by hindcast calculations, by direct measurement or by visual observation. Models of the spectrum are used to estimate the entire wave spectrum from a number of known parameter such as the significant wave height and the peak wave period. In this study, Pierson-Moskowitz (PM) and JONSWAP spectra were used to model the sea states for irregular waves. Note that the PM and JONSWAP spectra required in the experiment have been pre-coded using *Wave* program for wave generation in the wave flume (see Figure 4.9). Further illustration of generation of these irregular waves is presented in Section 4.5.2.

(a) *Pierson-Moskowitz (PM) spectrum*

The Pierson-Moskowitz spectrum (Pierson and Moskowitz, 1964) is used as a model spectrum for a fully developed sea which is an idealised equilibrium state reached when the duration and fetch are unlimited. This spectrum was obtained based on a series of measurements recorded on board by British weather ships positioned in the North Atlantic from 1955 to 1960. The PM spectrum has the form of

$$S(f) = \frac{\alpha g^2}{(2\pi)^4 f^5} \exp\left[-1.25\left(\frac{f_p}{f}\right)^4\right] \quad (3.30)$$

where α = the Philips empirical constant (8.1×10^{-3}), g = the gravitational acceleration, f = wave frequency and f_p = the peak wave frequency. Further discussion of the spectrum is provided by World Meteorological Organization (1998).

(b) *JONSWAP spectrum*

JONSWAP spectrum is used to characterise waves in a growing sea, whereby the height of waves is limited by fetch, *i.e.* the wave growth under a steady offshore wind is limited by the distance from the shore. The wave spectrum was produced by observations made during the Joint North Sea Wave Project (JONSWAP) (Hasselmann *et al.*, 1973). The JONSWAP spectrum has a similar form to that of the PM spectrum, but with sharper spectral peak. The spectral peak of the JONSWAP spectrum is controlled by a peak enhancement factor, γ which lies between 1 and 7 ($\gamma = 3.3$ is commonly used):

$$S(f) = \frac{\alpha g^2}{(2\pi)^4 f^5} \exp\left[-1.25\left(\frac{f_p}{f}\right)^4\right] \gamma^q \quad (3.31)$$

where q is

$$q = \exp\left(-\frac{(f - f_p)^2}{2\sigma^2 f_p^2}\right) \quad (3.32)$$

$\sigma = 0.07$ when $f \leq f_p$ and $\sigma = 0.09$ when $f > f_p$. This spectrum has been extensively useful in representing the sea conditions for many coastal and offshore engineering projects. More details of this model are described in World Meteorological Organization (1998).

3.4.2 Measurement of Incident and Reflected Waves

Wave reflection from model boundaries is a common problem in laboratory studies. It is desirable to separate the measured wave train into its incident and reflected wave components so that the model response can be linked to the actual incident wave field. Several analysis methods have been developed to resolve the problem. These include:

(a) Moving probe method

A wave probe is slowly moved along the direction of wave propagation to measure the maximum and minimum of the wave envelope for the derivation of the incident and reflected wave heights. See Hughes (1993) for more details.

(b) Two-probe method (Goda and Suzuki, 1976)

Two fixed wave probes at different locations measuring two wave heights and one phase angle.

(c) *Three-probe method* (Mansard and Funke, 1980)

Three fixed wave probes at different locations measuring three wave heights and two phase angles.

The moving probe method is practically difficult, time consuming and subject to human errors (Nallayarasu *et al.*, 1995); hence, this method is not suitable to be used for extensive experimental studies. The fixed probe methods are capable of overcoming these problems; however, these methods exhibit singularities and break down when the spacing between the wave probes equals to an integer number of half wave lengths. The two-probe method generates errors pertaining to the wave heights and phases due to nonlinearity in the wave in the two probe arrangement. The three-probe method is superior to the two-probe method because it has wider frequency range, reduced noise contamination on the measurement and lesser sensitivity to critical probe spacing (Mansard and Funke, 1980). A sensitivity analysis conducted by Isaacson (1991) indicated that the three-probe method was the most accurate one. Therefore, the three-probe method was adopted to measure the reflected waves in this experimental study.

The three-probe method (Mansard and Funke, 1980) estimates the incident and reflected waves based on a least-square technique applied to the measurements obtained by the three wave probes positioned at different locations. For normal reflection of regular waves, the free surface elevation, η is expressed as:

$$\eta = a_i \cos(kx - \sigma t) + a_r \cos(-kx - \sigma t + \beta) \quad (3.33)$$

where

a_i = amplitudes of the incident wave trains

a_r = amplitudes of the reflected wave trains

k = wave number = $2\pi/L$

σ = angular frequency = $2\pi/T$

t = time

β = phase angle between the incident and reflected waves

The amplitudes a_i and a_r are expressed as

$$a_i = \left| \frac{s_2 s_3 - 3s_4}{s_5} \right| \quad (3.34)$$

$$a_r = \left| \frac{s_1 s_4 - 3s_3}{s_5} \right| \quad (3.35)$$

where

$$s_1 = \sum_{n=1}^3 e^{i2\Delta_n} \quad (3.36)$$

$$s_2 = \sum_{n=1}^3 e^{-i2\Delta_n} \quad (3.37)$$

$$s_3 = \sum_{n=1}^3 A_n e^{i(\delta_n + \Delta_n)} \quad (3.38)$$

$$s_4 = \sum_{n=1}^3 A_n e^{i(\delta_n - \Delta_n)} \quad (3.39)$$

$$s_5 = s_1 s_2 - 9 \quad (3.40)$$

$$\Delta_n = k(x_n - x_1) \quad (3.41)$$

Δ_n in Equation (3.41) is the relative probe spacing; $(x_n - x_1)$ is the distance between the n th probe and the first probe; δ_n is the measured phase of the n th wave record relative to that of the first record; and A_n is the wave amplitude. The detailed derivations of the method used for irregular waves are presented by Mansard and Funke (1980). In short, the following probe spacing requirements must be fulfilled to eliminate singularities in the measurements:

For regular waves,

$$X_{12} = \frac{L}{10}; \quad \frac{L}{6} < X_{13} < \frac{L}{3}; \quad X_{13} \neq \frac{L}{5} \text{ and } X_{13} \neq \frac{3L}{10}$$

For irregular waves,

$$X_{12} \neq n \frac{L_p}{2}, \text{ where } n = 1, 2, \dots; \quad X_{13} \neq n X_{12}, \text{ where } n = 1, 2, \dots$$

where X_{12} = interval distance between probes 1 and 2, X_{13} = interval distance between probes 1 and 3, L = wavelength corresponding to the wave period in regular waves, and L_p = wavelength corresponding to the peak wave period in irregular waves.

Note that the three-probe method is integrated as one of the exclusive features in the data acquisition and processing software – *Wavelab* (refer to Section 4.9.2) used in this experimental study. The application has been used with the abovementioned probe spacing restrictions for the estimation of incident and reflected waves in the wave flume.

3.5 Horizontal Loadings under Wave Crests on a Free Surface Semicircular Breakwater

Measurement of the horizontal wave forces acting on a semicircular breakwater is the primary concern of this study. Nevertheless, it would be more creditable if the measured data could be compared against the computed results based on the existing estimation methods developed by other researchers. It must be stressed that, to the knowledge of the author, the estimation methods of the hydrodynamic loadings on the impermeable, free surface semicircular breakwater have not been proposed or published in the public domain. Therefore, an attempt is made in this research to compute the horizontal forces acting on the solid free surface semicircular breakwater using the design formulae proposed for the bottom seated semicircular breakwater. This exercise is particularly useful for two reasons: (1) to estimate the maximum loading on the load cells used for force measurement; and (2) to provide validation against the measured results.

The most widely used estimation method for wave forces under wave crests exerted on upright walls, breakwaters or seawalls was developed by Goda (1974; 1985). This method has been cited in a number of prominent coastal engineering references worldwide, *e.g.* British Standard BS6349 Part 1 (1984), Coastal Engineering Manual EM1110-2-1100 Part VI (2003) and CIRIA – The Rock Manual C683 (2007). Goda’s method assumes that wave pressures on the upright wall can be represented by a trapezoidal distribution, with the highest pressure at the still water level regardless of the wave conditions (breaking or non-breaking). The method defines wave pressure characteristics by considering the influence of relative depth to wavelength on the pulsating component, the effect of impulsive wave breaking due to the relative level of the rubble mound, and the effect of the relative breakwater draft and the relative water depth, which are represented by the coefficients of α_1 , α_2 and α_3 , respectively. For the prediction of the horizontal loadings under wave crests on the rubble mound semicircular breakwater, Tanimoto *et al.* (1994a) adopted Goda’s method with the use of a correction factor – phase-modification coefficient, λ_p to account for the change in breakwater geometry.

For the free surface semicircular breakwater (SCB), the horizontal wave forces under wave crests acting on the front face of the structure were computed based on Goda’s method incorporating the λ_p coefficient by developed Tanimoto *et al.* (1994a) and some other assumptions. These assumptions include:

- The free surface breakwater is composed of a solid semicircular structure with a plane wall at the bottom;
- The limit of wave run-up is one-half of the amplitude of the waves measured right in front of the test model; and
- Partial wave reflection occurs in front of the test models.

This model takes into consideration of the influence of overtopping waves. The distribution of the wave pressure on a free surface semicircular breakwater is shown in Figure 3.1. Wave pressures on the front face are distributed trapezoidally, reducing from p_1 at still water level to p_3 at the base of the semicircular caisson. Note that in the absence of a rubble mound structure α_2 and p_{G2} are therefore negligible. Above still water level, p_1 reduces to p_4 if the run up, η^* is less than the freeboard of the breakwater, h_c . In the case of $\eta^* > h_c$, p_4 reduces to zero.

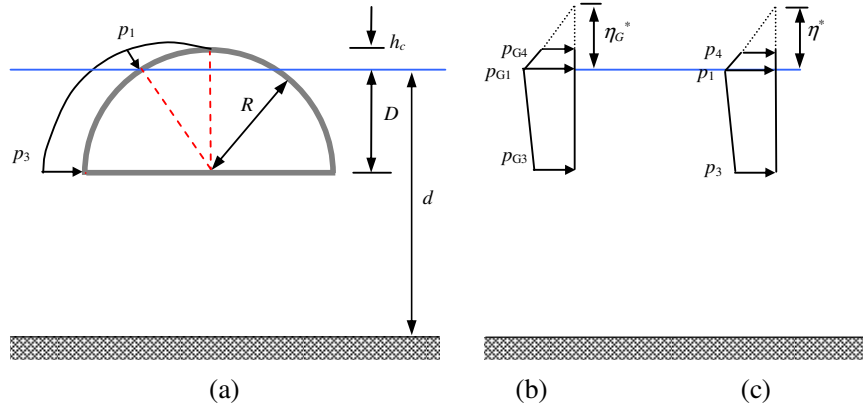


Figure 3.1: Wave pressure distributions – (a) pressure distribution on a semicircular structure; (b) pressure diagram for a vertical wall proposed by Goda (1974); and (c) pressure diagram for a free surface semicircular breakwater derived from the Goda's formulae.

Goda's method was developed for wave pressure estimation in irregular waves. However, the method was also found to be useful in calculating the horizontal wave pressures for a bottom-seated semicircular breakwater in regular waves (Wang, 2006). In this study, Goda's method is used for predicting horizontal wave forces in both regular and irregular waves. The design incident wave heights, H_D chosen for this model are the mean wave height, H_i for regular waves and the significant wave height, $H_{1/3}$ for irregular waves.

$$H_D = \begin{cases} H_i \\ H_{1/3} \approx 0.95H_{m0} \end{cases} \quad (3.42)$$

These wave parameters are chosen because they are directly related to the measured wave forces in the form of the mean wave force for regular waves and the average of the highest one-third of the wave forces for irregular waves. Similarly, the design wave periods, T_D for regular and irregular waves are denoted as T and $T_{1/3}$, respectively.

$$T_D = \begin{cases} T \\ T_{1/3} = 0.95T_p \end{cases} \quad (3.43)$$

Note that $H_{1/3}$ and H_{m0} , and $T_{1/3}$ and T_p have been found to be roughly equivalent (World Meteorological Organization, 1998; Reeve *et al.*, 2004).

Goda (1974) considered total reflection of waves taking place in front of the vertical wall for the calculation of p_{G1} and η_G^* as shown in the pressure diagram provided in Figure 3.1b. The use of these equations in computing p_1 and η^* for the free surface semicircular structure (see Figure 3.1c) may, however, result in over-predictions due to the fact that the convex surface is less reflective than the vertical surface (refer to Section 2.3.1). Since η^* has not been measured in the experiment, the limit of wave run-up above SWL can only be estimated by

$$\eta^* = 0.5H_f \quad (3.44)$$

where H_f is the wave height measured right in front of the breakwater. The equation for p_{G1} is modified to account for the wave reflection resulted by the front curved wall. The amount of wave reflection is addressed by a measured reflection coefficient C_R computed from Equation (3.19). Hence, the horizontal wave pressure at still water level, p_1 is given by

$$p_1 = 0.5(1 + C_R)\alpha_1\rho gH_D \quad (3.45)$$

where ρ is the density of fluid and g is the acceleration of gravity. The correction factor, α_1 is the mean tendency of wave pressure in that it increases with the wave period.

$$\alpha_1 = 0.6 + \frac{1}{2} \left[\frac{4\pi d / L}{\sinh(4\pi d / L)} \right]^2 \quad (3.46)$$

where d is the water depth and L is the wavelength. At the bottom of the front curve wall of the breakwater, the hydrodynamic pressure, p_3 is defined as:

$$p_3 = \lambda_p \alpha_3 p_1 \quad (3.47)$$

where α_3 is the coefficient based on the simplified assumption of a linear pressure variation between p_{G1} and p_{G3} along an upright section:

$$\alpha_3 = 1 - \frac{D}{d} \left[1 - \frac{1}{\cosh(2\pi d / L)} \right] \quad (3.48)$$

and λ_p is the phase modification coefficient for the semicircular section of the breakwater:

$$\lambda_p = \cos^4 \frac{2\pi\Delta l}{L} \quad (3.49)$$

Δl is the horizontal distance between the lower curved end and the point of intersection of the curved surface and the still water level. This is given by:

$$\Delta l = R - R \cos \left(\sin^{-1} \frac{D}{R} \right) \quad (3.50)$$

where R is the radius of the semicircle and D is the breakwater immersion depth.

Assuming a linear pressure variation between p_1 and p_4 , the effective wave pressure acting on the emerged part of the breakwater is:

$$p_4 = \alpha_4 p_1 \quad (3.51)$$

where α_4 is the coefficient based on the simplified assumption of a linear pressure variation between p_{G1} and p_{G4} along an upright section, *i.e.*:

$$\alpha_4 = 1 - \frac{h_c^*}{\eta^*}, \quad (3.52)$$

where
$$h_c^* = \min\{\eta^*, h_c\} \quad (3.53)$$

For non-wave overtopping cases,

$$\eta^* < h_c \rightarrow h_c^* = \eta^* \rightarrow \alpha_4 = 0 \rightarrow p_4 = 0$$

For wave overtopping cases,

$$\eta^* > h_c \rightarrow h_c^* = h_c \rightarrow \alpha_4 = 1 - \frac{h_c}{\eta^*} \rightarrow p_4 > 0$$

The total horizontal wave force under the wave crests (per meter length of breakwater) may be written as:

$$F_c = \frac{1}{2}(p_1 + p_4)h_c^* + \frac{1}{2}(p_1 + p_3)D \quad (3.54)$$

It is important to note that this is merely a simplified model giving a crude estimation of the horizontal wave force under the wave crest acting on the front wall of a solid free surface semicircular breakwater. The model does not account for the wave response at the rear wall, thus, this may underestimate the horizontal forces. Validation of the measured results with the computed results is presented in Chapter 8.

3.6 Dimensional Analysis

When a physical problem is too difficult to resolve via the theoretical approach, dimensional analysis can be used instead to great advantage. It provides a mathematical tool to supply both quantitative and qualitative relationships of a physical problem when combined with experimental procedures (Le Méhauté, 1990). Identification of the variables that influence the physics of the problem is important but difficult. Unimportant variables must be eliminated to reduce expensive and time-consuming experiments; however, omitting important variables will likely result in incorrect conclusions (Hughes, 1993). Therefore, selection of the affecting variable has to be handled with considerable insight into the problem and the governing physical laws.

3.6.1 For SCB: Hydraulic Coefficients

The hydraulic characteristics of the free surface semicircular breakwater (SCB) are primarily affected by the incident wave properties, structure geometry and placement, and the fluid properties. Since the wave interaction with the free surface breakwaters is a surface-denominated phenomenon, the viscous effect therefore becomes insignificant (Hughes, 1993) and is omitted from this study. For instance, the variables that potentially affect wave transmission by an SCB are listed as follows:

- a. Wave properties: Incident wave height, H_i
Transmitted wave height, H_t
Wavelength, L
- b. Structure geometry: Breakwater width, B

- Front wall porosity of the SCB, ε_{SCB}
- c. Structure placement: Breakwater immersion depth (draft), D
Water depth, d

The transmitted wave height can be described by the following independent variables:

$$H_t = f(H_i, L, B, D, d, \varepsilon_{SCB}) \quad (3.55)$$

Buckingham's Pi theorems are applied to form a complete set of dimensionless products expressed in π terms using the given set of variables outlined in Equation (3.55). Forming dimensionless products from the selected variables is somewhat arbitrary; and the common rule for this is to keep the dimensionless products simple and easy to work with when conducting experiments (Hughes, 1993). Equation (3.55) can also be expressed as

$$f^*(H_t, H_i, L, B, D, d, \varepsilon_{SCB}) = 0 \quad (3.56)$$

These seven variables ($n = 7$), which are described by the fundamental dimension of *length* system ($m = 1$), form $n - m = 6$ dimensionless products. Thus, the function can be expressed by using six Π -groups:

$$\phi(\Pi_1, \Pi_2, \Pi_3, \Pi_4, \Pi_5, \Pi_6) = 0 \quad (3.57)$$

According to the 2nd Pi theorem, each π group is a function of n repeating variables plus one of the remaining variables. Taking the repeating variable for *length* system as D , this produces a set of dimensionless products containing the six π terms:

$$\frac{H_t}{D}, \frac{L}{D}, \frac{H_i}{D}, \frac{B}{D}, \frac{d}{D}, \varepsilon_{SCB} = \pi_1, \pi_2, \pi_3, \pi_4, \pi_5, \pi_6 \quad (3.58)$$

The variable ε_{SCB} , which is already dimensionless, is left out of the analysis. Rearranging the π terms in Equation (3.58) gives

$$\frac{H_t}{H_i}, \frac{D}{L}, \frac{H_i}{L}, \frac{B}{d}, \frac{D}{d}, \varepsilon_{SCB} = \frac{\pi_1}{\pi_3}, \pi_2^{-1}, \frac{\pi_3}{\pi_2}, \frac{\pi_4}{\pi_5}, \pi_5^{-1}, \pi_6 \quad (3.59)$$

where	$\Pi_1 = C_T = \frac{H_t}{H_i}$	Transmission coefficient
	$\Pi_2 = \frac{D}{L}$	Relative wavelength
	$\Pi_3 = \frac{H_i}{L}$	Wave steepness
	$\Pi_4 = \frac{B}{d}$	Structure placement ratio or relative water depth
	$\Pi_5 = \frac{D}{d}$	Relative immersion depth
	$\Pi_6 = \varepsilon_{SCB}$	Porosity of the front curved wall of the SCB

All the π terms in Equation (3.59) can be shown to be independent, whereby one π term cannot be formed by some combination of the other two π terms. The relative breakwater width, B/L is a favourable design parameter that is frequently used by the engineers to compare the width of the breakwater with the total length of the design waves. Therefore, $\Pi_2 = D/L$ is replaced by $\Pi_2 = B/L$ as alternative since the effect of immersion has already been addressed by Π_5 . $\Pi_2 = B/L$ will take care of the effect of wave period as the breakwater width was kept unchanged in the experiments. Consequently, Equation (3.59) can be represented by:

$$\frac{H_t}{H_i} = C_T = f_i \left[\frac{B}{L}, \frac{H_i}{L}, \frac{B}{d}, \frac{D}{d}, \varepsilon_{SCB} \right] \quad (3.60)$$

where f_i is a function for transmission coefficient C_T . Similarly, dimensional analysis is carried out for the other hydraulic coefficients, producing:

$$\left. \begin{array}{l} C_R \\ C_L \\ C_F \\ C_C \end{array} \right\} = f_i \left[\frac{B}{L}, \frac{H_i}{L}, \frac{B}{d}, \frac{D}{d}, \varepsilon_{SCB} \right] \quad (3.61)$$

where f_i are the functions of reflection coefficient C_R ($i = R$), energy dissipation coefficient C_L ($i = L$), wave disturbance coefficient in front of the breakwater C_F ($i = F$) and wave disturbance coefficient in the interference chamber C_C ($i = C$). In the case of irregular waves,

the hydraulic coefficients in Equations (3.60) and (3.61) are expressed in terms of H_{m0} , giving:

$$\left. \begin{matrix} C_T \\ C_R \\ C_L \\ C_F \\ C_C \end{matrix} \right\} = f_i \left[\frac{B}{L_p}, \frac{H_{m0,i}}{L_p}, \frac{B}{d}, \frac{D}{d}, \varepsilon_{SCB} \right] \quad (3.62)$$

where $C_T = \frac{H_{m0,t}}{H_{m0,i}}$, $C_R = \frac{H_{m0,r}}{H_{m0,i}}$, $C_L = 1 - C_T^2 - C_R^2$, $C_F = \frac{H_{m0,f}}{H_{m0,i}}$ and $C_C = \frac{H_{m0,c}}{H_{m0,i}}$.

3.6.2 For SCB: Horizontal Loadings

Separate dimensional analysis was performed to evaluate the horizontal component of the hydrodynamic loadings on the SCB models. The variables thought to be important in predicting the horizontal wave force per unit width of the breakwater, F are listed as follows:

$$F = f(H_i, d, D, T, L, B, \rho, \varepsilon_{SCB}) \quad (3.63)$$

where T is the wave period and ρ is the density of water (refer to Section 3.6.1 for the descriptions of other nomenclatures). The porosity of the breakwater, ε_{SCB} is a dimensionless ratio; therefore, it is not included in the dimensional analysis. The variables in Equation (3.63) consist of force, length and time. A matrix of the variables and their fundamental dimensions are established as follows:

	F	H_i	d	D	T	L	B	ρ	ε_{SCB}
M	1	0	0	0	0	0	0	1	0
L	1	1	1	1	0	1	1	-3	0
T	-2	0	0	0	1	0	0	0	0

Equation (3.63) can be expressed as

$$f'(F, H_i, d, D, T, L, B, \rho, \varepsilon_{SCB}) = 0 \quad (3.63)$$

There are eight variables ($n = 8$) that can be described by the fundamental dimension of *force-length-time* system ($m = 3$), thus giving $n - m = 5$ dimensionless products, *i.e.*

$$\phi(\Pi_1, \Pi_2, \Pi_3, \Pi_4, \Pi_5) = 0 \quad (3.64)$$

where ϕ is the unknown function. The repeating variables of ρ , L and T are selected to represent the *force-length-time* system. As the π groups in Equation (3.64) are all dimensionless (*i.e.* they have dimensions $M^0L^0T^0$), the principle of dimensional homogeneity is used to equate the dimensions for each π group. This yields five π -groups:

$$\Pi_1 = \rho^a L^b T^c F \quad (3.65)$$

$$\Pi_2 = \rho^a L^b T^c H_i \quad (3.66)$$

$$\Pi_3 = \rho^a L^b T^c d \quad (3.67)$$

$$\Pi_4 = \rho^a L^b T^c D \quad (3.68)$$

$$\Pi_5 = \rho^a L^b T^c B \quad (3.69)$$

where a , b and c are exponents to be determined. Substitution of the fundamental units for each of the variables in Equations (3.65) – (3.69) gives

$$\frac{F}{\rho H_i^3 T^{-2}} = f_1 \left[\frac{d}{H_i}, \frac{D}{H_i}, \frac{L}{H_i}, \frac{B}{H_i}, \epsilon_{SCB} \right] \quad (3.70)$$

Using the wave dispersion relationship,

$$\sigma^2 = gk \tanh(kd)$$

$$\frac{1}{T^2} = \frac{g}{2\pi L} \tanh \frac{2\pi d}{L} \quad (3.71)$$

where g is the gravitational acceleration constant. Substituting Equation (3.71) to Equation (3.70) and rearranging the equation gives:

$$\frac{F}{\rho g H_i^2} = \frac{1}{2\pi} \left(\frac{H_i}{L} \right) \tanh \left(\frac{2\pi d}{L} \right) f_2 \left[\frac{d}{H_i}, \frac{D}{H_i}, \frac{L}{H_i}, \frac{B}{H_i}, \epsilon_{SCB} \right] \quad (3.72)$$

To include geometrical influence to the horizontal wave force parameter, Equation (3.72) can also be rewritten as:

$$\frac{F}{\rho g H_i D} = f_2 \left[\frac{d}{H_i}, \frac{D}{H_i}, \frac{L}{H_i}, \frac{B}{H_i}, \epsilon_{SCB} \right] = f_3 [\pi_1, \pi_2, \pi_3, \pi_4, \pi_5] \quad (3.73)$$

Rearranging the π terms in Equation (3.73) gives:

$$\frac{H_i}{d}, \frac{D}{d}, \frac{H_i}{L}, \frac{B}{d}, \epsilon_{SCB} = \pi_1^{-1}, \frac{\pi_2}{\pi_1}, \pi_3^{-1}, \frac{\pi_4}{\pi_1}, \pi_5 \quad (3.74)$$

where	$\Pi_1 = \frac{H_i}{d}$	Relative wave height
	$\Pi_2 = \frac{D}{d}$	Relative immersion depth
	$\Pi_3 = \frac{H_i}{L}$	Wave steepness
	$\Pi_4 = \frac{B}{d}$	Breakwater placement ratio
	$\Pi_5 = \epsilon_{SCB}$	Porosity of the front curved wall of the SCB

The horizontal force coefficients by the peak wave troughs ($F_{n,t}$) and by the peak wave crests ($F_{n,c}$) are expressed as:

$$\left. \begin{matrix} F_{n,t} \\ F_{n,c} \end{matrix} \right\} = \frac{F}{\rho g H_i D} = f_4 \left[\frac{H_i}{d}, \frac{D}{d}, \frac{H_i}{L}, \frac{B}{d}, \epsilon_{SCB} \right] \quad (3.75)$$

3.6.3 For SCB with Wave Screen: Hydrodynamic Coefficients

To optimise the performance of the SCB, the keel of the breakwater has been extended by wave screen(s). The total draft of the breakwater, D_T is the sum of the immersion depth of the SCB caisson, D and the length of the wave screen, D' , giving $D_T = D + D'$. For a given breakwater configuration (*i.e.* SCB with screen), dimensionless parameters that are potentially affecting the hydraulic coefficients for each configuration of the breakwater are:

$$\left. \begin{array}{l} C_T \\ C_R \\ C_L \\ C_F \\ C_C \end{array} \right\} = f_i \left[\frac{B}{L}, \frac{H_i}{L}, \frac{D_T}{d}, \frac{B}{d}, \epsilon_{SCB}, \epsilon_{screen} \right] \quad (3.76)$$

where f_i are the functions of transmission coefficient C_T ($i = T$), reflection coefficient C_R ($i = R$), energy dissipation coefficient C_L ($i = L$), wave disturbance coefficient in front of the breakwater C_F ($i = F$) and wave disturbance coefficient in the interference chamber C_C ($i = C$).

Similarly, the parametric relationship for the horizontal loadings on the each breakwater configuration is:

$$\left. \begin{array}{l} F_{n,t} \\ F_{n,c} \end{array} \right\} = \frac{F}{\rho g H_i D_T} = f_i \left[\frac{H_i}{d}, \frac{D_T}{d}, \frac{H_i}{L}, \frac{B}{d}, \epsilon_{SCB}, \epsilon_{screen} \right] \quad (3.77)$$

where f_i are the functions of the force coefficients for wave trough $F_{n,t}$ ($i = t$) and wave crest $F_{n,c}$ ($i = c$).

4

Experimental System

4.1 General

Laboratory measurements and observations are the key techniques used to understand and improve the knowledge of the underlying physics based on the physical processes that take place at and around the test models. These techniques allow the assessment of the performances of the breakwater design to be carried out in an accessible, controlled and repeatable environment at only a small fraction of the cost. The development of a free surface semicircular breakwater in this study is a new venture and the related studies on such structure are scarce as discussed in previous chapters. Wave interaction with the semicircular structure involves complex physical processes such as convective and dissipative nonlinear effects which may result in difficulties if one were engage in the mathematical modelling approach especially in the early stage of the research. The appropriateness of mathematical modelling is usually limited by the choice of the functional relationships on which they are based.

Physical modelling is particularly helpful in simulating a complex hydraulic problem that is beyond analytical skills. Dalrymple (1985) pointed out that the physical model integrates the appropriate equations governing the hydraulic processes without simplifying assumptions that have to be made for analytical or numerical models. The knowledge gaps in the present mathematical representations of hydraulic processes are often filled by experimental efforts because further progress in numerical models can only be gained by better understanding of the basic laws of fluid flow through physical modelling (Le Méhauté, 1990). Kamphuis (1991) also mentioned that observing a physical model in operation would give an immediate qualitative impression of the physical processes which in turn could help the experimenters focus on the study and reduce the planned testing.

Although there are several distinct advantages associated with physical modelling, these models do pose several drawbacks, most notably scale and laboratory effects. Scale effects occur when it is not possible to simulate all relevant variables in the correct relationship between the model and the prototype; whilst laboratory effects arise from limitations inherent in the laboratory facilities such as wave generation techniques, model boundaries, *etc.* A careful selection of the similarity criteria and the use of better instrumentation in the experiment would help to minimise the scale and laboratory effects but these efforts will not eliminate the effects completely. Even dealing with these issues, it is possible to test the model sensitivity by varying input conditions and thus the model results can be better interpreted (Kamphuis, 1991). Another shortcoming of physical modelling is the higher operating cost compared to numerical models. In situation where numerical models could produce accurate and reliable results, the numerical models may be a more viable choice. Despite the limitations inherent in physical modelling, physical modelling still is the best tool that an engineer can have to discover and verify engineering solutions (Hughes, 1993).

In general, there are two types of physical models of the coastal and offshore structures, namely process model and validation model (Hughes, 1993). Process model aims to improve knowledge of the underlying physics based on the physical processes that take place at and around the test models, whereas validation model is used to provide test data to compare, validate and calibrate the data obtained from the analytical and numerical models. In this study, a process model of the free surface semicircular breakwater has been constructed in order to investigate its hydrodynamic performance characteristics in response to a wide range of test conditions. The model provides qualitative insight into the resulting hydraulic phenomena that have yet to be described or understood or quantified by theoretical approaches. Further illustrations pertaining to the test models used in this research are presented in Section 4.2.

Apart from the development of the test models, this chapter also outlines the details of the test facilities and instrumentation employed in this experimental study. These apparatus were carefully inspected and calibrated to ensure the accuracy and quality of the measured data. The complete test programme towards achieving the research objectives is also explained in detail.

4.2 Free Surface Semicircular Breakwater Model

As mentioned in the earlier chapters, the design of the free surface breakwater in this study was inspired by the bottom-seated semicircular breakwaters that were successfully built in Japan and China. These breakwaters offer a number of advantages (see Section 1.4.2) and hence present a promising configuration that is worth further investigation. As a result, the semicircular caisson was selected as the key feature to the present design of the free surface breakwater. The proposed breakwater – the free surface semicircular breakwater is denoted as SCB hereafter for discussion purposes.

Based on the breakwater classification proposed by Sasajima *et al.* (1994) as presented in Section 2.6.1, two types of SCB caisson were chosen for physical modelling studies, namely the ‘solid type’ having impermeable front and rear walls and the ‘front-wave dissipating type’ having only a perforated front wall. The ‘permeable type’ having perforated front and rear walls was not considered due to large transmission of wave energy through the breakwater. In addition, the ‘rear wave-dissipating type’ having only a perforated rear wall was also not selected because it was mainly designed to absorb reflected waves from the protected basin.

For the ‘solid type’ breakwater (which is denoted as SCB0 hereafter), the model was constructed using a semi-cylindrical PVC tube with a wall thickness of 10 mm as shown in Figure 4.1a. The radius and breakwater length perpendicular to the wave direction of the SCB0 model were 0.25 m and 0.395 m, respectively. For the ‘front-wave dissipating type’ breakwater, the effect of the front wall porosity was explored by creating rectangular openings of various sizes on the front curved wall of the solid model. Rectangular openings of a matrix of 6×4 were evenly distributed across the front curved face of the model as presented in Figure 4.1b. The length of the openings was fixed at 60 mm and the width varied at 10 mm, 20 mm and 30 mm producing a front wall porosity of 9%, 18% and 27%, respectively. These perforated breakwaters are denoted as SCB9, SCB18 and SCB27 correspondingly. The wall perforation was created to produce various levels of energy dissipation during the passage of water flow. Two rows of 60 mm \times 30 mm rectangular openings were also provided near the crest of the rear wall so as to reduce the overtopping discharge by infiltration and to provide a getaway for the excessive run-up waves at the rear wall. The detailed dimensions of the SCB models are summarised in Table 4.1. Two clear Perspex sheets cut out into the shape of semicircles were attached at the ends of each model to increase its stability against wobbling effect during the wave-structure interactions and to

provide visibility of the wave response taking place in the interference chamber. Different perspective views of the SCB27 model are presented in Figure 4.2. The mounting of the SCB models is further illustrated in Section 4.6.1.

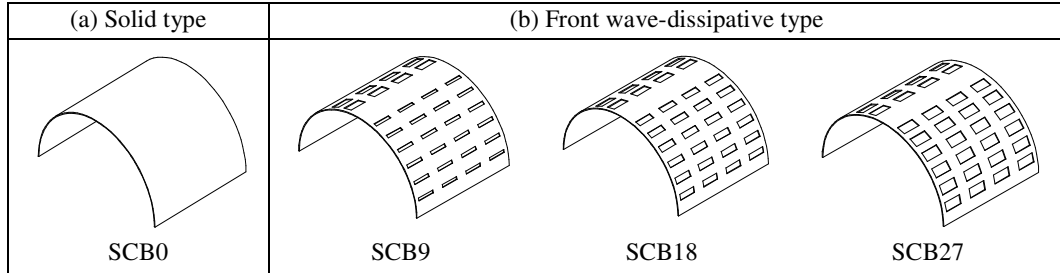


Figure 4.1: SCB models – (a) solid type; and (b) front wave-dissipating type

Table 4.1: Properties of the SCB models

Diagram of SCB model showing Rear Wall, Front Wall, dimensions $B = 0.50\text{ m}$ and $b = 0.395\text{ m}$, and wave height H_i .

B = Breakwater width
 b = Breakwater length

(a) Front wall openings
 Arrangement: 6×4 distributed across the front face of the SCB model

Dimension	SCB0	SCB9	SCB18	SCB27
Length (mm)	<i>n.a.</i>	60	60	60
Width (mm)	<i>n.a.</i>	10	20	30

(b) Rear wall openings
 Arrangement: 2×4 extended from the crown of the SCB model

Dimension	SCB0	SCB9	SCB18	SCB27
Length (mm)	<i>n.a.</i>	60	60	60
Width (mm)	<i>n.a.</i>	30	30	30

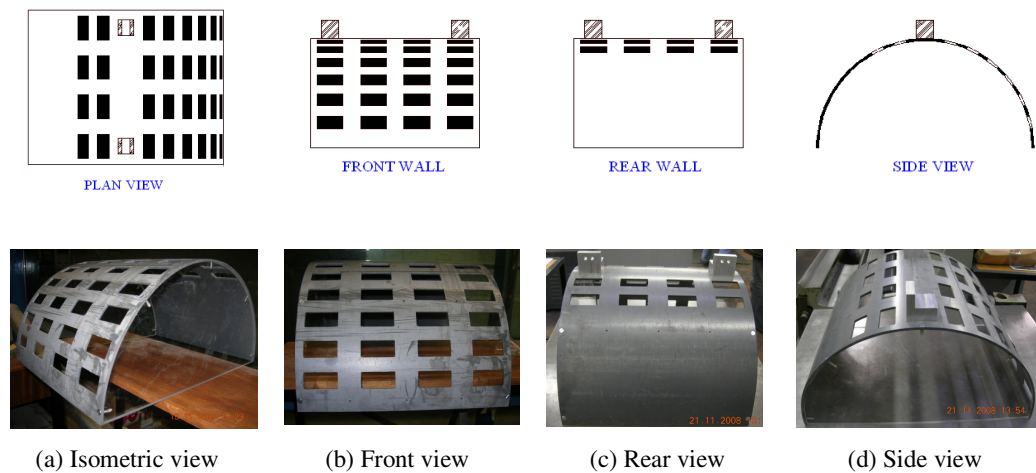


Figure 4.2: SCB27 model

Figure 4.3 provides a conceptual diagram of the front view of a perforated free surface SCB supported on a beam-pile system at a sea site. The semicircular caisson may be constructed in modular form of suitable lengths on-shore, then transported to the construction site and assembled together. The pile-beam supporting structure is designed to provide complete stability and stiffness to the breakwater by restraining displacements in response to wave actions. It is suggested that the piles be placed at the bottom edges of each SCB caisson to transfer the loading components (*i.e.* dead loads by the structure weight and live loads by wave actions) to the sea bottom. It is stressed that the design of such supporting structure is beyond the scope of this study; thus the SCB models have been tested without the influence of the pile-beam supporting structure.

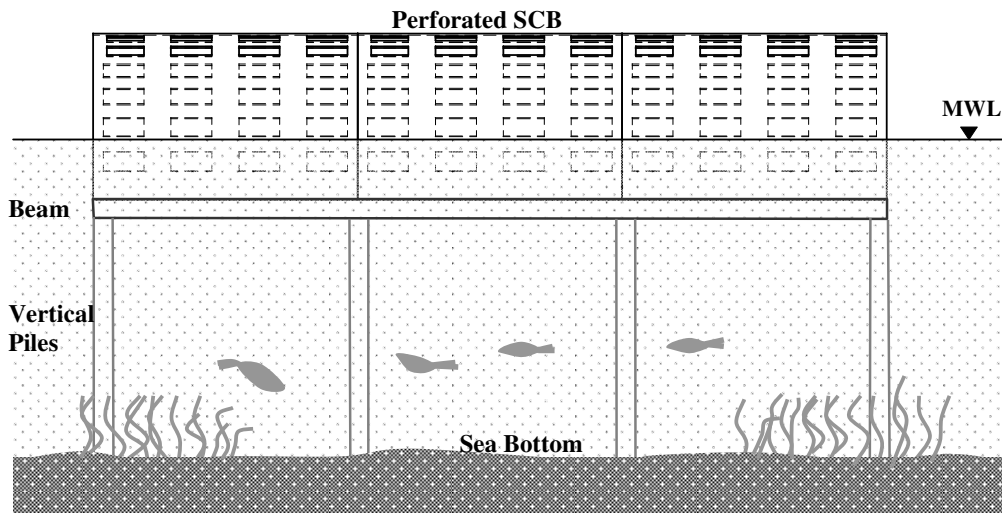


Figure 4.3: A conceptual diagram of the front view of the free surface semicircular breakwater

4.3 SCB with Wave Screen

When a free surface SCB is immersed with a limited depth, the large gap underneath the structure permits a considerable amount of wave troughs passing through the barrier resulting in high transmission of waves in the sheltered region. To address this problem, the draft of the free surface SCB has been extended by wave screen(s) as seen in Figure 4.4. The wave screen can be formed by a number of timber or concrete planks attached to the supporting piles with a specific spacing between them. It is believed that not only the screen is capable of enhancing the overall hydrodynamic performance of the breakwater; it also widens the operating tidal range of the structure. However, the presence of the screen potentially incurs higher wave reflection in front of the structure due to increased wave

exposure area. The reflective characteristics of the screen have been assessed using physical modelling.

The wave screen models were an assembly of a number of closely-spaced rectangular metal plates as shown in Figure 4.5a, each with dimensions of 39.5 mm long, 30 mm wide and 10 mm thick. The total extension length of the screens was fixed at 0.3 m. There were three screen configurations considered in this experimental study:

- (1) Front screen (FS) extended from the bottom edge of the front curved wall of the SCB;
- (2) Rear screen (RS) extended from the bottom edge of the rear curved wall of the SCB;
- and
- (3) Double screens (DS) extended from the bottom edges of the front and rear curved walls of the SCB.

The effect of the screen porosity on the hydrodynamic performance (particularly on wave reflection and transmission) was investigated by modelling a screen of 25%, 40% and 50% porosity for each of the above screen configuration. The properties of the wave screen with varying porosities are summarised in Table 4.2. Figure 4.5c displays a sample of a completed wave screen of 25% porosity. The set-up of the screen models in the wave flume is described in Section 4.6.2.

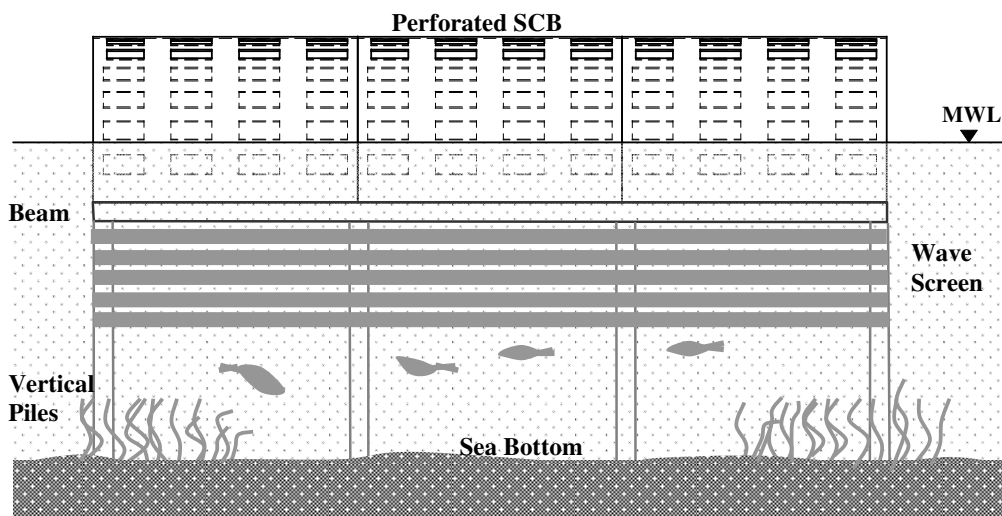


Figure 4.4: A conceptual diagram of the front view of the free surface semicircular breakwater with a front screen

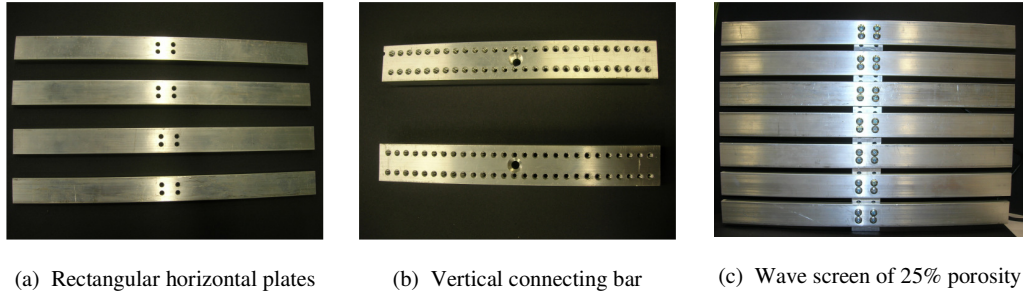


Figure 4.5: Modelling of a wave screen

Table 4.2: Properties of the wave screen(s)

Porosity of wave screen	Number of plates	Spacing between plates (mm)
25%	7	10
40%	6	20
50%	5	30

4.4 Model Scale

One of the major concerns with physical modelling is to ensuring that the test model with reduced scale behaves in a manner similar to the prototype it is intended to emulate. Complete similitude where all the factors influencing the reactions are equal between prototype and model is impossible to achieve except at prototype scale (Hughes, 1993). The differences between the prototype and model response that arise is termed as scale effect.

The majority of hydraulic models in coastal engineering are scaled according to the Froude model law (Hughes, 1993). The Froude number F_r is a parameter that quantifies the relative influence of inertial and gravity forces in a hydraulic flow, *i.e.*:

$$F_r = \frac{V}{\sqrt{gL}} \quad (4.1)$$

The Froude numbers of both prototype and model are essentially the same, *i.e.*:

$$\left(\frac{V}{\sqrt{gL}} \right)_p = \left(\frac{V}{\sqrt{gL}} \right)_m \quad (4.2)$$

Equation (4.2) is the Froude model criterion for modelling flows which assumes that the initial forces are balanced primarily by the gravitational forces. The present study deals with surface waves whereby the scaling is in accordance with the Froude scaling law. The Froude modelling scale adopted for the test models used in this study is 1:20.

Scale effects in the test models using Froude scaling result primarily from the scaling assumption may incorrectly scale other physical forces due to viscosity, surface tension, *etc.* Those forces are assumed to contribute little to the physical processes. The most important scale effect in coastal engineering models is the viscous forces associated with flow through the models. The viscous scale effects can be removed by using models at the largest scale possible. However, this is often impossible for small-scale test facilities. Oumeraci (1984), Van der Meer (1988) and Hughes (1993) suggested that the Reynolds number, R_e based on the characteristic dimension of the breakwater must be sufficiently large to ensure fully turbulent flow. For caisson-type models, the Reynolds numbers in the interference chambers are always in the fully-turbulent flow range because caissons are designed to permit transmission of a large portion of water flow into the chamber. As a result, viscous scale effects are not an issue for such models (Hughes, 1993). In addition, the measured forces in Froude-scaled models will be in similitude with the prototype equivalents provided the models are subjected to non-breaking waves and do not experience any impulsive loadings from wave breaking directly on the structure (Hughes, 1993).

Briggs (2001) defined the Reynolds number for free surface breakwaters as:

$$R_e = \frac{H_i}{L} \frac{D\sqrt{gL}}{\nu} \quad (4.3)$$

where H_i = incident wave height, L = wavelength, D = breakwater draft, g = acceleration of gravity and ν = kinematic viscosity. Viscous dissipation is dominant within the structure at $20 < R_e < 2000$; whereas strong turbulent dissipation would be expected at $R_e > 2000$. The Reynolds number used in the present study ranges from 2400 – 19200, which is clearly within the turbulent dissipation range. Therefore, viscous scale effects is negligible in the test models.

Potential wave decay due to internal friction by the path of wave propagation and viscous friction caused by water particles was also checked using Keulegan's models (1950a and

1950b). The formulations derived from the models and the computations are presented in Appendices A and B, and further explanation pertaining to these effects is presented in Section 4.10.1. Since the test waves propagate over a relatively short distance, the scale effects due to internal and viscous dissipation are rather minimal (less than 2.7%). Thus, these effects are typically not considered in experimentation.

Generally, the scale effect due to surface tension forces is not a problem in a Froude-scaled model provided that wave periods are more than 0.35 s and the water depth is more than 20 mm (Le Méhauté, 1976). Test ranges for wave period and water depth in this study are well beyond the aforementioned limits (see Section 4.10); hence, it could be safely said that the laboratory tests were free from surface tension scale effects. Other scale effects that may exist in experimentation are discussed in later sections.

4.5 Flume Facilities

4.5.1 Wave Flume

The laboratory tests were conducted in a 22 m long, 0.4 m wide and 1.0 m deep wave flume in the Hydraulics Laboratory of School of Engineering, the University of Edinburgh. The flume was of a modular construction, with each section approximately 3.3 m in length. The flume was raised approximately 1 m from the ground and the bottom and both sides were made of transparent glass panels of 25 mm thickness to provide visualisation of water flow behaviour in the flume during the experiment. At the top of the walls, a pair of mounting rails running the full length of the flume was used for the fittings of the experimental hardware. The flume was designed for transitional and deepwater wave tests, and has a nominal working water depth of 0.7 m. Reduced water depths, however, can also be created by fitting a flat false bottom in sections corresponding to the modular design of the wave flume. In addition, a sloping beach of various gradients can be incorporated in the flume to extend the applications of the flume.

In terms of the wave flume operation, the flume was filled with water through the inlet located at the rear of the wave flume. The water level in the flume was controlled by the drain valve located underneath the flume near the water outlet. The flume spent about 15 minutes to refill and a similar time to drain the water. A schematic diagram detailing the major elements of the flume is provided in Figure 4.6. Also, waves were generated by a computer-controlled wave generator (see Section 4.5.2) located at one end of the flume. At

the opposite end, a wave absorber (see Section 4.5.3) was installed to reduce the reflected waves in the flume during the experiment. This facility has been used in several coastal engineering studies, including the Violent Overtopping Waves at Seawalls (VOWS) project (<http://www.vows.ac.uk/>).

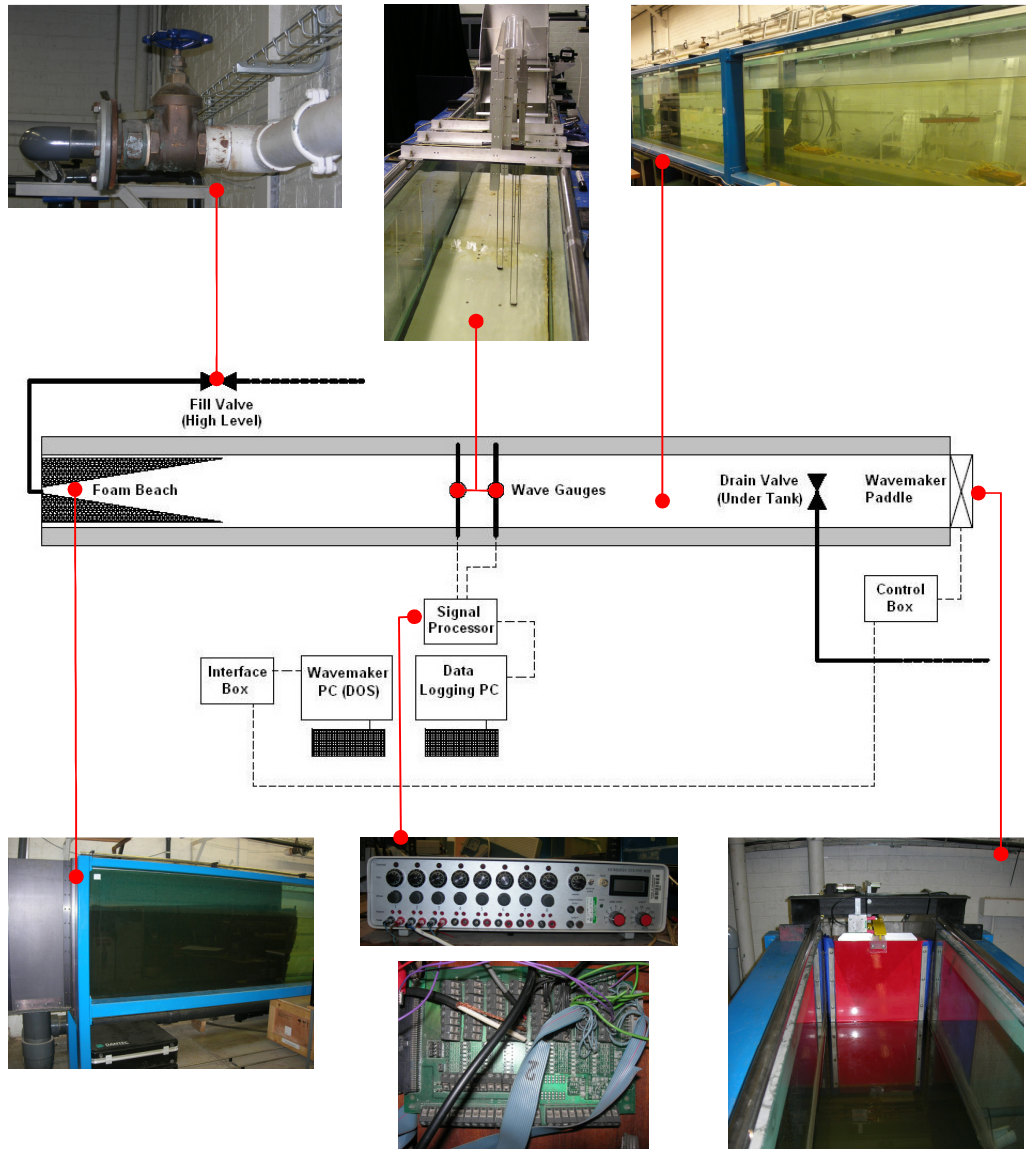


Figure 4.6: Plan view of the wave flume

4.5.2 Wave Generator

The wave flume described previously was equipped with a single hinged-flap type wave-maker (see Figure 4.6) designed and manufactured by *Edinburgh Designs Ltd*, in order to produce both regular and random waves in a water depth of 0.7 m. The wave-maker actively absorbed the reflected waves through the use of a force feedback system. The control of the wave-maker was operated using the *Ocean and Wave* software supplied by *Edinburgh Designs Ltd*. To generate waves in the wave flume, command signals coded using the *WAVE* program needs to be properly compiled to facilitate the computation of a wave elevation time series corresponding to the desired sea state.

Prior to wave generation, the paddle of the wave-maker was moved into the upright position. When the water in the tank was completely still, a “trimming” exercise was carried out using the control box in offline mode. The trim dial was adjusted until the adjacent LEDs were both turned off. The wave generator was subsequently switched online to read the signals from the computer. If the wave generator was incorrectly “trimmed”, the operation of the wave generator might come to a halt during the experiment. The details of the wave generating facility can be found in the *Edinburgh Designs Manual* (Rogers and Bolton King, 1997).

Calibration of the wave generating facility without the test model in place was undertaken to identify the limits of the test range and to ensure that specific incident wave conditions were included in the test program. The water surface profile was measured by resistance type wave probes (see Section 4.7) after they have been calibrated. For generation of regular waves, wave properties were defined in terms of wave frequency, f and wave amplitude, a in the command script as illustrated in Figure 4.7. A comparison between the targeted and measured wave heights for periods ranging from 0.7 s to 1.9 s is graphically displayed in Figure 4.8. The test series present a high degree of correlation between the measured and targeted wave heights, with approximately $\pm 5\%$ discrepancy. For larger wave heights, it can be seen that the measured wave heights are consistently less than the targeted wave heights. This is mainly due to the operational constraint of the wave generating facility. This laboratory effect becomes insignificant when data analysis is performed based on the measured wave heights.

```

experiment "sine" with ("junk,ttf")
begin
run "regular" with (10°)
makewave single (1b 0.05c) on 1.

```

Figure 4.7: Command signal for regular wave generation – sampling duration^a = 60 s; wave frequency^b, $f = 1$ Hz; and wave amplitude^c, $a = 0.05$ m.

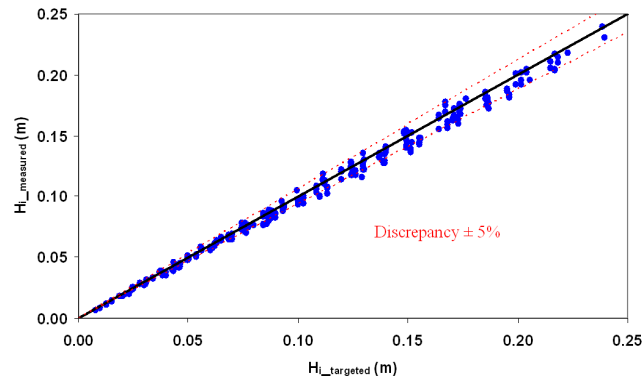


Figure 4.8: Comparison between measured and targeted wave heights for regular waves.

Irregular waves were generated through the input of a standard spectra defined by the peak frequency, f_p , the nominal gain function, G and the peak enhancement factor, γ . Transfer functions to relate the gain functions and the corresponding characterised wave heights were determined through a series of calibrations for each f_p . Figure 4.9 shows a sample command script for generation of the JONSWAP spectrum of a peak period, T_p of 1 s and the spectral zeroth moment wave height, H_{m0} of 0.075 m. The relationships between the G value and the corresponding H_{m0} for $0.7 < T_p < 1.8$ s, as illustrated in Figure 4.10, show that the G value for the corresponding T_p increases with the increasing H_{m0} . The relationship can be expressed in a polynomial function as follows:

$$G = aH_{m0}^2 + bH_{m0} + c \quad (4.4)$$

where a , b and c are the calibration constants as presented in Table 4.3. These calibration equations were used to obtain the G value corresponding to the targeted H_{m0} for a given T_p . The use of G values that are beyond the test limits should be avoided as it may go beyond the operating limit of the wave generator. In the case of irregular seas as described by the Pierson-Moskowitz (PM) spectrum, the calibration procedures for the wave generating facility are the same as before.

```
run "JONSWAP" with (12a,32,1,32)
wave xx =2.5b*jonswap(1c,0.0081,3.3,0.07,0.09);
wave yy=random(xx,3);
-
```

Figure 4.9: Command signal for a JONSWAP spectrum – sampling duration^a = 256 s; wave frequency^b, $f = 1$ Hz; and gain^c, $G = 2.5$

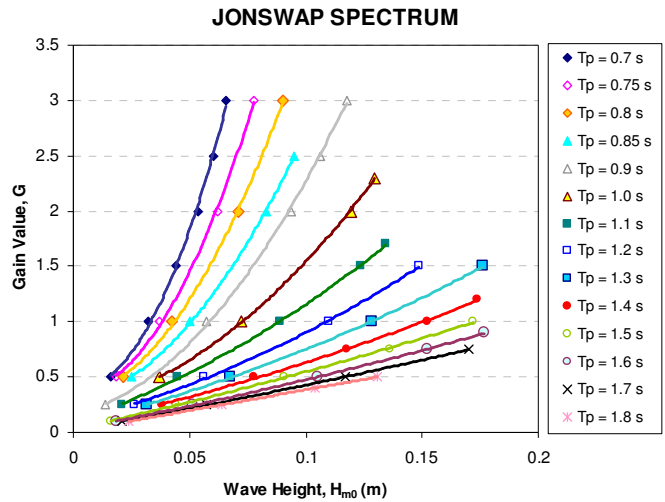


Figure 4.10: Calibration chart for irregular seas as described by the JONSWAP spectra

Table 4.3: Calibration constants for Equation (4.4)

T_p (s)	a	b	c
0.70	648.32	-4.15	0.42
0.75	432.23	0.10	0.36
0.80	294.50	3.26	0.30
0.85	204.65	3.90	0.28
0.90	165.89	4.47	0.17
1.00	92.62	3.89	0.23
1.10	36.05	6.98	0.10
1.20	28.20	5.16	0.10
1.30	17.60	4.95	0.08
1.40	11.43	4.47	0.07
1.50	6.00	4.57	0.03
1.60	5.80	3.87	0.03
1.70	3.11	3.75	0.02
1.80	-0.01	3.75	0.01

The ability to replicate individual waves accurately in an elevation time series is important for this research. In order to ensure the repeatability of the waves in the flume, a series of tests was undertaken prior to the placement of the test models. A wave probe was placed at the test section of the flume for measuring the water level changes. During all test runs the wave probes were calibrated frequently to minimise this source of error. Three identical tests were carried out for regular and irregular waves. For the regular wave case, the targeted mean wave height, H_i and mean period, T were 0.11 m and 1.0 s, respectively; whereas for irregular waves using a JONSWAP spectrum of $\gamma=3.3$, H_{m0} and T_p were expected to be 0.11 m and 1.2 s, respectively. A representative sample of the measured elevation time series is illustrated in Figure 4.11 for regular seas and Figure 4.12 for irregular seas. The JONSWAP spectra measured from the three identical repeat tests in irregular seas are also presented in Figure 4.13. Visual inspection of the time histories and wave energy density spectra indicates very good agreement between the repeat tests for both sea states. Tables 4.4 and 4.5 present some statistical representations of the three nominally identical repeat tests for regular and irregular waves respectively. The agreement between sea measurements from the repeat tests was examined in the time domain for regular seas, and in both time and frequency domains for irregular seas. Overall, there is good agreement between the three tests for each sea state with minor deviations. For regular waves, measurement of H_i and T show typical errors of less than 1.5% and 0.1% respectively. As for irregular waves, the errors of the sea parameters from the three identical repeat tests are less than 1%. The target peak frequency, entered as an input to the wave-maker software, was accurately reproduced in the flume. The error shown by the wave height parameters may be due to wave gauge drift.

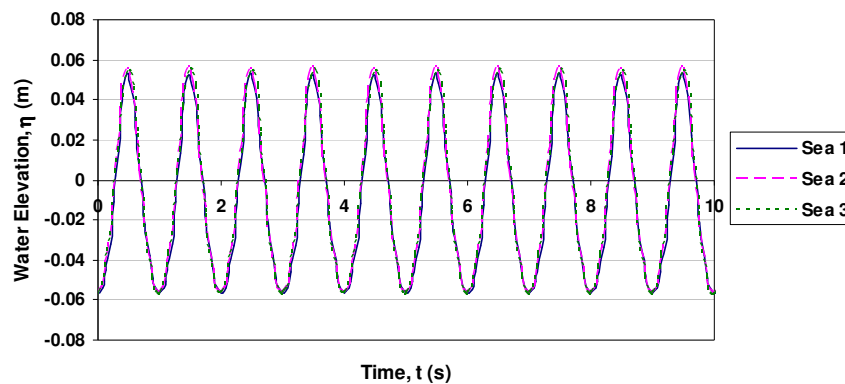


Figure 4.11: Water elevation time histories measured from three repeat tests for regular seas

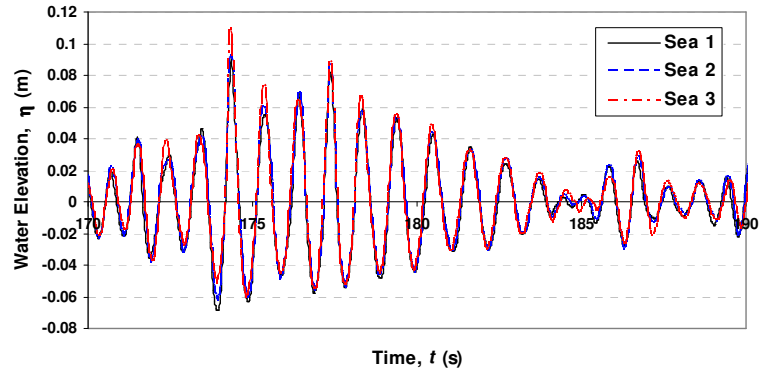


Figure 4.12: Water elevation time histories measured from three repeat tests for irregular waves

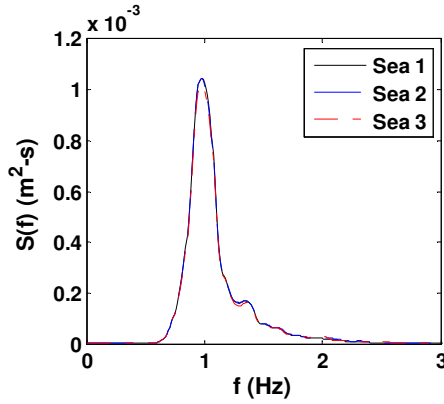


Figure 4.13: Wave spectra measured from three repeat tests

Table 4.4: Sea parameters from three nominally identical repeat tests for regular seas.

Sea Parameter	Sea 1	Sea 2	Sea 3	Mean
H_i (m)	0.1142	0.1122	0.1154	$0.1139 \pm 1.49\%$
T (s)	0.999	1.000	0.998	$0.999 \pm 0.10\%$

Table 4.5: Sea parameters from three nominally identical repeat tests for irregular seas.

Sea Parameter	Sea 1	Sea 2	Sea 3	Mean
H_{m0} (m)	0.1135	0.1139	0.1127	$0.1134 \pm 0.62\%$
T_p (s)	1.205	1.205	1.205	$1.205 \pm 0.00\%$
$T_{-1.0}$ (s)	1.152	1.155	1.152	$1.153 \pm 0.17\%$
T_m (s)	1.104	1.103	1.099	$1.102 \pm 0.27\%$
H_{max} (m)	0.1692	0.1683	0.1664	$0.1680 \pm 0.952\%$

The use of calibration seas as described previously requires a high degree of consistency of the wave generating facility. It is important to ensure that the variables being analysed (*e.g.* H_{m0}) are stationary and the properties are not affected by the sample length (*i.e.* the number of waves produced by the wave generator). In order to verify the consistency of the wave generating facility, four groups of test were carried out with different H_{m0} and T_p . Each group contained three tests of similar G value and f_p as inputs to the WAVE software, but with different run time, *i.e.* 128 s, 256 s and 512 s (the wave generator operated on the basis of 2^n , where $n = 1, 2, 3, \dots$, for generation of a complete series of a JONSWAP spectrum). The number of waves generated in the flume increased with the increasing run time stipulated for a particular test. Figure 4.14 displays the effect of run time on H_{m0} for T_p varying from 0.85 s and 1.40 s. Variation of H_{m0} with respect to run time is fairly small with deviations of less than 2.3% from the mean values. In short, the wave generating facility used in this research was well calibrated and maintained high level of sea repeatability and consistency when in operation.

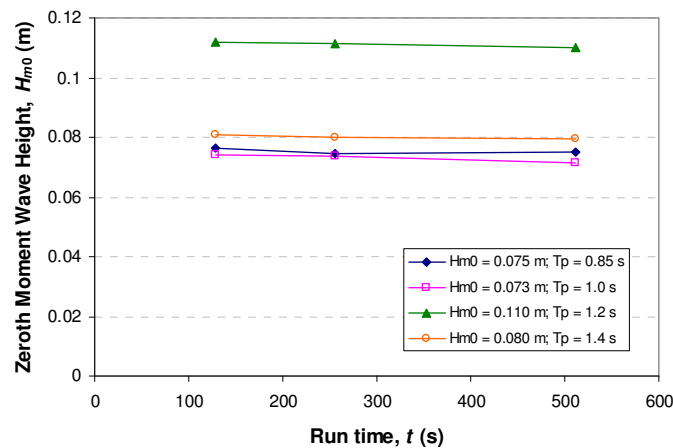


Figure 4.14: Variation of H_{m0} for different run times

4.5.3 Wave Absorber

Wave reflection from flume boundaries is one of the most common laboratory effects to plague physical model experiments. Unwanted reflection can modify the incident wave field, which consequently may impact test results. The effect can be minimised by utilising wave absorbers located at the down-wave end of the flume. In this study, passive-type wave absorbers comprised of two pieces of triangular profile, upright foam (see Figure 4.6) were utilised. They have been successfully used in previous research conducted in the wave

flume. The reflected waves generated in the flume were also minimised by the active absorption wave generator in which an actuating mechanism was installed.

Several test series were conducted in the absence of the test model to investigate the efficiency of the wave absorption system installed in the flume. The incident and reflected spectra were decomposed using the Least Square Method proposed by Mansard and Funke (1980) as described in Section 3.4.2. Figure 4.15 exhibits the degree of wave reflection expressed in term of the reflection coefficient, C_R (refer to Equation (3.19)) for wave period ranging from 0.7 s to 1.8 s and wave height ranging from 0.02 m to 0.20 m for the case of regular seas. The C_R data, which are shown to be more sensitive to the change of wave height than to the change of wave period, range from approximately 0.03 to 0.11. The absorbers performed reasonably well when fronted with shorter period waves. The trend observed for the case of irregular seas is similar to that observed for the regular seas, as illustrated in Figure 4.16; however, the data of irregular waves appear to be more consistent and are better defined by the respective test ranges of H_{m0} . The C_R values range from about 0.05 – 0.11. This amount of wave reflection does occur in a natural beach (Hughes, 1993; Goda, 1985). Jamieson and Mansard (1987) and Chakrabarti (1994) set a scale to an ‘effective’ wave absorber whereby the reflection coefficient should be consistently less than 10%. It is found that the majority of the C_R values are well below 10% in this investigation; therefore, it is believe that the amount of reflection in the flume is deemed to be acceptable without the need for any correction.

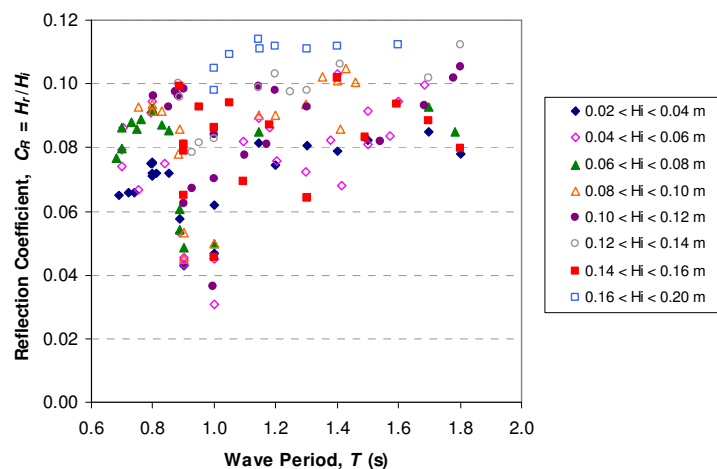


Figure 4.15: Wave reflection by the foam beach in regular seas prior to the installation of test model

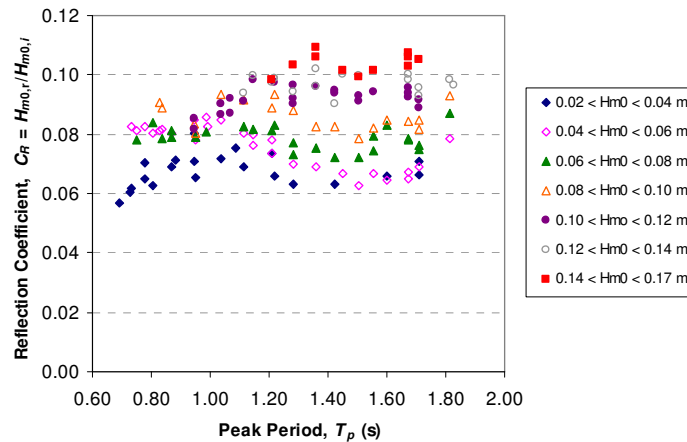


Figure 4.16: Wave reflection by the foam beach in irregular seas prior to the installation of test model

4.6 Model Installations

There are two types of test models being considered in this study, namely (i) SCB and (ii) SCB with wave screens (see Sections 4.2 and 4.3). These models were rigidly fixed to specially-designed, suspended mounting frames through load cells, in which wave loadings were measured. The details of the installation for both types of models are presented in the following sections.

4.6.1 SCB

The SCB model was rigidly fixed in between the side walls of the flume by a mounting frame that was made of stainless steel (see Figures 4.17a). The mounting frame was securely and firmly locked to the rails on the top of the wave flume by the means of brackets and bolts (see Figure 4.17b). A pair of stainless steel load cells (integrated as a part of the mounting frame) was connected to the SCB model at the crest of the structure for measuring horizontal wave forces (see Figure 4.17c). The model was held in suspension with a clearance of 2.5 mm between the model and the flume wall at each side. Using a position controller, the relative position of the model to the still water level was adjustable at arbitrary locations (see Figure 4.17d) such that the required immersion depth could be achieved.

The SCB models of varying porosity were immersed at water depths of 50 mm, 100 mm and 150 mm from the still water level for all the tests performed in this study. The natural frequencies corresponding to these immersion depths for each test model were ascertained by exerting blows of different intensities on the structure when the water was still. The

response of the model was measured by the load cell attached to the crest of the structure and samples of time series records for the SCB9 model at immersion depths of $D = 0.05$ m and 0.15 m are displayed in Figure 4.18. Table 4.6 summarises the mean values of natural frequency and damping ratio of the respective SCB models at $D = 0.05$ m, 0.10 m and 0.15 m. The natural frequencies of the test models ranged from 5.5 Hz – 12.9 Hz. Resonance of the test models was unlikely to occur as the smallest test frequency considered in the present experiments (*i.e.* $f = 1.4$ Hz) was far smaller than the natural frequency of the test models.

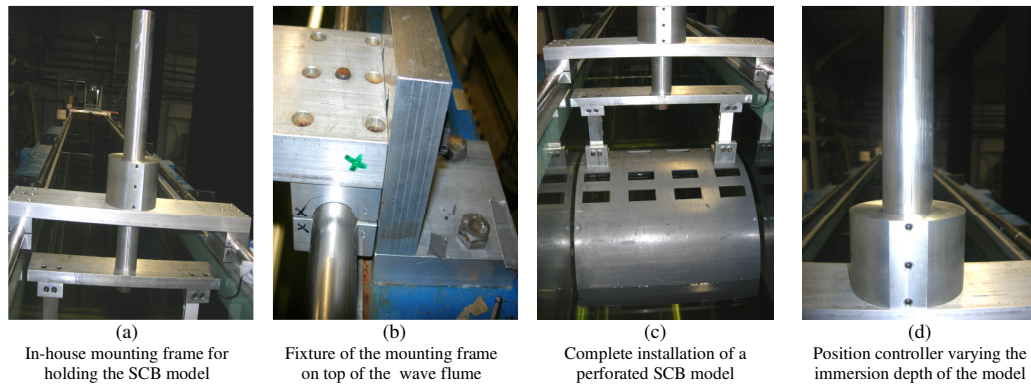


Figure 4.17: Mounting frame designed for fitting a SCB model

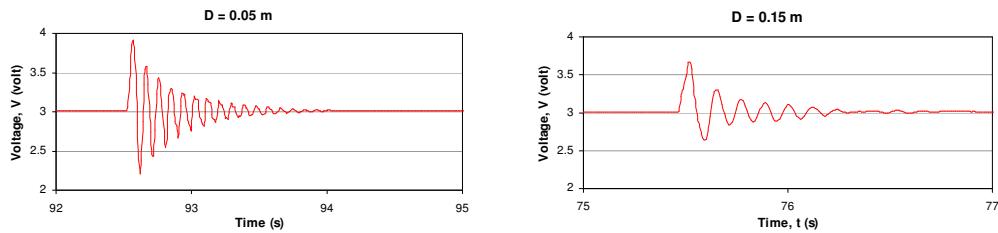


Figure 4.18: Natural frequencies of the SCB9 model at $D = 0.05$ m and 0.15 m

Table 4.6: Summary of natural frequencies and damping ratios of the SCB models

SCB Models	(a) Natural Frequency, f_n (Hz)		
	$D = 0.05$ m	$D = 0.10$ m	$D = 0.15$ m
SCB0	8.1	5.8	5.5
SCB9	11.2	8.7	7.6
SCB18	12.4	9.4	8.8
SCB27	12.9	10.5	9.8

SCB Models	(b) Damping Ratio		
	$D = 0.05$ m	$D = 0.10$ m	$D = 0.15$ m
SCB0	0.063	0.068	0.072
SCB9	0.040	0.050	0.052
SCB18	0.029	0.036	0.045
SCB27	0.025	0.021	0.015

4.6.2 Wave Screens

As described in Section 4.3, the vertical extent of the breakwater was enlarged by incorporating a single or double layer of 300 mm-long wave screens underneath the SCB model. The rectangular metal plates that formed the screen had four holes at the centre, through which screws were used to fix the plates to a vertical connecting bar as shown in Figure 4.5. The 280 mm-long connecting bar with a square cross section of 40 mm x 40 mm had 27 pairs of 5 mm circular holes (with full penetration through the bar). The holes were evenly distributed along the full length of the bar with a space interval of 10 mm. The arrangement of the circular holes on the bar also allowed attachment of horizontal plates with different spacing between them, which in turn led to variation of the wave screen's porosity.

To install the front screen in the wave flume, the screen component was firmly fixed to a suspended 'L' shape mounting frame through a watertight S-type load cell as shown in Figure 4.19. The mounting frame was securely fixed to the tops of the wave flume with the aid of G-clamps. The vertical length of the frame was adjustable to enable the submergence variation of the wave screen. The cross-sectional dimensions of the frame were fixed at 10 mm × 100 mm to provide adequate flexural resistance during wave actions. The edges of the frame were rounded to prevent the formation of vortex shedding in its vicinity. The wave interception area by the frame was considerably smaller than the wetted area; therefore, the flow disturbance caused by the frame was relatively small. For the rear screen, an 'I' shape mounting frame was used and the settings were similar to those of the 'L' shape frame. Both screens tested in this study were separated from the SCB model by 5 mm and the side walls of the wave flume by 2.5 mm so as to ensure all horizontal wave forces were transferred to the measuring load cell. The complete set-up of the wave screens of different configurations together with an SCB model are shown in Figure 4.20.

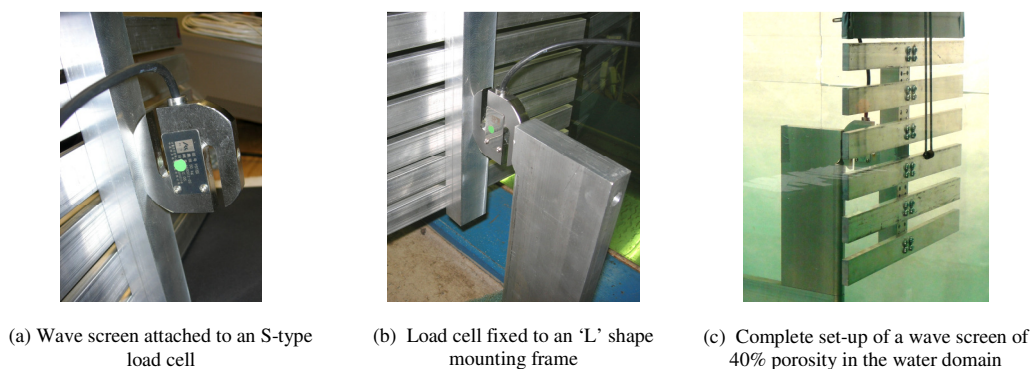


Figure 4.19: Installation of wave screen

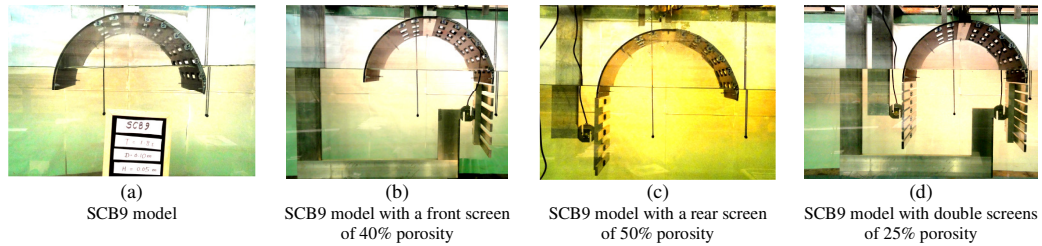


Figure 4.20: Complete installation of test models – SCB9 model and wave screens

The natural frequencies and damping ratios of wave screens of different porosities immersed at 0.05 m, 0.10 m and 0.15 m from the still water level were determined using the similar test procedures adopted for the SCB models as described in Section 4.6.1. Representative samples of time series records for rear screens of 40% porosity (RS40) and 50% porosity (RS50) measured using the ‘S’ type load cells are shown in Figure 4.21. A summary of the average natural frequencies and damping ratios of the respective test models is presented in Table 4.7. Note that the wave screens are distinguished with codes beginning with ‘FS’ (front screen) or ‘RS’ (rear screen), followed by the porosity of the screen in percentage. For instance, ‘FS25’ refers to a front screen of 25% porosity. Referring to the table, variations of the natural frequency and damping ratio are mainly affected by (i) the effective mass of the wave screen; (ii) the fitting between the load cell and the screen; and (iii) the type of mounting frame used. However, these variations are less influenced by the change of immersion depths from 0.05 m – 0.15 m.

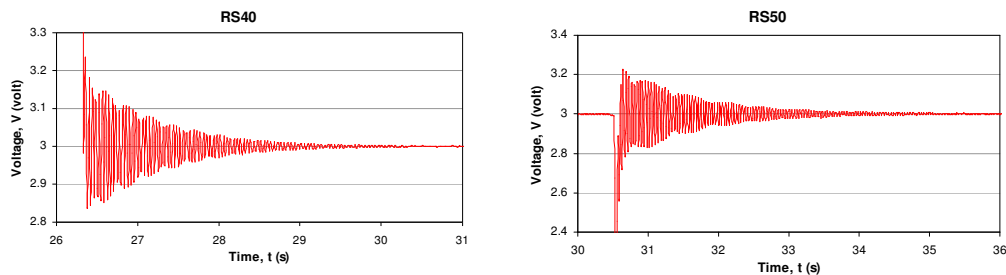


Figure 4.21: Natural frequencies of RS40 and RS25 at $D = 0.05$ m

Table 4.7: Summary of natural frequency for the SCB test models

Wave Screen Models	Natural Frequency, f_n (Hz)		
	$D = 0.05$ m	$D = 0.10$ m	$D = 0.15$ m
FS25	9.3	9.4	9.4
RS25	21.7	21.9	22.8
FS40	9.6	<i>n.a.</i>	<i>n.a.</i>
RS40	23.8	<i>n.a.</i>	<i>n.a.</i>
FS50	9.8	<i>n.a.</i>	<i>n.a.</i>
RS50	25.6	<i>n.a.</i>	<i>n.a.</i>

Wave Screen Models	Damping Ratio		
	$D = 0.05$ m	$D = 0.10$ m	$D = 0.15$ m
FS25	0.010	0.010	0.010
RS25	0.015	0.014	0.015
FS40	0.009	<i>n.a.</i>	<i>n.a.</i>
RS40	0.014	<i>n.a.</i>	<i>n.a.</i>
FS50	0.007	<i>n.a.</i>	<i>n.a.</i>
RS50	0.012	<i>n.a.</i>	<i>n.a.</i>

4.7 Wave Probes

The water surface elevation was measured using water-piercing resistance-type wave probes. These wave probes consisted of two vertical, thin parallel stainless metal rods of 1.6 mm aligned perpendicular to the advance direction of the wave. When immersed in water, the electrodes (metal rods) measured the conductivity of the instantaneous water volume between them. The conductivity changed proportionally to the variation of the water surface elevation. Therefore, it is important to ensure that the metal rods penetrate deep enough into the water to attain full exposure to the largest wave generated in the flume. The main advantages of the resistance-type wave probe are (i) high accuracy up to an error of ± 0.1 mm (Sharp, 1981); (ii) superior linear response between the water elevation and the measured voltage; and (iii) independence upon the wetness and water splashing on the measuring probe (Chakrabarti, 1994).

In this study, six wave probes were respectively attached to a calliper for calibration purpose. Each of the wave probes was fixed at the mid-width of the wave flume by a transverse metal bar rigidly clamped against the rails on the top of the flume walls as shown in Figure 4.6. These probes were plugged into the signal processing box according for data recording. Further description on the signal processing box will be elaborated in Section 4.9.1.

Static calibration of all the wave probes was carefully conducted at the beginning and the end of each set of experiments. If a long series of tests was carried out, the probes were recalibrated at short intervals to cope with the variation of water conductivity due to the change in water temperature. Prior to the calibration, waves were generated in the flume for a few minutes to have a good mixture of water and to ensure water conductivity was homogeneous throughout in the flume. The metal rods of the wave probes were cleaned by using a cloth to remove surfactant stuck on their surfaces. Calibration of wave probe was carried out when the water was completely still in the flume. All the probes were offset adjusted to “zero” position (datum) such that the voltage output was zero at still water level. The probes were then moved through a set distance, *i.e.* 100 mm, with the aid of the callipers mounted onto each probe as indicators. The “Gain” dial for each probe on the signal processing box was adjusted until the voltage desired was achieved. A default gain of 0.5 volts/cm was used for all the probes so that a common calibration factor could be established. These probes were subsequently returned to their original positions upon completion of the calibration. Given that the data acquisition card (see Section 4.9.1) offered an operating range of ± 10 volts, the maximum wave amplitudes that could be captured by the card would be ± 200 mm. Note that the gain value set for the wave probes was appropriate and there was no chance of the crests or troughs being “clipped” by the data logging system.

Figure 4.22 shows the calibration chart for one of the wave probes tested (WP1) for a number of immersion depths varying from -0.06 – 0.08 from SWL. The wave probe exhibited a total linear relation between the water elevation and the voltage output with standard deviation of less than 0.2%. Similar calibration results were also attained for other wave probes. This yielded a standard calibration factor for all the wave probes used in this experimental study:

$$Z = 0.02 V \quad (4.5)$$

where Z and V are the water level in meter and the corresponding voltages in volt, respectively.

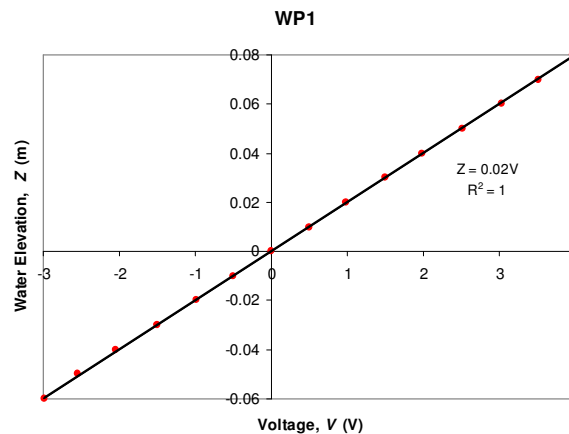


Figure 4.22: Calibration chart for WP1

4.8 Load Cells

A load cell is used to measure the strain of a hardcore material (*e.g.* aluminium and stainless steel) induced by the force applied to it. In this study, two types of load cells were used to measure the horizontal wave forces acting on the different models, *i.e.* binocular-type load cells for SCB models (see Figure 4.23a) and S-type load cells for wave screens (see Figure 4.23b). Both types of load cell were supplied by *Ningbo Xinlan Electric Appliances Co. Ltd*, China. The binocular-type load cells are made of aluminium having International Protection rating 67 (IP67). These load cells are protected against water ingress; however, they are not suitable for continuous immersion in water. Conversely, the S-type load cell, which is made of stainless steel, has an IP68 and is therefore totally water-proofed. Both types of load cells have a rated capacity of 50 kg and up to 150% overload, and 300% overload before permanent damage is incurred on the devices. These load cells were factory-calibrated by the manufacturer before commissioning.

The binocular-type and S-type load cells were attached to the test models from which a direct measurement of the total horizontal wave forces could be made (see Figures 4.17, 4.19 and 4.20). The outputs from these load cells were amplified by a KM02 Series Amplifier as shown in Figure 4.23c and logged by the data acquisition software – *WAVELAB* (see Section 4.9.2). The load cells required the test models to be free to move at slight displacements in response to wave actions, without any restraint from adjacent objects.

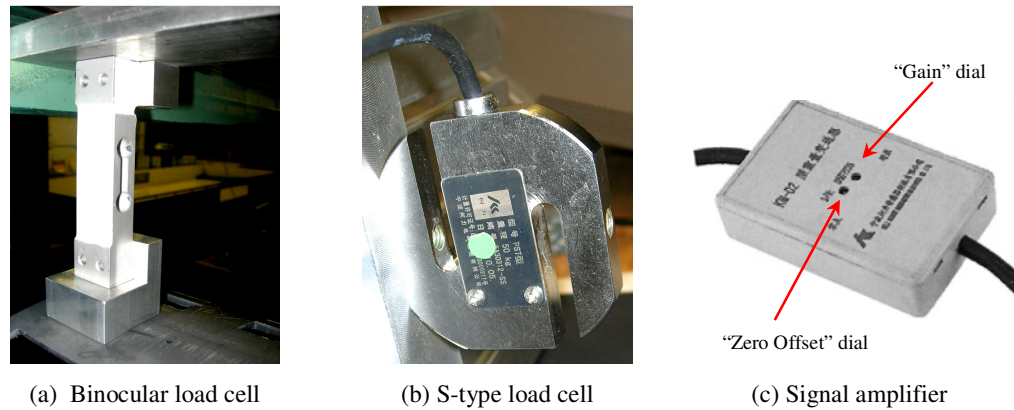


Figure 4.23: Load cells and amplifier

The load cells used in the study were vigilantly checked and calibrated prior to the experiments. The calibration was conducted in the flume when the water was completely calm. A pulley system (see Figure 4.24a) was developed to facilitate calibration of the load cells fixed to the mounting frames at arbitrary levels from SWL. A thin metal rope with low elasticity was tied to selected locations at the centre of the test models (see Figure 4.24b) and the other end of the rope was connected to a known load outside of the flume.

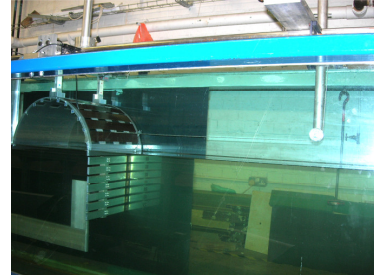
As mentioned earlier, the outputs from the load cells were logged by *WAVELAB* which confined the working range from -1 – 9 volts. Hence, the “zero” position (datum) was set at 3 volts in the absence of load by adjusting the “zero offset” dial of the operating amplifier. In the presence of the known weight acting on the test model, the “Gain” dial of the amplifier was adjusted until the voltage desired was attained. A default gain of 0.25 volts/kg with an accuracy of ± 20 g was employed for all the load cells so that a common calibration factor could be established with no “clipping” effect of the crest and trough of the force signals.

For the binocular-type load cells attached to the SCB model, the total weight (equivalent to the total horizontal wave force) exerted on the breakwater is the sum of the loads measured from both load cells ($W = W_{LC1} + W_{LC2}$). Each load cell has a calibration function of

$$W_{LC} = 9.81 (2V - 6) \quad (4.6)$$



(a) Calibration tools for load cells



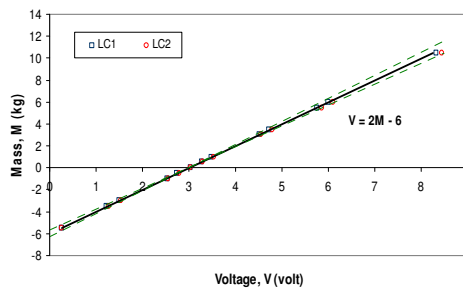
(b) Calibration of load cells

Figure 4.24: Load cell calibration

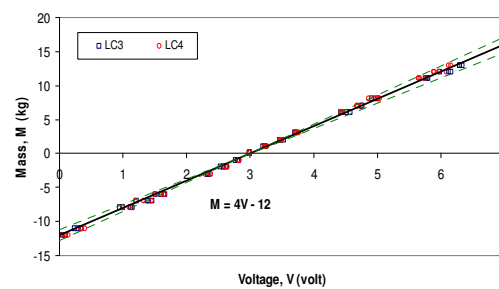
where W_{LC} is the loads measured in Newton (equivalent to the total horizontal wave force) and V is the voltage output from the load cell. For the S-type load cells, the calibration function is:

$$W = 9.81 (4V - 12) \quad (4.7)$$

Upon completing the tuning procedures, the linear response of the respective load cells was validated by applying various static loads in the form of weights using the similar pulley system, and the corresponding voltage variations were recorded. Figure 4.25 shows the measured loads for the binocular-type load cells (LC1 and LC2) and the S-type load cells (LC3 and LC4) validated against the targeted load calculated from Equations (4.6) and (4.7) for an SCB model immersed in a water depth of 0.05 m. It is evident that these load cells exhibit a strong positive linear relation between the mass and the voltage output. The measured loads from the load cells deviate from the predicted loads by less than 5%. Similar results were also obtained for models with other immersion depths. These load cell calibrations proved to be very stable, and no significant variation in the calibration function was noted.



(a) Binocular-type load cells – LC1 and LC2



(b) S-type load cells – LC3 and LC4

Figure 4.25: Load cell calibration charts at $D = 0.05$ m

An attempt was also made to investigate the response of the load cells to (i) the change in immersion depth for the test models; and (ii) the change of distribution of the point load acting on the test models. Calibration of load cells was repeated at immersion depth $D = 0.05$ m and 0.15 m. For each immersion depth, two loading locations were considered for the SCB models and three for the wave screen. Figure 4.26 shows the variations of the voltages for LC1 and LC3 with respect to breakwater immersion depths and loading distributions. It can be observed that the data points for the respective immersion depths, represented by the red/rounded and blue/square markers, are closely related with a deviation of $\pm 5\%$ from the targeted values. This implies that the forces acting on the test models are less influenced by the change in immersion depths. Further, the variation of mass is also found to be insignificant with respect to the change in loading locations. Hence, the calibration functions presented as Equations (4.6) and (4.7) can be safely used for $0.05 \text{ m} \leq D \leq 0.15 \text{ m}$ and, assumingly, for any wave loading distribution on the test models.

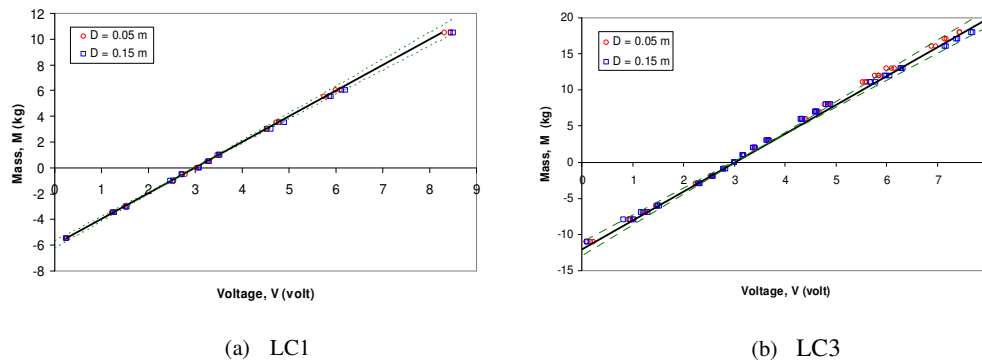


Figure 4.26: Load cell response to variation of the immersion depth of the test models

4.9 Data Acquisition System

The data acquisition system used in this study comprises of two components, *i.e.* data logging hardware and data acquisition software. The details of both components are provided in the following sections.

4.9.1 Data Logging Hardware

In this experimental study, the conversion of analogue signals to digital data was performed by a data logging hardware – DT3003 card supplied by *Data Translation*, as shown in Figure 4.6. It has 32 differential analogue input channels on a single PCI compatible board, with each channel able to log inputs in the range of ± 10 volts. The 12 bit card offers a resolution of $(2 \times 10V)/(2^{12}) = 0.0049$ volts. In cases where the input signals are relatively small (*e.g.*

the load cell signals), amplifiers are needed to boost the signal in order to work over the range of the card, with a margin to avoid any clipping of the signal. The hardware is compatible with most of the data acquisition software available in the market including the *WAVELAB* data acquisition and processing software.

A maximum of 10 channels (6 wave probes and 4 load cells) were employed for data collection in this study. The dynamic range of all the signals relative to the full-scale range of the A/D card (± 10 volts) was checked and adjusted in order to obtain the highest resolution possible. Payne (2008) recommended all incoming signals at maximum value should reach at least two-thirds of the absolute dynamic range so as to obtain the best resolution. Here in this study, a voltage range of ± 10 V was selected for the wave probes, giving a resolution as high as 0.1 mm. On the other hand, the working voltage range for the load cells was limited from -1 V to 9 V due to the constraint of the amplifiers, providing a resolution as good as 20 grams. The resolution level of the load cells was still considered satisfactory when compared to the smallest forces anticipated (approximately 300 grams) from the experiment. It gave a maximum deviation of 6% for small loads acting on the SCB model. It is worthwhile mentioning that the load lesser than 500 grams was approximately 5% of the entire range of data. Therefore, the working range selected for the load cells and the resulting accuracy level are considered acceptable.

The signal quality was constantly checked and monitored during the experiments. Prior to serious data acquisition, electrical noise generated by the equipment itself was identified by looking at each signal on the *WAVELAB* data acquisition program when water was completely calm in the flume. The problem was eliminated by the use of the low-pass filtering function equipped in *WAVELAB* knowing that most electrical noise would be at frequencies that are very much higher than the maximum wave frequencies selected for the experiments. Filtering of the signals sampled by the data acquisition system also helped to prevent the signal components at frequencies greater than half of the data sampling frequency from breaking through into the sampled signal band as 'aliasing'.

4.9.2 Data Acquisition and Processing Software

Data acquisition and part of the analysis were carried out using the *WAVELAB* software developed by the Department of Civil Engineering, Aalborg University, Denmark. The software has a user-friendly graphical interface that is helpful for planning, performing and analysing experiments. Besides data acquisition, it is capable of performing several other functions such as time series analysis, reflection analysis, wave height distribution, standard spectra generation, filtering, and others. The software has a unique capability to increase reliability of analyses by prompting warning texts when the measurements or results are less reliable. This feature prevents the experimenters from making wrong interpretation of the test results.

In this study, *WAVELAB* was mostly used for data acquisition. Some of the main inputs in the data acquisition process are data file name and path, sample frequency, sample duration, the number of channels to be logged and calibration functions (optional). As mentioned previously, the software is equipped with a number of data analysis components. The time series analysis component was used to analyse wave elevations in both time and frequency domains and forces in time domain. Another tool applied in this study was the reflection analysis component which adopted the Least Square Method (Mansard and Funke, 1980) for decomposition of incident and reflected waves. This exercise requires identification of the wave probes and their spacing, sample frequency, calibration function for each wave probe and water depth. The details of the method are provided in Section 3.4.2.

For further interpretation of the raw data, the data acquired by *WAVELAB* was stored in the form of data files and analysed using the *MATLAB* routines. All data channels, which were logged in the form of raw voltage inputs, were loaded into a larger *MATLAB* programme for further analysis. Calibration functions were applied in the program scripts to translate the raw data to the correct units. The data handling procedures used were intended to minimise the need for manual data entry. Also, the programs were mainly used to produce wave energy density spectra, statistical interpretation and graphs plotting.

In addition, a statistical software for data management and advanced statistical analysis – SPSS/PASW Statistics 17 by IBM was used to establish the empirical equations for prediction of the hydrodynamic performance of the tested SCB models, and to perform some statistical validations of the equations. Further details of the software are presented in Chapter 8.

4.10 Test Programme

A well organised test program is utmost important in ensuring completion of the experiments within the time frame and fulfilment of the test objectives upon completion. For the present study, several test objectives were outlined and relevant experiments planned carefully and systematically so as to ensure they were achievable within three years of course study.

4.10.1 Experimental Set-up

In this study, the test section was located at a distance of 12 m from the wave generator. Note that the wave decay by internal friction due to the propagation distance is less than 0.2% (see Appendix A); therefore, the scale effect is almost unnoticeable. Six resistance type wave probes (WP1 – WP6), as shown in Figure 4.27, were used to record the water surface elevations at different locations in the flume. The probes WP1, WP2 and WP3 located offshore of the model were used to separate the incident and the reflected waves using the Least Square method developed by Mansard and Funke (1980) (see Section 3.4.2). The wave probe WP3 was located seaward of the structure with a distance of 2.5 m, which was more than half of the longest wave length generated in the flume. Note that wave decay by viscous boundary layer friction at the test section varied from 0.6% – 2.7% (see Appendix B) which was relatively small. The separations between WP1, WP2 and WP3 set for each wave period are presented in Appendix C. The probe WP4 located at a distance of 50 mm from the seaward wall of the model was used to measure the water surface elevation in front of the model. For the perforated models, probe WP5 was positioned through one of the rectangular openings near the crown to measure the fluctuation of water level within the interference chamber. For the SCB0 model, an opening which was small enough to insert the wave probe WP5 was made at the crown of the breakwater for water level measurement. The transmitted waves were measured by probe WP6, which was located at a distance 2.5 m from the leeward wall of the model. A series of experiments were then conducted in both regular and irregular wave conditions. The sampling durations for regular and irregular waves were 20 s and 256 s, respectively, with a sampling frequency of 100 Hz. The test environments encompassed both deep and intermediate water conditions.

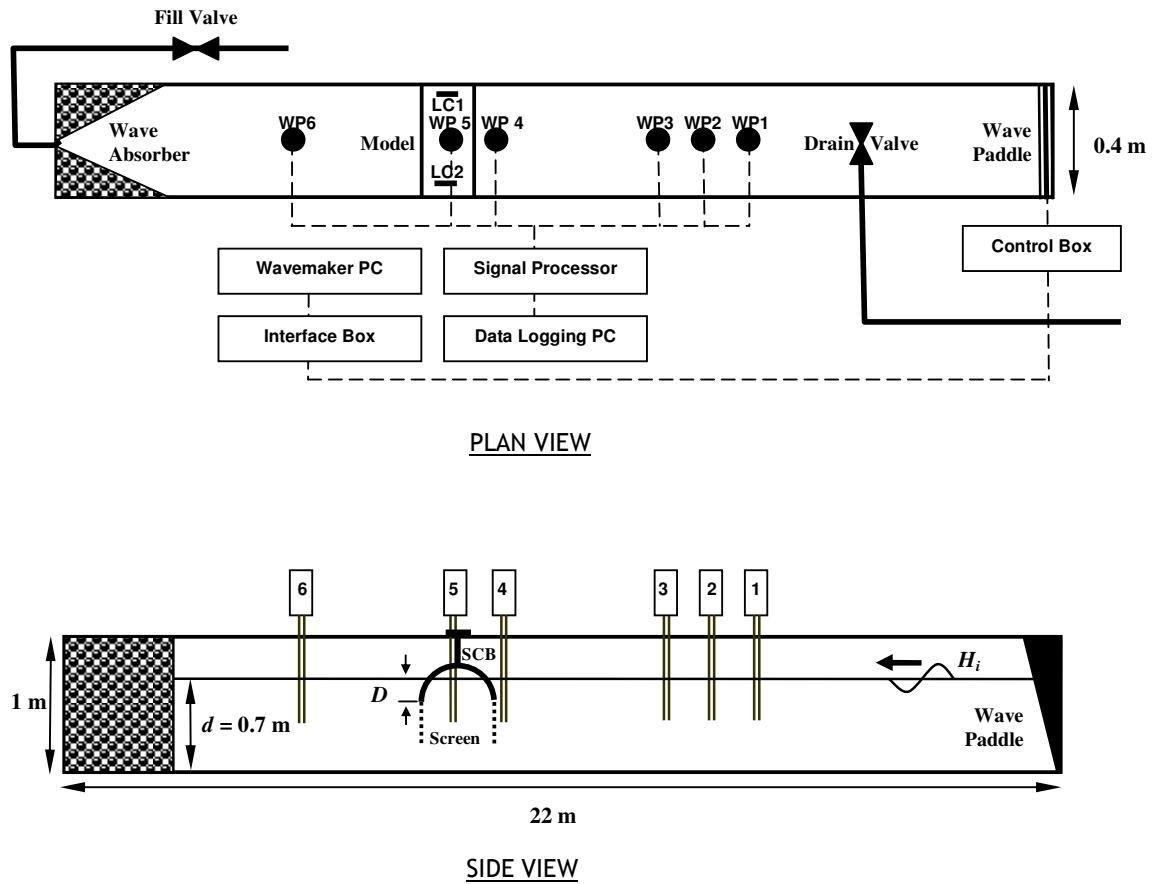


Figure 4.27: Laboratory set-up

4.10.2 Test Series

The tests in this study have been grouped into two series according to the model types, namely:

- Series A:* SCB models of various porosities
- Series B:* SCB9 model with wave screen(s)

Table 4.8 summarises the variety of tests undertaken for experimental *Series A* and *Series B*. Considering the fact that the test programme for each experimental series is rather complex; more details of the programme are given explicitly in the subsequent sections.

Table 4.8: Test matrices for experiment Series A and Series B – wave types and water depths

(a) Experiment Series A

	Wave Types			Water Depth, d			Immersion Depth, D		
	REG	JONS	PM	0.3 m	0.5 m	0.7 m	0.05 m	0.10 m	0.15 m
SCB0	√	√				√	√	√	√
SCB9	√	√		√	√	√	√	√	√
SCB9X	√	√				√	√	√	√
SCB18	√	√				√	√	√	√
SCB27	√	√	√			√	√	√	√

(b) Experiment Series B

		Wave Types			Water Depth, d			Immersion Depth, D		
		REG	JONS	PM	0.3 m	0.5 m	0.7 m	0.05 m	0.10 m	0.15 m
SCB9	FS25	√	√				√	√	√	√
SCB9	FS40	√	√				√	√		
SCB9	FS50	√	√				√	√		
SCB9	RS25	√	√				√	√	√	√
SCB9	RS40	√	√				√	√		
SCB9	RS50	√	√				√	√		
SCB9	DS25	√	√				√	√	√	√
SCB9	DS40	√	√				√	√		
SCB9	DS50	√	√				√	√		
	SS25	√	√				√	√		

Abbreviation:

SCB0	SCB with a solid wall
SCB9/18/27	SCB with a front wall of $\epsilon_{SCB} = 9\%, 18\%, 27\%$
SCB9X	SCB with a front wall of $\epsilon_{SCB} = 9\%$ and a solid rear wall
FS25/40/50	Front screen of $\epsilon_{screen} = 25\%, 40\%, 50\%$
RS25/40/50	Rear screen of $\epsilon_{screen} = 25\%, 40\%, 50\%$
DS25/40/50	Double screen of $\epsilon_{screen} = 25\%, 40\%, 50\%$
SS25	Single screen of $\epsilon_{screen} = 25\%$
REG	Regular waves
JONS	JONSWAP spectrum
PM	Pierson-Moskowitz spectrum

4.10.2.1 Experiment *Series A*: SCB Models of Various Porosities

Experiment *Series A* aims at determining the hydrodynamic characteristics of the SCB under various geometrical and wave effects, and identifying the most optimum configuration of the SCB for coastal protection. These objectives could be achieved via four experimental steps as listed below:

- Series A1*: To evaluate the hydrodynamics of the SCB models of various front wall porosities;
- Series A2*: To investigate the effect of water depth on the hydrodynamics of the SCB9 model;
- Series A3*: To investigate the effect of wave spectra on the hydrodynamics of SCB27 model; and
- Series A4*: To evaluate the effect of the rear wall openings on the hydrodynamics of the SCB9 model

(a) *Series A1*

Experiment *Series A1* aims at investigating the effect of breakwater porosity on the hydrodynamic characteristics of the SCB model in various test conditions. The front porosity of the model was varied at 0%, 9%, 18% and 27% (denoted as SCB0, SCB9, SCB18 and SCB27). These models were tested in a constant water depth of 0.7 m in both regular and irregular waves. For each test model, three relative depths of immersion were studied, *i.e.* the bottom surface of the model was lowered by 0.05 m, 0.10 m, and 0.15 m relative to the still water level, so that the ratio $D/d = 0.071, 0.143$ and 0.214 , where D and d are the breakwater draft and water depth, respectively. Table 4.9 summarises the test parameters selected for *Series A*, and more details of the respective test are presented in Appendices D. In total, 1377 tests were conducted for this test series.

(b) *Series A2*

Experiment *Series A2* aims at examining the hydrodynamic response of the SCB9 model with respect to the change in water depth in both regular and irregular seas. The model was tested in water depths of 0.3 m and 0.5 m (note that SCB9 at $d = 0.7$ m was already tested in *Series A1*). The summary of the test parameters is presented in Table 4.9 and the details of the tests are presented in Appendix E. A total of 402 tests were carried out for *Series A2*.

(c) *Series A3*

Experiment *Series A3* aims at investigating the performance of the SCB27 model under irregular waves as described by the JONSWAP spectrum (for fully developed seas) and the Pierson-Moskowitz spectrum (for growing seas). The former wave type had already been tested in *Series A1*; therefore it was not considered in this test series. This reduced the number of test runs to 84. Details of the experimental variables are presented in Table 4.9 and Appendix F.

(d) *Series A4*

The effect of the rear wall openings was compared between SCB9 (with rear wall openings) and SCB9X (without rear wall openings) under similar test conditions. The details of the tests are tabulated in Table 4.9 and Appendix G. A total of 279 tests were undertaken for this series of experiment.

Dimensionless analysis for Experiment *Series A* has been outlined in Section 3.6.1 for hydraulic coefficients and Section 3.6.2 for horizontal loadings. The ranges of the dimensionless parameters tested in this study are presented in Table 4.10.

Table 4.9: Test parameters for Experiment *Series A*

(a) Regular waves

Series No.	Test Model	d (m)	Type of waves	T (s)	H_i (m)	D (m)	No. of Tests
A1	SCB0	0.7	REG	0.8 - 1.8	0.02 - 0.21	0.05, 0.10, 0.15	144
	SCB9	0.7	REG	0.7 - 1.8	0.02 - 0.20	0.05, 0.10, 0.15	171
	SCB18	0.7	REG	0.7 - 1.8	0.02 - 0.20	0.05, 0.10, 0.15	156
	SCB27	0.7	REG	0.7 - 1.9	0.02 - 0.22	0.05, 0.10, 0.15	321
A2	SCB9	0.3	REG	0.7 - 1.6	0.05 - 0.15	0.05, 0.10, 0.15	87
	SCB9	0.5	REG	0.7 - 1.7	0.05 - 0.15	0.05, 0.10, 0.15	102
A4	SCB9X	0.7	REG	0.7 - 1.8	0.02 - 0.20	0.05, 0.10, 0.15	171
Total =							1152

(b) Irregular waves

Series No.	Test Model	d (m)	Type of waves	T_p (s)	H_{m0i} (m)	D (m)	No. of Tests
A1	SCB0	0.7	JONS	0.8 - 1.8	0.04 - 0.15	0.05, 0.10, 0.15	123
	SCB9	0.7	JONS	0.7 - 1.8	0.02 - 0.16	0.05, 0.10, 0.15	168
	SCB18	0.7	JONS	0.7 - 1.8	0.03 - 0.15	0.05, 0.10, 0.15	138
	SCB27	0.7	JONS	0.7 - 1.9	0.03 - 0.15	0.05, 0.10, 0.15	156
A2	SCB9	0.3	JONS	0.7 - 1.6	0.04 - 0.12	0.05, 0.10, 0.15	90
	SCB9	0.5	JONS	0.7 - 1.7	0.04 - 0.14	0.05, 0.10, 0.15	123
A3	SCB27	0.7	PM	0.8 - 1.3	0.04 - 0.13	0.05, 0.10, 0.15	84
A4	SCB9X	0.7	JONS	0.7 - 1.8	0.03 - 0.14	0.05, 0.10, 0.15	108
Total =							990

Table 4.10: Ranges of the dimensionless parameters

Types of Parameter	Dimensionless Parameter	Range
Porosity of the front curve wall	ϵ_{SCB}	0%, 9%, 18% 27%
Structure placement ratio	$\frac{B}{d}$	0.714, 1.000, 1.667
Relative water depth	$\frac{D}{d}$	0.071 – 0.500
Relative breakwater width	$\frac{B}{L}$ (regular)	0.124 – 0.654
	$\frac{B}{L_p}$ (irregular)	0.124 – 0.654
Wave steepness	$\frac{H_i}{L}$ (regular)	0.01 – 0.12
	$\frac{H_{m0,i}}{L_p}$ (irregular)	0.01 – 0.10
Relative wave height	$\frac{H_i}{d}$ (regular)	0.17 – 0.50 ($d = 0.3$ m)
		0.10 – 0.30 ($d = 0.5$ m)
		0.03 – 0.31 ($d = 0.7$ m)
	$\frac{H_{m0,i}}{d}$ (irregular)	0.13 – 0.40 ($d = 0.3$ m)
		0.08 – 0.28 ($d = 0.5$ m)
		0.03 – 0.23 ($d = 0.7$ m)

4.10.2.2 Experiment Series B: SCB9 model with Wave Screen

Experiment *Series B* incorporates a front screen (FS), a rear screen (RS) or double screens (DS) for draft extension of the SCB9 model. For each screen configuration, the screen porosity was varied at 25%, 40% and 50%. The main purpose here was to propose a free surface SCB that is functional viable and environmentally friendly based on the evaluation of the experimental results. In pursuit of this ultimate goal, three experimental steps were undertaken for *Series B*:

Series B1: To investigate the effect of a single submerged wave screen on the hydraulic performance of the test models;

Series B2: To evaluate the effects of the screen porosity and configuration on the hydrodynamics of the test models; and

Series B3: To assess the influence of immersion depth on the performance characteristics of the breakwater with optimum screen configuration and porosity.

(a) *Series B1*

Experiment *Series B1* aims to explore the feasibility of using a submerged, truncated wave screen as a supplementary part of the SCB9 model in improving its hydraulic performance. The assessment was undertaken by comparing the model performance in two test scenarios, *i.e.* (i) single submerged wave screen of 25% porosity (denoted as SS25 hereafter); and (ii) SCB9 with a submerged front screen of 25% porosity (denoted as SCB9-FS25). The variation of the hydraulic coefficients between the two models is solely due to the effect of the wave screen. The test models were immersed at 0.05 m from still water level in a 0.7 m water depth, subjected to both regular and irregular seas (the characteristics of the test waves are presented in Appendix H). In total 68 tests were carried out for this test category. A summary of this test series is tabulated in Table 4.11.

(b) *Series B2*

Experiment *Series B2* aims to propose an efficient screen design to be integrated as a part of the SCB9 model so as to enhance the overall hydraulic performance. The screen design varied in terms of the configuration and porosity. Three screen configurations were tested in this study, *i.e.* front screen (FS), rear screen (RS) and double screen (DS). The screen in each configuration varied in porosity, with $\epsilon_{screen} = 25\%$, 40% and 50%. These produced 9 combinations of test models, namely SCB9-FS25, SCB9-FS40, SCB9-FS50, SCB9-RS25, SCB9-RS40, SCB9-RS50, SCB9-DS25, SCB9-DS40 and SCB9-DS50. A control model SCB9 was also tested using similar conditions adopted for the others so that the results could be used as reference or base values for comparisons. These models were tested in 0.7 m water depth and immersed at 0.05 m below still water level, subjected to wave period ranging from 0.7 s to 1.8 s. The details of the test variables are included in Table 4.11 and Appendix I. A total of 960 tests were conducted for both regular and irregular seas.

(c) *Series B3*

From experiment *Series B2*, two SCB designs with greater hydraulic potentials were selected for further testing in other immersion depths, *i.e.* $D = 0.10$ m and 0.15 m. Similarly, SCB9, which served as a control model, was tested using identical test conditions. Other test details are shown in Table 4.11 and Appendix J. In total 294 tests were carried out for this set of experiment.

Table 4.11: Test parameters for Experiment Series B

(a) Regular waves

Series No.	Test Model	d (m)	Type of waves	T (s)	H_i (m)	D (m)	No. of Tests
B1	SS25	0.7	REG	0.8 - 1.8	0.05 - 0.15	0.05	17
	SCB9-FS25	0.7	REG	0.8 - 1.8	0.05 - 0.15	0.05	17
B2	SCB9	0.7	REG	0.7 - 1.8	0.05 - 0.15	0.05	38
	SCB9-FS25	0.7	REG	0.7 - 1.8	0.05 - 0.15	0.05	38
	SCB9-FS40	0.7	REG	0.7 - 1.8	0.05 - 0.15	0.05	38
	SCB9-FS50	0.7	REG	0.7 - 1.8	0.05 - 0.15	0.05	38
	SCB9-RS25	0.7	REG	0.7 - 1.8	0.05 - 0.15	0.05	38
	SCB9-RS40	0.7	REG	0.7 - 1.8	0.05 - 0.15	0.05	38
	SCB9-RS50	0.7	REG	0.7 - 1.8	0.05 - 0.15	0.05	38
	SCB9-DS25	0.7	REG	0.7 - 1.8	0.05 - 0.15	0.05	38
	SCB9-DS40	0.7	REG	0.7 - 1.8	0.05 - 0.15	0.05	38
	SCB9-DS50	0.7	REG	0.7 - 1.8	0.05 - 0.15	0.05	38
B3	SCB9	0.7	REG	0.7 - 1.8	0.05 - 0.15	0.10, 0.15	38
	SCB9-RS25	0.7	REG	0.7 - 1.8	0.05 - 0.15	0.10, 0.15	38
	SCB9-DS25	0.7	REG	0.7 - 1.8	0.05 - 0.15	0.10, 0.15	38
Total =							528

(b) Irregular waves

Series No.	Test Model	d (m)	Type of waves	T_p (s)	H_{m0si} (m)	D (m)	No. of Tests
B1	SS25	0.7	JONS	0.8 - 1.8	0.04 - 0.12	0.05	17
	SCB9-FS25	0.7	JONS	0.8 - 1.8	0.04 - 0.12	0.05	17
B2	SCB9	0.7	JONS	0.7 - 1.8	0.02 - 0.16	0.05	80
	SCB9-FS25	0.7	JONS	0.7 - 1.8	0.02 - 0.16	0.05	80
	SCB9-FS40	0.7	JONS	0.7 - 1.8	0.04 - 0.16	0.05	46
	SCB9-FS50	0.7	JONS	0.7 - 1.8	0.04 - 0.16	0.05	46
	SCB9-RS25	0.7	JONS	0.7 - 1.8	0.04 - 0.16	0.05	72
	SCB9-RS40	0.7	JONS	0.7 - 1.8	0.04 - 0.16	0.05	46
	SCB9-RS50	0.7	JONS	0.7 - 1.8	0.04 - 0.16	0.05	46
	SCB9-DS25	0.7	JONS	0.7 - 1.8	0.04 - 0.16	0.05	72
	SCB9-DS40	0.7	JONS	0.7 - 1.8	0.04 - 0.16	0.05	46
	SCB9-DS50	0.7	JONS	0.7 - 1.8	0.04 - 0.16	0.05	46
B3	SCB9	0.7	JONS	0.7 - 1.8	0.04 - 0.14	0.10, 0.15	68
	SCB9-RS25	0.7	JONS	0.7 - 1.8	0.04 - 0.14	0.10, 0.15	44
	SCB9-DS25	0.7	JONS	0.7 - 1.8	0.04 - 0.14	0.10, 0.15	68
Total =							794

Dimensionless analysis for Experiment *Series B* is given in Section 3.6.3 for both hydraulic coefficients and horizontal loading coefficients. Since the length of the wave screen, D' remain unchanged, the corresponding D_T/d for $D/d = 0.071, 0.143$ and 0.214 are $0.500, 0.571$ and 0.643 , respectively. Also note that for experiment *Series B3* the porosities of the SCB, ϵ_{SCB} and wave screen, ϵ_{screen} , and the breakwater placement ratio, B/d have been kept as constants so as to limit the number of experiments in this study. These parameters are subsequently excluded from Equations 3.68 and 3.69.

4.11 Summary

The experimental study for this research was carefully formulated to ensure the quality of the laboratory tests and measurements. Nevertheless, the tests were still subjected to some scale and laboratory effects that were difficult to quantify in practice. These effects can only be studied by comparing small and large scale models, which is beyond the scope of the present study. The hydrodynamic response of the test models were examined via approximately 3500 tests undertaken in stages over a period of 30 months at the Hydraulic Laboratory of the University of Edinburgh. The test data were vigilantly analysed and presented in various forms. The experimental results of *Series A* are presented in Chapter 5, and those of *Series B1 & B2* and *Series B3* are given in Chapter 6 and Chapter 7, respectively.

5

Solid and Perforated Semicircular Breakwaters: Results and Discussions

5.1 General

Free surface semicircular breakwaters of different porosities (as described in Section 4.2) were systematically tested using experimental program *Series A* as indicated in Section 4.10.2.1. These test models include the SCB with a solid front and rear walls (*i.e.* SCB0) and those with perforated front walls of different porosities (*i.e.* SCB9, SCB18 and SCB27). Wave surface elevations were measured at different locations upstream and downstream of these models and the coefficients of wave transmission, reflection and energy dissipation (refer to Equations (3.17), (3.19) and (3.21), respectively) were evaluated. Wave climates in the vicinity of the breakwater models were quantified by the wave disturbance coefficients (refer to Equations (3.24) and (3.25)). The horizontal wave forces on the structure were also measured and represented by a normalised force coefficient as presented in Equation (3.67). These hydrodynamic coefficients were related to several potential affecting parameters identified from dimensionless analysis, as described in Sections 3.6.1 and 3.6.2, by the means of a series of plots, through which the characteristics of the breakwater could be ascertained. The ultimate goal of this exercise is to identify the optimum porosity of the SCB that would meet the targeted hydraulic performance, *i.e.* low wave reflection and high energy loss.

5.2 Hydraulic Characteristics of the SCB

5.2.1 Wave Transmission Coefficients - C_T

The degree of wave transmission of a breakwater is quantified by the transmission coefficient, C_T . The C_T of the SCB0, SCB9, SCB18 and SCB27 models plotted against relative breakwater width, B/L at different ranges of wave steepness for three relative immersion depths, $D/d = 0.071, 0.143$ and 0.214 are presented in Figure 5.1 for regular waves and Figure 5.2 for irregular waves. For irregular waves, the relative breakwater width and the wave steepness are represented by B/L_p and $H_{m0,i}/L_p$, respectively. However, these dimensionless variables are referred to as B/L and H/L (similar to those used for regular waves) in the discussion hereafter for ease of illustration. The wave transmission performance of these test models is discussed with respect to (a) the relative breakwater width, (b) the breakwater porosity, (c) wave steepness and (d) the relative immersion depth.

(a) Effect of Relative Breakwater Width – B/L

The relative breakwater width, B/L compares the breakwater width with the full length of the incident wave. $B/L < 1$ indicates that the wavelength is larger than the width of the breakwater; and a relatively small value of B/L (*i.e.* $B/L \ll 1$) implies that the breakwater is subjected to longer period waves in which the wavelengths are longer. It can be observed from Figures 5.1 and 5.2 that the wave attenuation performance of the test models is less influenced by the types of seas tested (*i.e.* regular and irregular waves). The C_T of the test models immersed at varying levels shows a nearly linear decrease with the increase in B/L , which implies that the solid and perforated SCB models attenuate more wave energy when subjected to smaller period waves regardless of the sea states. The effect of wave period on wave attenuation of the SCB0 model is illustrated in Figure 5.3. Under similar test conditions where $D = 0.10$ m and $H_i = 0.16$ m as displayed in the figure, the SCB0 model makes a better wave attenuator when subjected to smaller period waves (*i.e.* $T = 1$ s).

(b) Effect of Breakwater Porosity – ϵ_{SCB}

For the perforated breakwaters (*i.e.* SCB9, SCB18 and SCB27), the C_T values are found to be closely related with one another for all the test cases of D/d , as seen in Figures 5.1 and 5.2. This shows that the porosity of the front wall has a little influence on the wave transmission, particularly when the waves are irregular. Even so, a small variation of C_T is noticeable in regular waves with the increase in the porosity of the front wall, in which the SCB9 model seems to perform better than other perforated models. On the other hand, the

SCB0 model is evidently superior to the perforated ones, particularly when D/d is small. For the case of regular waves, the SCB0 model is found to outperform the perforated ones by about 11 – 58%, 12 – 42% and 6 – 30% for $D/d = 0.071$, 0.143 and 0.214, respectively. For the case of irregular waves, wave attenuation ability of the solid model is enhanced by 25 – 46% for $D/d = 0.071$, 20 – 31% for $D/d = 0.143$ and 14 – 21% for $D/d = 0.214$. Figure 5.4 illustrates wave propagation past the SCB0 and SCB27 models, with both models immersed at $D = 0.10$ m and subjected to a train of regular waves of $T = 1$ s and $H_i = 0.16$ m. From the figure, the wave activity at the leeside of the SCB0 model is noticeably smaller than that of the SCB27 model.

(c) Effect of Wave Steepness – H_i/L

A wide range of wave steepness has been investigated in the present study, *i.e.* $0.009 < H_i/L < 0.12$ for regular waves and $0.009 < H_{m0}/L_p < 0.10$ for irregular waves. Figures 5.1 and 5.2 show the C_T of the respective test models plotted with respect to different ranges of wave steepness, *i.e.* $0.009 < H_i/L < 0.02$, $0.02 < H_i/L < 0.04$, $0.04 < H_i/L < 0.06$, $0.06 < H_i/L < 0.08$, $0.08 < H_i/L < 0.10$ and $0.10 < H_i/L < 0.12$. In general, the variation of C_T for the respective test models is small regardless of their immersion levels.

(d) Effect of Immersion Depth – D/d

The relative immersion depth, D/d plays an important role in determining the degree of wave transmission for the SCB models. The C_T in Figures 5.1 and 5.2 shows a rapid decrease as D/d increases from 0.071 to 0.214. The reduction of C_T is particularly obvious for the perforated breakwaters. This indicates that SCB models with increased draft would effectively block the transmission of waves to their lee sides. The finding is further validated by visual observation of the wave transmission past the SCB27 model tested in a series of regular waves of $T = 1.1$ s and $H_i = 0.12$ m as shown in Figure 5.5. In the figure, the SCB27 model immersed at 0.15 m displayed a smaller wave activity at its lee side compared to that immersed at 0.05 m.

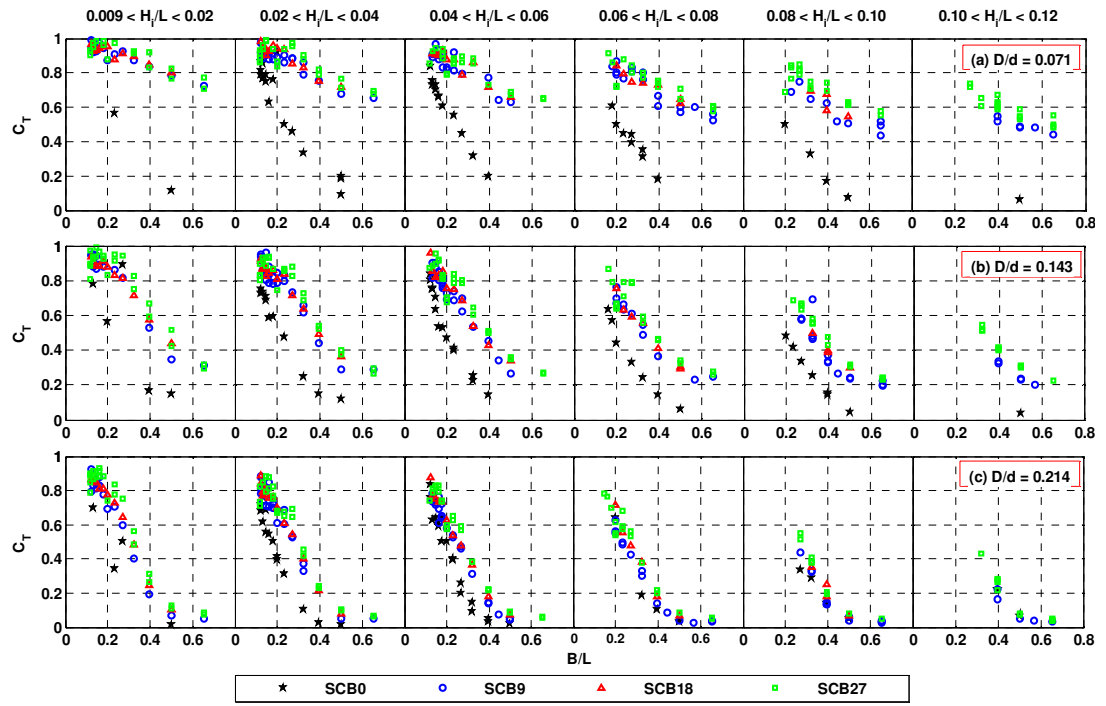


Figure 5.1: C_T for the SCB models in regular waves

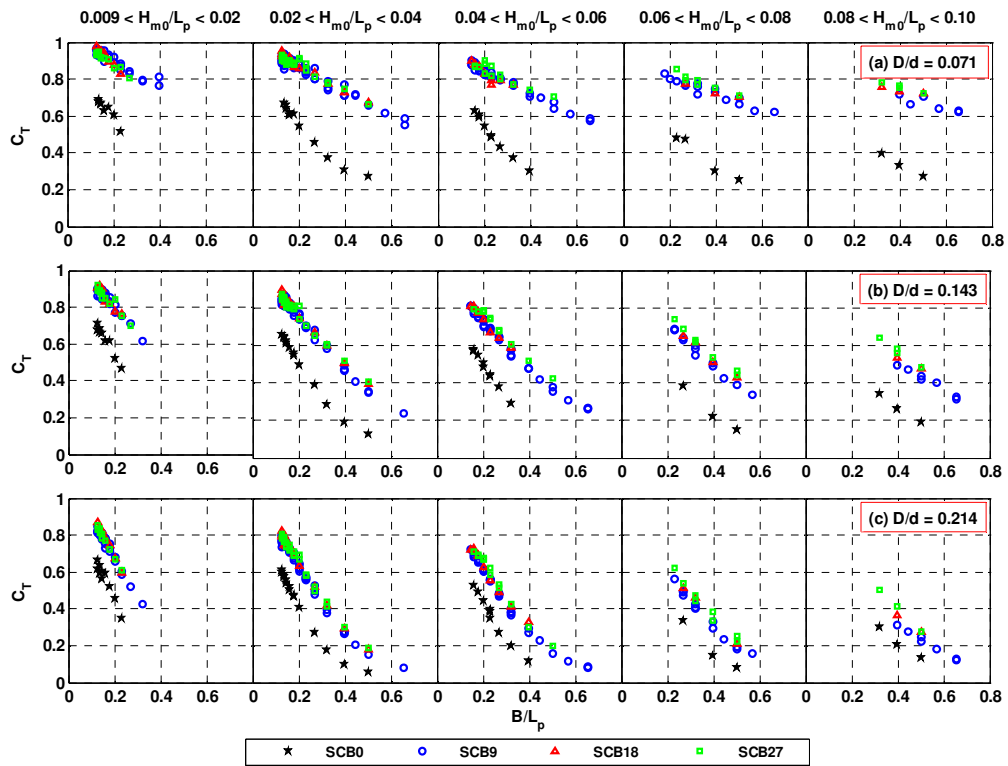


Figure 5.2: C_T for the SCB models in irregular waves

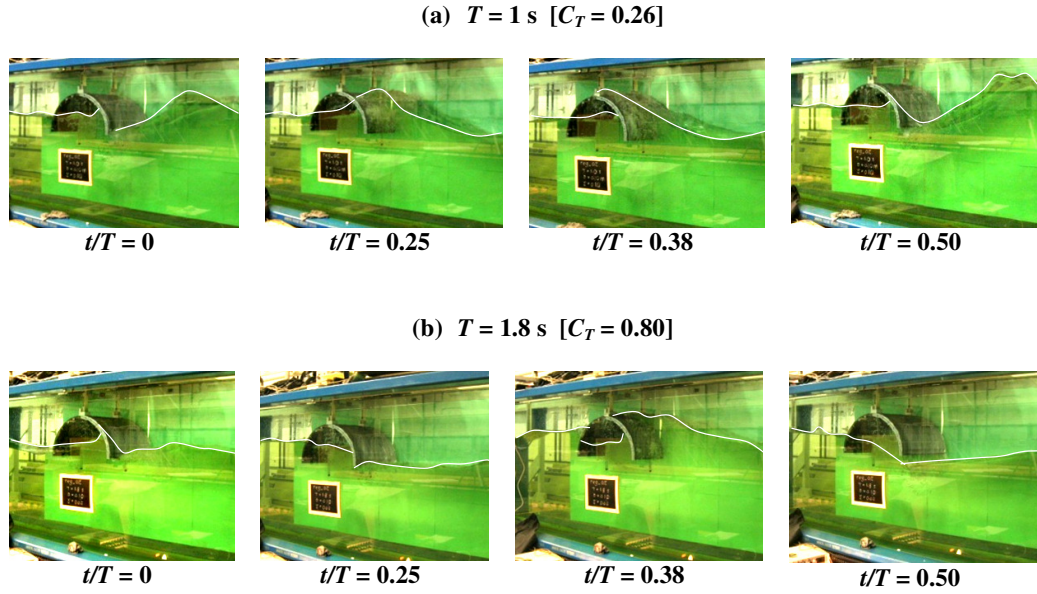


Figure 5.3: The effect of wave period on wave transmission past the SCB0 model of $D = 0.10 \text{ m}$ when exposed to regular waves of $H_i = 0.16 \text{ m}$ – (a) $T = 1 \text{ s}$, $H_i/L = 0.103$; and (b) $T = 1.8 \text{ s}$, $H_i/L = 0.039$. The level of wave transmission is indicated by the transmission coefficient, C_T as shown above. Note that the incident waves propagated from the left of the test model

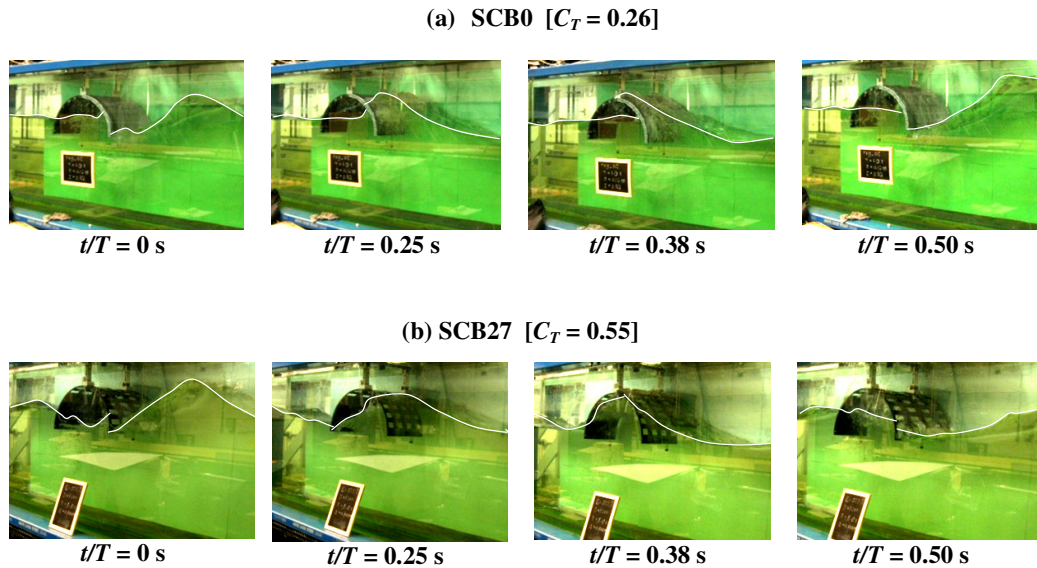


Figure 5.4: The effect of breakwater porosity on wave transmission past the test models of $D = 0.10 \text{ m}$ when exposed to regular waves of $T = 1 \text{ s}$ and $H_i = 0.16 \text{ m}$ ($H_i/L = 0.103$) – (a) SCB0; and (b) SCB27. The level of wave transmission is indicated by the transmission coefficient, C_T as shown above. Note that the incident waves propagated from the left of the test model

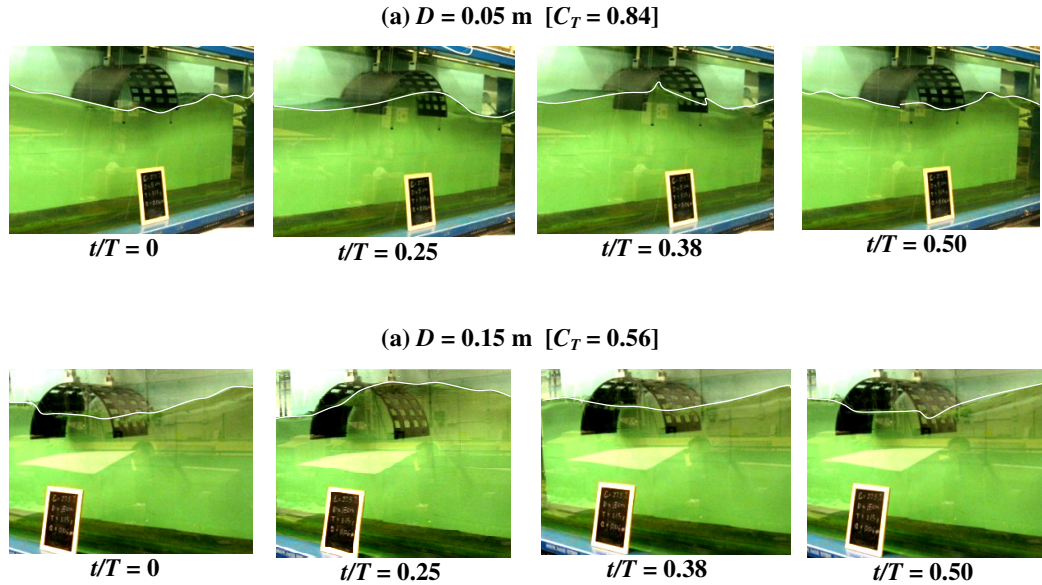


Figure 5.5: The effect of immersion depth on wave transmission past the SCB27 model when exposed to regular waves of $T = 1.1$ s and $H_i = 0.12$ m ($H_i/L = 0.065$) – (a) $D = 0.05$ m; and (b) $D = 0.15$ m. The level of wave transmission is indicated by the transmission coefficient, C_T as shown above. Note that the incident waves propagated from the left of the test model

Table 5.1 summarises the ranges of C_T for the SCB0, SCB9, SCB18 and SCB27 models corresponding to $D/d = 0.071, 0.143$ and 0.214 within the test ranges of $0.12 < B/L < 0.50$ and $0.009 < H_i/L < 0.10$ in regular and irregular wave environments. As far as wave attenuation is concerned, the SCB0 model has proven to be highly efficient in any depths of immersion tested; and it almost stops the short period waves completely in larger immersions. On the other hand, wave suppression efficiency of the perforated SCB models is generally low at $D/d = 0.071$ but improves with the immersion depth. At $D/d = 0.214$, the models were able to dampen up to 95% of H_i in regular waves and up to 85% of $H_{m0,i}$ in irregular waves.

Table 5.1: Ranges of C_T for the SCB models ($0.12 < B/L < 0.50$ and $0.009 < H_i/L < 0.10$)

D/d	(a) Regular Waves		(b) Irregular Waves	
	SCB0	SCB9/18/27	SCB0	SCB9/18/27
0.071	0.08 – 0.87	0.55 – 0.99	0.25 – 0.69	0.66 – 0.98
0.143	0.04 – 0.84	0.24 – 0.99	0.13 – 0.71	0.35 – 0.92
0.214	0.01 – 0.84	0.04 – 0.93	0.05 – 0.67	0.15 – 0.87

5.2.2 Wave Reflection Coefficient – C_R

The wave reflection coefficient, C_R is a measure of the intensity of the reflected waves in front of the breakwaters. Figure 5.6 presents the C_R of the SCB0, SCB9, SCB18 and SCB27 models plotted against the relative breakwater width, B/L at different ranges of wave steepness for three relative immersion depths, $D/d = 0.071, 0.143$ and 0.214 in regular waves. The C_R of the respective SCB models in irregular seas is shown in Figure 5.7.

(a) Effect of Relative Breakwater Width – B/L

The reflective characteristics of the SCB0 model with respect to B/L greatly differ from those of the perforated ones. The C_R values of the solid model increase with the increase of B/L as shown in Figures 5.6 and 5.7. This indicates that the SCB0 model is more reflective to the shorter period waves. For perforated SCB models, the C_R values fluctuate considerably as B/L increases in regular waves; however, the effect is less appreciable in irregular waves. For regular waves, the C_R values of the perforated models first display small wavy undulations with peaks (the first resonance) occurring at $0.2 < B/L < 0.3$ and troughs at $0.3 < B/L < 0.4$, then this is followed by a sharp increase in C_R at $B/L > 0.4$. The second resonance, which is anticipated to attain much higher C_R value, may be insufficiently covered by the test range. This behaviour of C_R , which is often referred as the ‘Bragg reflection’ (Jeon and Cho, 2006), is also observed for some of the free surface breakwaters, *e.g.* the caisson-type breakwaters (Brossard et al, 2003), the quadrant front face breakwater (Sundar and Subba Rao, 2003), the H-type breakwater (Neelamani and Vedagiri, 2002) and the porous-pile breakwater (Hsiao *et al.*, 2008). It is worth noting that the ‘Bragging’ effect of C_R is only dominant in regular waves with a constant period. The effect is less seen in random waves that consist of a wide range of wave periods.

(b) Effect of Breakwater Porosity – ϵ_{SCB}

The C_R results demonstrated in Figures 5.6 and 5.7 show that the SCB0 model is literally a very good wave reflector. The C_R values are consistently higher than those of the perforated SCB models, and achieve values as high as 0.9 in shorter period waves. It is clear that wave reflection is the primary wave reduction mechanism for the SCB0 model. This explains the superiority of the SCB0 model over the other perforated SCB models in attenuating wave energy as seen in Figures 5.1 and 5.2. For the perforated SCB models, the reflectivity is found to be less affected by the variation in porosity of the front curved wall (*i.e.* $9\% < \epsilon_{SCB} < 27\%$). However, it might be possible that the front wall porosity could be a major affecting parameter for breakwaters with $0\% < \epsilon_{SCB} < 9\%$.

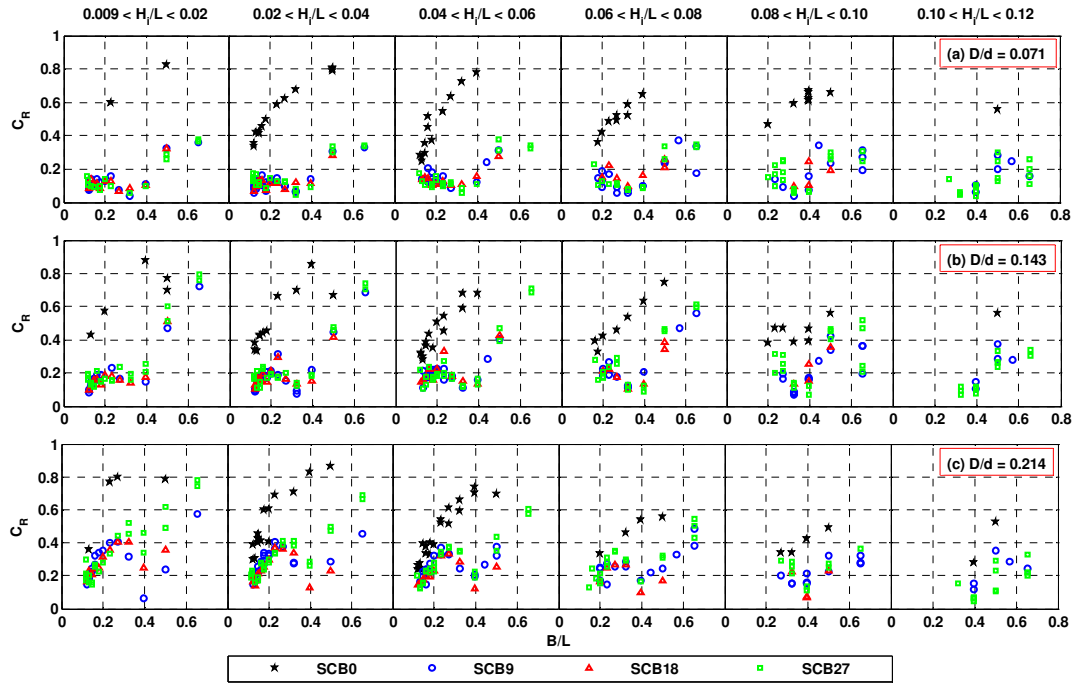


Figure 5.6: C_R for the SCB models in regular waves

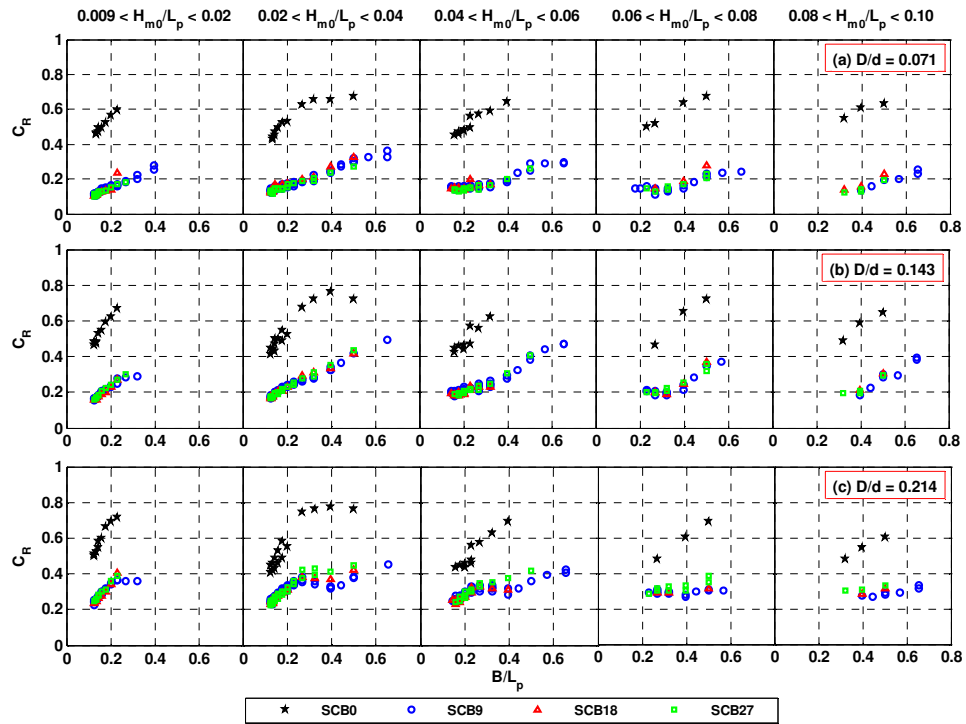


Figure 5.7: C_R for the SCB models in irregular waves

(c) Effect of Wave Steepness – H/L

Wave steepness seems to have a strong influence on the C_R of the SCB0 model, in which steeper waves tend to produce lower reflection. This response is also present in the perforated breakwaters but the influence is comparatively smaller. These results are somehow consistent with those of the bottom seated semicircular caisson (Tanimoto and Yoshimoto, 1982). Reduction of C_R in the presence of high steepness waves could be explained by the fact that such waves release a large amount of wave energy when interacting with breakwaters, thereby limiting the energy reflected to seaside.

(d) Effect of Relative Immersion Depth – D/d

The relative immersion depth has ‘inconsistent’ contribution to the C_R of the SCB models. For the SCB0 model, the C_R variation with the change in D/d is small, as seen in Figures 5.6 and 5.7. For perforated SCB models, a stronger control of C_R by the relative immersion depth is observed in regular waves, *i.e.* at $B/L < 0.4$ the peak C_R increases with D/d ; and at $B/L > 0.4$ the C_R seems to achieve higher values at $D/d = 0.143$. The former observation can be explained by the fact that when exposed to longer period waves the reflectivity of the perforated models increases with an increase of breakwater draft. Whilst, the latter observation is mainly due to effective interception of the shorter period waves by both the breakwater draft and freeboard from the SWL at $D/d = 0.143$. Note that the reduction of C_R at $D/d = 0.214$, as seen in Figure 5.6, is resulted from wave overtopping due to the limited freeboard of the structure at this stage. These C_R characteristics are also noticed in irregular waves (see Figure 5.7); however, the C_R variation with respect to D/d is comparatively small.

A summary of the C_R ranges for the SCB0 and perforated models confined to the test ranges of $0.12 < B/L < 0.50$ and $0.009 < H/L < 0.10$ in regular and irregular wave environments is given in Table 5.2. The C_R values reveal that the SCB0 model is highly reflective to incident waves (with the highest C_R of 0.87 recorded in regular waves and 0.78 recorded in irregular waves). The excessive waves reflected from the breakwater may lead to a confusing sea state in front of the structure (refer to Section 5.2.5) and pose detrimental implications to the integrity of the structure, marine traffic, operation of the harbour and coastal environment. On the other hand, the perforated SCB models are good anti-reflection breakwaters (with the highest C_R of 0.62 recorded in regular waves and 0.45 recorded in irregular waves); hence may find their applications in providing wave protection to some of the marine facilities.

Table 5.2: Ranges of C_R for the SCB models ($0.12 < B/L < 0.50$ and $0.009 < H/L < 0.10$)

D/d	(a) Regular Waves		(b) Irregular Waves	
	SCB0	SCB9/18/27	SCB0	SCB9/18/27
0.071	0.24 – 0.83	0.04 – 0.38	0.43 – 0.67	0.10 – 0.32
0.143	0.28 – 0.87	0.07 – 0.60	0.41 – 0.76	0.16 – 0.43
0.214	0.24 – 0.86	0.06 – 0.62	0.41 – 0.78	0.23 – 0.45

5.2.3 Energy Dissipation Coefficient – C_L

In the absence of advanced measuring equipment such as a PIV, the hydraulic processes taking place in the vicinity of the SCB models can be visualised using the means of still and video cameras. The hydraulic processes observed during the experiments which are deemed to contribute to the energy damping are shown in Figure 5.8. These energy dissipation mechanisms include: (i) exchange of water jet flow around the porous front wall during the passage of waves; (ii) wave run-up at the front wall; (iii) the occasional wave overtopping above the test models; (iv) formation of eddies around the bottom walls; (v) water infiltration into the wave chamber and turbulent flow within the chamber; and (vi) flow instability close to the free surface at the leeside of the breakwater due to pressure difference. The intensity of these processes occurring in the vicinity of the SCB models vary with test conditions.

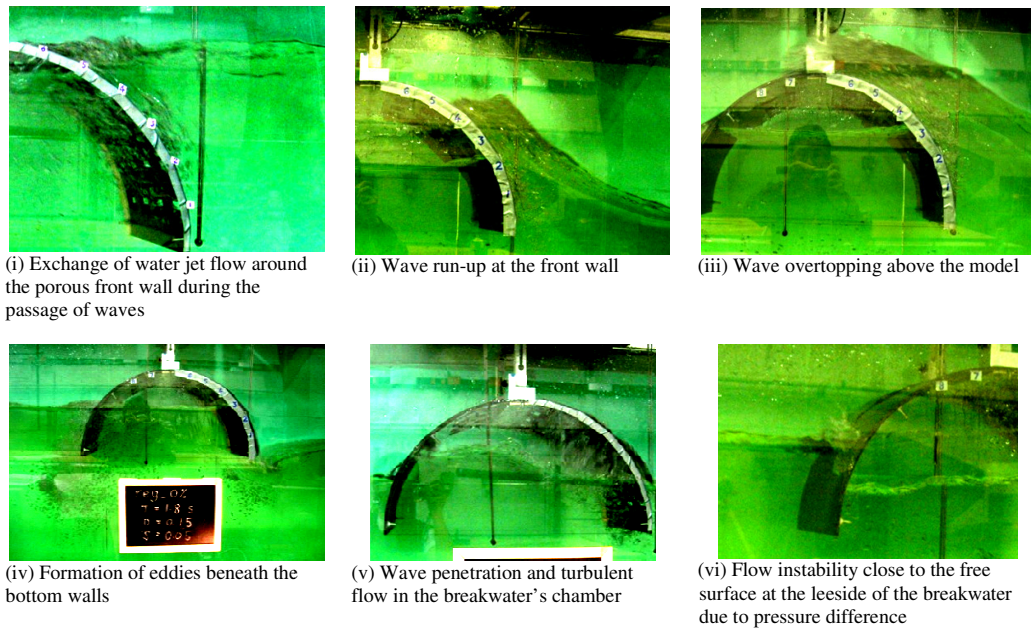


Figure 5.8: Hydraulic processes observed in the experiment. Note that the incident waves propagated from the left of the test model

In this study, the energy loss introduced by the SCB models is quantified by C_L (refer to Equation (3.21)). The C_L values of the SCB models corresponding to different D/d ratios for various ranges of H/L are presented in Figure 5.9 for the case of regular waves, and Figure 5.10 for the case of irregular waves.

(a) Effect of Relative Breakwater Width – B/L

In Figures 5.9 and 5.10, the C_L values for the SCB0 model differ from those of the perforated ones in the sense that they have smaller variations and exhibit a varying pattern with B/L , in both regular and irregular seas. The SCB0 model proved to be a better energy dissipater when subjected to longer period waves ($B/L < 0.3$); nonetheless, this ability deteriorates in shorter period waves ($B/L > 0.3$) due to the increasing wave reflection. For the perforated SCB models, the C_L values increase with the increasing B/L for $D/d = 0.071$. At higher D/d ratios, the increment of C_L is only observed at $B/L < 0.4$; beyond which the C_L values decrease with B/L for regular waves (see Figure 5.9), and remain rather constant thereafter for irregular waves (see Figure 5.10). The drop of C_L at $B/L > 0.4$ in regular waves could be due to the considerable enhancement of the reflection efficiency of the perforated models when exposed to shorter period waves (see Figure 5.7). It is interesting to note that both the maximum C_L and the minimum C_R occur at $B/L \approx 0.4$. In other words, the perforated SCB models serve as good anti-reflection breakwaters that are highly energy dissipative for waves when the width of the breakwater chamber is built at 0.4 times the design wavelength. Therefore, $B/L = 0.4$ could be used as a design parameter for determining the size of a perforated semicircular breakwater caisson.

(b) Effect of Breakwater Porosity – ϵ_{SCB}

Breakwater porosity in regular waves has more influence on the C_L of the perforated SCB models than that in irregular waves, whereby the C_L values decrease with the increasing porosity of the front curved wall. The SCB0 model is an advanced energy dissipater in shorter period waves; however, in longer period waves the energy dissipation performance of the perforated models is more satisfactory as shown in Figures 5.9 and 5.10. These findings can be confirmed via visual inspection of the hydraulic processes induced by the SCB0 and SCB9 models in Figures 5.11 and 5.12, respectively. When the test models were subjected to a wave period of 1.6 s ($B/L = 0.15$) as seen in Figure 5.11, the SCB0 model incurred wave run-up at the front wall and formation of eddies at the bottom edges which led to significant energy dissipation; whilst the SCB9 model allowed large waves passing underneath the structure without much interception. When wave period reduced to 0.8 s ($B/L = 0.50$) and the

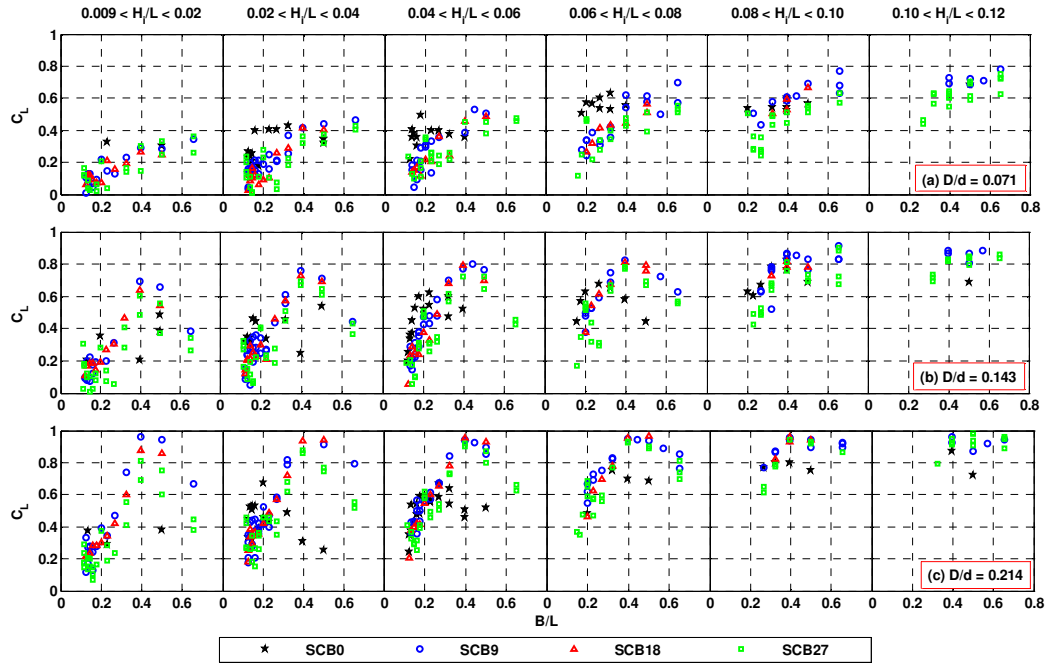


Figure 5.9: C_L for the SCB models in regular waves

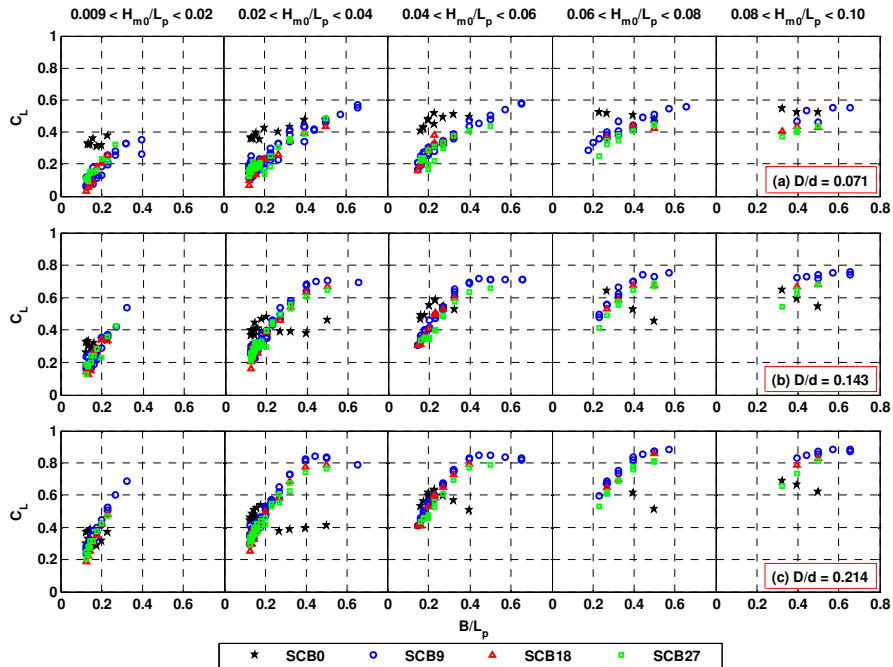


Figure 5.10: C_L for the SCB models in irregular waves

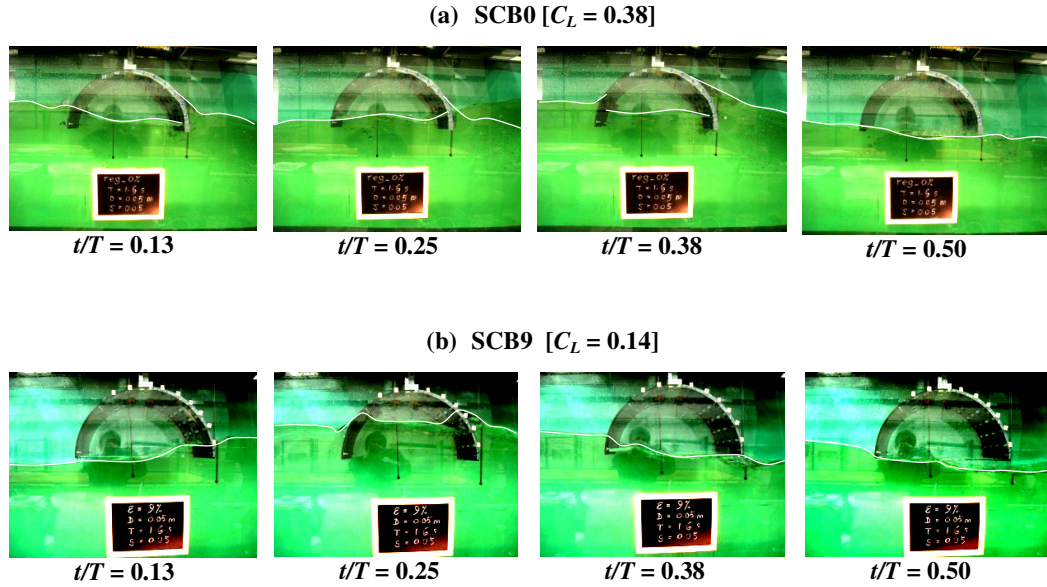


Figure 5.11: Hydraulic processes induced by the SCB0 and SCB9 models immersed at $D = 0.05$ m and subjected to a train of regular waves of $T = 1.6$ s ($B/L = 0.15$) and $H_i = 0.10$ m ($H_i/L = 0.05$). The level of energy loss induced by the models is indicated by the energy dissipation coefficient, C_L as shown above. Note that the incident waves propagated from the left of the test model

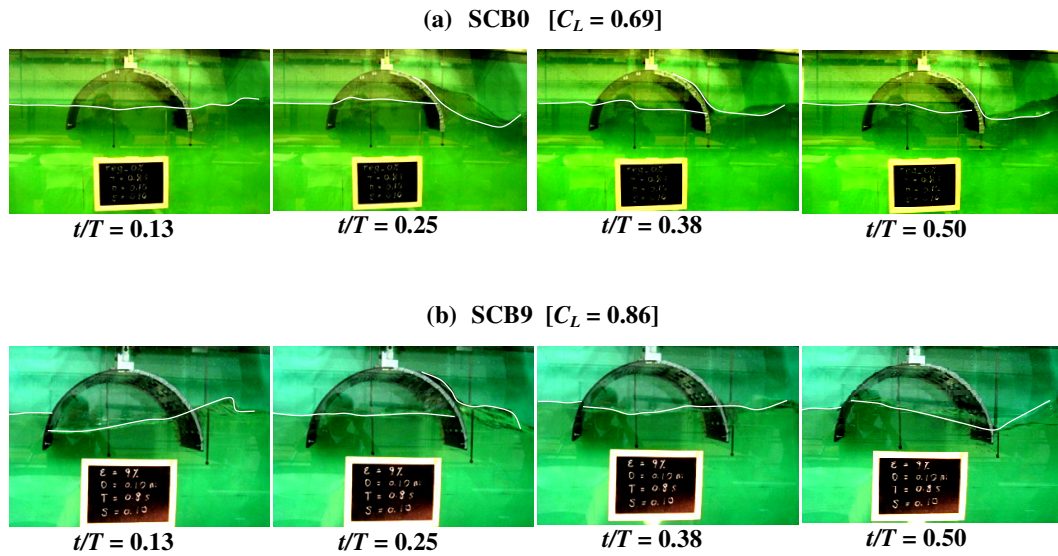


Figure 5.12: Hydraulic processes induced by the SCB0 and SCB9 models immersed at $D = 0.10$ m and subjected to a train of regular waves of $T = 0.8$ s ($B/L = 0.50$) and $H_i = 0.17$ m ($H_i/L = 0.10$). The level of energy loss induced by the models is indicated by the energy dissipation coefficient, C_L as shown above. Note that the incident waves propagated from the left of the test model

breakwater draft increased to 0.10 m as shown in Figure 5.12, the SCB9 model outperformed the SCB0 model by about 17% in energy dissipation; and the water exchange through the openings at the front wall was identified to be the primary cause to the energy dissipation.

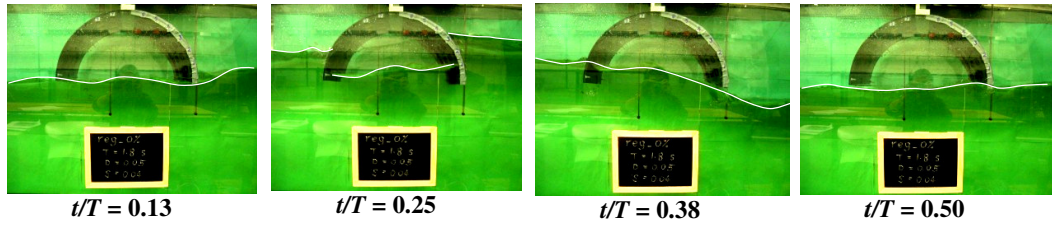
(c) Effect of Wave Steepness – H/L

Wave steepness has a dominant effect on the C_L of the SCB models, whereby higher energy dissipation is caused by steeper waves as can be seen in Figures 5.9 and 5.10. Waves of higher H/L tend to be less stable and are easily deformed by the semicircular breakwaters; hence, substantial amount of energy is released at the structures.

(d) Effect of Relative Immersion Depth – D/d

The influence of the relative immersion depth on C_L of the SCB models is strong. Figures 5.9 and 5.10 show that for all ranges of H/L the C_L values of the SCB models increase as D/d increases. The increase of C_L for the perforated models is particularly immediate compared to that of the SCB0 model. This is because the perforated breakwaters of larger immersion depths provide larger area for wave-structure interactions which consequently allows greater energy dissipation. The maximum C_L values for the perforated breakwaters in regular waves are about 0.75, 0.85 and 0.95 for $D/d = 0.071, 0.143$ and 0.214 , respectively; and 0.58, 0.75, and 0.88 for irregular waves, correspondingly. The hydraulic processes corresponding to the breakwater immersion depth are illustrated in Figures 5.13 and 5.14. At $T = 1.8$ s and $D = 0.05$ m ($D/d = 0.071$), the presence of the SCB0 model resulted in flow instability in the chamber due to pressure difference (see Figure 5.13a); nevertheless, the effect was not observed in SCB9 model (Figure 5.13b). As the draft of the breakwater models increased to 0.15 m ($D/d = 0.214$), both models exhibited much better interactions with the incoming waves as seen in Figure 5.14. The SCB0 model induced large overtopping of waves and significant eddies were found to be moving in an anti-clockwise direction around the rear wall (see Figure 5.14a). On the other hand, most of the overtopping water on the SCB9 model infiltrated into the chamber through the openings, resulting in turbulence of the water in the chamber as shown in Figure 5.14b.

(a) SCB0 [$C_L = 0.13$]



(b) SCB9 [$C_L = 0.05$]

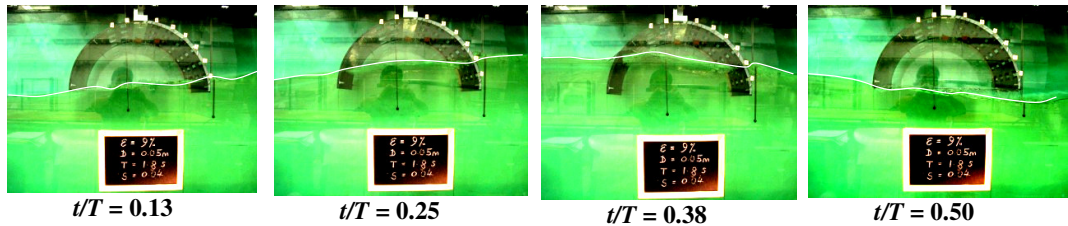
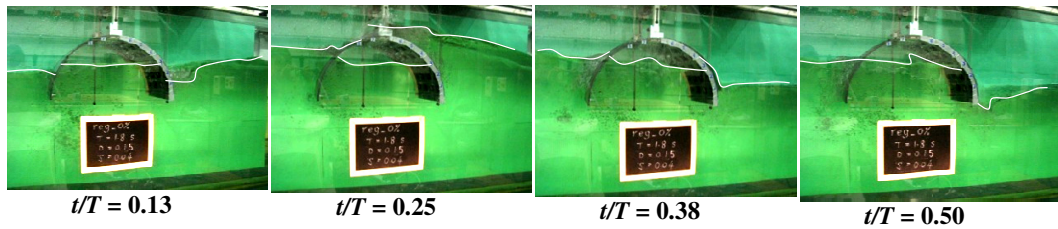


Figure 5.13: Hydraulic processes induced by the SCB0 and SCB9 models immersed at $D = 0.05$ m and subjected to a train of regular waves of $T = 1.8$ s ($B/L = 0.12$) and $H_i = 0.16$ m ($H_i/L = 0.04$). The level of energy loss induced by the models is indicated by the energy dissipation coefficient, C_L as shown above. Note that the incident waves propagated from the left of the test model

(a) SCB0 [$C_L = 0.35$]



(b) SCB9 [$C_L = 0.30$]

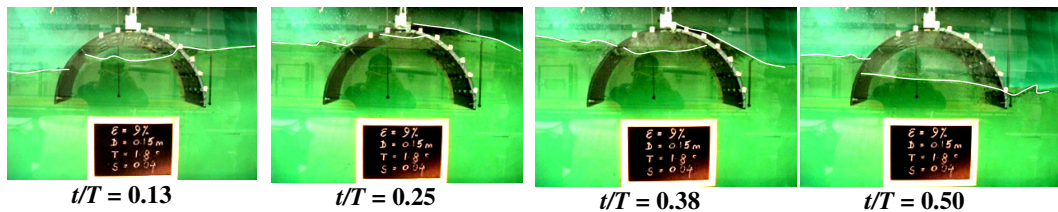


Figure 5.14: Hydraulic processes induced by the SCB0 and SCB9 models immersed at $D = 0.15$ m and subjected to a train of regular waves of $T = 1.8$ s ($B/L = 0.12$) and $H_i = 0.16$ m ($H_i/L = 0.04$). The level of energy loss induced by the models is indicated by the energy dissipation coefficient, C_L as shown above. Note that the incident waves propagated from the left of the test model

Table 5.3 presents the variation of C_L for the SCB models for $0.12 < B/L < 0.50$ and $0.009 < H/L < 0.10$ in both regular and irregular seas. The figures suggest that the perforated SCB models can potentially be effective energy dissipaters if properly designed. They are highly dissipative to the shorter period waves and achieve optimum performance (*i.e.* low reflection and high energy dissipation) at $B/L = 0.4$. On the other hand, the SCB0 model has also been shown to be a better energy dissipater in longer period waves; however, the spread of strong vortices formed beneath the rear wall to deeper water column may pose a certain degree of interference to the bedloads.

Table 5.3: Ranges of C_L for the SCB models ($0.12 < B/L < 0.50$ and $0.009 < H/L < 0.10$)

D/d	(a) Regular Waves		(b) Irregular Waves	
	SCB0	SCB9/18/27	SCB0	SCB9/18/27
0.071	0.10 – 0.63	0.01 – 0.67	0.31 – 0.55	0.04 – 0.48
0.143	0.20 – 0.82	0.01 – 0.86	0.26 – 0.64	0.13 – 0.72
0.214	0.24 – 0.80	0.07 – 0.97	0.28 – 0.68	0.19 – 0.87

5.2.4 Wave Disturbance Coefficient in Front of the Breakwater – C_F

The wave disturbance coefficient, C_F is used to quantify the local wave climate at the front of the test models (refer to Equation (3.24)). $C_F > 1$ indicates an increase of wave activity and $C_F < 1$ indicates a decrease of wave activity in front of the SCB models; whilst $C_F = 1$ implies no change in local wave climate. The C_F of the solid and perforated SCB models are plotted using similar format as previously adopted by the hydraulic coefficients. The results for regular and irregular seas are presented in Figure 5.15 and Figure 5.16, respectively.

(a) Effect of Relative Breakwater Width – B/L

The C_F of the SCB0 and perforated models exhibits arbitrary trends as B/L increases as shown in Figures 5.15 and 5.16. For the SCB0 model, an increase of C_F with respect to B/L can be seen for $D/d = 0.071$ and 0.143 for different ranges of H/L ; however, at $D/d = 0.214$ the C_F displays a parabolic trend, in which the C_F peak shifts from $B/L = 0.18$ to $B/L = 0.50$ as H/L increases. For the perforated breakwaters, a fluctuation of C_F with double peaks at $B/L \approx 0.18$ and 0.50 and a trough at $0.34 < B/L < 0.4$ are spotted in the figures. The fluctuation of the C_F somewhat resembles that of the C_R as shown in Figures 6.6 and 6.7, implying that the wave activity in front of the breakwater and the resulting wave reflection may be correlated to some extent.

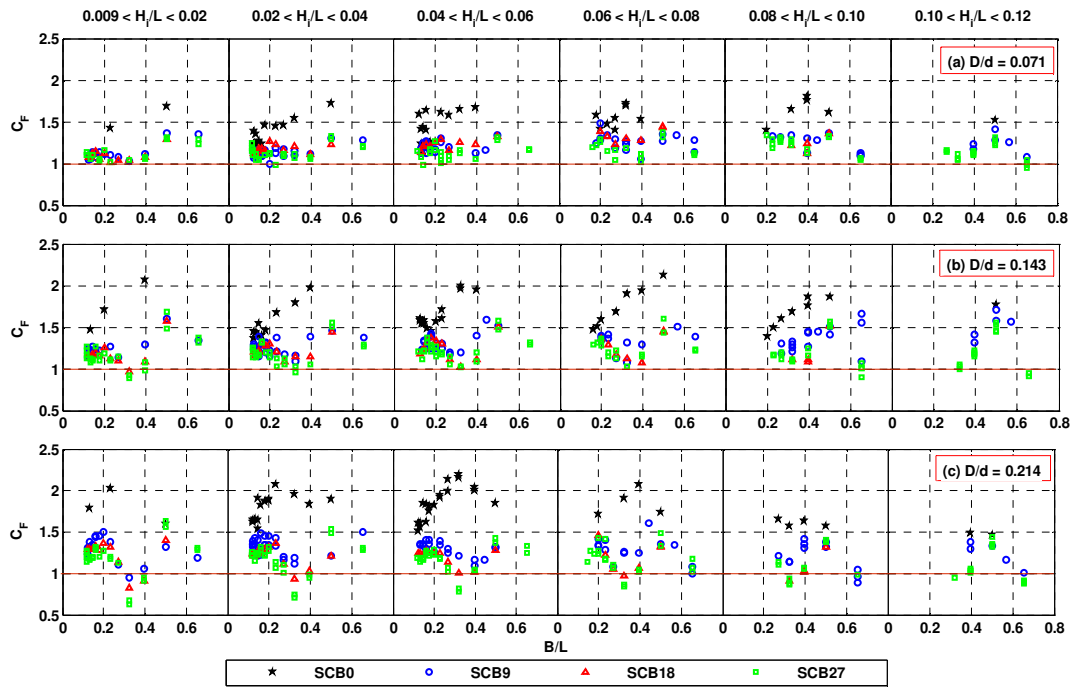


Figure 5.15: C_F for the SCB models in regular waves

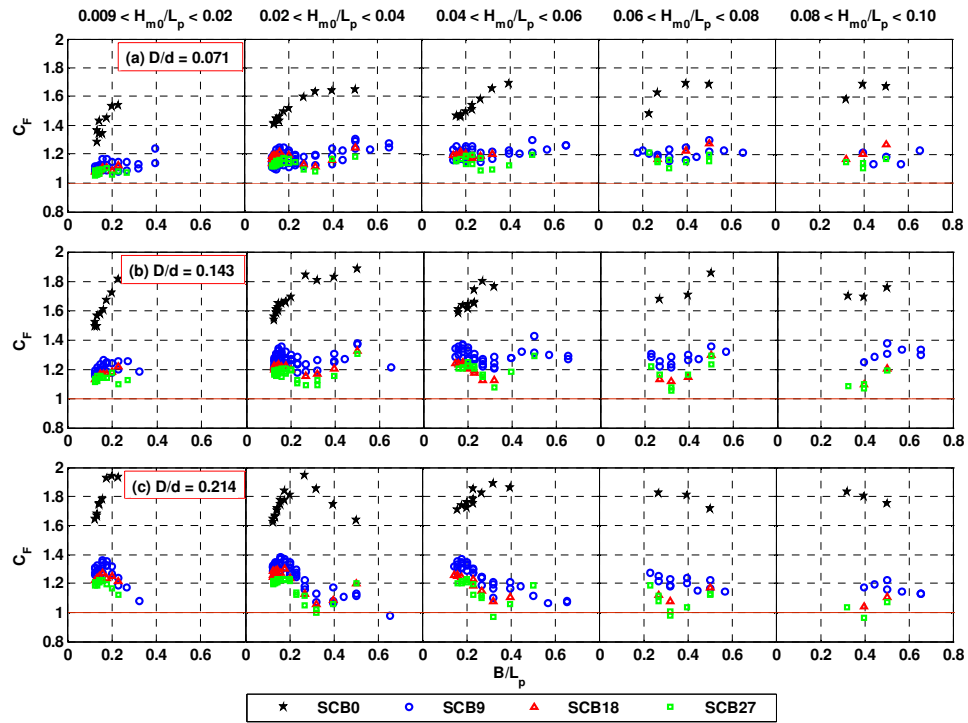


Figure 5.16: C_F for the SCB models in irregular waves

(b) Effect of Breakwater Porosity – ϵ_{SCB}

Breakwater porosity does not show much impact on the energy coefficient (*i.e.* C_T , C_R and C_L) of the perforated SCB models; however, the influence on the C_F is found to be significant as shown in Figures 5.15 and 5.16. Perforated breakwaters with less porosity tend to create greater margin to the water level variation in front of the models. In comparison with the SCB0 model, the wave climate at the front of the perforated models is relatively mild with maximum C_F of 1.69 for regular waves and 1.43 for irregular waves; whereas for the SCB0 model the highest C_F measured are 2.20 and 1.94 for regular and irregular waves, respectively, at $D/d = 0.214$.

(c) Effect of Wave Steepness – H/L

Figures 5.15 and 5.16 show that the C_F of the SCB models are less affected by the wave steepness in both regular and irregular seas.

(d) Effect of Relative Immersion Depth – D/d

With increased breakwater draft, the SCB0 model shows a tendency of having larger wave excitation at the front. Nonetheless, this does not apply to the perforated SCB models. The perforated models show a larger variability of C_F when immersed in deeper depth (see Figures 5.15 and 5.16). The variations of the C_F for the SCB0, SCB9, SCB18 and SCB27 models corresponding to $D/d = 0.071, 0.143$ and 0.214 are given in Table 5.4.

Table 5.4: Ranges of C_F for the SCB models ($0.12 < B/L < 0.50$ and $0.009 < H/L < 0.10$)

(a) Regular Waves				
D/d	SCB0	SCB9	SCB18	SCB27
0.071	1.25 – 1.80	1.01 – 1.48	1.04 – 1.44	0.95 – 1.38
0.143	1.37 – 2.12	1.02 – 1.52	0.93 – 1.51	0.90 – 1.69
0.214	1.46 – 2.20	0.98 – 1.61	0.84 – 1.47	0.63 – 1.63

(b) Irregular Waves				
D/d	SCB0	SCB9	SCB18	SCB27
0.071	1.28 – 1.69	1.10 – 1.31	1.09 – 1.28	1.09 – 1.21
0.143	1.49 – 1.88	1.18 – 1.43	1.17 – 1.32	1.07 – 1.30
0.214	1.62 – 1.94	1.12 – 1.38	1.04 – 1.30	0.97 – 1.25

The above discussion confirms that the SCB0 model, being the highly reflective breakwater, induces excessive wave activity in front of the structure (with a maximum of about twice the incident wave height irrespective of the type of sea state). As mentioned earlier, this may potentially cause scouring problem for the foundation of the supporting structures and presents a navigation hazard to the small floating vessels in the vicinity of the breakwater. On the other hand, the wave climate in front of the perforated SCB model is found to be less severe (with a maximum of about 1.5 times the incident wave height irrespective of the type of sea state). If the design parameter B/L is 'tuned' properly, a C_F that is close to unity may be obtained.

5.2.5 Wave Disturbance Coefficient in the Interference Chamber – C_C

The wave climate in the inference chamber may be of interest to the design engineers for many reasons. The degree of wave activity in the chamber is expressed as C_C (refer to Equation (3.25)). A C_C of beyond unity is a representation of increased wave activity in the breakwater chamber; and a C_C of less than unity implies a reduction in wave height in the chamber. The C_C of the tested SCB models are plotted against B/L for various ranges of H/L at $D/d = 0.071, 0.143$ and 0.214 and the results for regular and irregular waves are presented in Figure 5.17 and 5.18, respectively.

(a) Effect of Relative Breakwater Width – B/L

The correspondence of C_C to B/L for perforated models varies with the breakwater porosity as shown in Figures 5.17 and 5.18. The C_C of the SCB9 model seems to peak at $0.25 < B/L < 0.32$ and subsequently decreases at larger range of B/L . A similar trend is also observed for the SCB18 model at $D/d = 0.214$; however, at $D/d = 0.071$ and 0.143 the C_C value remains at unity. For the SCB27 model, the C_C values are consistently larger than unity and increase with increasing B/L . For the SCB0 model, the C_C values are generally not dependent upon B/L for both regular and irregular seas.

(b) Effect of Breakwater Porosity – ϵ_{SCB}

Breakwater porosity has a strong influence on the C_C of the perforated models that are deeply immersed. The wave excitation in the chamber of the SCB27 model is the strongest, followed by SCB18, then SCB9. The amount of wave penetration through the perforated front wall is directly proportional to the breakwater porosity. The higher the breakwater porosity, the higher will be the wave penetration through the perforated front wall; thereby resulting in considerable wave-structure interactions within the chamber and subsequently

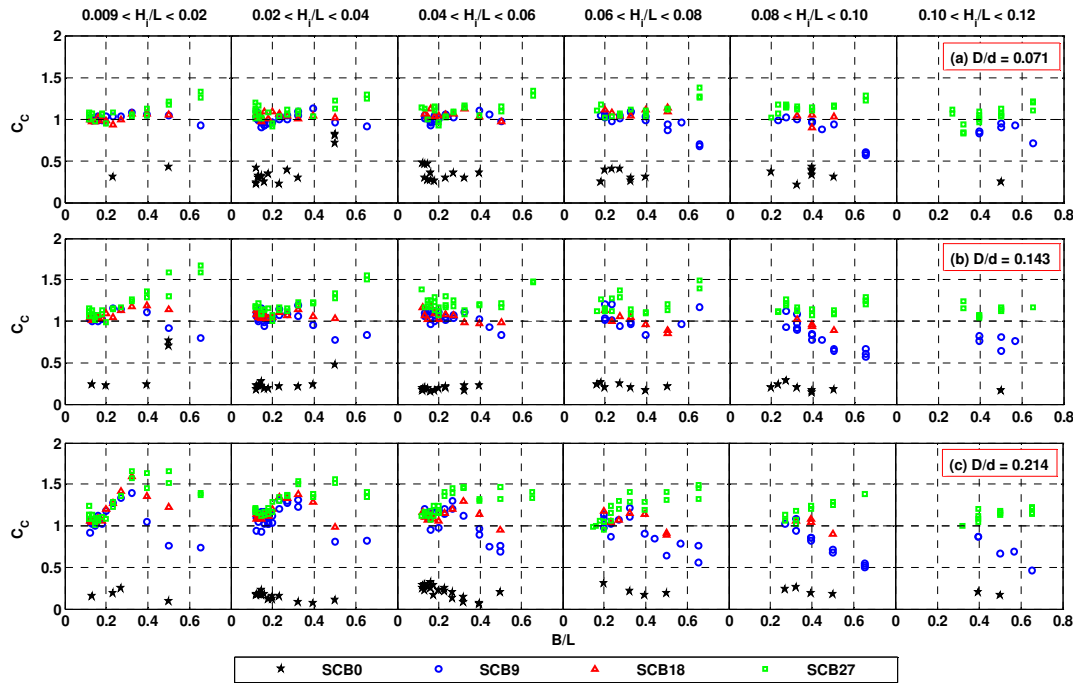


Figure 5.17: C_C for the SCB models in regular waves

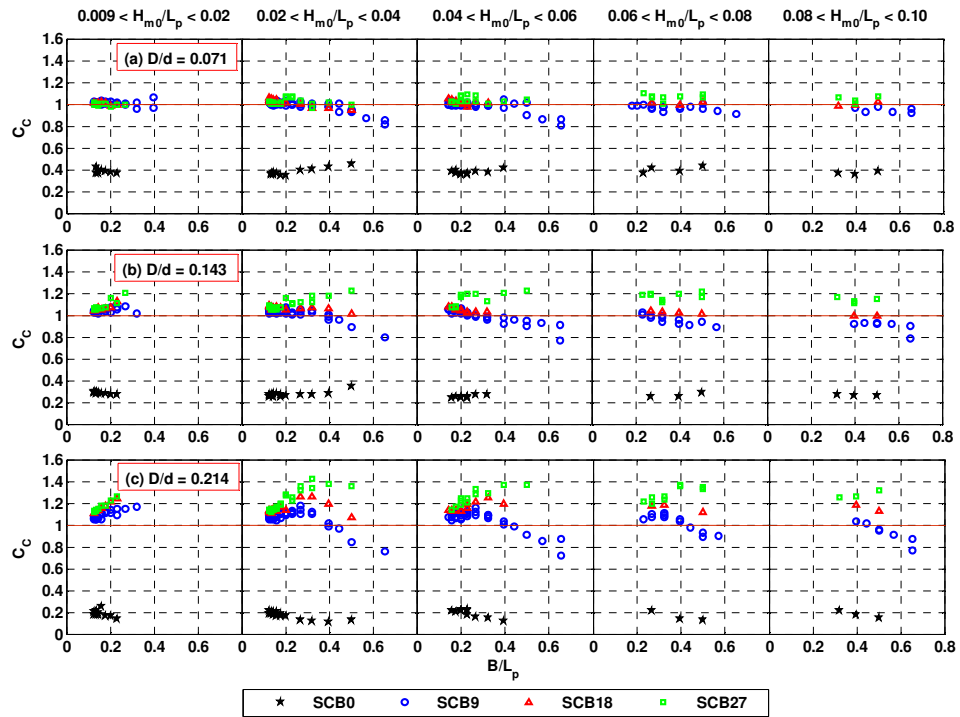


Figure 5.18: C_C for the SCB models in irregular waves

leading to larger wave activity. The C_C values of the SCB0 model are mostly less than 0.5 in all test cases. The water in the chamber is particularly calm when the breakwater is deeply immersed (see Figures 5.3, 5.11a, 5.12a, 5.13a and 5.14a). It is further learnt from Figures 5.15 – 5.18 that C_C and C_F of the SCB models are in inversed relations. For instance, the SCB0 model causes large wave agitation (up to $C_F = 2.2$) in front of the structure, yet the water in the chamber is extremely calm; on the other hand, even though the SCB27 model does not promote much amplification of waves at the front, the water within the chamber is greatly disturbed.

(c) Effect of Wave Steepness – H/L

The variation of C_C with respect to different ranges of H/L is insignificant for all the SCB models in regular and irregular waves as can be seen in Figures 5.17 and 5.18, respectively. Therefore, it can be deduced that wave steepness does not govern the wave behaviour in the breakwater chambers in an appreciable manner.

(d) Effect of Relative Immersion Depth – D/d

For the SCB0 model, the C_C values decrease as D/d increases as shown in Figures 5.17 and 5.18. The mean values for the C_C of $D/d = 0.071, 0.143$ and 0.214 in regular waves are 0.36, 0.23 and 0.18, respectively; and those in irregular waves are 0.38, 0.27 and 0.18, respectively. The wave calming effect within the breakwater chamber due to increased immersion depth is mainly attributed to (i) the deeper intrusion of the breakwater draft to withstand wave energy; (ii) less interference by the energy flux transmitted beneath the structure; and (iii) the presence of compressed air pressure that is trapped within the chamber. Note that the entrained air may induce added uplift loadings to the breakwater during the rise of the water level in the chamber. For the permeable SCB models, the C_C values of the SCB18 and SCB27 models increase with the increase in D/d ; whereas the C_C values of the SCB9 model display mixed characteristics, whereby they increase with the increasing D/d at $B/L < 0.4$ and subsequently drop to unity at $B/L \approx 0.4$ and further decrease at higher range of B/L as D/d increases. The ranges of C_C for the respective SCB models corresponding to $D/d = 0.071, 0.143$ and 0.214 within the test ranges of $0.12 < B/L < 0.50$ and $0.009 < H/L < 0.10$ in regular and irregular seas are summarised in Table 5.5.

Table 5.5: Ranges of C_C for the SCB models ($0.12 < B/L < 0.50$ and $0.009 < H/L < 0.10$)

(a) Regular Waves				
D/d	SCB0	SCB9	SCB18	SCB27
0.071	0.20 – 0.82	0.86 – 1.13	0.90 – 1.14	0.91 – 1.22
0.143	0.14 – 0.76	0.65 – 1.20	0.85 – 1.19	0.99 – 1.59
0.214	0.06 – 0.32	0.64 – 1.40	0.89 – 1.60	0.95 – 1.66

(b) Irregular Waves				
D/d	SCB0	SCB9	SCB18	SCB27
0.071	0.34 – 0.45	0.92 – 1.06	0.95 – 1.06	0.97 – 1.10
0.143	0.24 – 0.34	0.89 – 1.08	0.99 – 1.13	1.05 – 1.23
0.214	0.11 – 0.25	0.84 – 1.16	1.07 – 1.26	1.12 – 1.43

The chamber of the SCB was designed to permit reasonable amount of wave activity taking place from within so as to maximise the energy dissipation. The above experimental results show that the chambers of the perforated SCB models are utilised for this purpose more effectively than that of the SCB0 model. Nonetheless, extreme and uncontrolled wave action in the chambers of the perforated models, particularly during high tides, increases the chances of wave slamming onto the inner shell of the barriers, which in turn leave the breakwaters prone to structural failure. It is anticipated that the wave impact could be alleviated by the front and rear openings about the crest of the caisson which provide immediate escape for the rising water. This may help reduce uplift forces acting on the perforated breakwaters.

5.2.6 Effect of Breakwater Placement Ratio – B/d

The results discussed in Sections 5.2.1 – 5.2.5 are based on outputs obtained from Experiment *Series A*, whereby the water depth was fixed at 0.7 m throughout the experiments. This gives a breakwater placement ratio of $B/d = 0.714$. In this study, an attempt was made to provide insight into how other B/d ratios change the hydraulic performance of the SCB model. To further this study, only the SCB9 was selected as the test model and it was tested in water depths of 0.3 m and 0.5 m, giving $B/d = 1.000$ and 1.667. For each water depth, the SCB9 model was immersed at 0.05 m, 0.10 m and 0.15 m from SWL. The hydraulic coefficients (*i.e.* C_T , C_R , C_L , C_F and C_C) of the SCB9 model are plotted against D/d for $B/d = 0.714$, 1.000 and 1.667 in regular and irregular waves in Figure 5.19. Other test parameters associated with the B/d ratios are detailed in Table 5.6. It is important

to stress that the Figure 5.19 presented here is to help illustrate the hydraulic response of the SCB9 model corresponding to B/d and D/d ; and it therefore not suitable to be used for design purpose. The broad range of a hydraulic coefficient for a given D/d as shown in the figure is mainly due to the influence of B/L which has not been a concern for this stage of the study.

For ease of illustration, the results shown in Figure 5.19 was generalised and assessed by the means of the linear regression technique. The overall data trend shows that the C_T of the SCB9 model for respective B/d decreases with an increase in D/d ; however, the decrease of C_T with an increase in B/d is found to be less significant. This indicates that D/d has more control over the C_T of the SCB9 model than B/d . For wave reflection, the variations of C_R for the respective B/d ratios are relatively small. A gradual increase of the C_R is detected as (i) D/d increases; and (ii) B/d decreases, for both regular and irregular wave cases. Further, the C_L appears to be an inverse of the C_T and the dependence of C_L upon B/d is almost negligible.

The decision whether to drop B/d from the empirical expression in Equations (3.58) – (3.60) is further investigated using some statistical techniques. Multiple linear regression analyses were conducted to identify the relative contribution of the respective predictor variables, *i.e.* B/d , B/L , D/d and H/L in affecting the energy coefficients. The *t*-tests are the tests of significance for each parameter estimate, *i.e.* the predictor variables are tested by null hypothesis that there is no linear relationship between the criterion and predictor variables and this hypothesis has to be rejected in order to become statistically significant. This hypothesis testing technique was applied to test the significance of each predictor variable for this study. The statistical outputs presented in Appendices M and N show that the B/L and D/d are the most influential predictor variables for C_T , C_R and C_L ; whilst B/d contributes the least (or marginally) in both sea states. Nevertheless, the statistical results suggest that B/d , in most cases, should be retained as a predictor variable for the energy coefficient even though the relative contribution is marginal. Note that the level of contribution from each variable is determined by the standardised beta coefficient (presented in Appendices M and N) which gives the number of standard deviations change on the energy coefficient that will be produced by a change of one standard deviation on the predictor variable concerned. The larger the absolute value of the beta coefficient, the greater level of the contribution will be. Detailed description on the multiple linear regression analysis is given in Chapter 8. The plots in Figure 5.19 are also presented in the form of box plots in Figures 5.20 and 5.21 to show the relevant statistical parameters, *i.e.* the smallest observation, lower quartile, median,

upper quartile and largest observation.

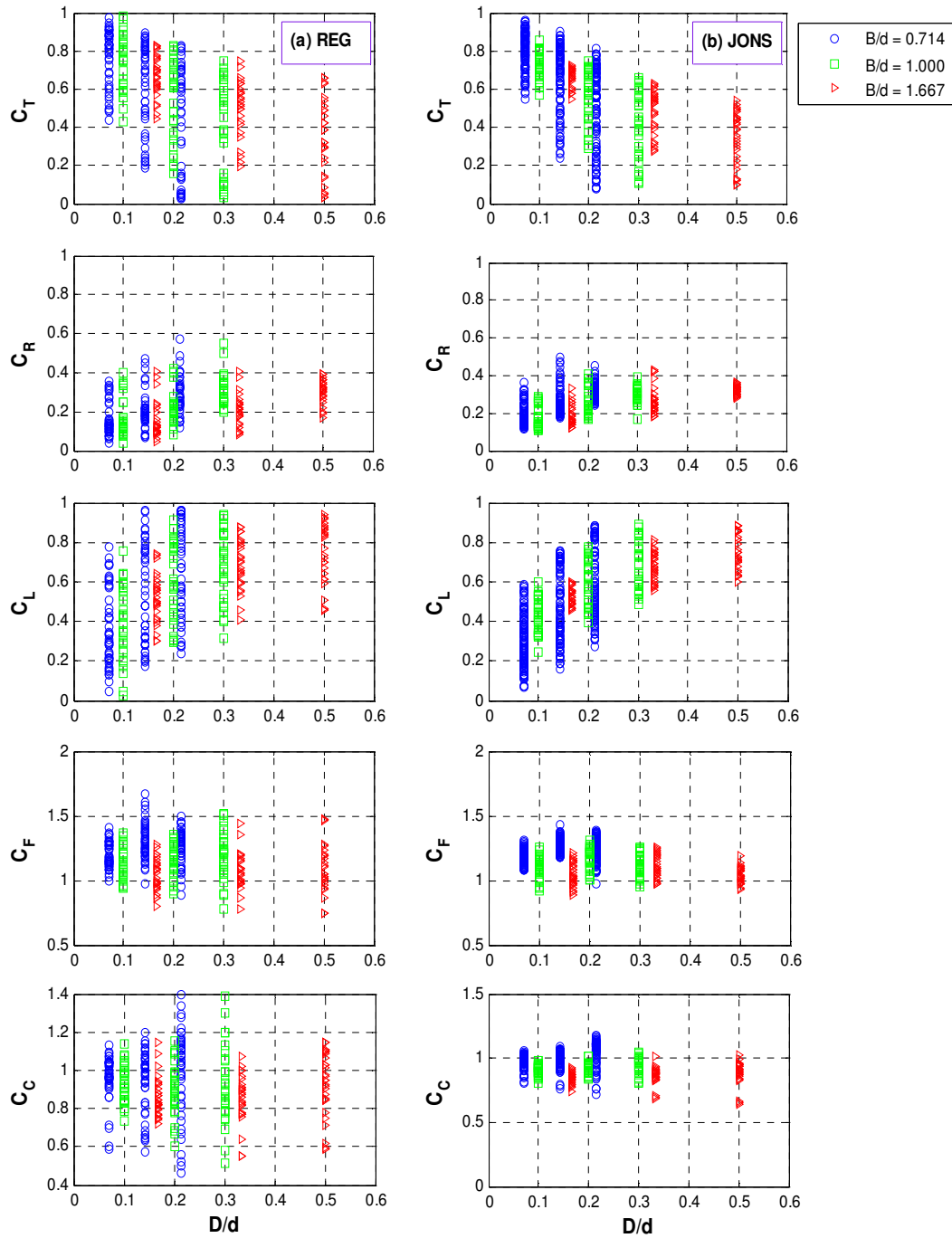


Figure 5.19: The effect of the breakwater placement ratio on the hydraulic coefficients for the SCB9 model in regular waves and irregular waves

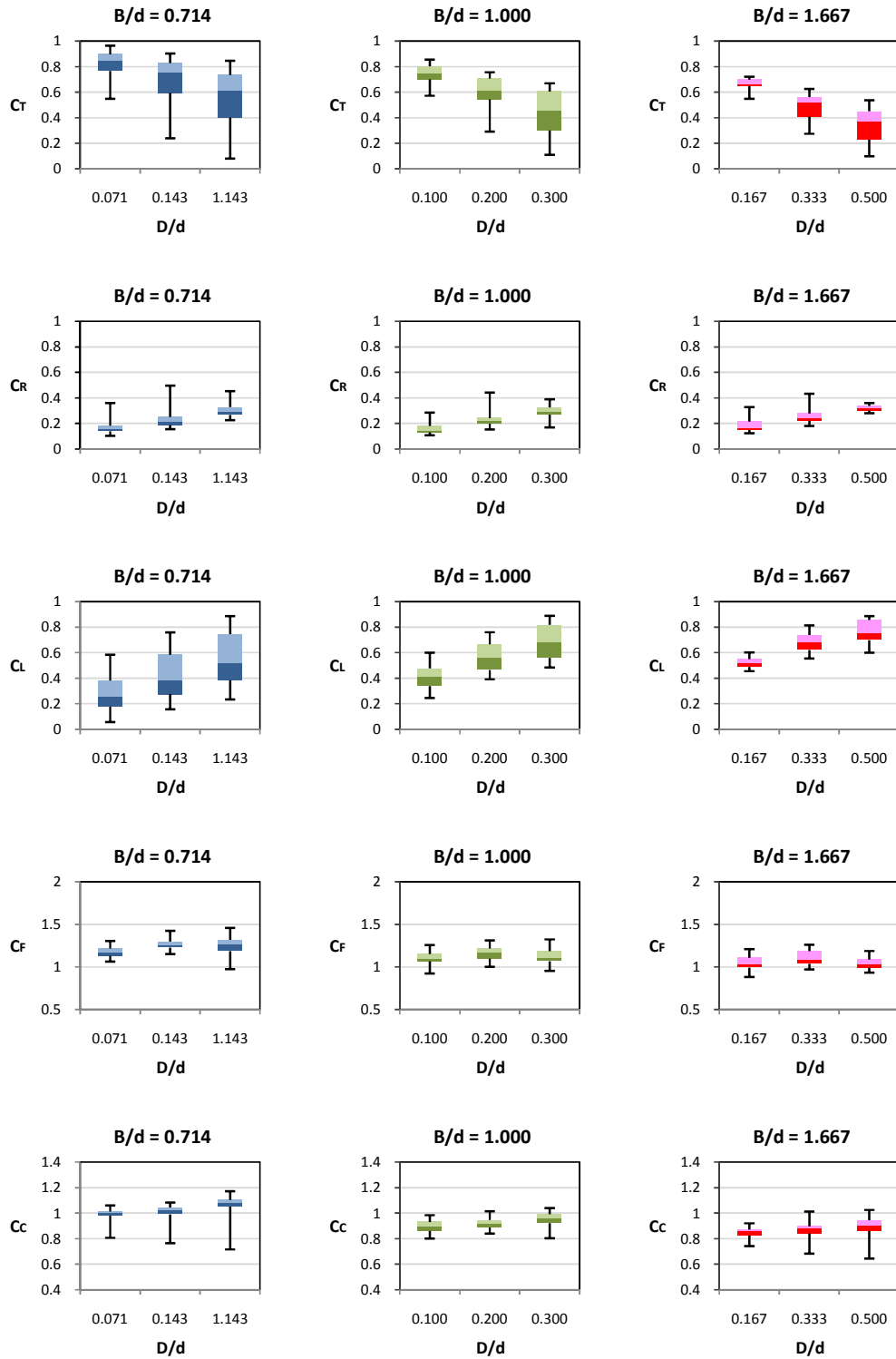


Figure 5.20: Box plots of the hydraulic coefficients for the SCB9 model corresponding to the breakwater placement ratios in regular waves

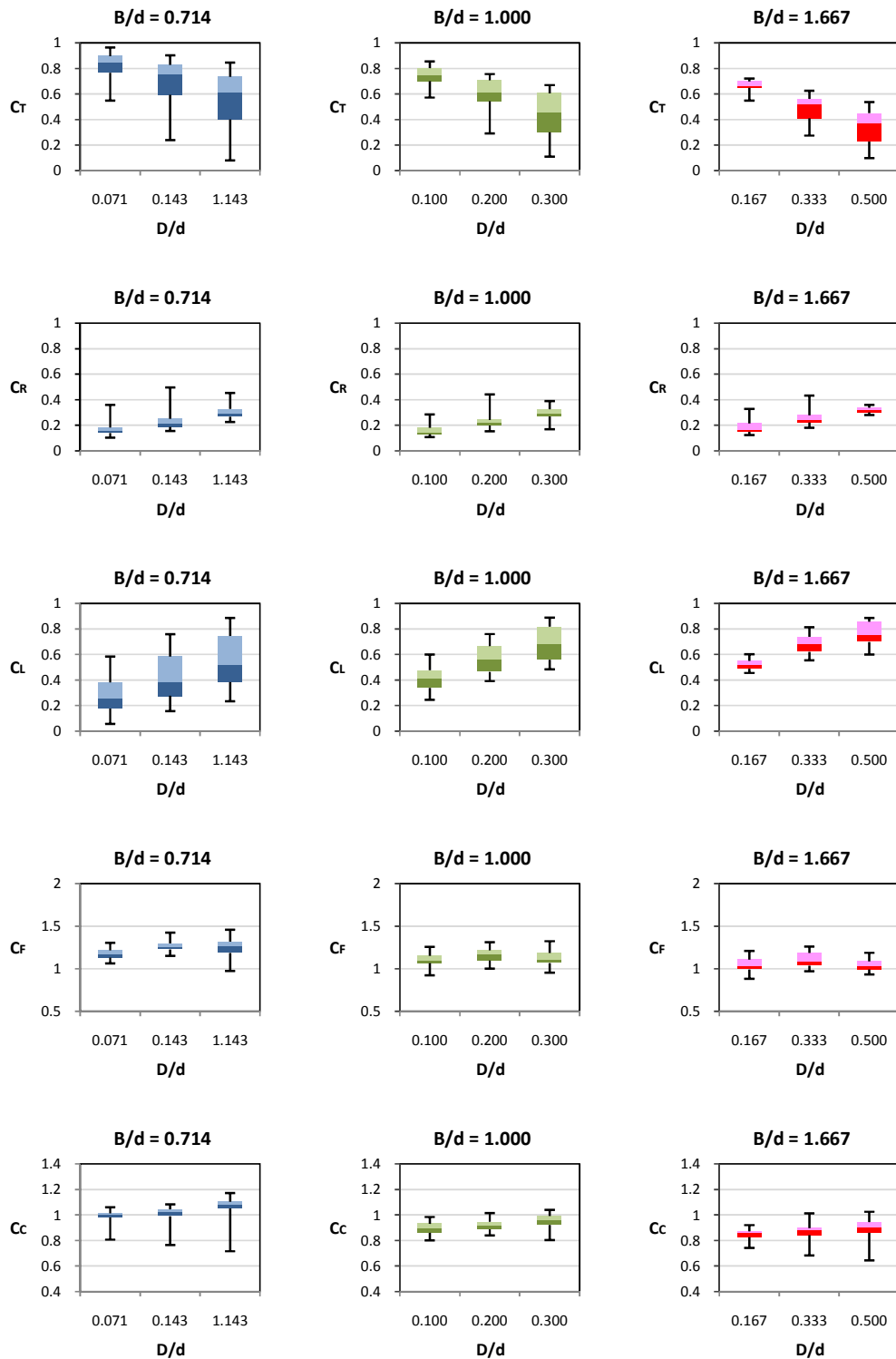


Figure 5.21: Box plots of the hydraulic coefficients for the SCB9 model corresponding to the breakwater placement ratios in irregular waves

Table 5.6: The ranges of B/L for respective water depths

B/d	D/d	B/L	H_i/L
0.714 ($d = 0.7$ m)	0.071 ($D = 0.05$ m) 0.143 ($D = 0.10$ m) 0.214 ($D = 0.15$ m)	0.124 – 0.569	0.009 – 0.12 (Regular) 0.009 – 0.10 (Irregular)
1.000 ($d = 0.5$ m)	0.100 ($D = 0.05$ m) 0.200 ($D = 0.10$ m) 0.300 ($D = 0.15$ m)	0.150 – 0.570	
1.667 ($d = 0.3$ m)	0.167 ($D = 0.05$ m) 0.333 ($D = 0.10$ m) 0.500 ($D = 0.15$ m)	0.198 – 0.584	

The breakwater placement ratio has gained more importance in the characterisation of the wave climate in proximity of the SCB9 model. It is clear from Figure 5.19 that the C_F and C_C values decrease as B/d increases from 0.714 to 1.667. This entails that the wave excitation around the front wall and in the chamber is weakened by the limited depth of water. The influence of B/d on the wave climate coefficients, which is quantified as a standardised coefficient in Appendices M and N, is also shown to be the strongest (or most significant) among the predictor variables as far as linear relationship is concerned. Including B/d as one of the design parameters for C_F and C_C is, therefore, highly recommended.

In short, increasing the breakwater placement ratio, B/d from 0.714 to 1.667 does not bring much improvement to wave attenuation; nevertheless, it helps in ‘smoothing’ the wave climates in the vicinity of the structure.

5.2.7 Effect of the Rear Wall Perforation

As mentioned in Section 4.2, the two-row openings near the crest of the rear wall of the SCB are principally used to enhance the infiltration of overtopping waves; and secondly, to provide a getaway to the built-up pressure as well as the waves rising in the chamber. The efficiency of the design was evaluated by comparing with a similar model but without a solid rear wall. For this exercise, an SCB model with a front wall porosity of 9% was selected. The one with the rear openings is denoted as SCB9, and that with the solid wall with no openings is denoted as SCB9X. The hydraulic performance of these models was assessed by the hydraulic coefficients, namely C_T , C_R , C_L , C_F and C_C . The results are shown in Figures

5.22 and 5.23. Note that the hydraulic coefficients are plotted against the relative breakwater width, B/L regardless of the H/L .

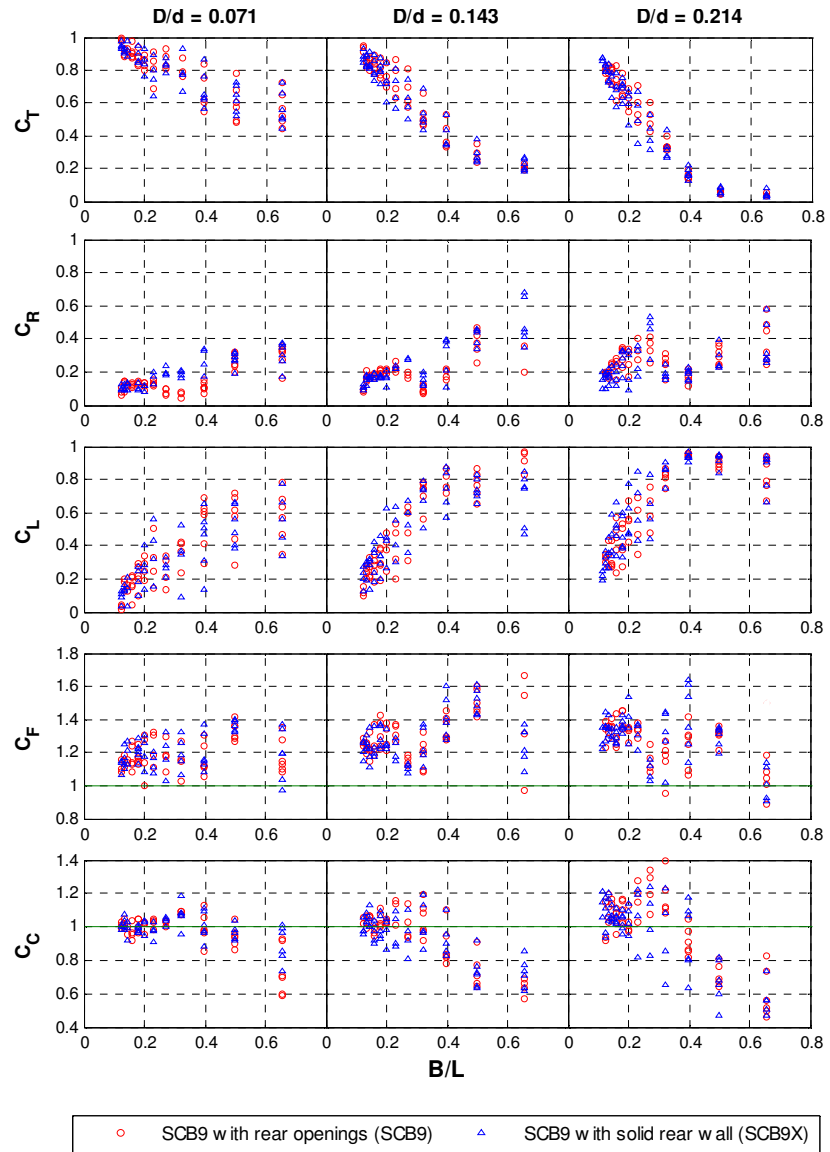


Figure 5.22: Effect of the rear wall openings on the hydraulic coefficients in regular waves

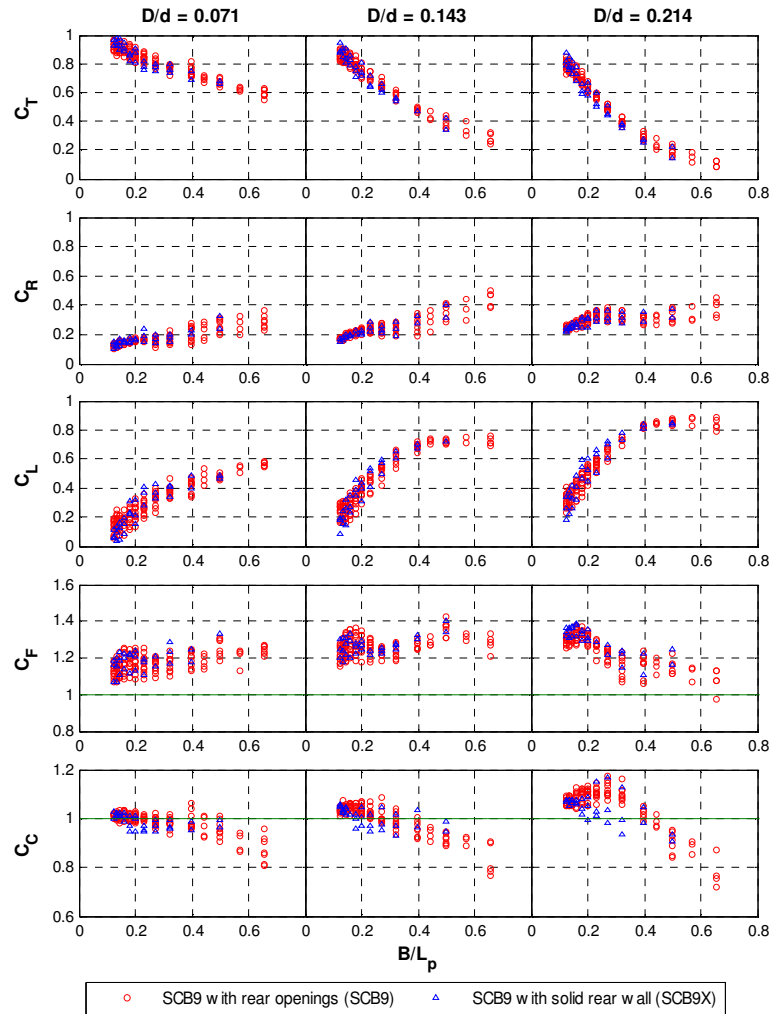


Figure 5.23: Effect of the rear wall openings on the hydraulic coefficients in irregular waves

In general, the majority of the hydraulic coefficients of the SCB9 and SCB9X are found to be coinciding closely with each other in both regular and irregular waves. This indicates that the hydraulic performance of the semicircular breakwater with rear wall openings and that of the breakwater with a solid rear wall are both comparable with no marked difference. However, the C_C of the SCB9X for $D/d = 0.214$ tend to be slightly lower than those of the SCB9 for both regular and irregular seas as can be seen in Figures 5.22 and 5.23. This is due to the fact that the air pressure entrained in the chamber of the SCB9X was higher. It is recommended that the openings at the rear wall be retained in the breakwater design because the perforation would help to reduce the uplift force caused by the rising waves on the inner shell. Even though the rear wall openings may occasionally result in water splashing from the breakwater chamber, the disturbance caused to the leeward sea is found to be almost negligible.

5.2.8 Effect of Wave Spectra (Sea States)

The effect of wave spectra on the performance characteristics of the SCB27 model is addressed in Figure 5.24. The model was subjected to two types of wave spectra that are typically used for applications in offshore engineering, *i.e.* Pierson-Moskowitz (PM) spectrum and JONSWAP spectrum (see Section 3.4.1). Both spectra described by $0.8 \text{ s} < T_p < 1.3 \text{ s}$, $0.04 \text{ m} < H_{m0} < 0.12 \text{ m}$ and $0.02 < H_{m0}/L_p < 0.08$, were used to characterise the wave behaviour in the experiments. No distinct variation of C_T , C_R , C_L , C_F and C_C are seen from the figure, implying that the hydraulic performance of the breakwater is insignificant to the spectral shape. It is anticipated that the breakwater could be useful at locations of fully or partially developed seas.

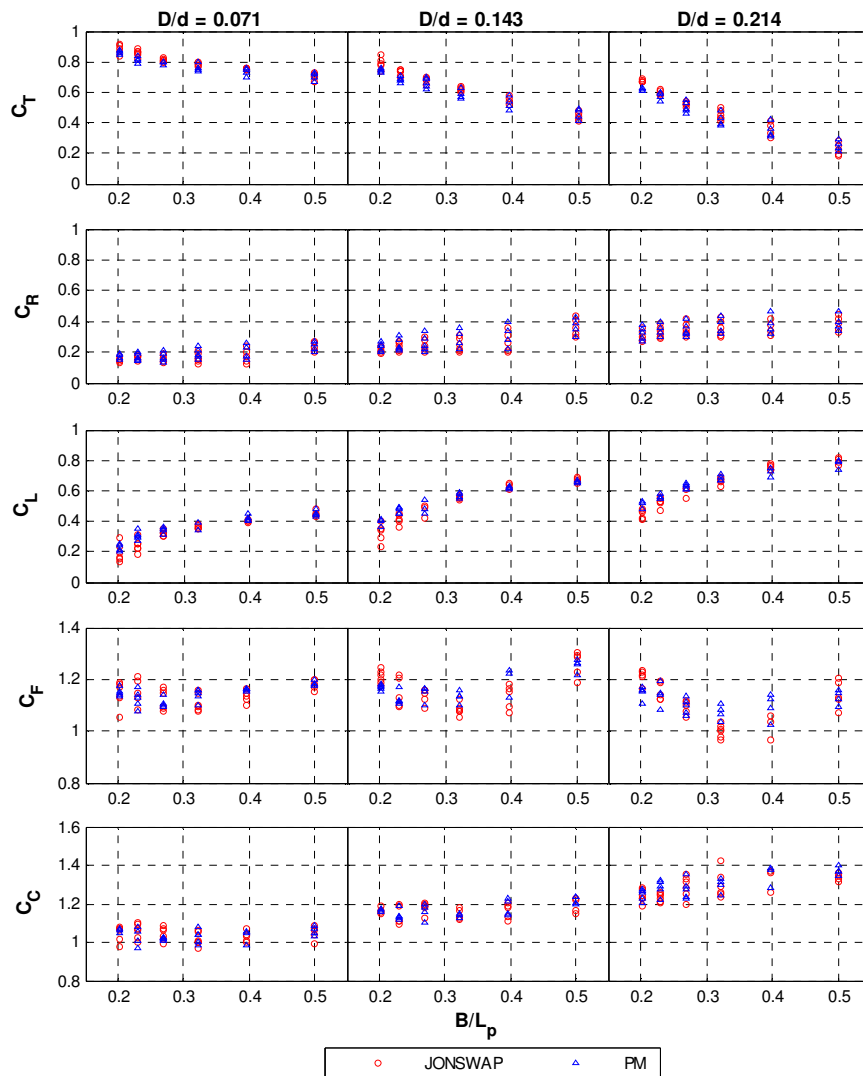


Figure 5.24: Effect of spectral types on hydraulic coefficients of the SCB27 model

5.2.9 Results Comparison

The efficiency of the SCB models is assessed by comparing their hydraulic characteristics with those of the free surface breakwaters developed by other researchers. For this exercise, the SCB0 and SCB9 models were chosen to represent the impervious and perforated SCB breakwaters in this study. The other breakwater designs adopted for comparison include:








- the box-type barrier (Koftis and Prinos, 2005; Koutandos and Prinos 2005);
- the cylindrical-type barrier (Li *et al.*, 2005);
- the quadrant front face-type barrier (Sundar and Subbarao, 2002; Sundar and Subbarao, 2003);
- the catamaran-type barrier (Koftis and Prinos 2005); and
- the trapezoidal-type barrier (Koftis and Prinos, 2005).

Table 5.7 summarises the details and test conditions of these breakwaters. Note that these models were tested on fixed barriers, with the exception of the quadrant front face breakwater which was seated on a group of piles arranged in a way that the pile gap was five times greater than the pile diameter. The relative immersion depths for these breakwaters mostly vary at $0.20 < D/d < 0.33$. For the SCB models, the test data for $D/d = 0.214$ were selected for comparison. A direct evaluation of the efficiency of the respective breakwaters is difficult to carry out due to the fact that each breakwater is unique in design (with different dimensions) as well as variations in the test procedures. It is worth mentioning that the following comparisons are made on the basis of $0.20 < D/d < 0.33$ and $0.015 < H/L < 0.044$. The results are discussed broadly based on the type of sea states, *i.e.* regular waves and irregular waves.





From a display of the wave transmission coefficients C_T data for the selected breakwaters in regular waves in Figure 5.25, it is found that the C_T values of the present test models are in good agreement with other breakwater models. The SCB0 model of $D/d = 0.214$ is found to outperform the quadrant front face breakwater of $D/d = 0.313$ at $B/L > 0.3$. The wave attenuation ability of the SCB0 model is even comparable to the cylindrical structure immersed at $D/d = 0.50$. On the other hand, the wave attenuation performance of the SCB9 model is somewhat weak especially when compared with breakwaters of larger D/d . The trapezoidal breakwater of $D/d = 0.325$ is shown to offer the highest wave dampening efficiency among the breakwaters.

Table 5.7: Details of the breakwaters selected for comparison.

(a) Regular waves

Breakwater type	Cross section	Modelling type	D/d	H/L	Reference
Cylinder		Numerical (<i>Modified Tsay & Liu's approximation</i>)	0.250 0.500 0.750	n.a.	Li <i>et al.</i> 2005
SCB0		Experimental	0.214	0.015 – 0.044	Present study
SCB9		Experimental	0.214	0.015 – 0.044	Present study
Quadrant front face with supporting piles		Experimental	0.313	n.a.	Sundar and Subbarao, 2002
Box		Numerical (<i>COBRAS model</i>)	0.325	0.021 -0.042	Koftis and Prinos 2005
Trapezoid		Numerical (<i>COBRAS model</i>)	0.325	0.021 -0.042	Koftis and Prinos 2005
Catamaran		Numerical (<i>COBRAS model</i>)	0.325	0.021 -0.042	Koftis and Prinos 2005

(b) Irregular waves

Breakwater type	Cross section	Modelling type	D/d	H/L	Reference
SCB0		Experimental (JONSWAP)	0.214	0.020 – 0.042	Present study
SCB9		Experimental (JONSWAP)	0.214	0.020 – 0.042	Present study
Quadrant front face with supporting piles		Experimental (PM)	0.313	n.a.	Sundar and Subbarao, 2002
Box		Experimental	0.325	0.021 -0.042	Koutandos and Prinos, 2005

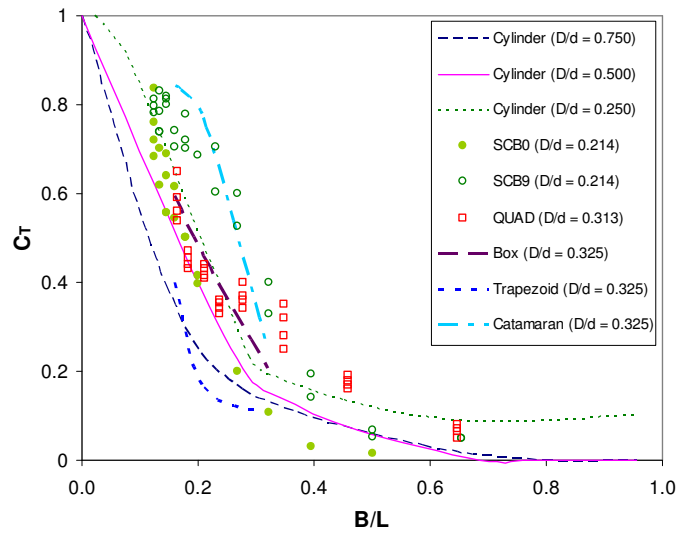


Figure 5.25: Comparison of C_T for $0.015 < H_i/L < 0.044$ in regular waves

Figure 5.26 shows the reflection capability of the aforementioned breakwaters with the exception of the cylindrical structure. The solid breakwaters, *i.e.* the box-type and the trapezoidal-type, appear to be highly reflective structures. The reflectivity of the quadrant front face breakwater is surprisingly low; which might be attributed to the influence of breakwater geometry as well as the influence of the closely-spaced piles that facilitate a large amount of energy dissipation. It is apparent from the figure that the SCB9 model is the best anti-reflection structure as it produces the lowest C_R among the breakwaters in comparison. Both SCB9 and the quadrant-front-face breakwaters exhibited a Bragg effect in their C_R , with the resonance occurring at $B/L \approx 0.25$.

The energy dissipation ability of the breakwaters, which is demonstrated in Figure 5.27, shows no definite trend of the C_L among the test models. The C_L values of the box-type, catamaran-type, trapezoidal-type and the SCB0 are relatively low ($C_L < 0.5$) compared to those of the SCB9 and quadrant front face breakwater. It is, therefore, safe to say that the models with quadrant front faces are better energy dissipaters than the remaining test models.

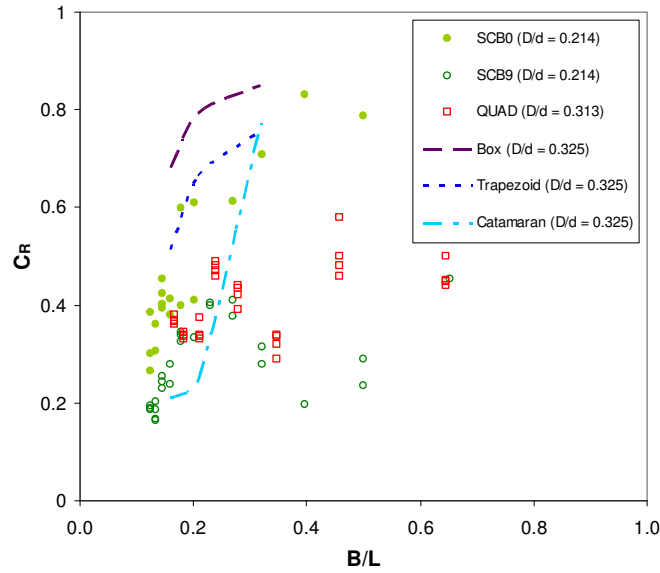


Figure 5.26: Comparison of C_R for $0.015 < H_s/L < 0.044$ in regular waves

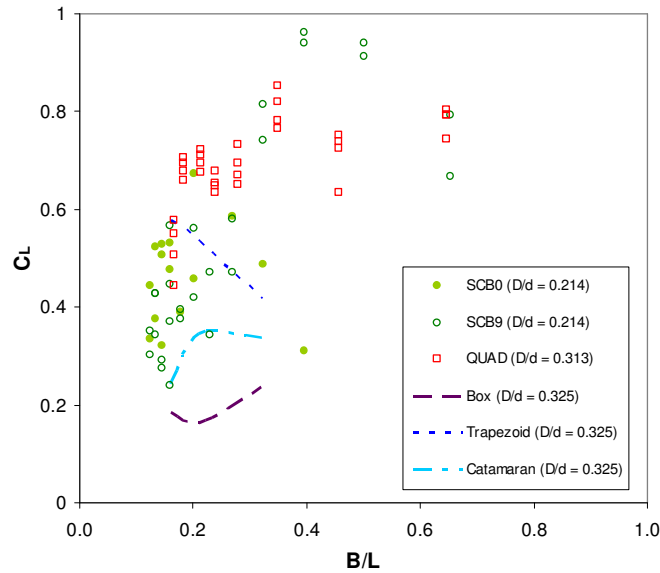


Figure 5.27: Comparison of C_L for $0.015 < H_s/L < 0.044$ in regular waves

Figure 5.28 demonstrates another form of comparison of the energy coefficients in regular waves, for which the coefficients are plotted against D/d . In this study, the experimental results of the SCB0 and SCB9 models were compared with the numerical results of the box-type, trapezoidal-type and catamaran-type breakwaters developed by Koftis and Prinos (2005), with both results taken at $B/L = 0.32$. Again, a direct comparison of results may be

difficult because different ranges of D/d were used in the existing study for the SCB models and for other test models. Nevertheless, it can be postulated from the projected trend of the plots that the SCB0 model is an effective wave attenuator with high reflection ability; whereas the SCB9 model is a good anti-reflection structure with high energy dissipation potentials.

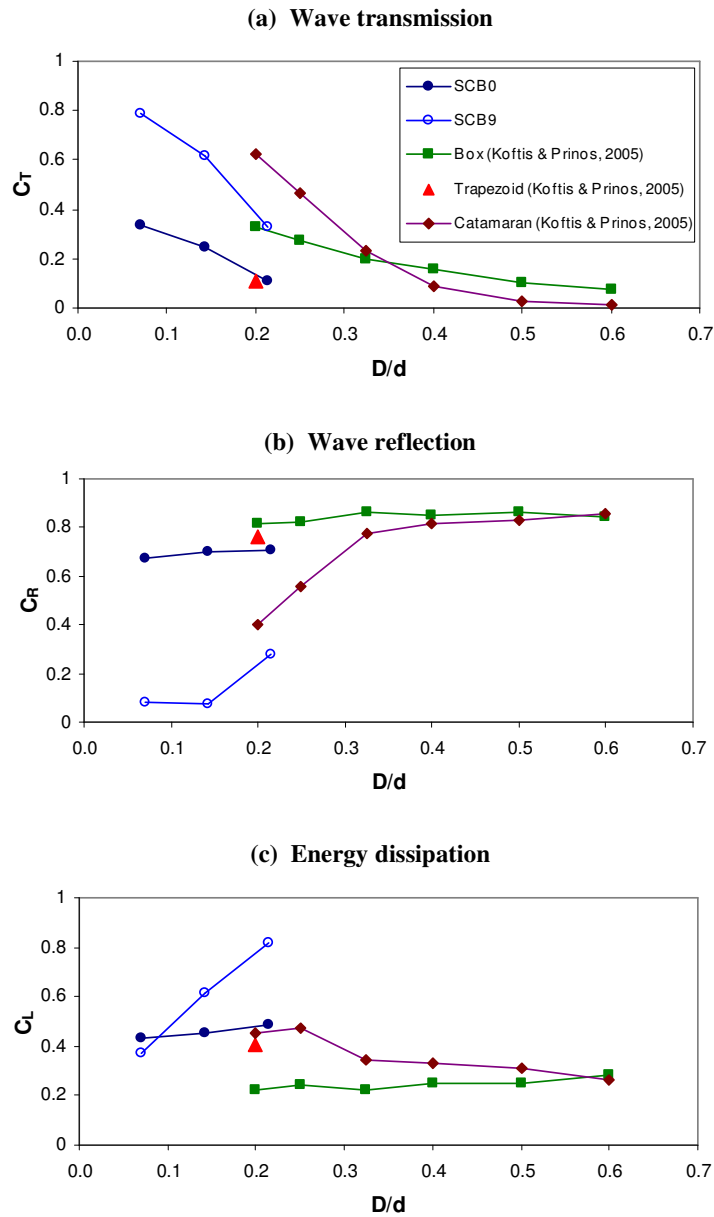


Figure 5.28: Comparison of energy coefficients for $0.02 < H/L < 0.04$ and $B/L = 0.32$ in regular waves

For the case of irregular waves, the comparison of the energy coefficients as shown in Figure 5.29 is restricted to the quadrant front face breakwater (Sundar and Subbarao, 2003), the box-type breakwater (Koutandos and Prinos, 2005) and the existing SCB models, *i.e.* SCB0 and SCB9. The details of these test models are presented in Table 5.7b. The overall outcomes of the comparisons are in good consensus with those of the regular waves.

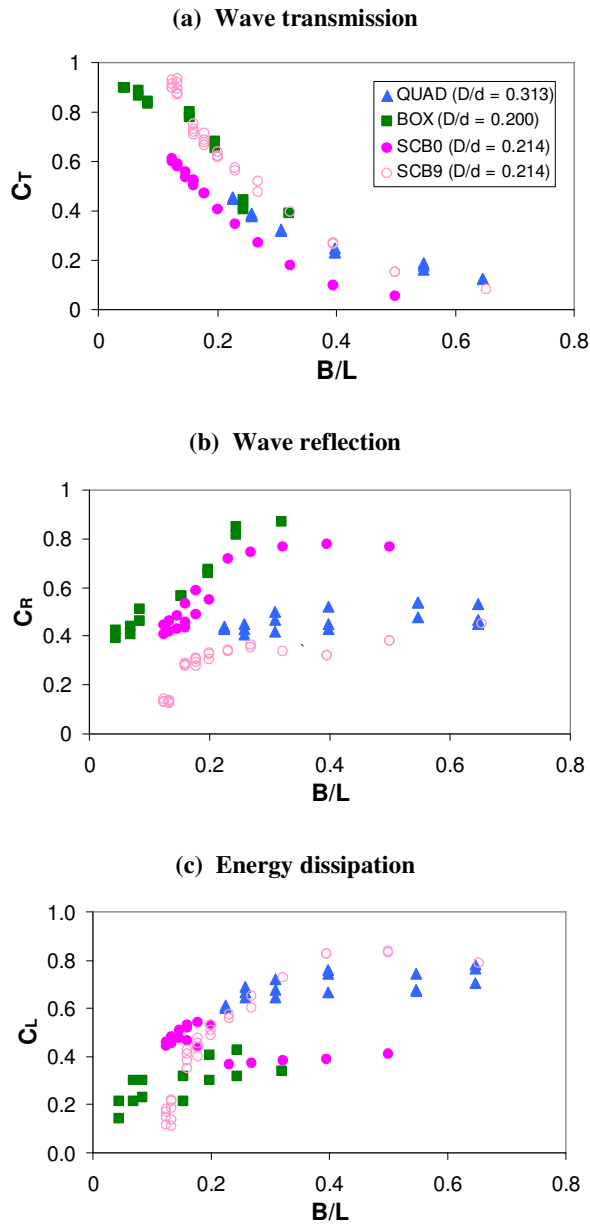


Figure 5.29: Comparison of energy coefficients for $0.02 < H_i/L < 0.042$ in irregular waves

5.3 Horizontal Loadings on the Free Surface SCB models

5.3.1 Horizontal Force Coefficient – F_n

Determination of hydraulic loadings is another important concern to the design of breakwaters. Hydraulic loadings to be considered vary significantly between different structure types. For instance, the uplift forces are important design issues to a jetty deck; however, it is seldom predicted by opened piled structures. In this study, an emphasis was given to the measurement of the horizontal wave forces. These are slowly varying wave-induced forces (quasi-static loads) in which the magnitude is generally a function of the incident wave height. For regular waves, these forces were computed from the average of their crest or trough peaks. For irregular waves, the forces were represented by the average of the highest one-third of the measured data under the wave crests or troughs. The horizontal wave loadings acting on the SCB models are presented in the form of dimensionless force coefficients, $F_n = F/\rho g H_i D$ (refer to Section 3.6.2), where F is the horizontal wave force per unit length of the SCB models, ρ is the density of the fluid, and g is the acceleration due to gravity. The force coefficient for the positive wave force induced by the peak wave crest is denoted as $F_{n,c}$, and that for negative wave force induced by the peak wave trough is denoted as $F_{n,t}$. The force coefficients for the test models, *i.e.* SCB0, SCB9, SCB18 and SCB27, are plotted with respect to relative wave height at three relative immersion depths for different ranges of wave steepness in Figures 5.30 and 5.31. These coefficients are discussed comprehensively with respect to their potential affecting parameters, *i.e.* H/d , ε_{SCB} , H/L and D/d .

(a) Effect of Relative Wave Height – H/d

The relative wave height, H/d used in this study varies from 0.03 to 0.30, which was well below the breaking index, $\gamma = H/d = 0.78$. Further, the highest wave steepness tested was 0.12, which was again lower than the theoretical wave breaking limit, $H/L = 1/7$. Therefore, the waves generated from the flume were non-breaking waves. In Figures 5.30 and 5.31, the $F_{n,c}$ values of the SCB models increase as H/d increases in both sea states; nonetheless, the increase of $F_{n,t}$ with respect to H/d is negligible. It is evident from the figures that $F_{n,c}$ is consistently higher than $F_{n,t}$ in all test cases. This is to be expected because the free surface breakwaters are mostly designed to withstand positive forces under wave crests. The observation is further validated by the design diagram for the positive and negative wave forces acting on a vertical wall structure developed by Goda (1967) (see Figure 5.32). From this force distribution diagram, the maximum positive force takes place at the free surface;

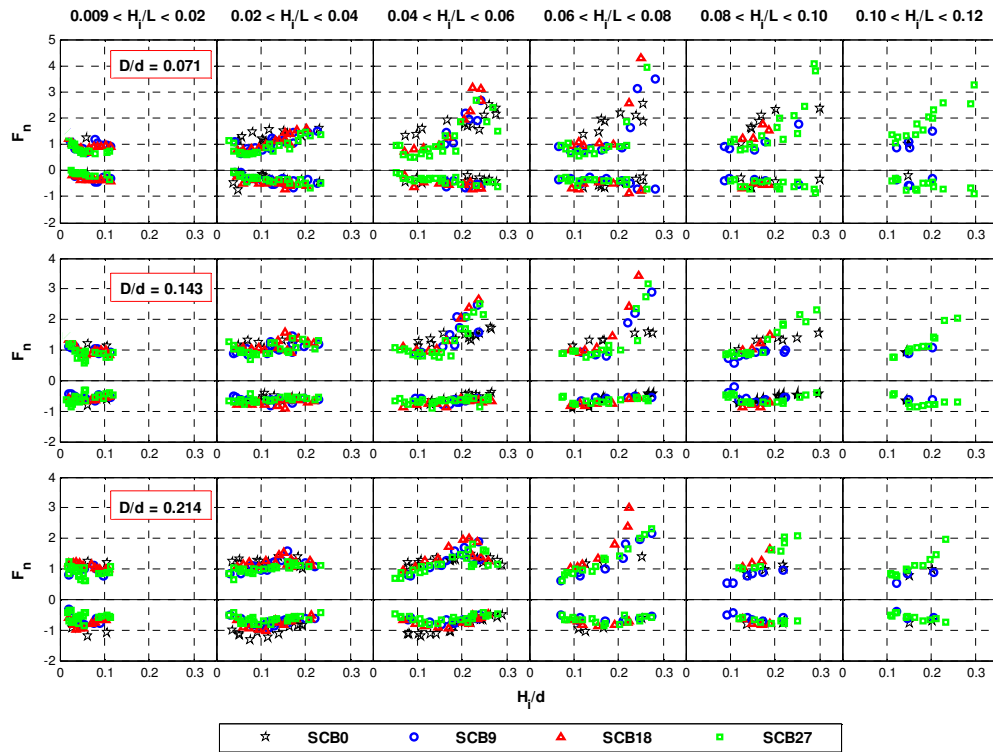


Figure 5.30: Force coefficients of the SCB models in regular waves

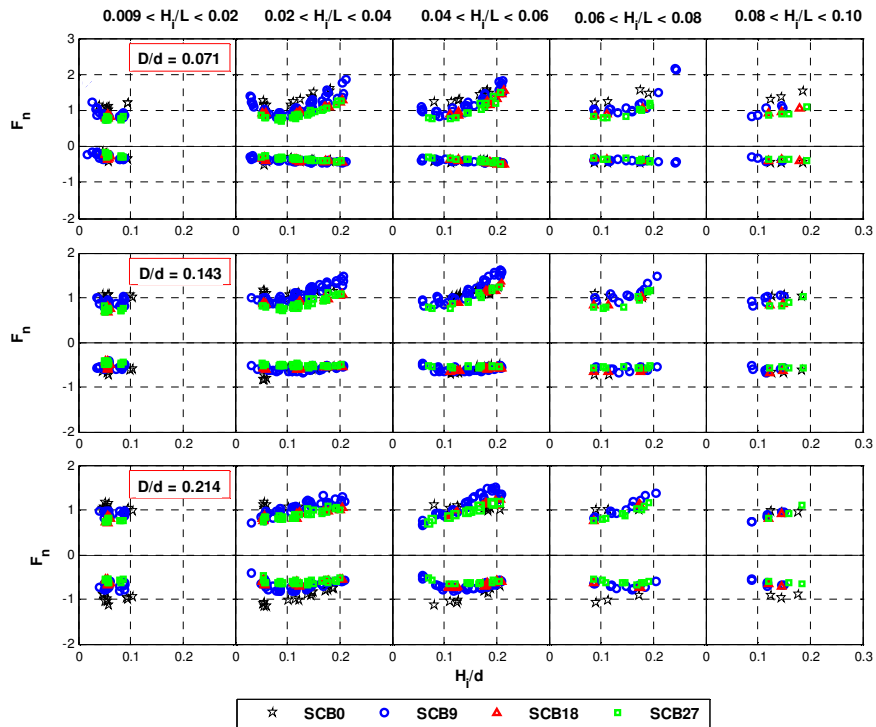


Figure 5.31: Force coefficients of the SCB model in irregular waves

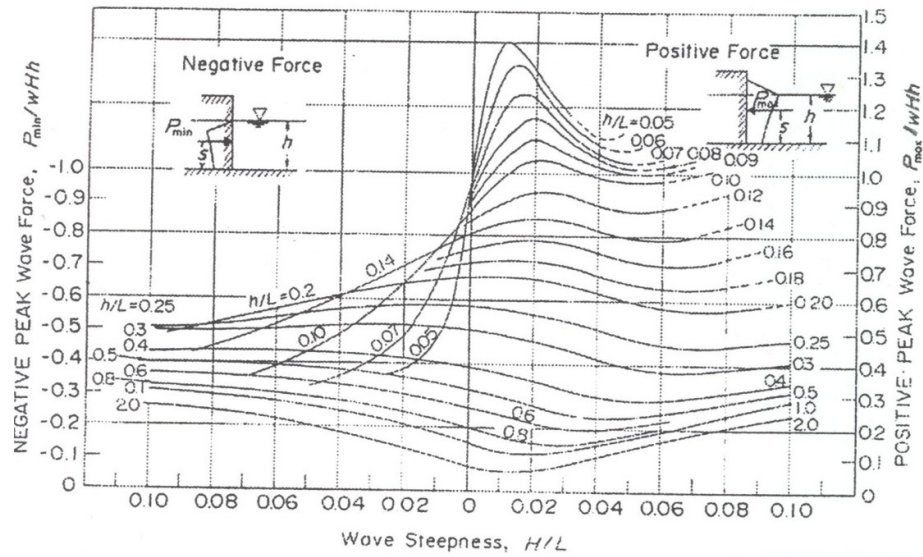


Figure 5.32: Design diagram for positive and negative forces developed by Goda and Kakizaki (1967)

whereas the negative force at free surface is zero, and subsequently increases as the draft increases. Even though different breakwater types are used, it is believed that the wave force distribution concept developed by Goda (1967) also holds true for free surface breakwaters.

(b) Effect of the Breakwater Porosity – ϵ_{SCB}

The breakwater porosity poses some influence on the force coefficients of the SCB models. For the SCB0 model, the normalised force coefficients, F_n tend to be higher than those of the perforated breakwaters when the waves are small ($H/d < 0.2$). However, as wave height increases ($H/d > 0.2$), the F_n values are not as significant as those of the perforated ones. This is mainly due to the fact that the curvature of the solid front wall promotes significant run-up and overtopping of the larger waves instead of direct intercepting the waves. Further, as the waves run up the slope, the flow path is diverted according to the curvature of the structure with increased vertical component of the wave pressure acting in a downward direction close to the crest of the breakwater. At this instance, some of the wave forces acting on the semicircular section are directed to the centre of the curvature, which subsequently offers greater sliding stability against waves. If the run-up exceeds the crest height of the SCB0 model, wave overtopping takes place above the breakwater. The negative horizontal forces resulted from water running down the rear wall may also offset the positive forces. For the perforated models ($9\% \leq \epsilon_{SCB} \leq 27\%$), the variations of the $F_{n,c}$ values become more noticeable than those of the $F_{n,t}$. In regular waves, the $F_{n,c}$ values of the SCB18 model are found to be exceptionally high at the higher range of H/d ; this might be due to the

combined wave interception by both the front and rear walls of the perforated model being at maximum in this test condition. However, similar observation is not obtained for the case of irregular waves.

(c) Effect of Wave Steepness – H/L

Overall, the $F_{n,t}$ and $F_{n,c}$ values of the SCB models do not seem to respond to the change of H/L very much regardless of the sea states. Hence, it can be deduced that the effect of wave steepness on the force coefficients of the SCB models is rather weak.

(d) Effect of Relative Immersion Depth – D/d

The influence of the relative immersion depth on the $F_{n,t}$ of the SCB models is more significant than on the $F_{n,c}$ in both regular and irregular waves. This is because the negative wave forces increase from zero at the free surface to larger values at deeper draft. The result is in agreement with the design diagram developed by Goda (1967) as shown in Figure 5.32.

Similar to the hydraulic coefficients described in Section 5.2.7, a multiple regression analysis was conducted to evaluate the impact of the predictor variables (*i.e.* H/d , ε_{SCB} , H/L and D/d) on the force coefficients. The *t*-tests results showed that all of the predictor variables were statistically significant in influencing the force coefficients. The $F_{n,c}$ was found to be strongly subjected to the change of H/d ; whilst the $F_{n,t}$ was greatly influenced by D/d in both regular and irregular waves. Therefore, these variables are recommended to be included in the empirical model in predicting the horizontal loadings acting on the SCB models.

5.3.2 Effect of Breakwater Placement Ratio – B/d

The horizontal loadings on the SCB9 model corresponding to placement ratios, $B/d = 0.714, 1.000, 1.667$ are presented in Figure 5.33 for regular waves and Figure 5.34 for irregular waves. Similarly, the F_n data are plotted against H/d for different wave steepness ranges. It can be seen from the figures that the $F_{n,t}$ and $F_{n,c}$ values increase with the decreasing B/d , *i.e.* breakwaters located in deeper waters are exposed to higher horizontal wave forces. This finding is reasonable in that the horizontal loadings on the breakwaters are greatly controlled by the wave activities at the front and in the chamber. This can be seen in Figure 5.19 whereby larger wave excitation is observed around the breakwaters in deeper waters. Therefore, the breakwater placement ratio is an important variable that governs the force coefficients of the SCB models considerably.

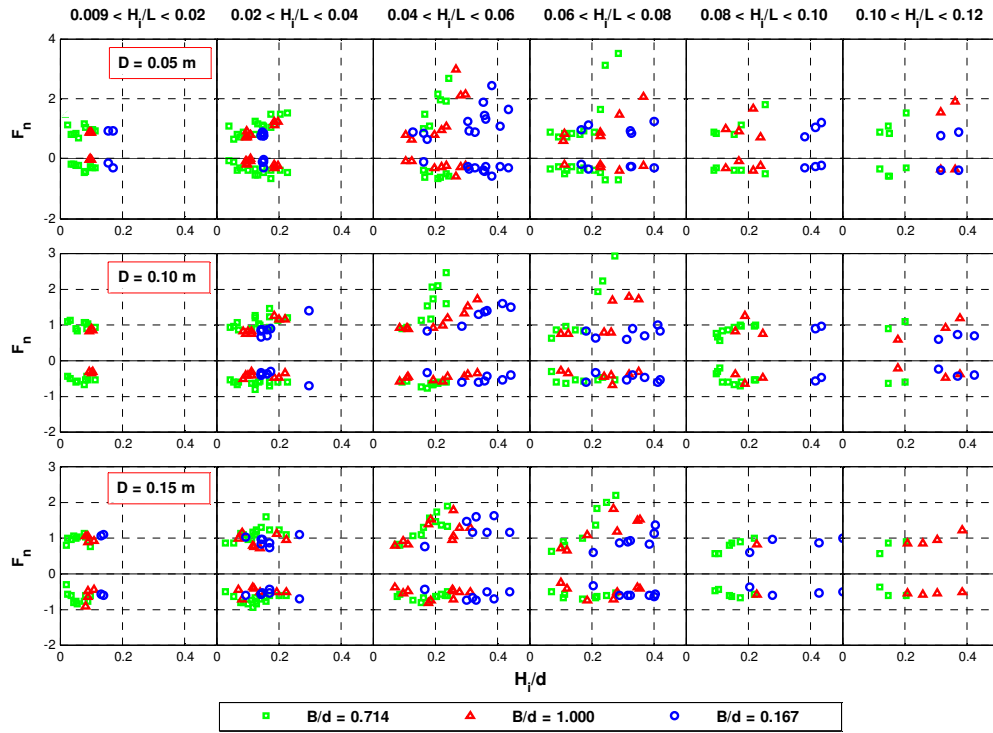


Figure 5.33: Effect of B/d on the force coefficients of the SCB9 model in regular waves

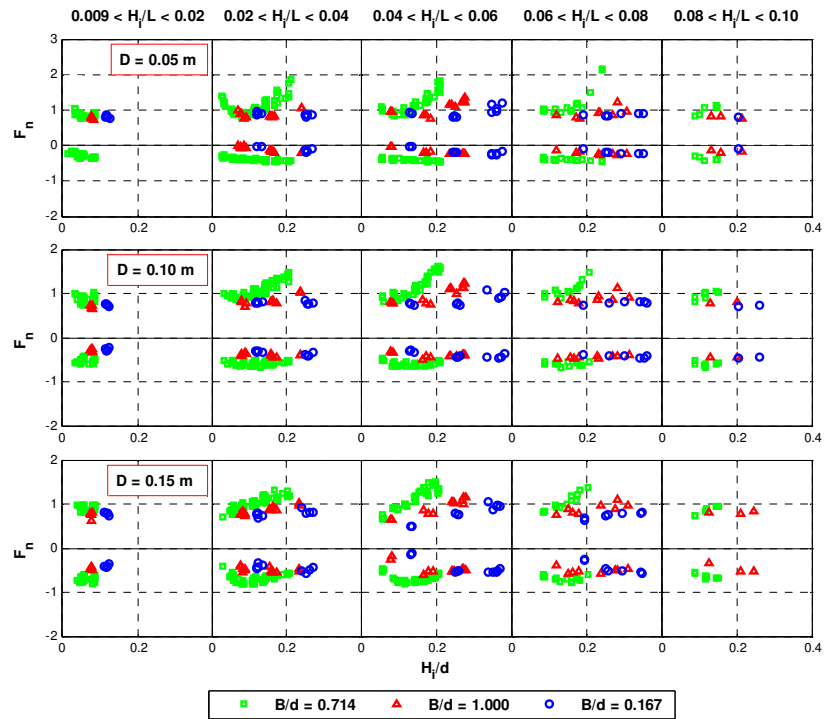


Figure 5.34: Effect of B/d on the force coefficients of the SCB9 model in irregular waves

5.3.3 Effect of the Rear Wall Perforation

The effect of the rear wall perforation on the horizontal loadings acting on the SCB9 model (with rear wall perforation) and the SCB9X model (with solid rear wall) is assessed based on the results shown in Figures 5.35 and 5.36. It is shown that the presence of the rear wall perforation does not reduce the horizontal wave forces acting on the structure. As mentioned in Section 5.2.7, due to the reduction in the uplift force, the SCB9 model with rear perforation near the crest is much more preferable from an engineering design perspective.

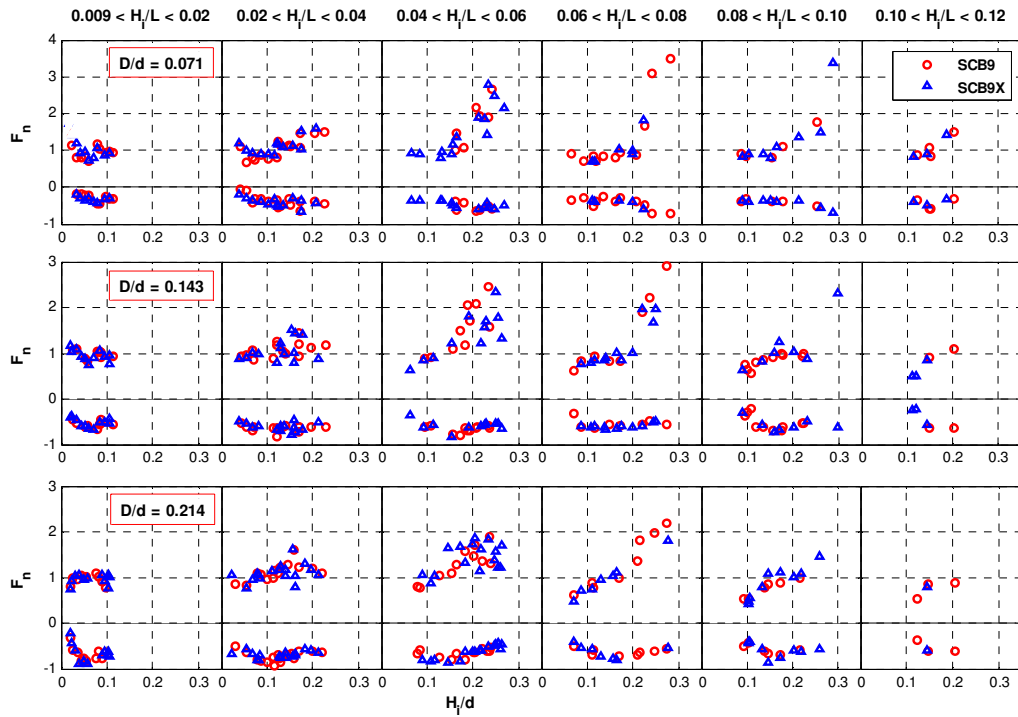


Figure 5.35: Effect of the rear wall openings on the force coefficients in regular waves

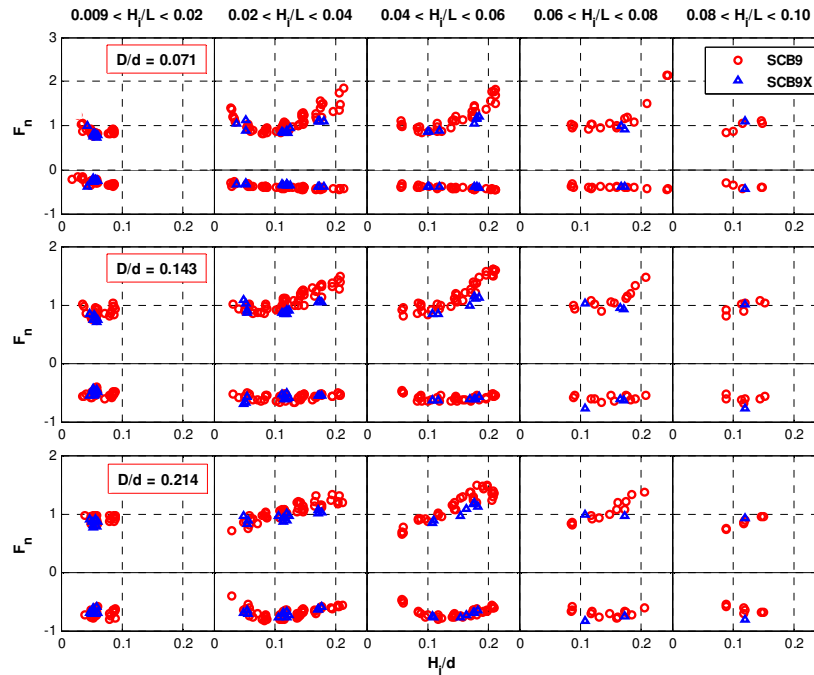


Figure 5.36: Effect of the rear wall openings on the force coefficients in irregular waves

5.3.4 Effect of Wave Spectra (Sea States)

Limited tests were carried out in the experiment to study the effect of the wave spectra (*i.e.* PM and JONSWAP) on the horizontal wave force coefficients of the SCB27 model. The results shown in Figure 5.37 demonstrate that the force coefficients of the model are not subjected to the types of wave spectra as the variations of F_n under the influence of PM and JONSWAP spectra are insignificant.

5.3.5 Statistical Distributions of Forces

In random seas, the wave forces acting upon the SCB models are highly variable. Hence, wave forces may best be described by their statistical distributions. One way to proceed is to fit a probability distribution to the force data. This probability distribution is particularly useful when applied to identify forces corresponding to the extreme events. The Weibull distribution is commonly used to examine any link with the statistics of wave heights in a random sea as wave heights generally fit a Rayleigh distribution, which in itself is a special case of the Weibull distribution (Allsop *et al.*, 1996). Therefore, attempts were made in this study to fit the force data using a Weibull distribution.

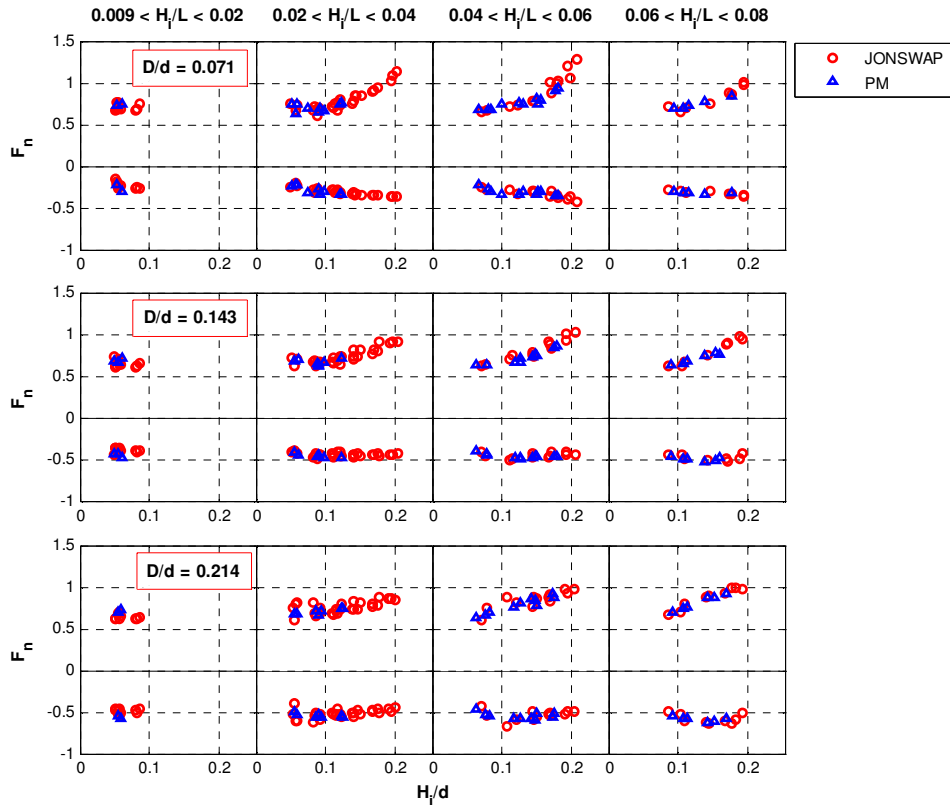


Figure 5.37: Effect of wave spectral types on the force coefficients of the SCB27 model

An analysis program was first coded to identify the peak horizontal forces in the entire time series for each test run. To examine the statistical distribution, these peak forces were ranked in order, allowing the exceedance distribution to be plotted on Weibull probability axes. The probability of exceedance for Weibull distribution is related by:

$$P = 1 - e^{-\left(\frac{F}{\lambda}\right)^k} \quad (5.1)$$

where k is the shape parameter, and λ is the scale parameter. The goodness of fit of the force data to a Weibull distribution can be visually evaluated by a Weibull probability plot. The Weibull probability plot is a plot of cumulative distribution function, P of the force data on special axes, *i.e.* $\ln(-\ln(1-P))$ versus $\ln(F)$. Note that Equation (5.1) can be rewritten as:

$$-\ln(1-P) = \left(\frac{F}{\lambda}\right)^k$$

$$\ln[-\ln(1 - P)] = k \ln F - k \ln \lambda \quad (5.2)$$

where the gradient refers to the shape parameter k , and the scale parameter λ can be inferred from the y -intercept. If the force data fit a Weibull distribution then a straight line can be expected on a Weibull plot. Such exceedance distributions are commonly used to describe the types of forces acting on a coastal structure: (i) pulsating forces are defined by those data varying linearly with exceedance probability on a Weibull distribution; whilst (ii) impact forces increase rapidly over the upper part of the distribution, resulting in the force data deviating from the straight line (Allsop *et al.*, 1996).

In this analysis, the peak forces due to wave crests (positive forces, F_c) and troughs (negative forces, F_t) for each test were non-dimensionalised by their standard deviations, σ_F . Figure 5.38 shows the sample Weibull probability plots of the F/σ_F for the SCB9 model exposed to $H_{m0} \approx 0.06$ m and $T_p = 1.0$ s, 1.3 s and 1.8 s for $D/d = 0.071$, 0.143 and 0.214. The corresponding force spectra for the respective test cases were shown in Figure 5.39. From Figure 5.38, the peak forces generally follow the Weibull distribution quite well, except at the lower range of F/σ_F . The deviations of the force data resemble those of the incident peak wave crests and troughs at their lower range as shown in Figure 5.40. This indicates that the peak wave forces are strongly correlated with the peak wave crests and troughs. Although the results for other SCB models are not included here, the general trend is found to be similar to the above. This indicates that the peak wave forces acting on the SCB models may be adequately predicted by the Weibull distribution.

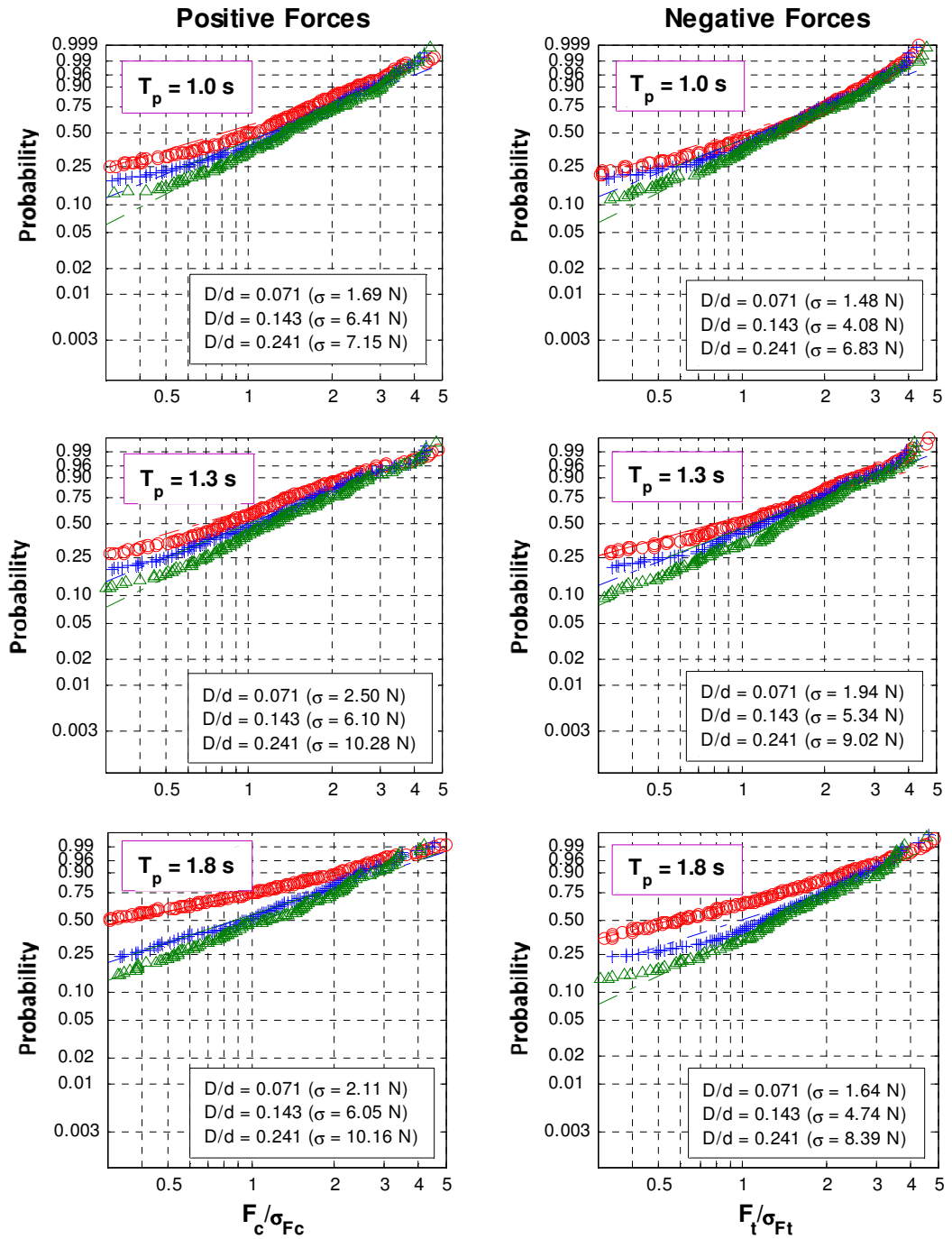
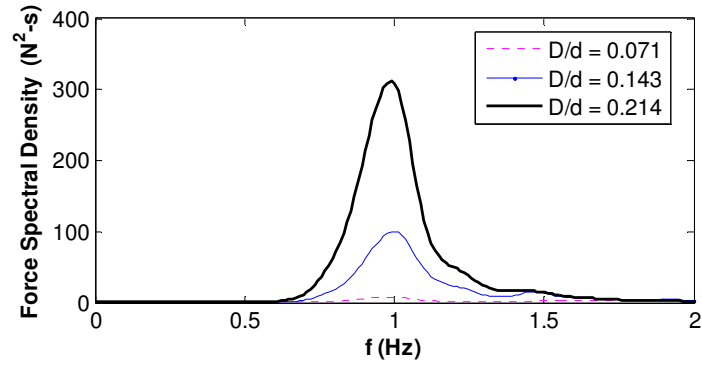
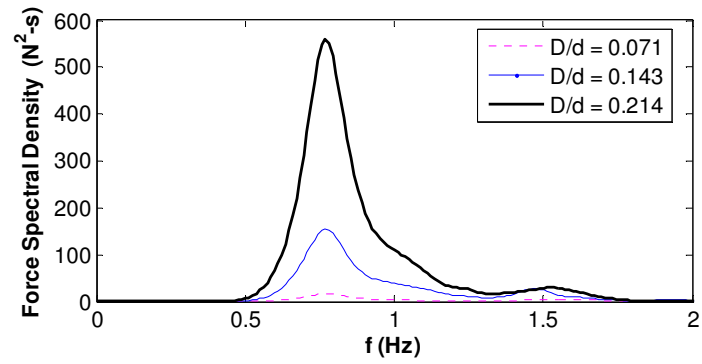


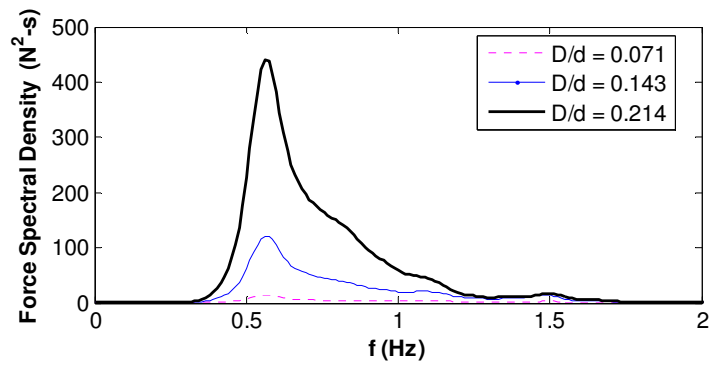
Figure 5.38: Weibull probability plots of the horizontal wave forces for the SCB9 model corresponding to $T_p = 1.0$ s, 1.3 s and 1.8 s, and $H_{m0} \approx 0.06$ m



(a) $T_p = 1.0$ s; $H_{m0} \approx 0.06$ m



(b) $T_p = 1.3$ s; $H_{m0} \approx 0.06$ m



(c) $T_p = 1.8$ s; $H_{m0} \approx 0.06$ m

Figure 5.39: Force spectra for the SCB9 model of $T_p = 1.0$ s, 1.3 s and 1.8 s, and $H_{m0} \approx 0.06$ m

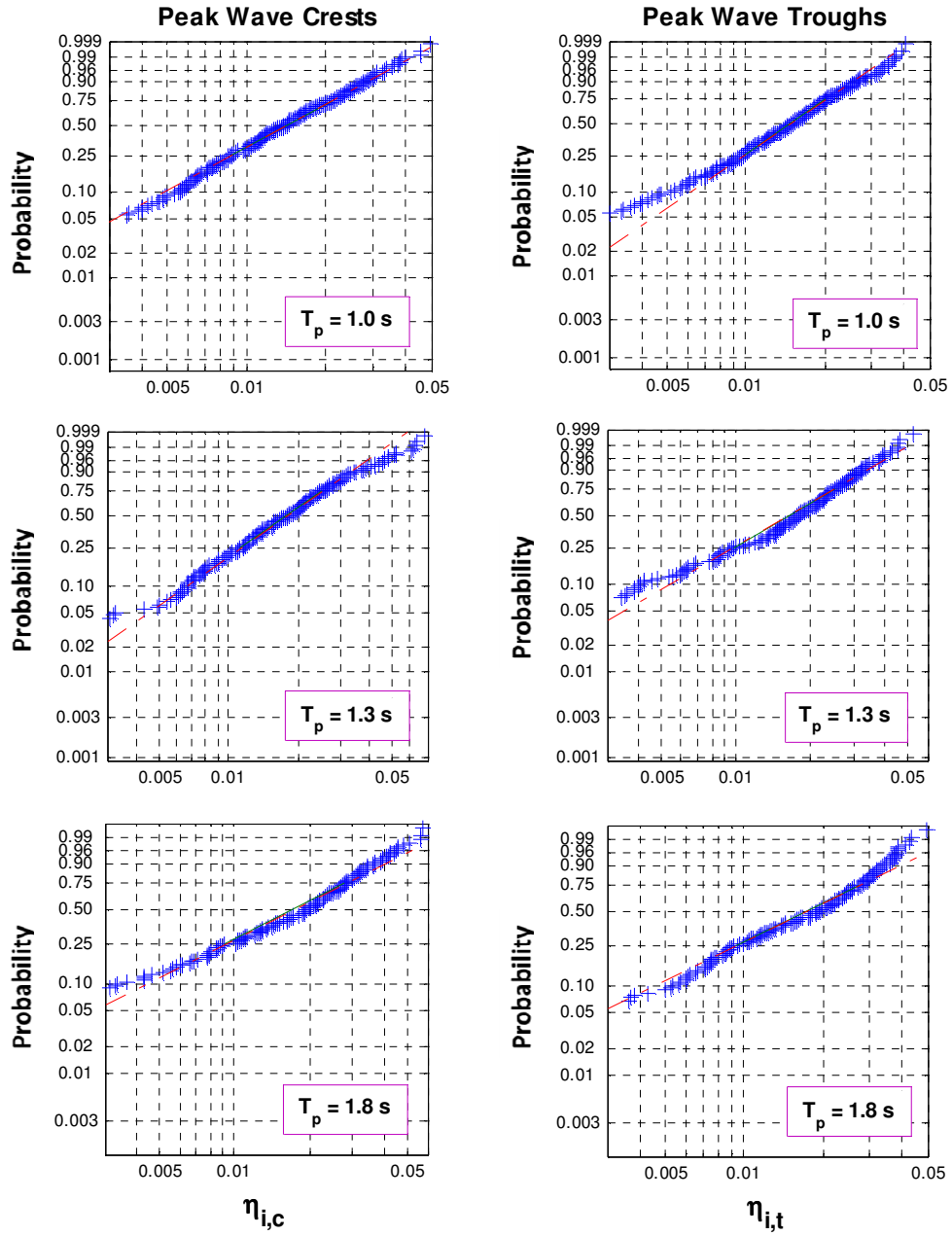


Figure 5.40: Weibull probability plots of the peak wave crests and troughs for $T_p = 1.0$ s, 1.3 s and 1.8 s, and $H_{m0} \approx 0.06$ m

5.4 Selection of the Optimum Breakwater Design

The hydrodynamic characteristics of the SCB models of different porosities at the front screens have been described comprehensively in the previous sections. The effect of the rear wall perforation on the efficiency of the breakwater has also been explored. The findings derived from these studies form a basis in determining the ultimate configuration of the SCB model that offers the highest hydraulic efficiency, which is, in this context, to possibly reduce the wave transmission and reflection by at least 50%.

The solid SCB model – SCB0 has supreme wave attenuation ability that significantly surpasses the performance of the perforated SCB models especially in depth limited waters. However, it impedes the wave energy mainly by reflection, giving rise to standing waves that are about 2 times the incident wave heights (refer to Figures 5.15 and 5.16), which excite restlessly in front of the breakwater. This may consequently lead to several issues associated with the increased wave activity in the vicinity of the breakwater as mentioned in Section 5.2.2. As a result, the use of the SCB0 model as a sea defence structure for ports and harbours may not be a realistic solution.

The perforated SCB models, on the other hand, are less invasive for the marine environment as they are good anti-reflection structures. They suppress the wave height mainly by energy dissipation in various forms. The perforated breakwaters with sufficient drafts manage to dampen the height of the incident waves by half when the width (diameter) of the semicircular caisson is greater than 0.4 times the design wavelength (refer to Figures 5.1 and 5.2); and higher wave transmission can be expected by the breakwaters with limited drafts. Overall, the perforated semicircular breakwaters were found to be more relevant to the design objectives set for this study despite the fact that the wave attenuation performance of these structures may not be as good as the SCB0 model.

Among the perforated models, the SCB9 model appears to be superior to the others in terms of wave attenuation and energy dissipation. Moreover, the wave excitation in the breakwater chamber is comparatively small, thus reducing the risk of wave slamming onto the inner shell. The wave reflection induced by the SCB9 model is comparable to those induced by breakwaters of higher porosities, and is about half of that induced by the SCB0 model. Having said these, the SCB9 model may be the most viable breakwater design of all the models tested. However, it is without doubt that wave transmission by the SCB9 model with limited immersion is somewhat high ($C_T > 0.5$), which may not be tolerable for some marine

applications. Therefore, strategies have to be explored to improve the hydraulic efficiency of the breakwater at low immersion, and particularly to further limit the wave transmission. This aspect of the study has been dealt with and the results are reported in Chapter 6.

5.5 Summary

The experimental works described in this chapter aim to propose a free surface semicircular breakwater (SCB) that is hydraulically efficient. To attain this goal, a number of SCB models were constructed and investigated with variations in their front wall porosity and rear wall perforation. These models were rigorously tested in both regular and irregular waves through physical modelling. The hydraulic characteristics of the breakwaters were evaluated in the form of the coefficients of transmission, C_T , reflection, C_R , and energy dissipation C_L , which in turn were presented as functions of the breakwater porosity, ε_{SCB} , the relative breakwater width, B/L , the relative breakwater immersion, D/d , the wave steepness, H/L and the structure placement ratio, B/d . The wave activities in front of the breakwaters and within the chambers were measured and reported as wave disturbance coefficients, C_F and C_C . Besides, the horizontal wave forces acting on the SCB models were also determined and quantified as the normalised force coefficients, F_n .

In general, the energy coefficients (*i.e.* C_T , C_R and C_L) of the SCB models were strongly influenced by B/L and D/d , while the wave disturbance coefficients (C_F and C_C) influenced by ε_{SCB} , D/d and B/d . For the perforated SCB models, the influence of breakwater porosity on the disturbance coefficients was more significant than on the energy coefficients. For the horizontal wave forces, the dependence of F_n upon H/d (the relative wave height), D/d and B/d was more significant than the other affecting parameters. The effects of the rear wall perforation and the wave spectral types on the hydrodynamic performance of the SCB models were insignificant.

The impervious model (SCB0) was a better wave attenuator than the perforated SCB models; however, it produced severe wave reflection in front of the structure. Conversely, the perforated SCB models served as effective anti-reflection structures and good energy dissipaters, whereby these characteristics comply with the design objectives more. The present study inferred that the semicircular breakwater with a front wall of 9% porosity (SCB9) was the most hydraulically effective configuration; and the claim was mainly attributed to two reasons: (i) the SCB9 resulted in milder wave climate in the breakwater chamber; and (ii) the SCB9 is the structurally more rigid than the perforated breakwaters.

6

Perforated Semicircular Breakwater with Wave Screens: Results and Discussion

6.1 General

The primary concern with the existing free surface breakwater has been its wave absorption efficiency over a broad range of wave condition. In Chapter 5, the ‘front-wave dissipating type’ free surface SCB was proven experimentally to be a better anti-reflection structure than the ‘solid-type’ breakwater; and the SCB9 model outperformed the other SCB models with higher front wall porosities. For these reasons, the SCB9 model has been selected as the most optimum breakwater configuration. Nevertheless, the SCB9 model demonstrates poor wave attenuation ability when its immersion depth is small. To rectify the problem, it is suggested that a submerged wave screen is to be extended from the bottom edge of the SCB9 model as shown in Figure 4.20.

The purpose of this chapter is to report the results from Experiment *Series B1* and *B2* (see Section 4.10.2.2). Experiment *Series B1* is a series of preliminary tests aimed at investigating the impact of a single submerged wave screen on the overall hydraulic performance of the SCB9 model; whereas Experiment *Series B2* aims to determine the best screen configuration and porosity that would provide optimum performance of the SCB9 model. These test series were entirely conducted at $D/d = 0.071$ where the SCB9 model contributed the least wave attenuation. Table 6.1 provides the abbreviations of all the breakwater configurations tested in this study, in which they will be referred to thereafter.

Table 6.1: Abbreviations for test model

Abbreviation	Description
SCB9	Free surface semicircular breakwater with 9% front wall porosity
SS25	Single wave screen with 25% porosity
FS25	Front screen with 25% porosity
FS40	Front screen with 40% porosity
FS50	Front screen with 50% porosity
RS25	Rear screen with 25% porosity
RS40	Rear screen with 40% porosity
RS50	Rear screen with 50% porosity
SCB9-FS25	SCB9 with a front screen of 25% porosity
SCB9-FS40	SCB9 with a front screen of 40% porosity
SCB9-FS50	SCB9 with a front screen of 50% porosity
SCB9-RS25	SCB9 with a rear screen of 25% porosity
SCB9-RS40	SCB9 with a rear screen of 40% porosity
SCB9-RS50	SCB9 with a rear screen of 50% porosity
SCB9-DS25	SCB9 with double screens (front and rear screens) of 25% porosity
SCB9-DS40	SCB9 with double screens (front and rear screens) of 40% porosity
SCB9-DS50	SCB9 with double screens (front and rear screens) of 50% porosity

6.2 Efficiency of a Wave Screen

As mentioned earlier, the objective of this test series is to ascertain the hydraulic contribution of a wave screen in two configurations: single submerged, truncated upright screen (denoted as SS25), and the SCB9 model with a front screen (denoted as SCB9-FS25). Both porosity of both screen was set at 25%. For the SS25 model, the 300 mm long screen was submerged at a depth of 50 mm from SWL. For the SCB9 model with a front screen of 25% porosity (denoted as SCB9-FS25), the SCB9 was immersed at 50 mm from SWL and the screen of 300 mm long was extended from the bottom edge of the caisson front wall. The test parameters employed for this experiment are presented in Experiment *Series B1* in Table 4.11. The experimental results for these models are shown in Figure 6.1 for regular seas and Figure 6.2 for irregular seas. The results of SCB9 at $D/d = 0.071$ are also displayed on the plots for comparison purposes.

In general, the SS25 model exhibits a rather low hydraulic efficiency within the test range. Even though the waves reflected from the screen is relatively low, the SS25 model is a poor wave attenuator as it is only capable of suppressing up to 20% of the incident wave height in all test cases. Figure 6.3 shows that the presence of the SS25 model did not alter the wave profile very much. It can be seen that the wave troughs were better intercepted by the upper portion of the screen compared to the crests due to the fact that the water surface was closer to the structure. On the other hand, the SCB9 model exhibits higher hydraulic efficiency because the wave energy that is mostly distributed at the upper column of the water is better

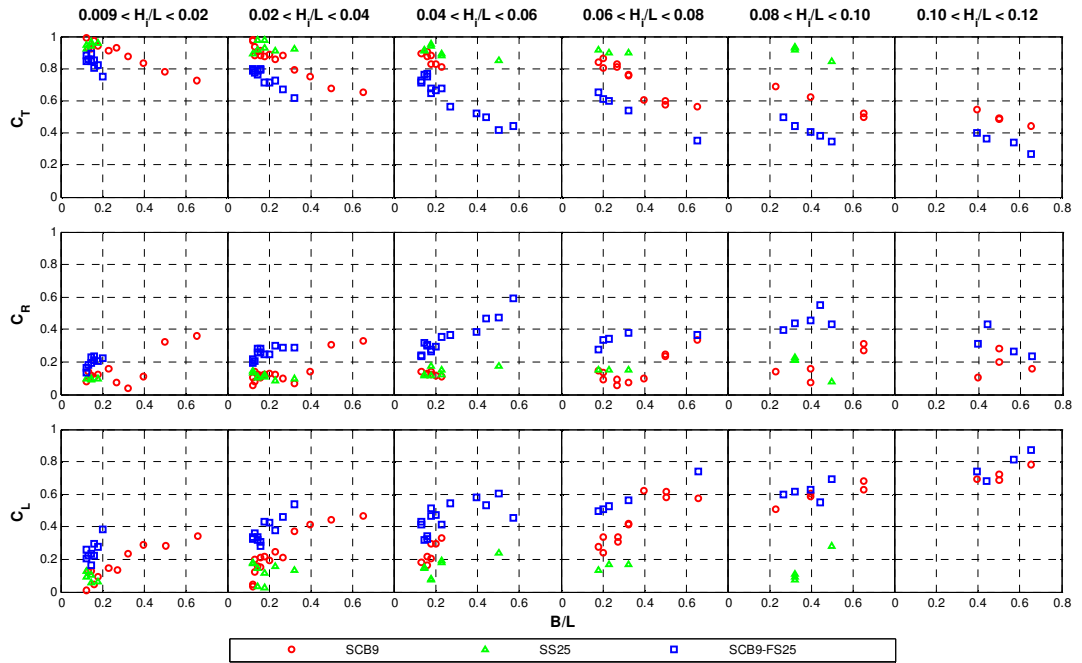


Figure 6.1: Energy coefficients of the SCB9, SS25 and SCB9-FS25 models in regular waves

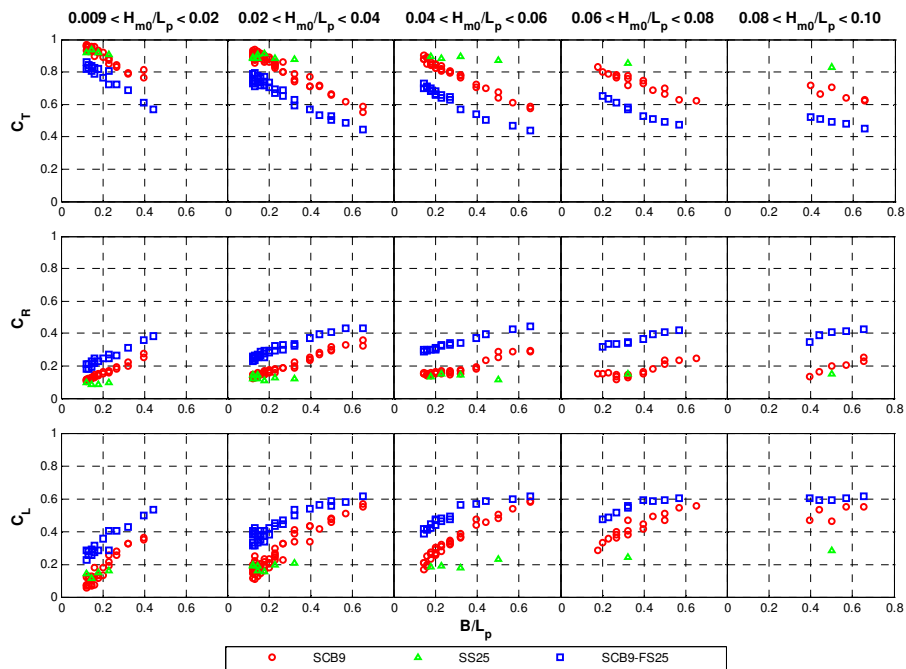


Figure 6.2: Energy coefficients of the SCB9, SS25 and SCB9-FS25 models in irregular waves

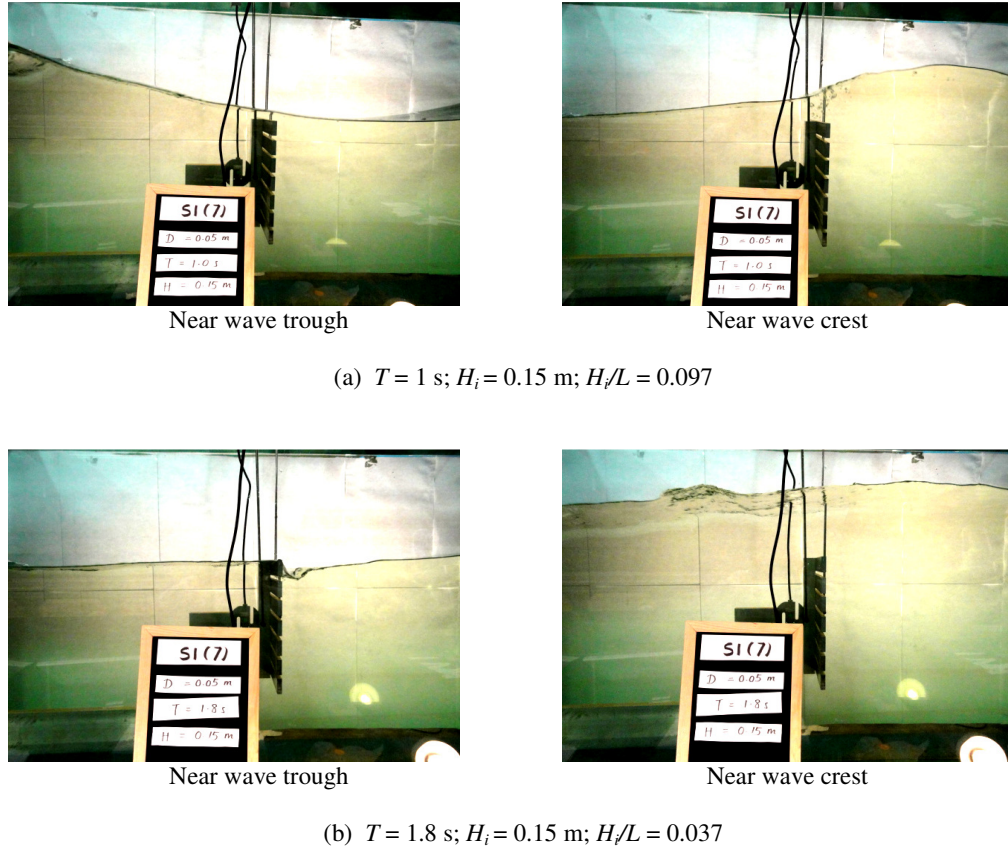


Figure 6.3: Wave interaction with the SS25 model. Note that the incident waves propagated from the left of the test model

arrested by the free surface breakwater. A significant improvement of wave suppression is attained when the screen is incorporated with the SCB9 model, giving a C_T variation of about 0.2 between SCB9 and SCB9-FS25 throughout the B/L range. Energy loss resulted from longer period waves (*i.e.* C_L at lower range of B/L) is minimal for both SS25 and SCB9; however, the energy is found to be effectively dissipated by the front screen of the SCB9-FS25 model. Due to the increase of breakwater draft, the SCB9-FS25 model reflects higher amount of waves, resulting in a maximum C_R of about 0.6 for regular waves and about 0.4 for irregular waves (both occurring at shorter period waves).

The response of horizontal loadings acting on the SS25 model plotted with respect to incident wave height for respective wave periods is presented in Figure 6.4. The force under the wave crests is termed the positive or landward force, F^+ and that under the wave troughs is termed as the negative or seaward force, F^- . It is apparent from the figure that the horizontal wave forces are strongly controlled by the incident wave height and not by the wave period in both regular and irregular seas. It is interesting to note that the negative

forces under the wave troughs are greater than the positive ones ($|F^+| < |F^-|$) for most of the test cases, particularly in irregular waves. The explanation to this phenomenon is further described in Section 6.5.

In summary, the use of the SS25 or SCB9 model in providing wave protection to coastal facilities may not be functionally compatible especially when these structures are subjected to longer period waves and small immersion depth. Nonetheless, when these structures work together as a composite breakwater their hydraulic efficiency is significantly enhanced. This indicates that the wave screen does play an important role in improving the performance of the SCB9 model and it is, therefore, worth investigating the screen effects further. This is done in the following section.

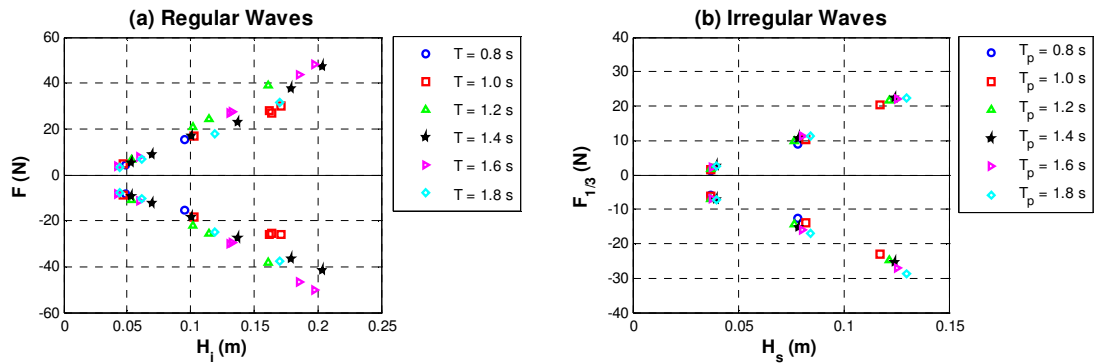


Figure 6.4: Measured horizontal wave force on the SS25 model in regular and irregular seas

6.3 Hydraulic Characteristics of the SCB9 model with a Wave Screen(s)

This section investigates the efficiency of wave screens of different configurations and porosities in enhancing the hydraulic performance of the SCB9 model that is immersed at limited depth, *i.e.* $D/d = 0.071$. A wave screen was extended beneath the SCB9 model from the front wall (denoted as SCB9-FS) and from the rear wall (denoted as SCB9-RS) as shown in Figure 4.20. The SCB9 model with double screens (denoted as SCB9-DS) was also considered in this study. For each screen configuration, the porosity varied at 25%, 40% and 50%, giving a total of 9 types of SCB models namely SCB9-FS25, SCB9-FS40, SCB9-FS50, SCB9-RS25, SCB9-RS40, SCB9-RS50, SCB9-DS25, SCB9-DS40 and SCB9-DS50. Further details of the test models can be referred to Table 6.1. These models were tested using the test program presented in Experiment *Series B2* in Section 4.10.2.2(b).

For the experimental data analysis, hydraulic performance of the test models is presented in terms of C_T , C_R , C_L , C_F and C_C , and each coefficient is plotted with respect to the relative breakwater width, B/L and wave steepness, H/L in regular waves, and B/L_p and H_{m0}/L_p in irregular waves. It is noted that the relative breakwater width and wave steepness in both sea states are expressed as B/L and H/L , respectively, hereafter for ease of illustration. The impact of the wave screen(s) on hydraulic performance of the breakwater is reflected by the variation of the respective hydraulic coefficients, ΔC_i :

$$\Delta C_i = C_{i,composite} - C_{i,SCB9} \quad (6.1)$$

where $C_{i,composite}$ is the hydraulic coefficient of the SCB9 model with a wave screen(s), $C_{i,SCB9}$ is the hydraulic coefficient of the SCB9 model, and i is the annotation for the coefficients of transmission (T), reflection (R), energy dissipation (L), and wave climate at the breakwater (F & C). A positive value of ΔC_i shows an increment of the hydraulic coefficient based on the reference value of the $C_{i,SCB9}$, and vice versa. For instance, a negative ΔC_T value indicates an improvement in wave attenuation by the wave screen, and a positive ΔC_R value indicates the amount of reflected waves induced by the wave screen. Further description about the implication of the ΔC_i values on the hydraulic performance of the wave screens is presented in Table 6.2.

Table 6.2: Effect of ΔC_i on the hydraulic performance of wave screens

	$\Delta C_i < 0$ (Negative values)	$\Delta C_i > 0$ (Positive values)
ΔC_T	Improvement in wave attenuation	Reduction in wave attenuation
ΔC_R	Reduction in wave reflection	Increment in wave attenuation
ΔC_L	Reduction in energy dissipation	Enhancement in energy dissipation
ΔC_F	Decrement of wave activity in front of the breakwater	Increment of wave activity in front of the breakwater
ΔC_C	Decrement of wave activity in the breakwater chamber	Increment of wave activity in the breakwater chamber

6.3.1 Wave Transmission Coefficient – C_T

Wave transmission characteristics of the SCB9 model with a front screen (SCB9-FS) of different screen porosities in regular and irregular waves are shown in Figure 6.5. The C_T for the models decreases almost linearly with an increase in B/L , and the decrease of C_T is also observed for an increment of wave steepness and a reduction of the screen porosity. It was also found that the front screen with porosity, ϵ_{screen} of 25%, 40% and 50% improves wave attenuation of the SCB9 model (expressed in terms of ΔC_T) shows by 10% – 27%, 4% – 19% and 3% – 15% for regular waves, respectively, and 10% – 22%, 5% – 19% and 2% – 15%, for irregular waves, respectively, whereby significant improvement of performance seems to occur at $0.2 < B/L < 0.4$ for both sea conditions. Thus, the SCB9 with a front screen of smaller porosity (*i.e.* $\epsilon_{screen} = 25\%$) offers higher wave attenuation efficiency.

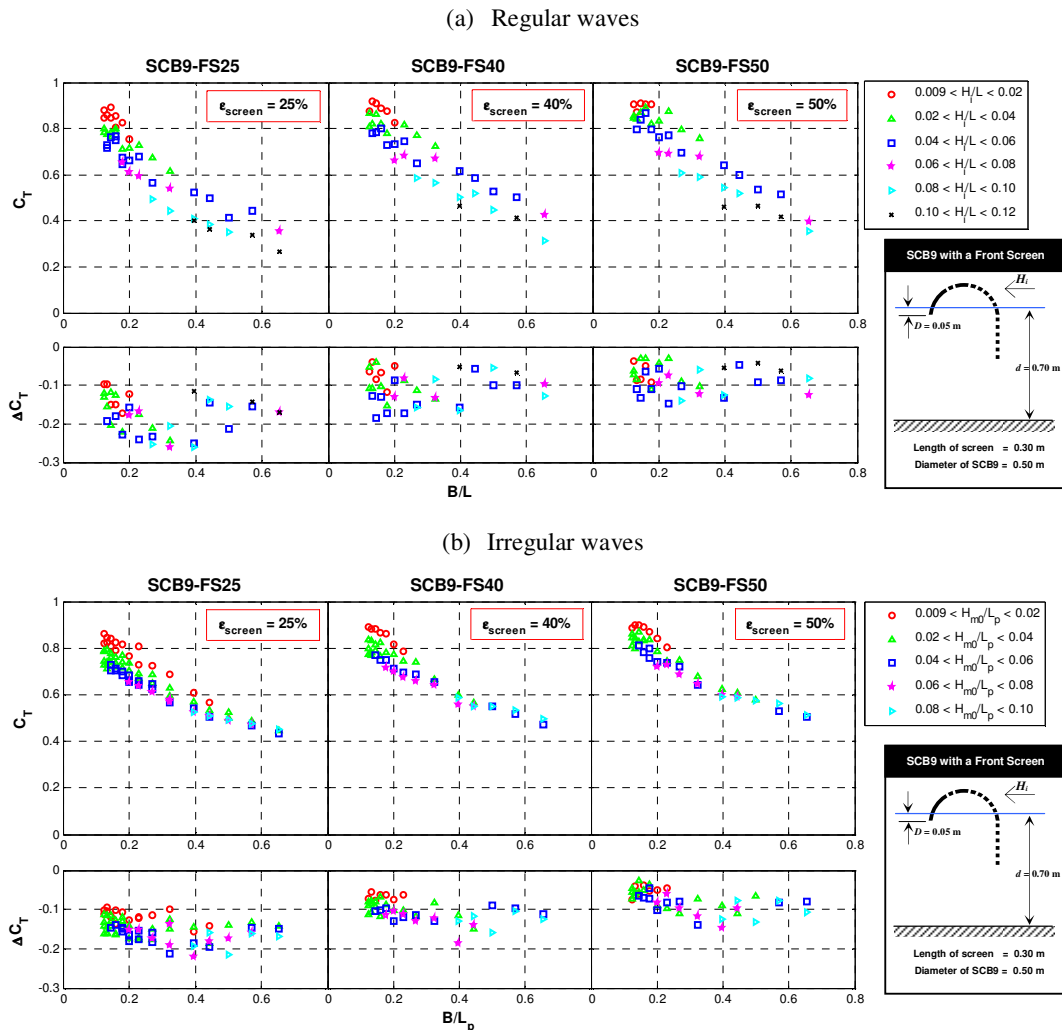


Figure 6.5: C_T and ΔC_T of the SCB9-FS models in regular and irregular waves

The plots of C_T for the SCB9 models with a rear screen (SCB9-RS) and those with double screens (SCB9-DS) are presented in Figures 6.6 and 6.7, respectively. The C_T values display similar trends when compared to those of the SCB9-FS models with corresponding relative breakwater width, screen porosity and wave steepness. The contribution of the rear screen to the enhancement of the breakwater performance (expressed in terms of ΔC_T) is greater than that of the front screen but less than that of the double screen. As a result, the SCB9-DS models offer the highest wave attenuation performance by reducing the incident wave height as much as 80% regardless of screen porosity.

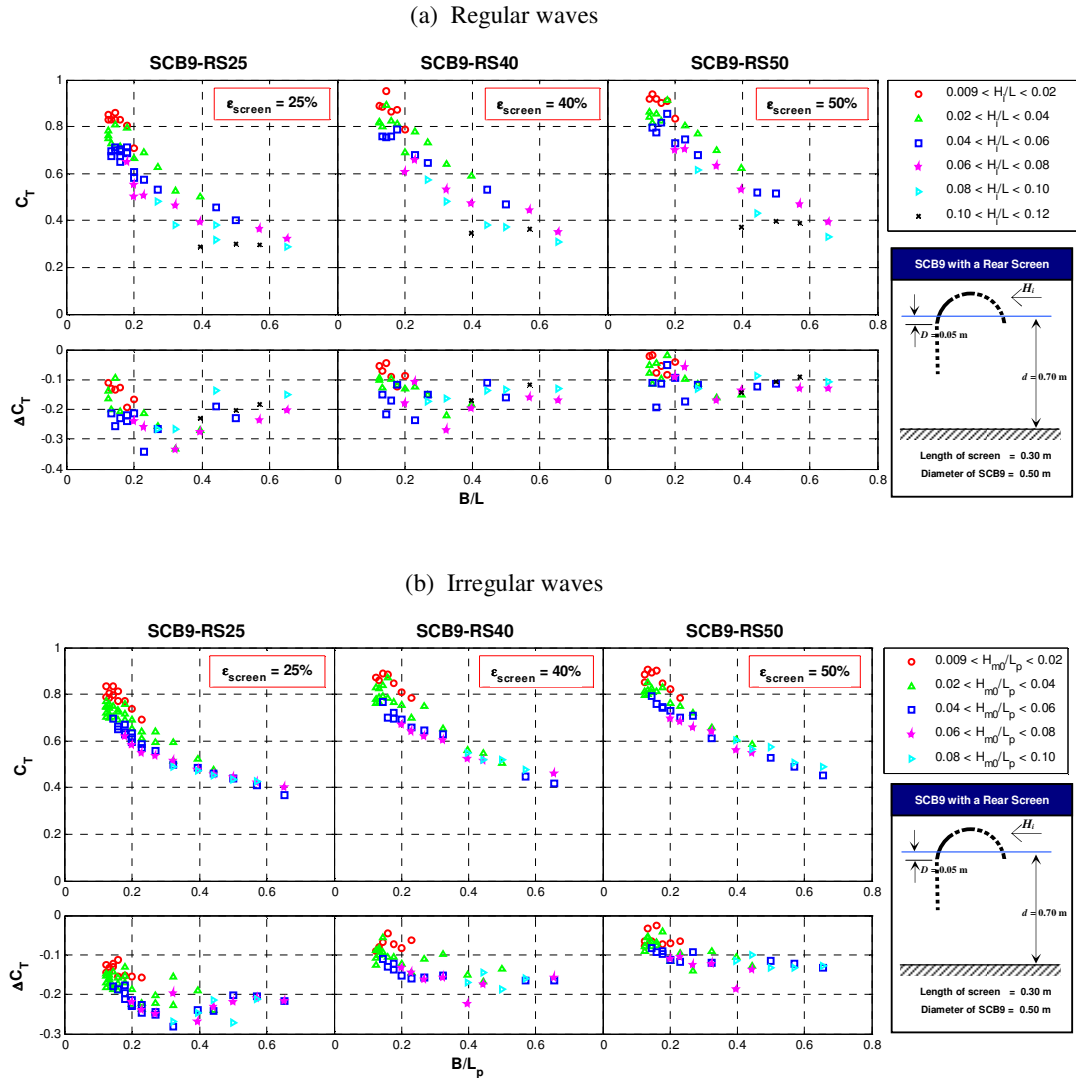


Figure 6.6: C_T and ΔC_T of the SCB9-RS models in regular and irregular waves

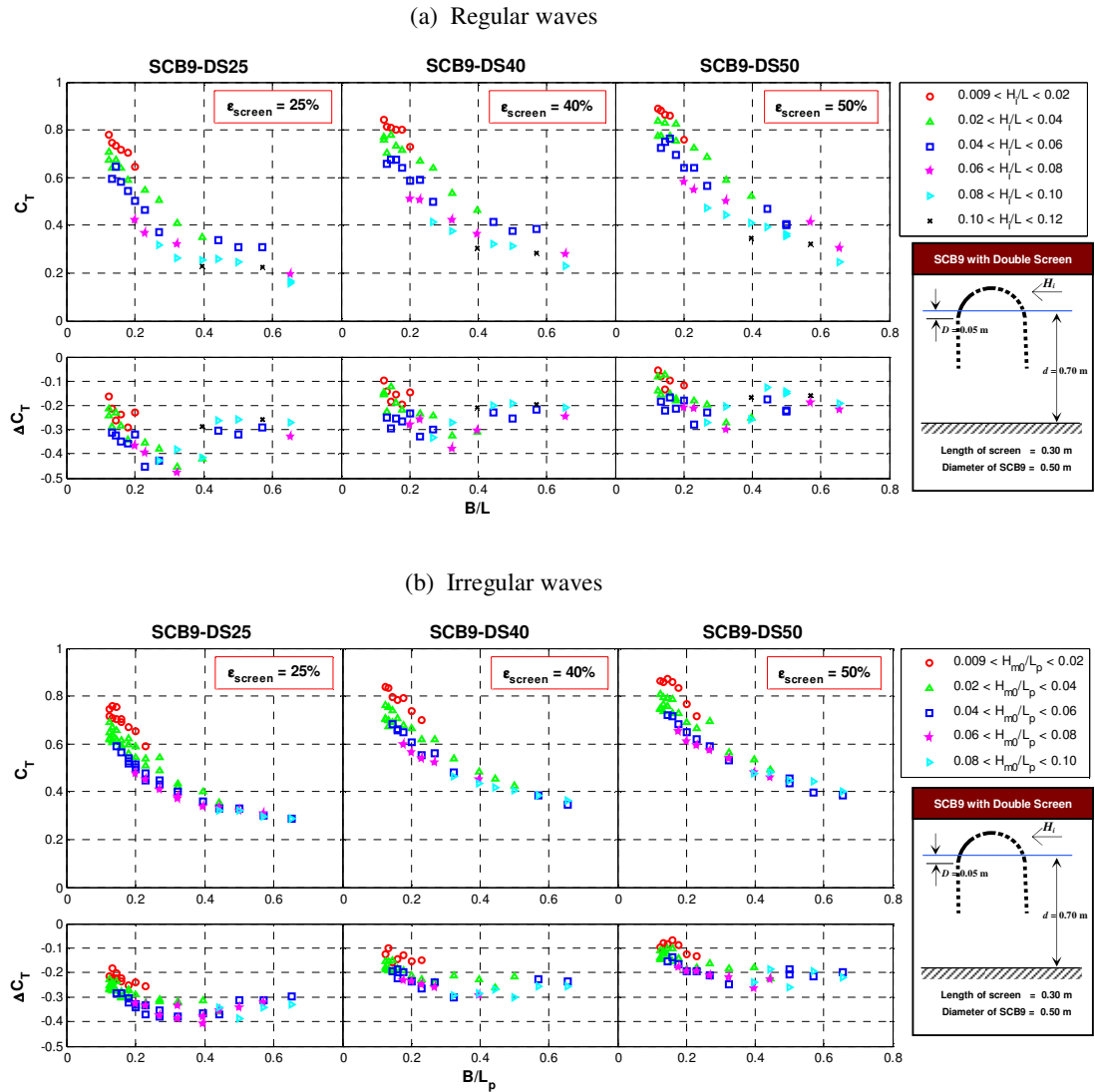


Figure 6.7: C_T and ΔC_T of the SCB9-DS models in regular and irregular waves

6.3.2 Wave Reflection Coefficient – C_R

Wave reflection characteristics of the SCB9-FS, SCB9-RS and SCB9-DS models with wave screen(s) of different porosities are presented in Figures 6.8 to 6.10. A ‘bragging’ effect, as discussed in Section 2.3.2.2, is clearly shown in the C_R values of the test models as B/L increases in regular waves; however, the effect is less apparent in irregular waves. Overall, the C_R values of the test models are more affected by the screen porosity than by the wave steepness. The ΔC_R values induced by the FS, RS and DS decrease with an increase in screen

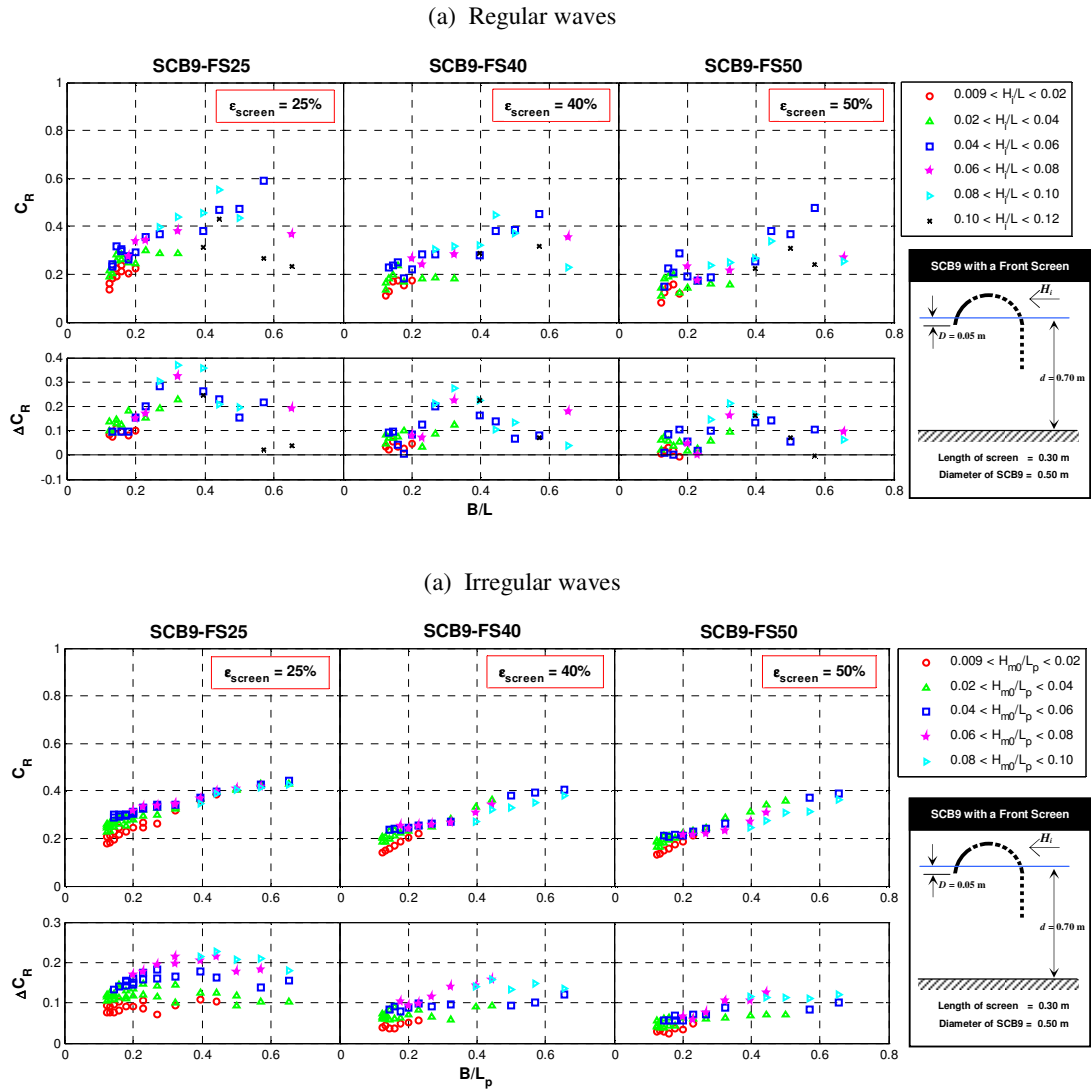


Figure 6.8: C_R and ΔC_R of the SCB9-FS models in regular and irregular waves

porosity, and the variations are particularly obvious for the FS of which the ΔC_R range is 0.02 – 0.38 in regular waves and 0.06 – 0.22 in irregular waves, for a screen of 25% porosity. For regular waves, the C_R maxima for the SCB9 model (see Figure 5.6) and the ΔC_R maxima for the FS, RS and DS (see Figures 6.8 – 6.10) always occur ‘out-of-phase’. For instance, the ΔC_R maxima for the screens mostly occur when $0.3 < B/L < 0.4$ during which the troughs (or minima) of C_R for the SCB9 model are found; while strong reflection is found at higher range of B/L for the SCB9 model when the corresponding ΔC_R values for the screens are usually at a minimal. The unique characteristics of the SCB9 model and the screen(s) alleviate the impact of reflection over the entire test range as they are used as a

composite structure. The maximum C_R values recorded for the SCB9-FS25, SCB9-RS25 and SCB9-DS25 models are 0.59, 0.48 and 0.57 for regular waves, respectively, and 0.42, 0.40 and 0.43 for irregular waves, respectively. Note that the porosity of the wave screen is indicated in the last part of the abbreviation.

In terms of screen configuration, the ΔC_R values of the FS, RS and DS are found to be comparable with each other regardless of the screen porosity. This implies that the reflection ability of the test models is less affected by the screen configuration. For this reason, it is deduced that the contribution of the rear screen of the DS on the overall wave reflection could be relatively insignificant.

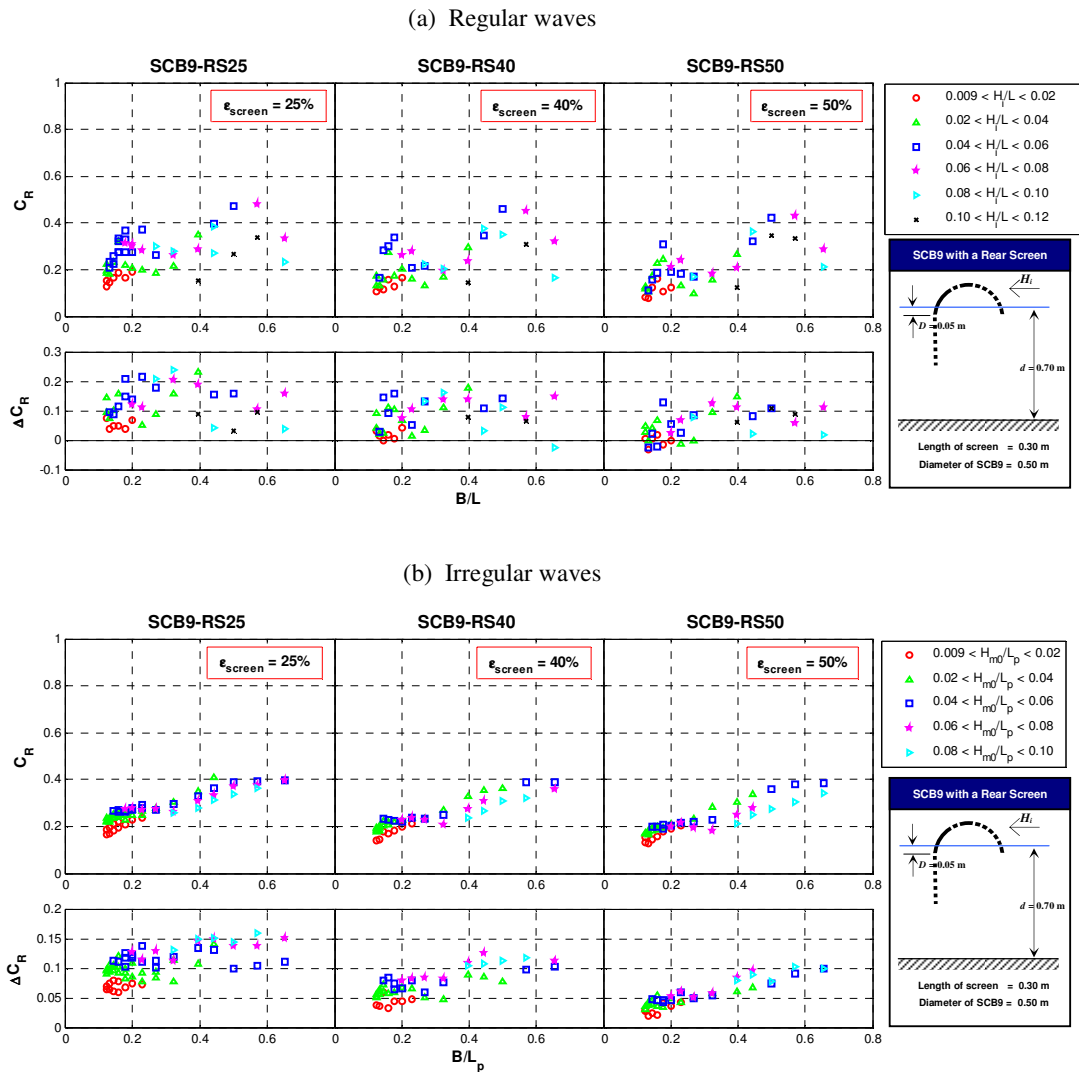


Figure 6.9: C_R and ΔC_R of the SCB9-RS models in regular and irregular waves

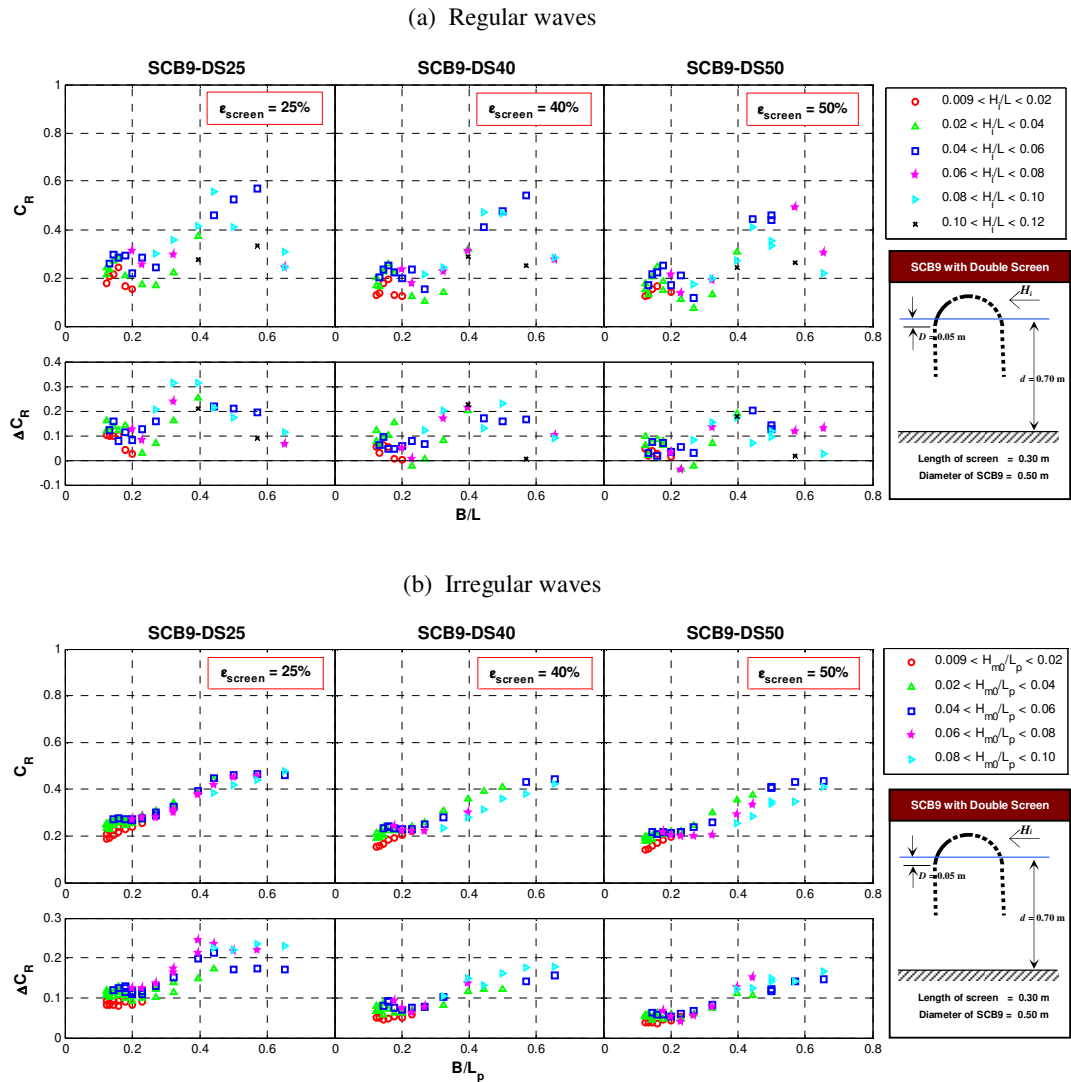


Figure 6.10: C_R and ΔC_R of the SCB9-DS models in regular and irregular waves

6.3.3 Energy Dissipation Coefficient – C_L

The energy dissipation ability of the SCB9-FS, SCB9-RS and SCB9-DS models in regular and irregular waves is demonstrated in Figures 6.11 to 6.13. For regular waves, the C_L values of the test models initially increase rapidly with the rise in relative breakwater width when $B/L < 0.4$; subsequently the values exhibit a slight drop at $0.4 < B/L < 0.6$ before surging again for the greater range of B/L . The maximum C_L values achieved by these models are beyond 0.8 at $B/L = 0.65$. Note that the decline of C_L is mainly attributed to the primary influence of the wave reflection within the range as seen in Figures 6.7 to 6.10. For irregular waves, the C_L of the test models responds in the same manner as that of the regular waves

but with the absence of the dip of C_L at $B/L > 0.4$. Instead, the C_L values at this range remain as constants, *i.e.* around 0.6 for the SCB9-FS models, 0.65 for the SCB9-RS models, and 0.70 for the SCB9-DS models, irrespective of the wave steepness and screen porosity.

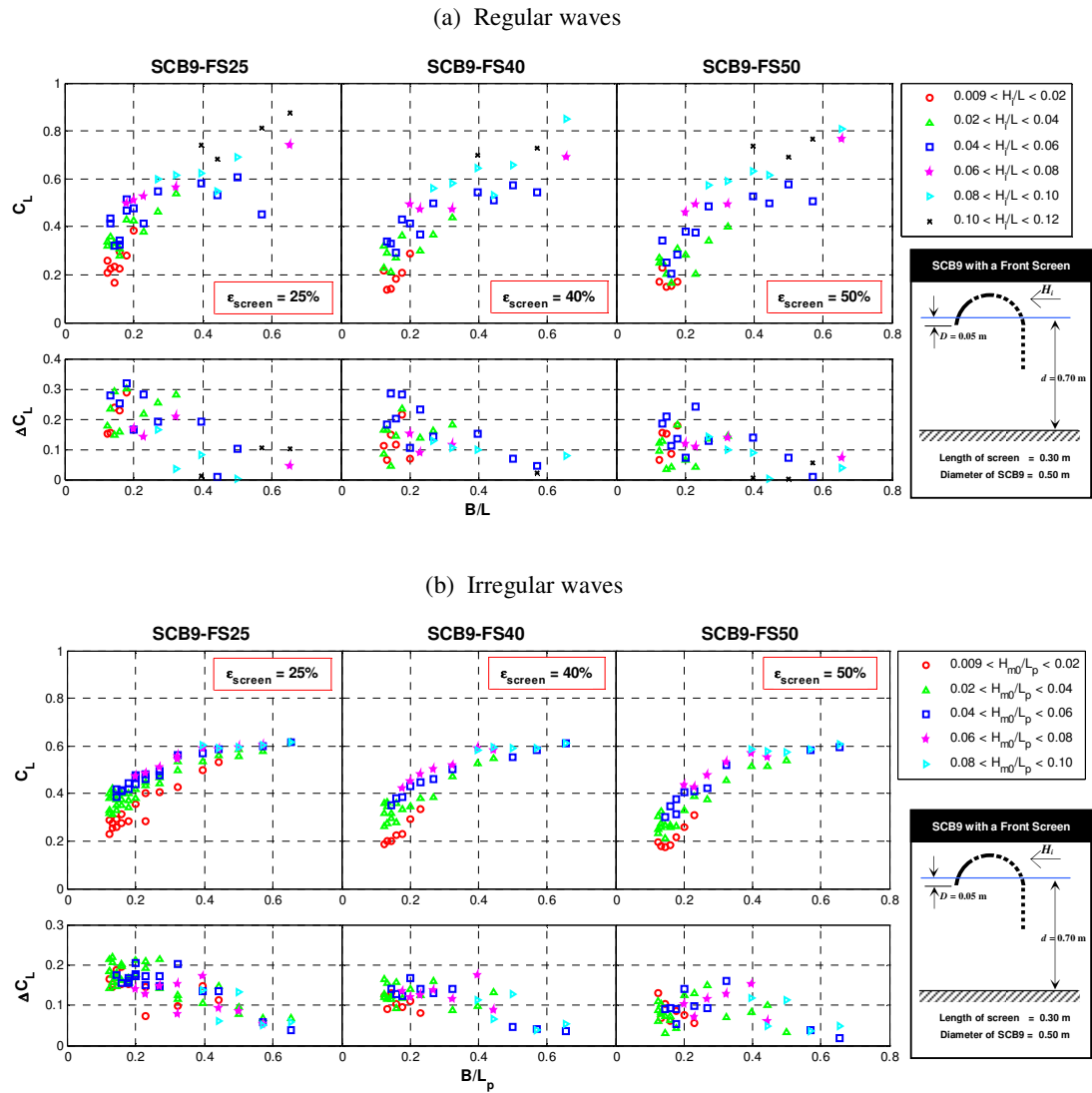


Figure 6.11: C_L and ΔC_L of the SCB9-DS models in regular and irregular waves

For both sea states, energy loss generated by the models is largely controlled by the wave steepness, *i.e.* waves of higher H/L range tend to attain higher C_L values. Besides, C_L of the test models also increases with a decrease in the screen porosity. The ΔC_L for the front screen (FS), rear screen (RS) and double screens (DS) achieves higher values at lower range of B/L in regular and irregular waves, entailing that the screens are particularly effective in dissipating the energy of longer period waves regardless of the screen porosity. The maximum ΔC_L values recorded for the FS25, RS25 and DS25 models in regular waves are 0.32, 0.42 and 0.57, respectively, and in irregular waves, 0.22, 0.30 and 0.43, respectively. These values also suggest that the DS25 model is the most optimum screen configuration for energy dissipation among the tested screens, and the screen is particularly useful when dealing with longer period waves that the SCB9 model fails to stop.

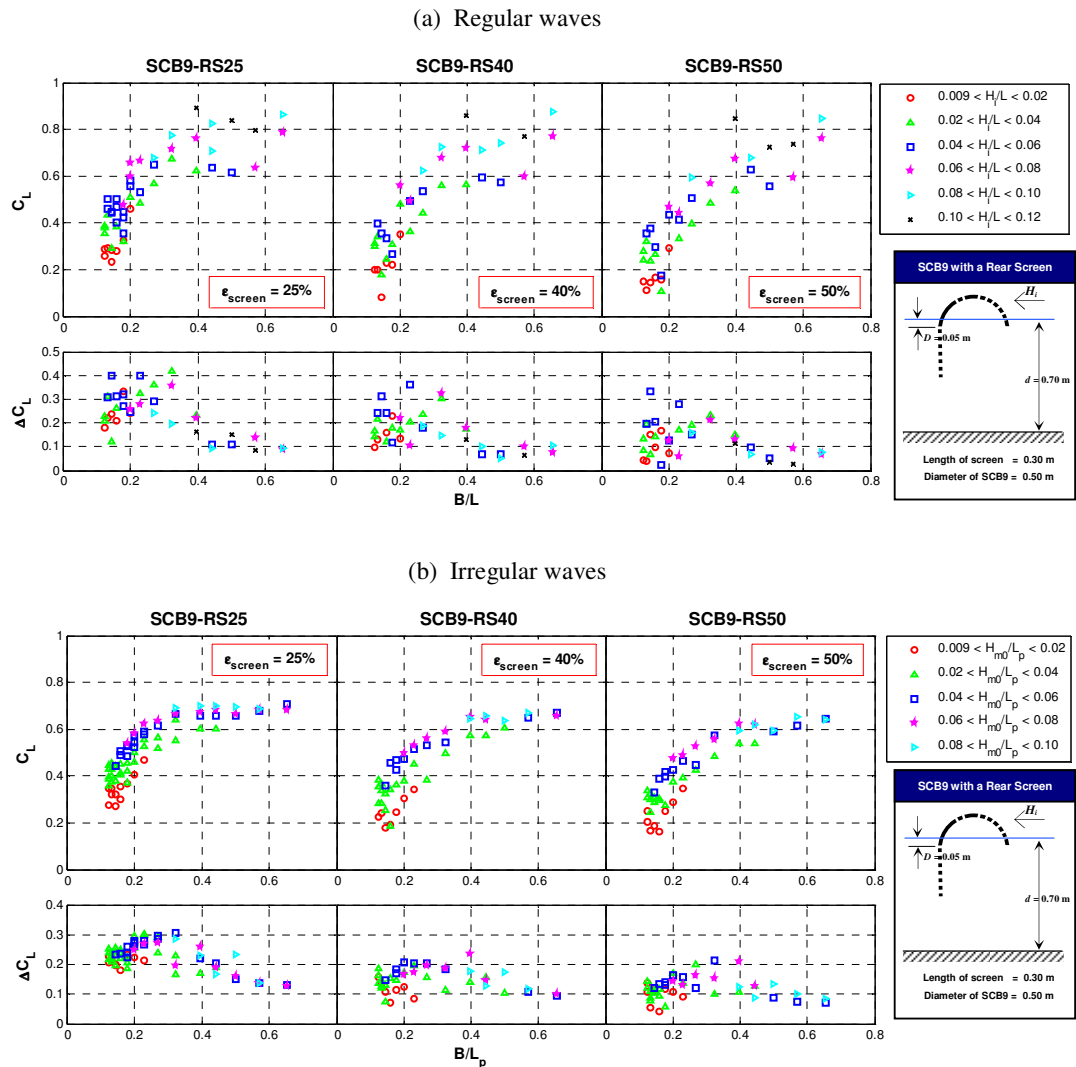


Figure 6.12: C_L and ΔC_L of the SCB9-RS models in regular and irregular waves

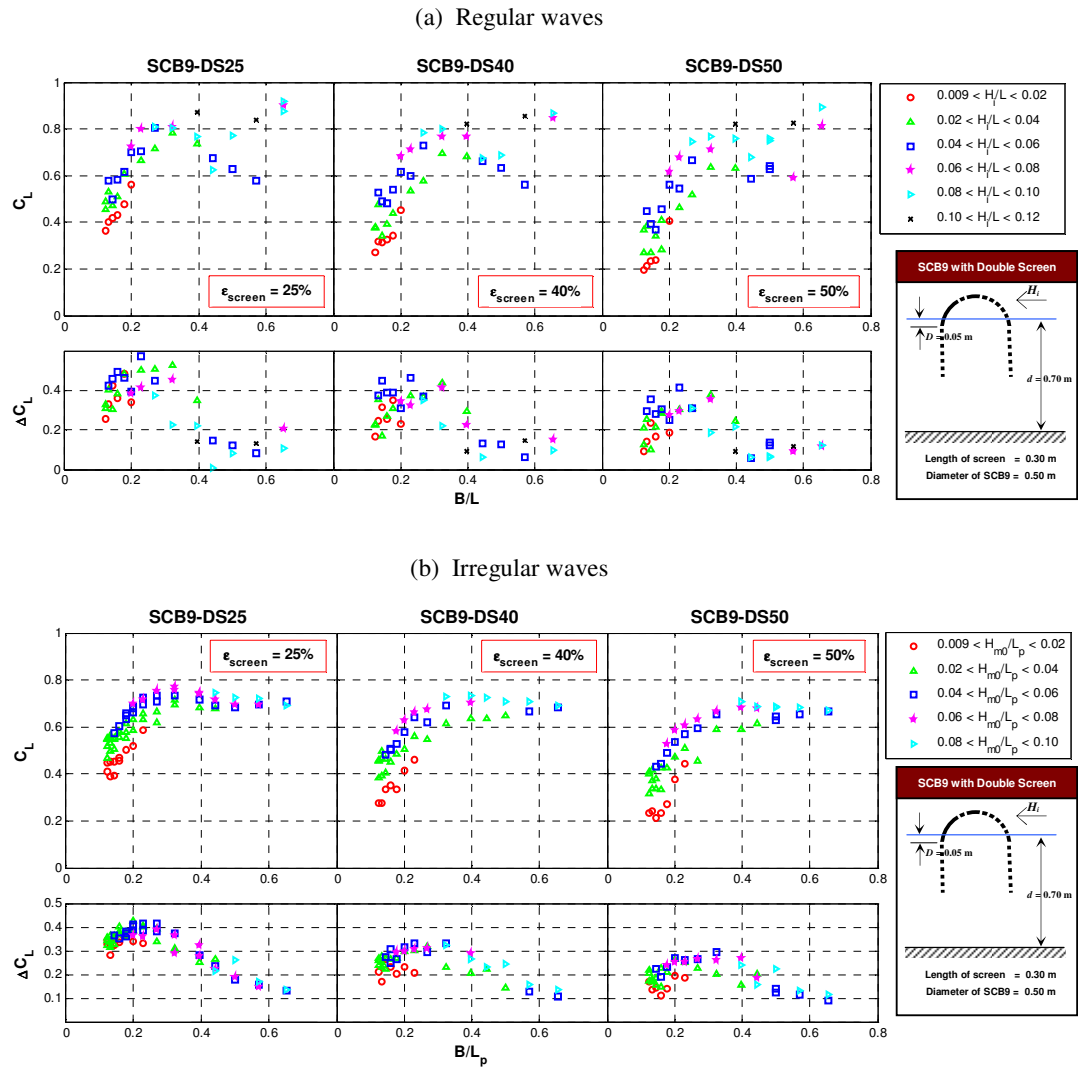
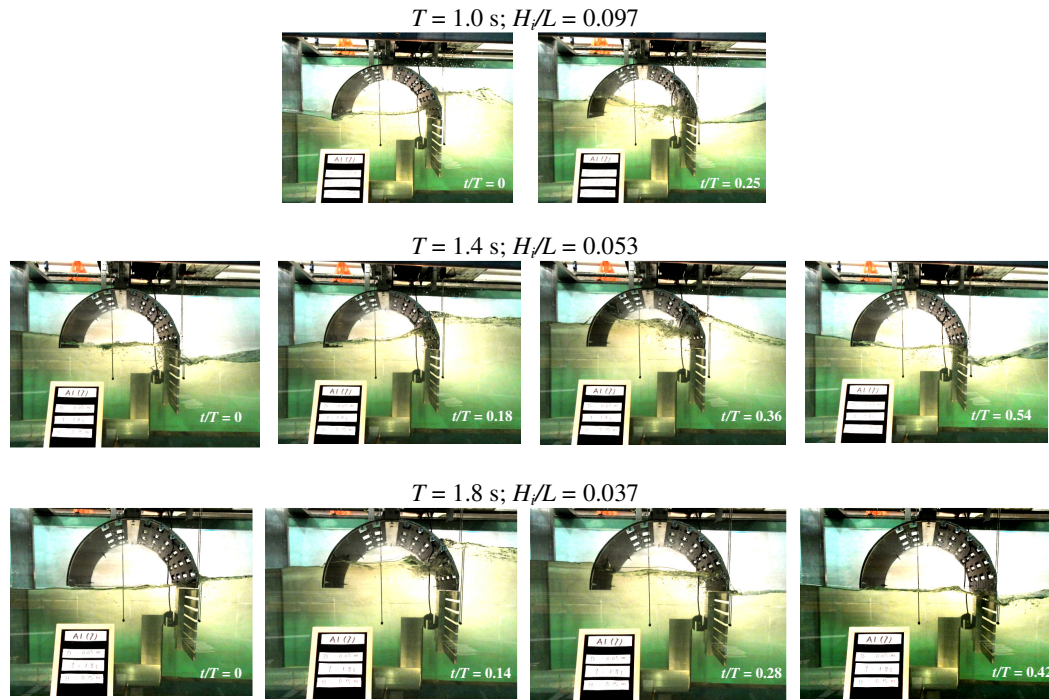


Figure 6.13: C_L and ΔC_L of the SCB9-DS models in regular and irregular waves

Figures 6.14 to 6.16 show a sequence of wave interaction with the SCB9-FS, SCB9-RS and SCB9-DS models subjected to regular waves of $T = 1.0$ s, 1.4 s and 1.8 s and $H_i = 0.15$ m. It is observed from Figure 6.14 that large amount of wave disturbance occurred at the front face of the SCB9-FS models. These include wave run-up, water infiltration and formation of eddies around the perforated front wall. Only small amount of disturbance induced by the upper tip of the screen(s) was detected under the wave troughs; whilst the flow behaviour at the deeper extension of the wave screen was hardly identified by using the still cameras during the experiment. These wave responses are directly related to energy dissipation by the models and the intensity becomes less when the structures are exposed to larger period waves or if the screen porosity is larger. For the SCB9-RS models as shown in Figure 6.15,

(a) SCB9-FS25 ($\epsilon_{\text{screen}} = 25\%$)



(b) SCB9-FS50 ($\epsilon_{\text{screen}} = 25\%$)

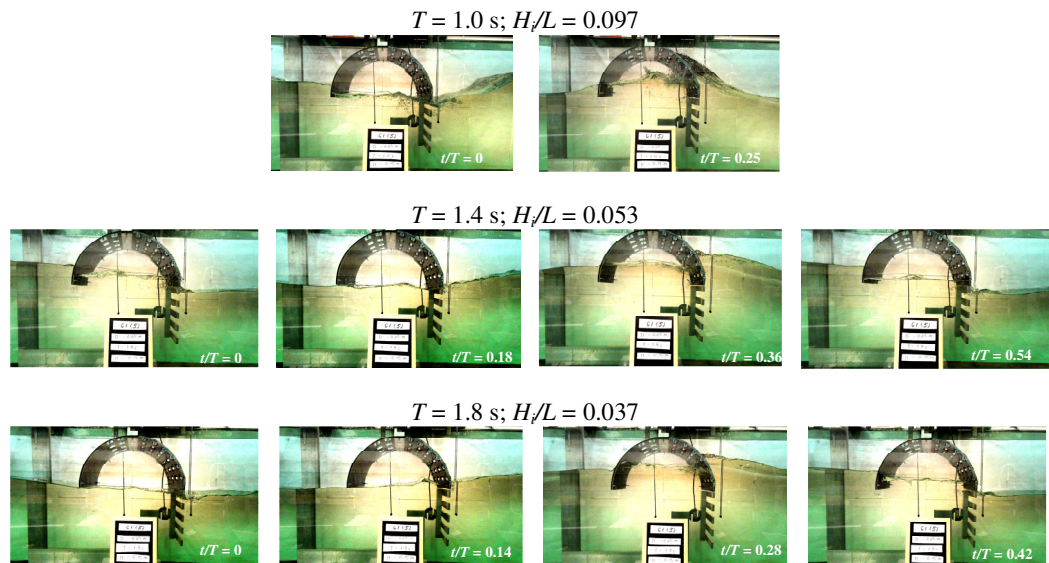
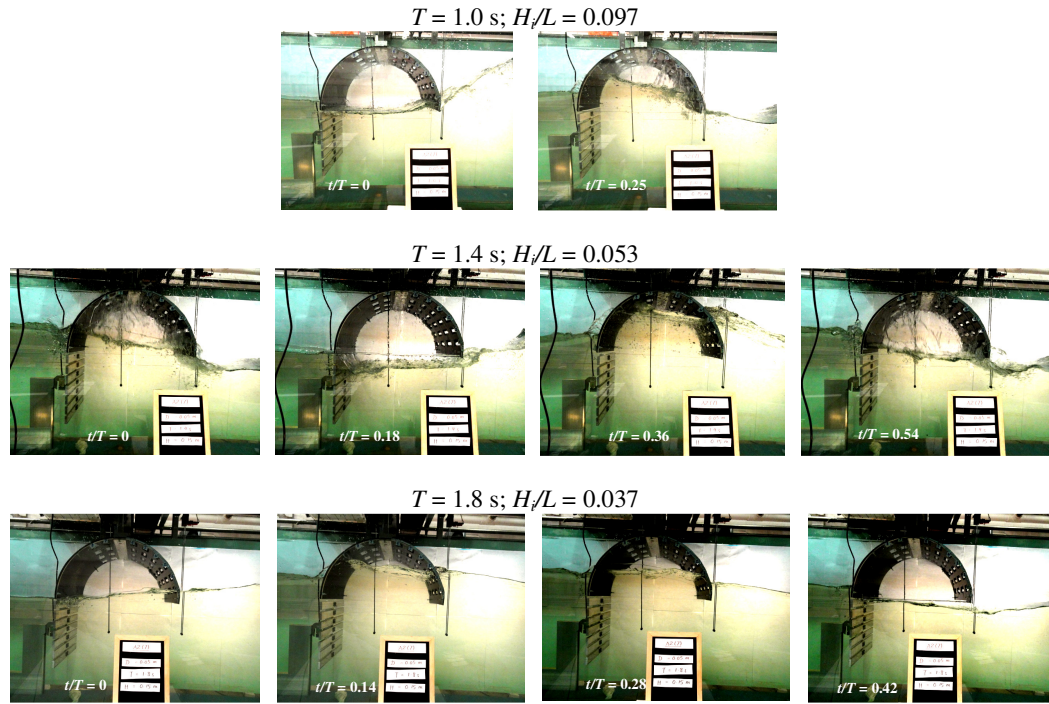


Figure 6.14: Wave interaction with SCB9-FS25 and SCB9-FS50 models in regular waves at $T = 1.0 \text{ s}, 1.2 \text{ s}, 1.8 \text{ s}$ and $H_i = 0.15 \text{ m}$. Note that the incident waves propagated from the left of the test model

(a) SCB9-RS25 ($\epsilon_{screen} = 25\%$)



(b) SCB9-RS50 ($\epsilon_{screen} = 50\%$)

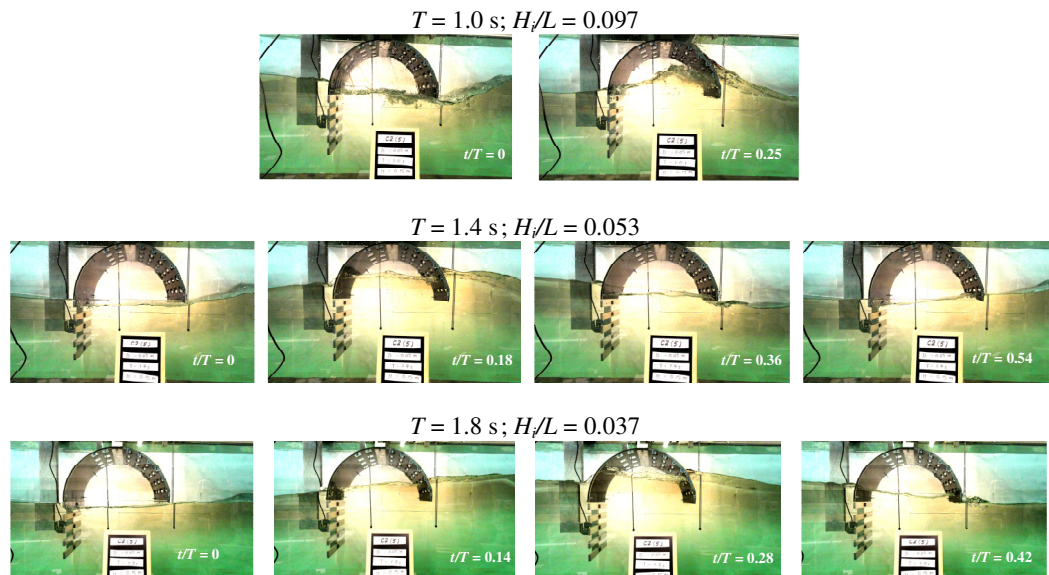
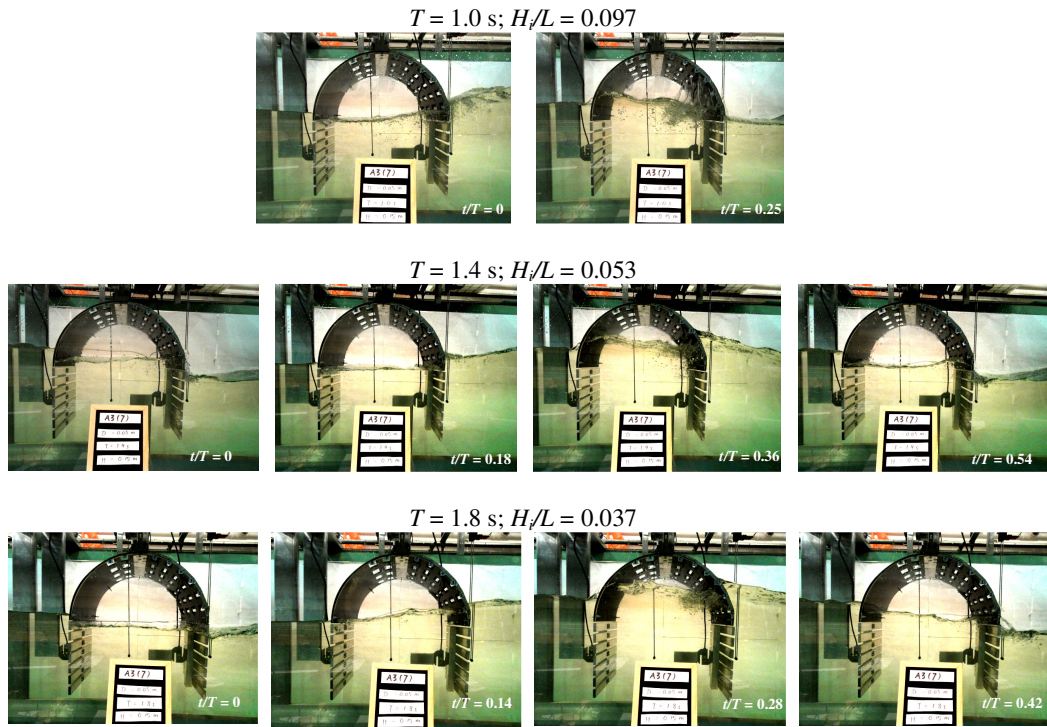


Figure 6.15: Wave interaction with SCB9-RS25 and SCB9-RS50 models in regular waves at $T = 1.0 \text{ s}, 1.2 \text{ s}, 1.8 \text{ s}$ and $H_i = 0.15 \text{ m}$. Note that the incident waves propagated from the left of the test model

(a) SCB9-DS25 ($\epsilon_{screen} = 25\%$)



(b) SCB9-DS50 ($\epsilon_{screen} = 50\%$)

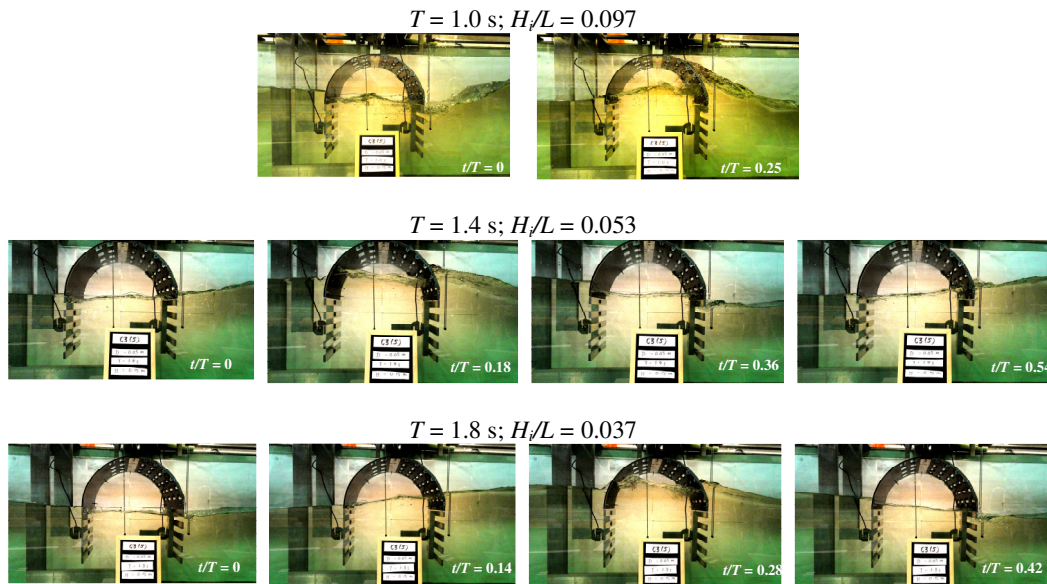


Figure 6.16: Wave interaction with SCB9-DS25 and SCB9-DS50 models in regular waves at $T = 1.0 \text{ s}, 1.2 \text{ s}, 1.8 \text{ s}$ and $H_i = 0.15 \text{ m}$. Note that the incident waves propagated from the left of the test model

it is seen that both front and rear parts of the breakwater played roles in wave interception, *i.e.* apart from energy dissipation at the front curved wall as mention earlier the reverted flow from the rear wall set water in turbulence in the chamber, through which greater loss in wave energy was resulted. On the other hand, wave activity in the chamber of the SCB9-DS models (see Figure 6.16) seems to be less aggressive due to wave protection by the frontal barrier (*i.e.* the front curved wall of the SCB9 and the front wave screen); and the waves were effectively intercepted by the front and rear parts of the structure.

6.3.4 Wave Climate in Front of the Breakwater – C_F

Wave climate in front of the SCB9-FS, SCB9-RS and SCB9-DS models is characterised using C_F and the values are presented in Figures 6.17 to 6.19 for regular and irregular waves.

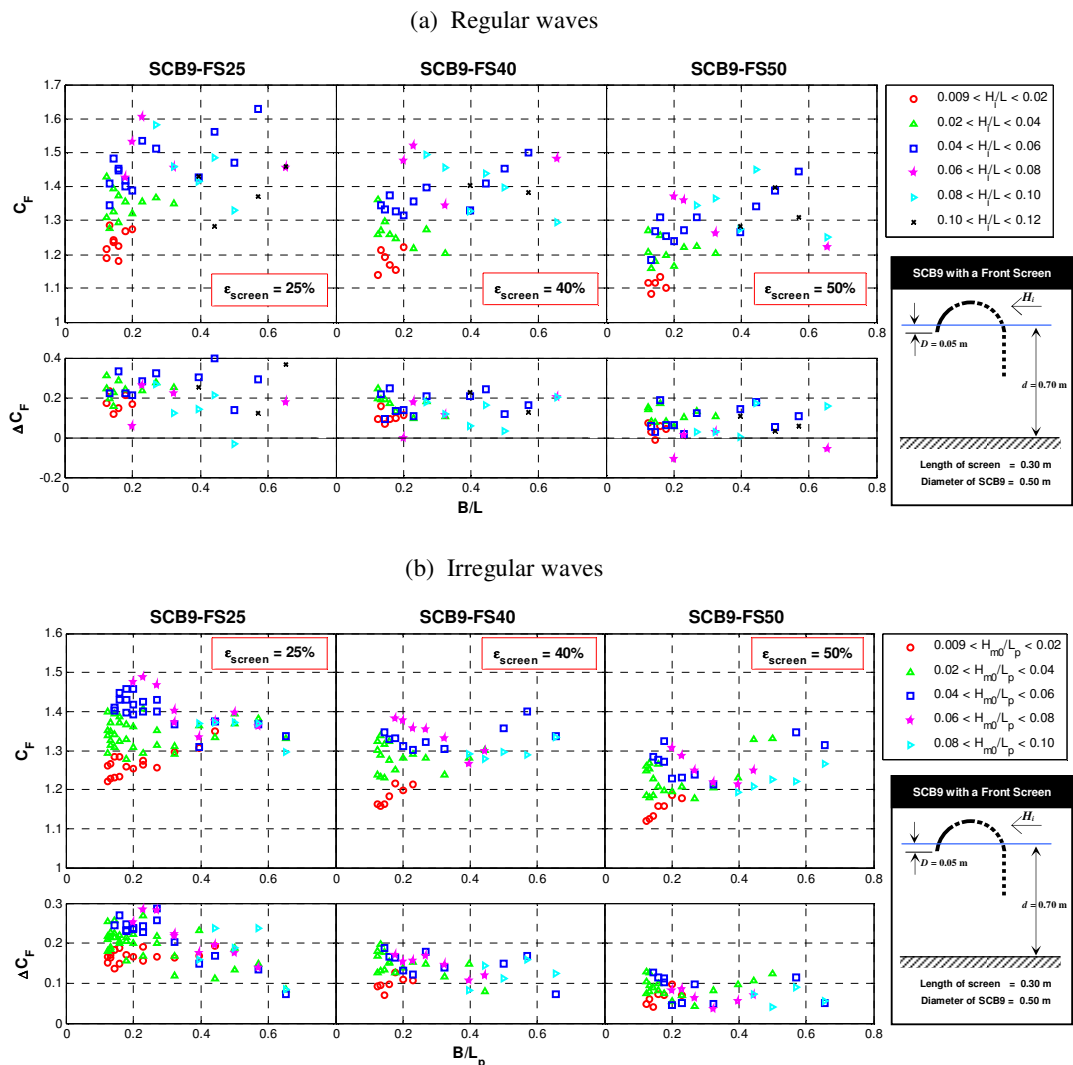


Figure 6.17: C_F and ΔC_F of the SCB9-FS models in regular and irregular waves

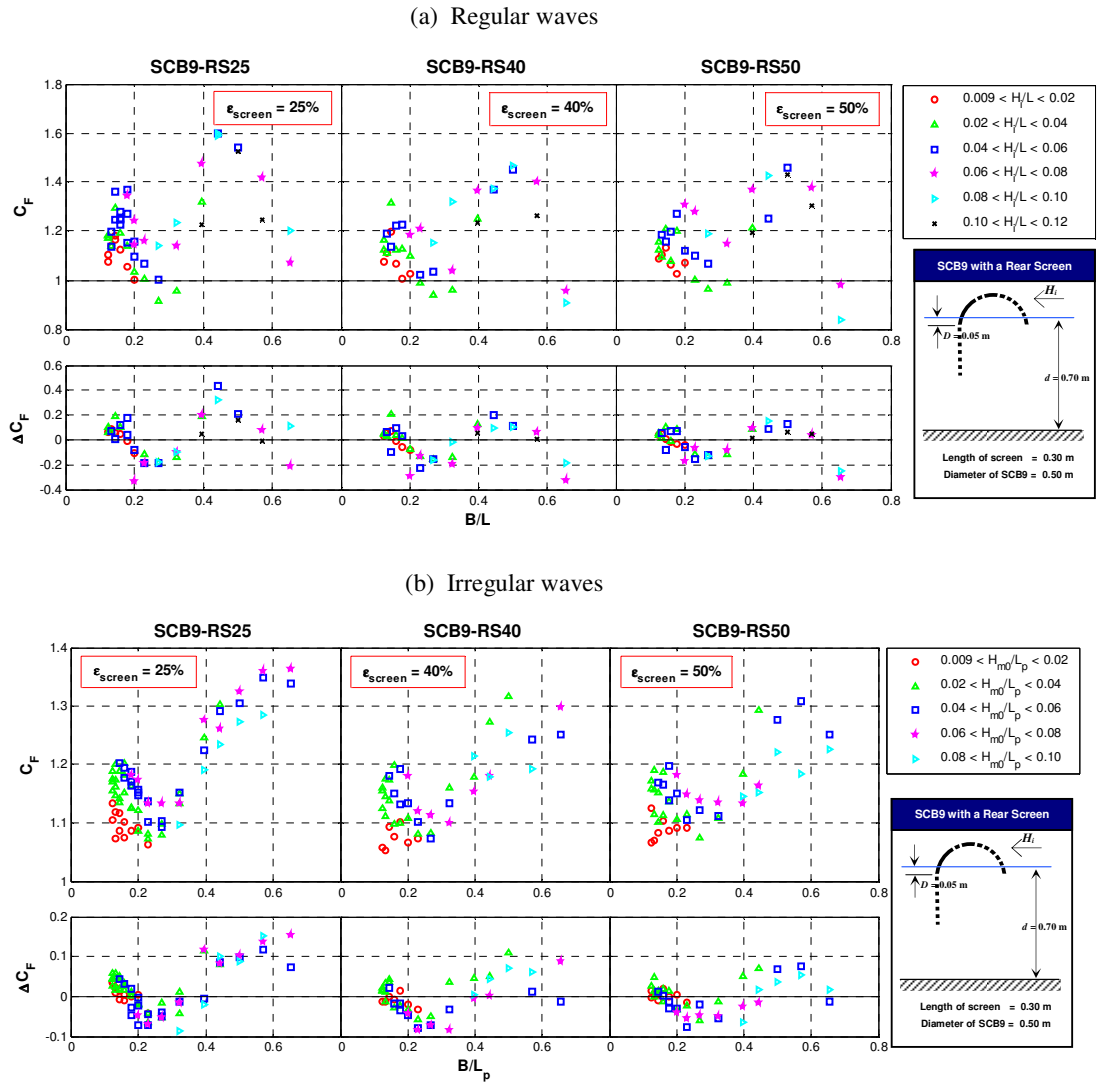


Figure 6.18: C_F and ΔC_F of the SCB9-RS models in regular and irregular waves

The majority of the C_F values are above unity due to increased wave activity just in front of the test models. In general, they fluctuate in irregular patterns as B/L increases. At this point, emphasis is given to the change of wave climate caused by the wave screens, which is quantified in terms of ΔC_F . Maximum ΔC_F added to the corresponding C_F of the SCB9 model in any test cases is no more than 0.4 (equivalent to increment of wave activity by 40%) regardless of their screen configuration and porosity. It can be seen that the ΔC_F values of the FS and DS models are not affected by B/L as much as those of the SCB9-RS model. The majority of the ΔC_F values for the FS and DS models are above zero, indicating that the presence of the screen causes amplification of wave activity in front of the test models. For

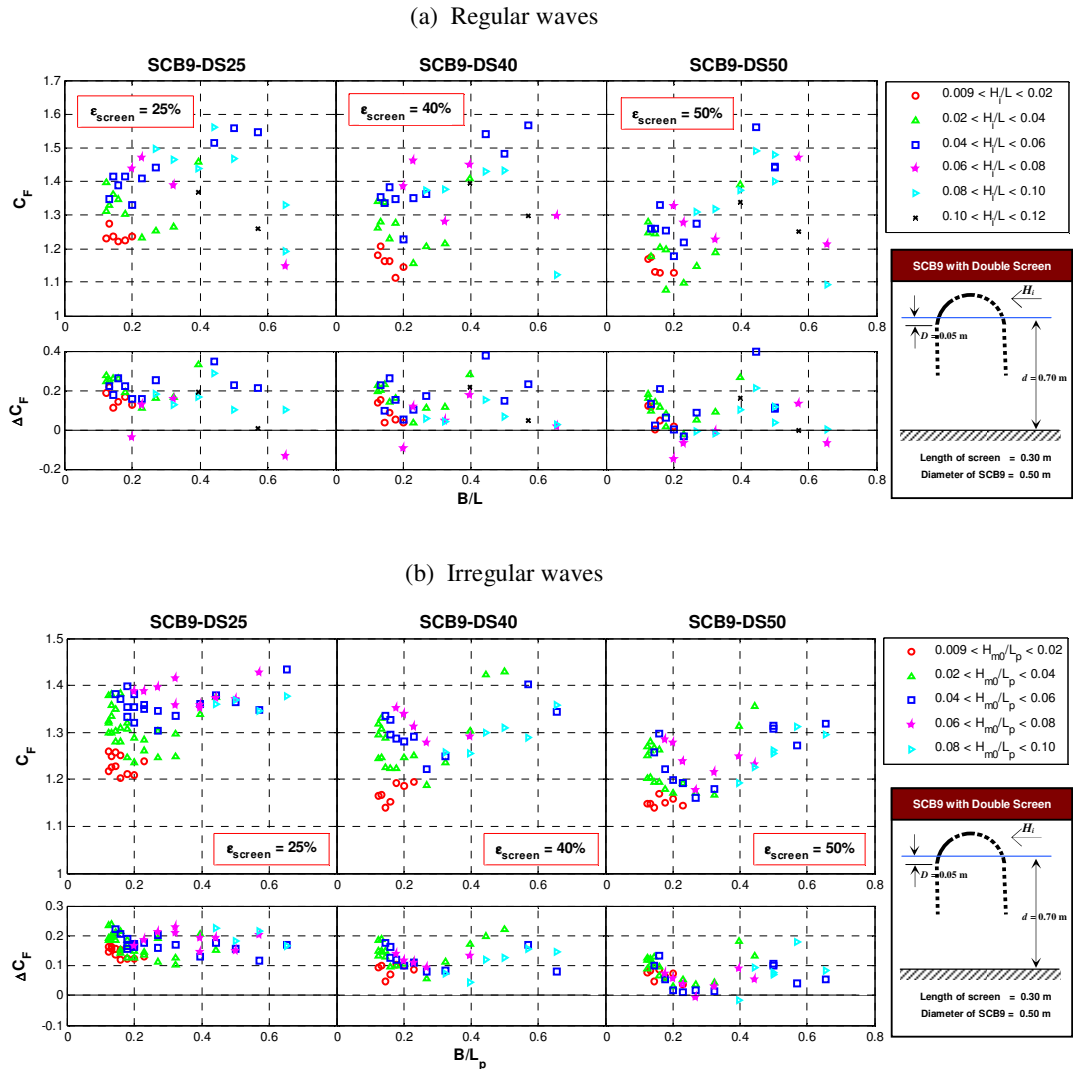


Figure 6.19: C_F and ΔC_F of the SCB9-DS models in regular and irregular waves

the RS models (see Figure 6.18), the ΔC_F seems to fluctuate uniformly about the zero reference line as B/L increases, such that waves build up greater than the incident wave heights at $B/L < 0.18$ and $0.37 < B/L < 0.6$.

Based on the C_F response of the SCB9-FS, SCB9-RS and SCB9-DS models, the waves build-up in front of the SCB9-FS and SCB9-DS models are regarded as significant, with the C_F reaching as high as 1.6 for $\epsilon_{screen} = 25\%$. This amount of wave agitation in front of the breakwaters is acceptable provided that the structures are not accessible to the public due to safety concerns. On the other hand, the wave climate in front of the SCB9-RS models is comparatively mild due to large transmission of waves into the chamber by the limited draft

of the SCB9 model. It is also observed that the characteristic performance of the C_F for the test models somewhat resembles that of the C_R (see Figures 6.8 – 6.10), implying that the wave climate in front of the models may be partly controlled by the reflected waves. The other affecting factor contributing to the water level variation in front of the breakwaters is the water build-up induced by the frontal barrier of the model.

6.3.5 Wave Climate in the Breakwater Chamber – C_C

Wave agitation behaviour in the chamber of the SCB9-FS25, SCB9-FS40 and SCB9-FS50 models for regular and irregular wave conditions is demonstrated in Figures 6.20 to 6.22. The intensity of the wave climate is indicated by C_C . A C_C of greater than unity indicates wave amplification in the interference chamber and vice versa.

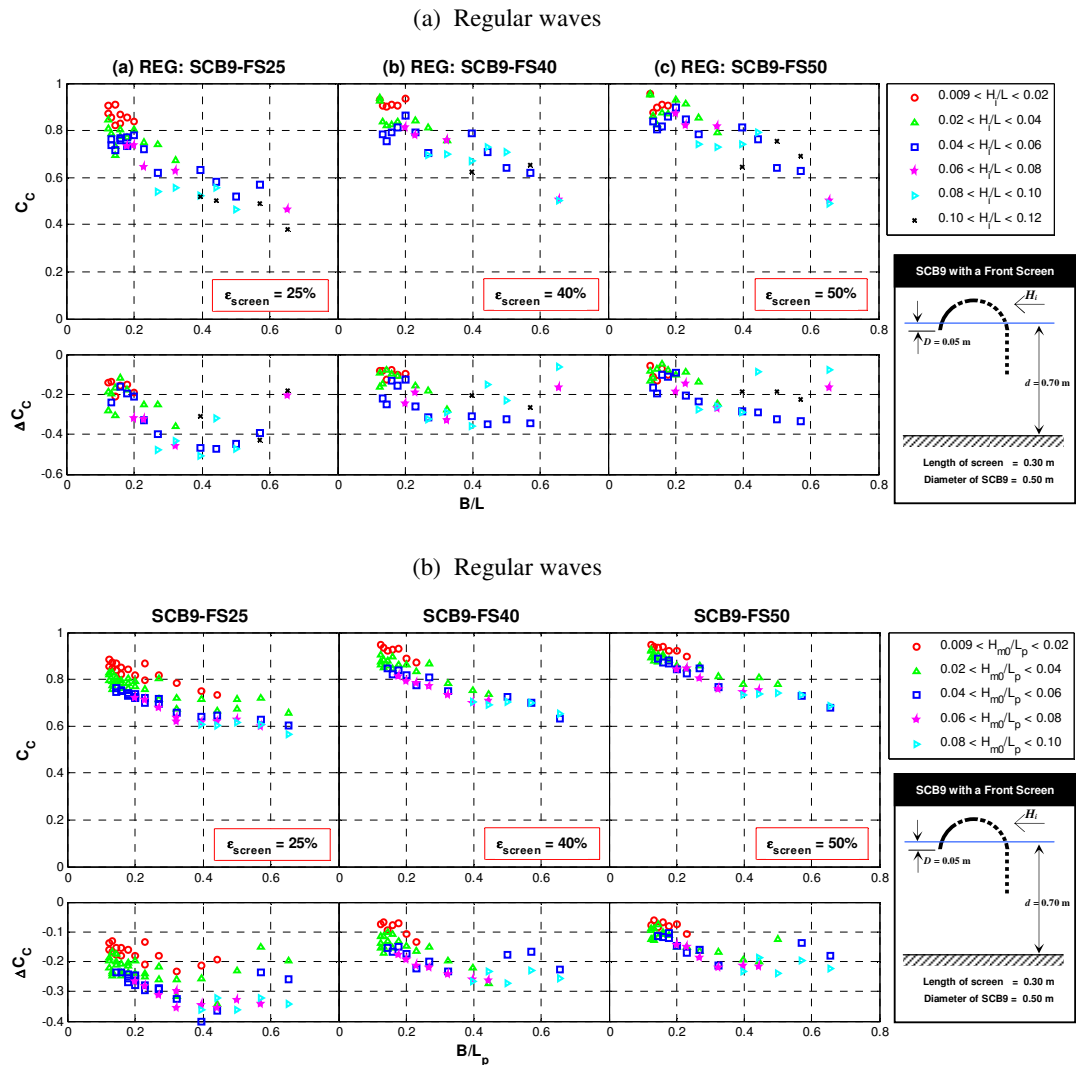


Figure 6.20: C_C and ΔC_C of the SCB9-FS models in regular and irregular waves

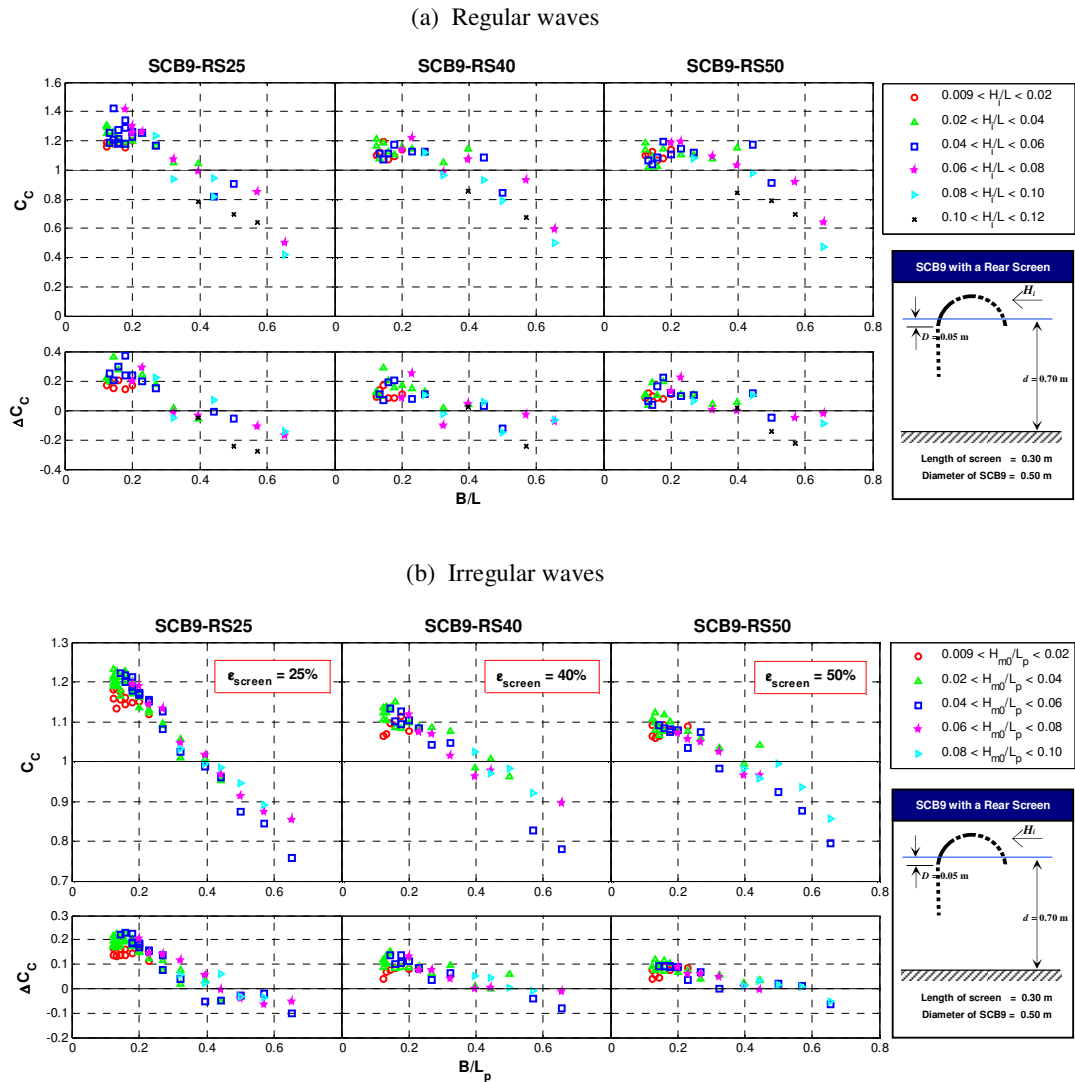


Figure 6.21: C_C and ΔC_C of the SCB9-RS models in regular and irregular waves

The C_C characteristics of the test models are somewhat in agreement, whereby they decrease drastically with an increase in B/L and they are less affected by the wave steepness. For the SCB9-FS models, the C_C values are consistently below unity (see Figure 6.20), indicating that wave activity in the chamber is less aggressive. On the other hand, mixed wave behaviour is seen in the chamber of the SCB9-RS models (see Figure 6.21), *i.e.* $C_C > 1$ for $B/L < 0.4$ and $C_C < 1$ for $B/L > 0.4$. More aggressive wave activity (with a maximum C_C of 1.42 in regular waves and 1.26 in irregular waves) is observed when the models are subjected to longer period waves. The rear screen acts as a partial wave reflector and thus blocks the wave flow in front of the screen, resulting in higher water level agitation in the chamber. Similar observation is also obtained for the SCB9-DS models whereby the C_C just

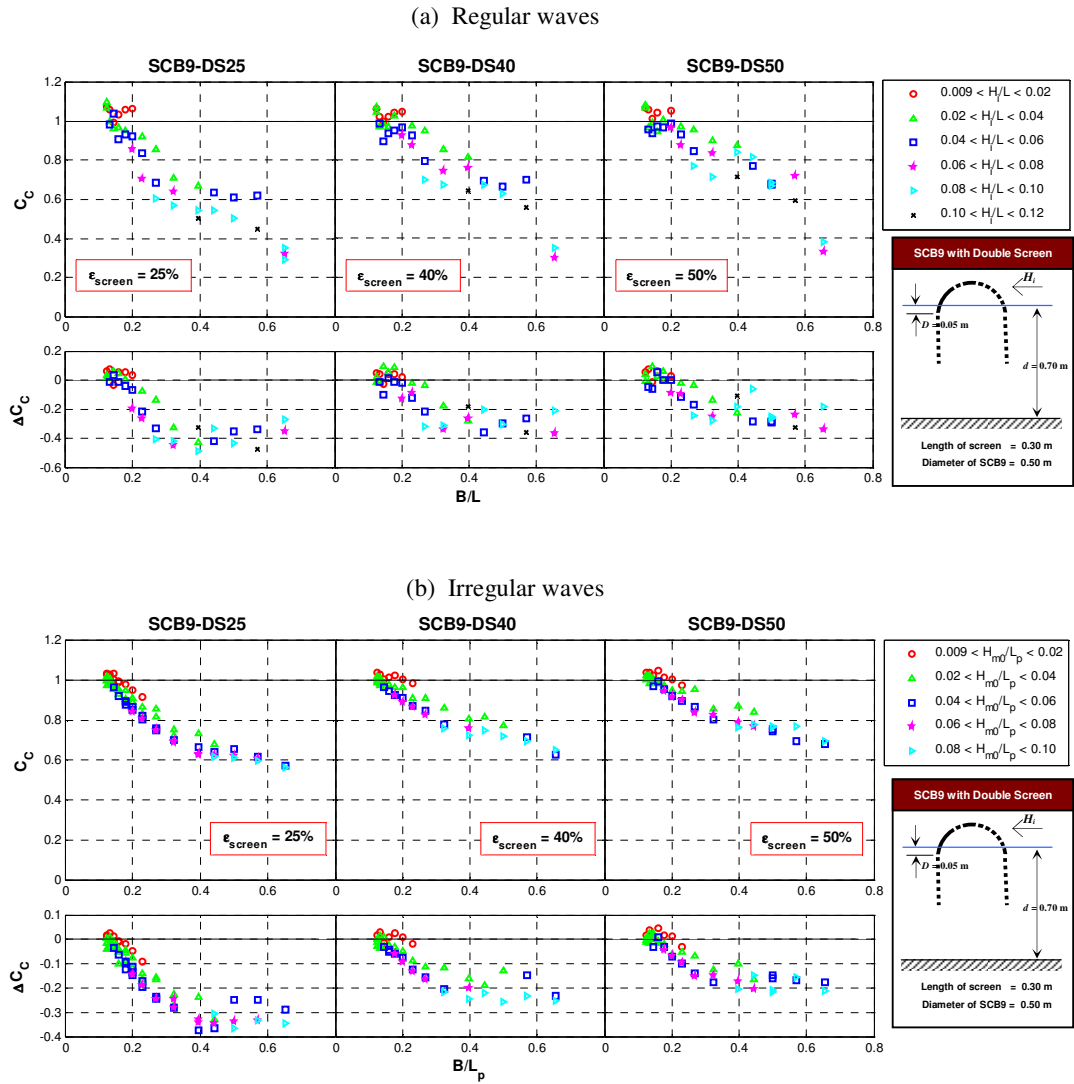


Figure 6.22: C_c and ΔC_c of the SCB9-DS models in regular and irregular waves

reach about 1 for $B/L < 0.2$ and $C_c < 1$ for $B/L > 0.2$, and the maximum C_c recorded is about 1.1 (see Figure 6.22).

The impact of the wave screens is reflected by the ΔC_c , in which a positive value indicates increment of wave activity in the interference chambers in comparison to the SCB9 model and vice versa. The ΔC_c values of the front screens of the SCB9-FS models are well below zero, and this explains the wave suppression in the chamber (see Figure 6.20). The larger the screen porosity, the smaller will be the screen effect on the ΔC_c . The variation of C_c for the SCB9-RS and SCB9-DS models is found to be in correspondence when compared to their

ΔC_C values as shown in Figures 6.21 and 6.22, indicating that the screens have a considerable effect on the wave climate in the interference chamber. The rear screen of the SCB9-RS25 models induced stronger wave activity in the chamber due to increased draft with more exposure area for wave attack. On the contrary, the double screens of the SCB9-DS25 model produced a calmer sea state with $\Delta C_C < 0$, in general, in comparison to the use of double screens of higher porosities due to supreme wave filtering ability of the frontal portion of the test model.

6.4 Optimisation of the Hydraulic Efficiency of the Breakwater: Evaluation

This research project aims to optimise the hydraulic efficiency of the SCB9 model by adding wave screens. It is hoped that the ultimate configuration of the breakwater would be able to withstand the longer period waves mainly by energy dissipation even in limited immersion depth. The previous section presented the overall hydraulic characteristics (in the forms of C_T , C_R , C_L , C_F and C_C) of the SCB9-FS, SCB9-RS and SCB9-DS models with $\varepsilon_{screen} = 25\%$, 40% and 50%, whereby the ranges for the respective test models are summarised in Table 6.3. The average efficiency of the screens, which influences the overall performance of the breakwaters, is computed from the means of ΔC_T , ΔC_R , ΔC_L , ΔC_F and ΔC_C and the results are presented in Figure 6.23.

Figure 6.23 is useful for evaluating the performance of the wave screen when adopted as a supplementary structure for the SCB9 model. Here, it is clear that screen porosity is an important factor influencing the hydraulic performance of these filtering structures. Screens of lower porosities contribute to higher wave reflection and energy loss and consequently result in higher wave attenuation; and the wave climate at the front tends to be more severe than that in the interference chambers. Having said that, a wave screen with 25% porosity may be the most hydraulically efficient structure that could be introduced to the SCB9 model.

For single screen structures, the rear screen of the SCB9-RS models is hydraulically superior to that of the SCB9-FS models because it produces lower reflection of about 2% – 3%, higher energy dissipation of about 5% – 9% and higher wave attenuation of about 2% – 5%. The configuration of the SCB9-RS models is such that the wave crests first interact with the front wall of the SCB9 model and the troughs that are subsequently transmitted into the chamber get dissipated by the rear portion of the breakwater. As a result, the energy loss for the SCB9-RS models is particularly high. For SCB9-DS models, the double screen is shown

to be a better wave filter than the single screen models in terms of energy dissipation and wave attenuation. Even though the amount of wave reflection caused by the double screens is relatively high, the total C_R for the SCB9-DS models is still within acceptable limits particularly in longer period wave field (see Figure 6.10), with $C_R < 0.4$ at $B/L < 0.4$ for both sea states. It is also learnt that the waves in the chamber of the SCB9-DS models are not greatly dampened by the breakwater as larger energy loss is usually facilitated by the aggressive wave climate in the chamber. As far as the screen configuration is concerned, the double screen is clearly shown to provide better hydraulic performance than the single screen.

Table 6.3: Variations of hydraulic coefficients for the SCB9-FS, SCB9-RS and SCB9-DS models in regular and irregular waves

(a) Regular waves

	C_T		C_R		C_L		C_F		C_C	
	Min	Max	Min	Max	Min	Max	Min	Max	Min	Max
SCB9-FS25	0.27	0.89	0.14	0.59	0.41	0.94	1.18	1.63	0.38	0.91
SCB9-FS40	0.31	0.92	0.11	0.45	0.37	0.92	1.14	1.52	0.50	0.94
SCB9-FS50	0.36	0.91	0.08	0.48	0.38	0.90	1.09	1.45	0.49	0.96
SCB9-RS25	0.29	0.86	0.13	0.48	0.48	0.95	0.92	1.60	0.42	1.42
SCB9-RS40	0.31	0.95	0.11	0.46	0.29	0.94	0.91	1.47	0.50	1.22
SCB9-RS50	0.33	0.94	0.08	0.43	0.33	0.92	0.84	1.46	0.47	1.19
SCB9-DS25	0.16	0.78	0.15	0.57	0.60	0.96	1.15	1.56	0.29	1.10
SCB9-DS40	0.23	0.84	0.10	0.54	0.52	0.93	1.11	1.57	0.30	1.08
SCB9-DS50	0.25	0.89	0.08	0.49	0.44	0.94	1.08	1.56	0.33	1.09

(b) Irregular waves

	C_T		C_R		C_L		C_F		C_C	
	Min	Max	Min	Max	Min	Max	Min	Max	Min	Max
SCB9-FS25	0.44	0.86	0.18	0.44	0.48	0.79	1.22	1.49	0.60	0.89
SCB9-FS40	0.47	0.89	0.14	0.41	0.43	0.78	1.16	1.40	0.63	0.95
SCB9-FS50	0.50	0.90	0.13	0.39	0.42	0.77	1.12	1.35	0.68	0.95
SCB9-RS25	0.37	0.84	0.17	0.41	0.52	0.84	1.06	1.35	0.76	1.23
SCB9-RS40	0.42	0.89	0.14	0.39	0.42	0.82	1.05	1.32	0.78	1.15
SCB9-RS50	0.45	0.91	0.13	0.39	0.40	0.81	1.07	1.31	0.80	1.12
SCB9-DS25	0.29	0.76	0.19	0.46	0.62	0.88	1.20	1.43	0.57	1.04
SCB9-DS40	0.34	0.84	0.15	0.44	0.53	0.85	1.14	1.42	0.63	1.04
SCB9-DS50	0.38	0.87	0.14	0.43	0.46	0.83	1.14	1.36	0.68	1.05

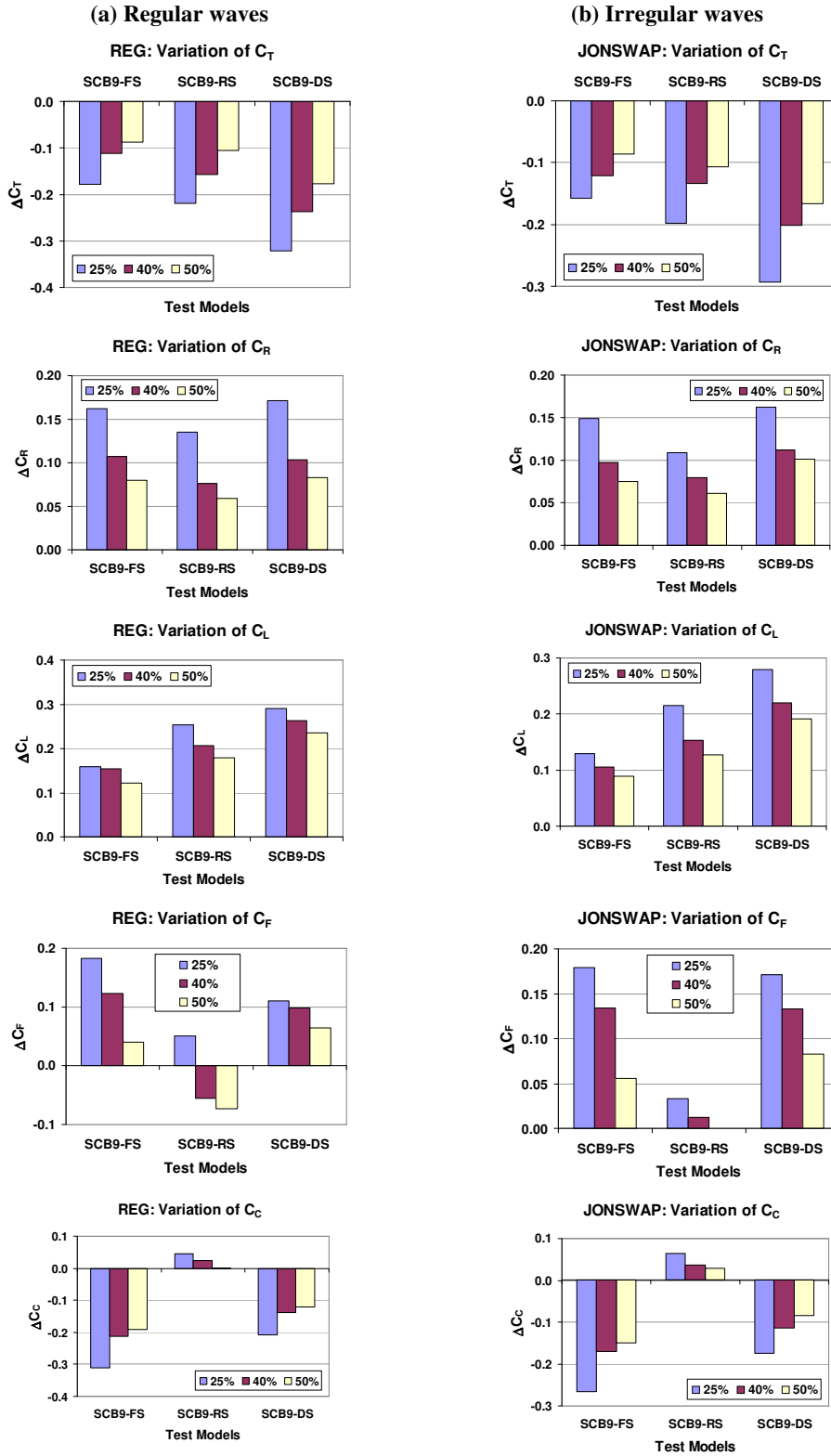


Figure 6.23: Mean variations of the hydraulic coefficients for the SCB9-FS, SCB9-RS and SCB9-DS models of different screen porosities in regular and irregular waves

Taking both screen configuration and the porosity into consideration, the double screen of 25% porosity (DS25) is recommended as the most viable supplementary structure to the SCB9 model. This composite model – SCB9-DS25 is a highly dissipative structure and particularly effective in attenuating the longer period waves. Alternatively, the SCB9-RS25 is also suggested if a single screen system is preferable. It is important to mention that these findings are valid provided the structure is immersed in a limited depth. The hydraulic characteristics of the SCB9-DS25 and SCB9-RS25 models in deeper immersion are explored in Chapter 7.

6.5 Horizontal Wave Loadings on the SCB9 model with Wave Screens

Horizontal wave forces were measured individually on the SCB9 model, the front and rear screens of 25%, 40% and 50% porosities using well-calibrated load cells as discussed in Section 4.8. The measured forces were divided into (i) the forces under the wave crests, F^+ (also named as positive forces and seaward/offshore forces); and (ii) the forces under the wave troughs, F^- (also named as negative forces and landward/onshore forces). For regular waves, these forces were computed from the average of their crest or trough peaks. For irregular waves, the forces were represented by the average of the highest one-third of the measured data under the wave crests or troughs. Figures 6.24 to 6.26 present the relationship between the horizontal wave forces (acting on the SCB9, FS and RS respectively) and the incident wave heights for the SCB9-FS, SCB9-RS and SCB9-DS models of different screen porosities in regular and irregular waves. The figures also demonstrate the correspondence between F^+ and F^- for the respective breakwater elements, *i.e.* SCB9, FS and RS. For illustration purposes, horizontal forces under the wave crests acting on the SCB9 model is denoted as F_{SCB9}^+ and those caused by wave troughs is denoted as F_{SCB9}^- . Likewise, the forces acting on the FS and RS models are denoted as F_{FS} and F_{RS} , respectively. The type of forces is indicated by the sign conventions shown in the annotations.

6.5.1 SCB9-FS models

Figure 6.24 shows the horizontal loading behaviour for the SCB9-FS models, whereby the blue rounded markers indicate the forces acting on the SCB9 model and the red squared markers indicate the forces acting on the FS models of different porosities. It is clear from the figure that the horizontal wave forces are directly proportional to the incident wave height in both sea states. For the SCB9 model, both F_{SCB9}^+ and F_{SCB9}^- are almost unaffected by the change of the porosity of the front screen; however, the increase of F_{SCB9}^+ is far more

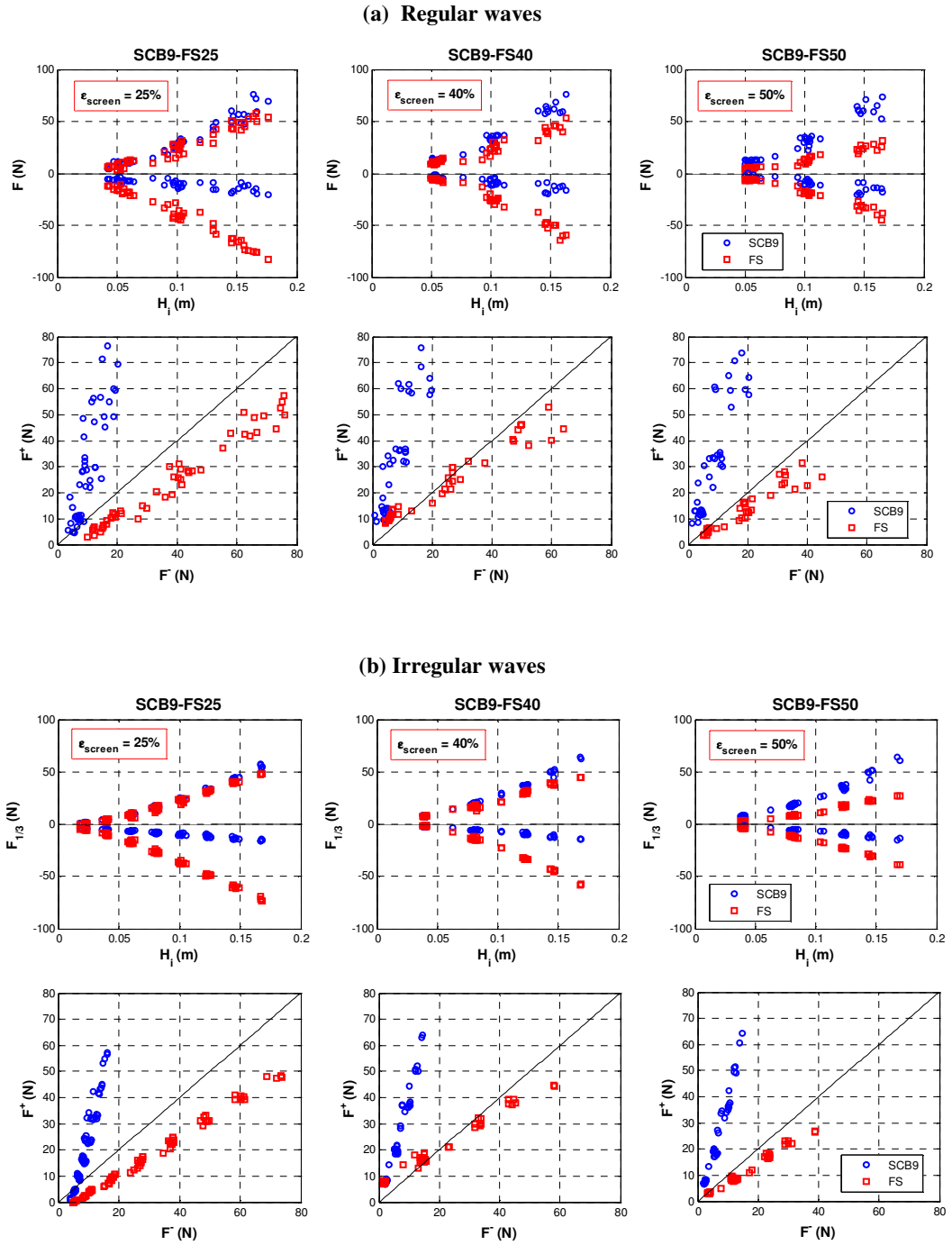


Figure 6.24: Measured horizontal wave forces on the SCB9-FS models in regular and irregular waves

rapid than that of F_{SCB9}^- for a given incident wave height. F_{SCB9}^+ is clearly proportional to F_{SCB9}^- as can be observed in the corresponding F^+ vs. F^- plots. Overall, these plots show a good linearity between the positive and negative forces. The values of F_{SCB9}^+ are nearly four times higher than their negative values for both sea conditions. These results are somewhat in agreement with findings by Goda and Kakizaki (1967), whereby at free surface the positive force acting on a vertical structure is maximum while the negative force is close to zero (see Figure 5.32).

For the front screens alone (FS models), which are represented by the red squared markers in Figure 6.24, the wave screen porosity appears to be an important factor to the horizontal forces, such that the forces reduce with the increasing screen porosity. Further, F_{FS}^- is found to be higher than F_{FS}^+ by a factor of approximately 1.3 regardless of the screen porosity and sea states. The observation of $|F_{FS}^-| > |F_{FS}^+|$ can be explained by the fact that the waves that run down the SCB9 model produce pressure forces on the water in front of the screen such that the water particles do not move in elliptical motion like the water particles in front of the vertical breakwater; hence, the water particle velocity in the opposite direction becomes greater. This phenomenon was captured by Wang (2006) for a bottom seated semicircular breakwater in the presence of pulsating waves. On the other hand, Goda and Kakizaki (1967) and McConnell *et al.* (1999) observed that for vertical wall structures the highest $|F^-|$ occurred at a small distance below the free surface as shown in Figure 5.32.

6.5.2 SCB9-RS models

Figure 6.25 presents the response of the SCB9-RS models to the horizontal wave loadings in regular and irregular waves. The overall force behaviour of the models is comparable to that of the SCB9-FS models except that the F_{SCB9}^+ exhibits higher values at larger wave height in both sea states. The force increment by F_{SCB9}^+ is mainly ascribed to the larger wave action in the chamber of the SCB9-RS models with large transmission of waves below the front wall of the SCB9 model. From the F^+ vs. F^- plots in Figure 6.25, the F_{SCB9}^+ for the tested models is about 6 times greater than the corresponding F_{SCB9}^- and the F_{FS}^- is larger than F_{FS}^+ by about 25% regardless of the sea conditions.

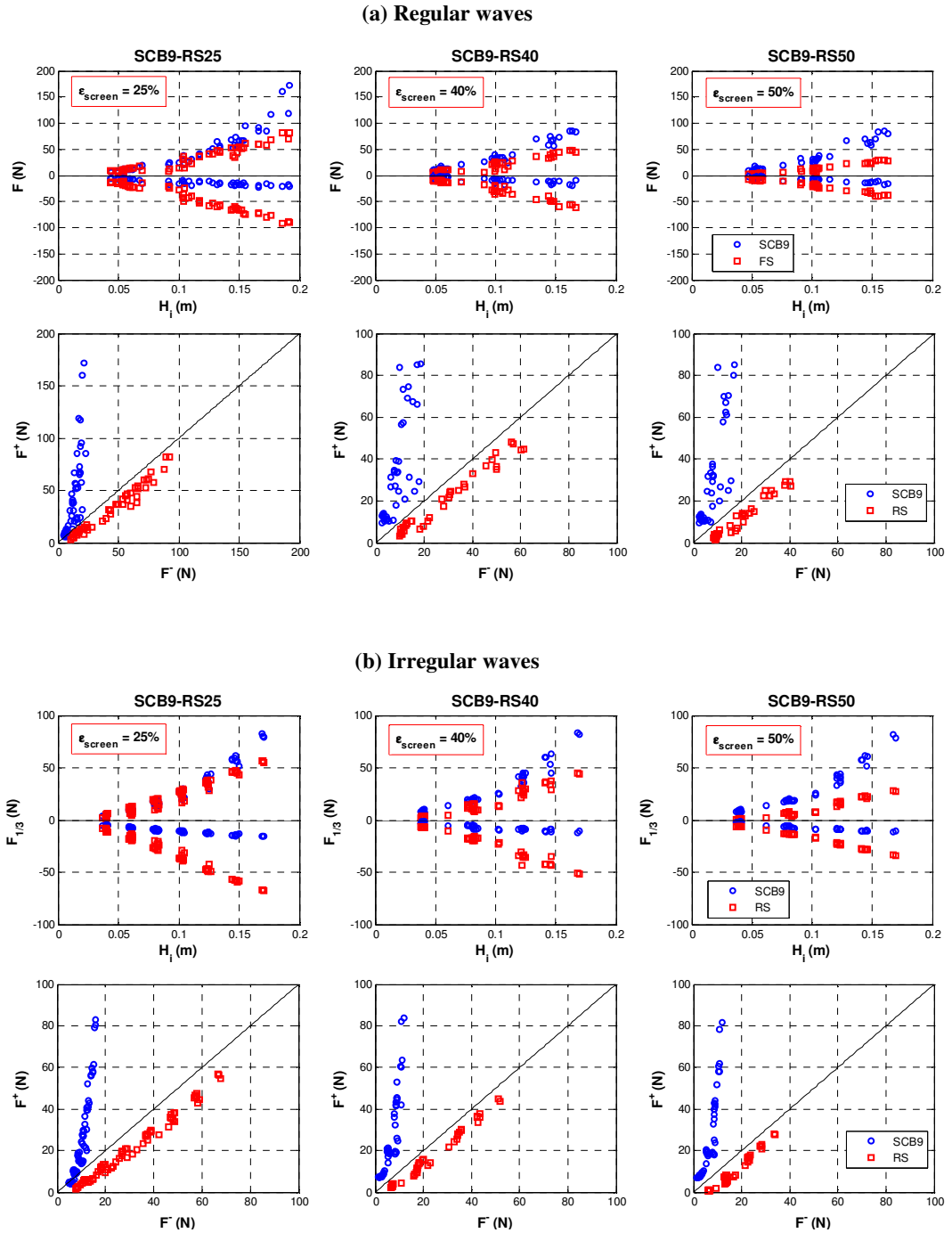


Figure 6.25: Measured horizontal wave forces on the SCB9-RS models in regular and irregular waves

6.5.3 SCB9-DS models

Horizontal forces exerted on the separate parts of the SCB9-DS models are shown in Figure 6.26. The force components for the SCB9 and the FS models are almost identical to those of the SCB9-FS models as exhibited in Figure 6.24. For the RS models of different porosities as represented by the green triangular markers, the scatter of the force data (*i.e.* F_{RS}^+ and F_{RS}^-) is principally due to the effect of wave period. They are obviously smaller than the forces acting on the front screens (*i.e.* F_{FS}^+ and F_{FS}^-) due to reduced wave activity in the interference chambers as shown in Figure 6.22. This shows that the front screens are subjected to more wave action than the rear screens. From the F^+ vs. F^- plots shown in Figure 6.26, the F^- for both front and rear screens appears to be higher than the F^+ due to the distortion of the water particles in front of the screens by the run-down waves from the SCB9 model.

6.5.4 Evaluation

The total horizontal loadings on the SCB9-FS, SCB9-RS and SCB9-DS models (*e.g.* the total F^+ acting on the SCB9-DS25 model is the sum of the F^+ acting on SCB9, FS and RS, respectively) are shown in Figure 6.27. The F^+ acting on the test models are generally higher than the corresponding F^- , whereby the major contribution to the F^+ is the force acting on the SCB9 model whereas for the F^- it originated from the screen(s). The SCB9-DS models are the most receptive to the horizontal wave forces due to the effect of double screens. For the SCB9 model with a single screen, the positive forces acting on the SCB9-FS models seem to be smaller than those on the SCB9-RS models; and the variation of the negative forces is insignificant. It is also observed from the figure that the total forces acting on the test models increase with the decrease in the screen porosity.

Emphasis is given herein to the SCB9-RS25 and SCB9-DS25 models, which have been described as hydraulically efficient breakwaters in Section 6.4. Even though the use of DS25 as a supplementary structure to the SCB9 model may incur higher total horizontal forces compared to a single screen of similar porosity, the improvement in hydraulic efficiency it provides is considerable (see Figures 6.1 and 6.2). The total horizontal forces under the wave crests and troughs acting on the SCB9-DS25 are almost equal where $F^+ \approx |F^-|$ as shown in Figure 6.27. Furthermore, excessive horizontal loading on the breakwater is usually not an issue since this can be addressed with careful engineering design in practice. Alternatively, the SCB9-RS25 is also recommended if the single screen option is preferable; however, the rear wall of the SCB9 must be carefully designed to against the excessive wave action.

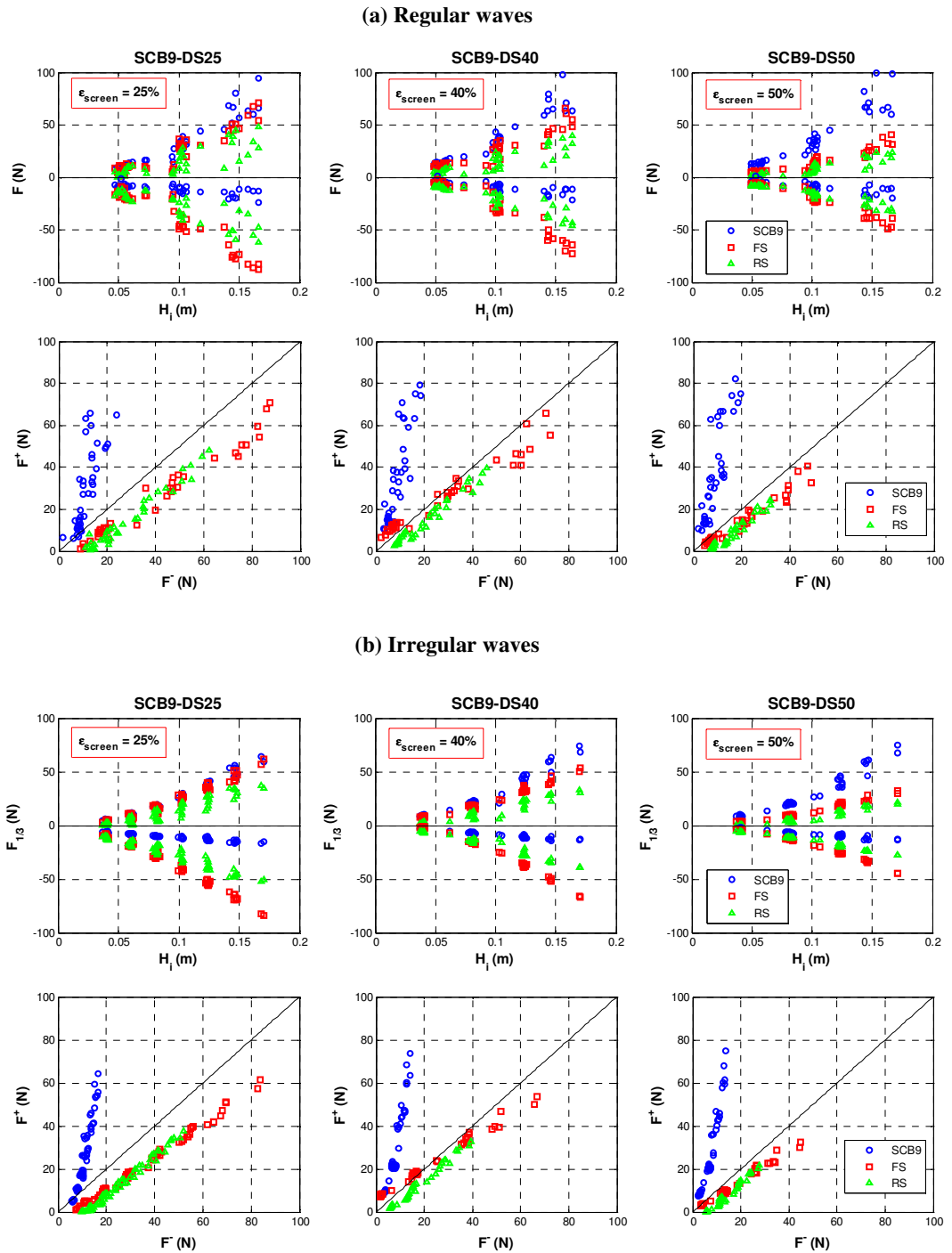


Figure 6.26: Measured horizontal wave forces on the SCB9-RS models in regular and irregular waves

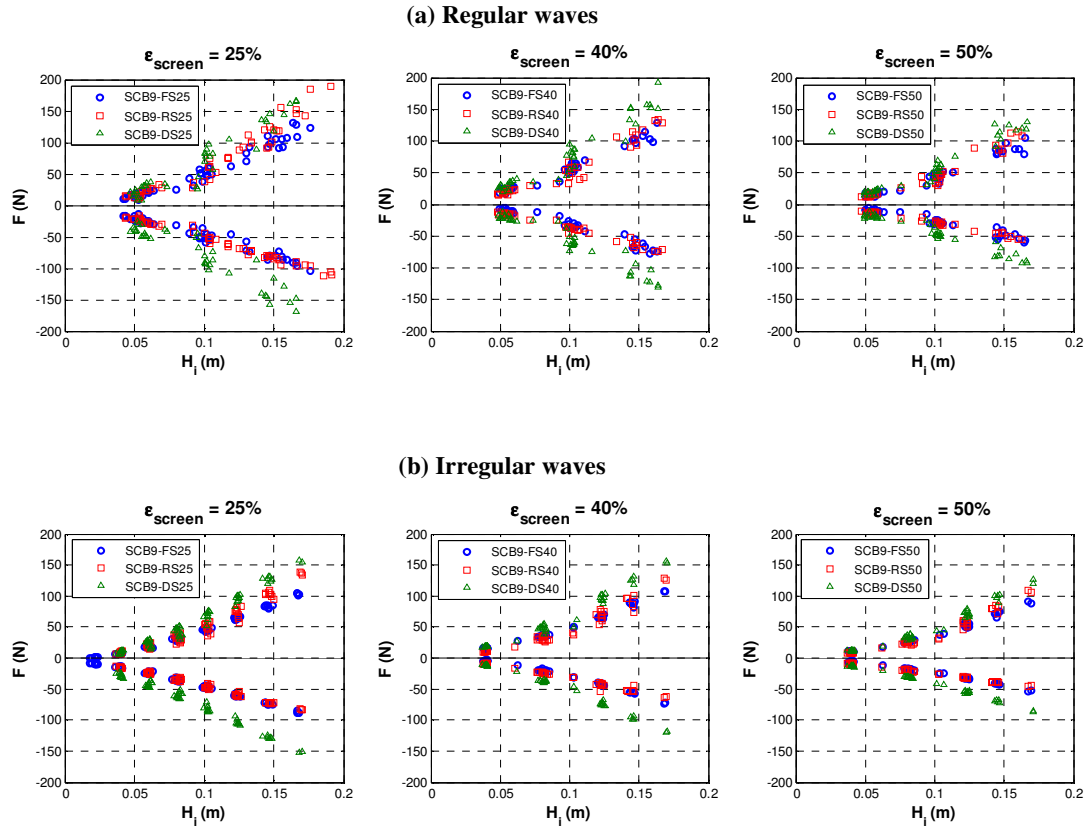


Figure 6.27: Total horizontal wave forces by the SCB9-FS, SCB9-RS and SCB9-DS models of different screen porosities in regular and irregular waves

6.6 Summary

The SCB9 model has been experimentally proven to be an effective energy dissipater and an anti-reflection structure. The performance characteristics of the breakwater, however, deteriorated with a decrease in the immersion depth. To improve the performance of the breakwater in this limiting condition, wave screens of different configurations (*i.e.* a front screen, a rear screen and double screens) and porosities (*i.e.* 25%, 40% and 50%) were introduced at the bottom of the free surface semicircular caisson. The hydrodynamic characteristics of such composite breakwaters were investigated in regular and irregular waves. Experimental results showed that the SCB9 model with double screens of 25% porosity (denoted as SCB9-DS25) provided the highest hydraulic efficiency even though the horizontal forces acting on the breakwater were higher than those for models with a single screen. The double screen of the breakwater was particularly helpful in dissipating the energy of the longer period waves. The SCB9-DS25 model has been found to be an effective

wave attenuator when immersed at a limited depth. It is anticipated that the efficiency can be further enhanced with deeper immersion. Detailed discussion on the hydrodynamic characteristics of the SCB9-DS25 model with respect to different immersion depths is given in Chapter 7.

7

Perforated Semicircular Breakwater with Optimum Screen Configurations: Results and Discussions

7.1 General

As noted in Chapter 6, the SCB9-DS25 model has produced the highest wave dampening ability; however, its reflectivity is rather high when dealing with shorter period waves. In contrast, the SCB9-RS25 model is a better anti-reflection structure but its wave attenuation efficiency is comparatively low and the horizontal wave forces acting on the rear wall of the SCB9 model is somewhat high. The functionality of the SCB9-FS25 model is not as versatile as the aforementioned breakwater models; it is therefore omitted from further study. Both the SCB9-DS25 and SCB9-RS25 models have their merits and limitations during their operations. The suitability of the breakwater for a particular application primarily depends on the level of wave protection required, the type of application, the local maritime regulations, the ecological and budget constraints, *etc.*

In this chapter, emphasis has been given to the examination of the hydrodynamic characteristics of the SCB9-DS25 and SCB9-RS25 models in a larger range of immersion depth. Note that D_T is the draft of the breakwater, which is the sum of the immersion depth of the SCB9 model (D) and the length of the wave screen (D'), *i.e.* $D_T = D + D'$. The corresponding D_T/d for $D/d = 0.071, 0.143$ and 0.214 are $0.500, 0.571$ and 0.643 ,

respectively. The porosities of the SCB and wave screens were fixed at 9% and 25%, respectively, and the breakwater placement ratio were kept at $B/d = 0.714$, so as to limit the number of experiments in this study. Hence, ε_{SCB9} , ε_{screen} and B/d can be excluded from Equations (3.68) and (3.69). The relationships of the hydrodynamic coefficients of the SCB9-RS25 and SCB9-DS25 models with respect to the relative breakwater width, B/L , the relative immersion depth, D_T/d , and the wave steepness, H/L , are ascertained in this chapter.

7.2 Hydraulic Performance of the SCB9-RS25 and SCB9-DS25 Models

Visual observations of wave response at the SCB9-RS25 and SCB9-DS25 models of $D_T/d = 0.500$ have previously been provided in Figures 6.15a and 6.16a, respectively. Wave interactions with the models at higher relative immersion depths, $D_T/d = 0.571$ and 0.643 , are shown in Figures 7.1 and 7.2. These figures show that wave-structure interactions are mostly induced by the SCB9 model. The hydraulic responses include wave run-up at the perforated front wall and the solid rear wall of the SCB9 model, water infiltration into the interference chamber, wave overtopping, turbulence within the chamber and formation of eddies near the wetted perforated front wall. The hydraulic interactions at the wave screens failed to be observed especially in deeper submergence relative to the still water level. Nevertheless, the amount of energy loss at the screens, which corresponds to the wave-structure interactions, can be estimated by ΔC_L as shown in Equation (6.1).

Similarly, the hydraulic performance of the SCB9-RS25 and SCB9-DS25 models are reported in terms of C_T , C_R , C_L , C_F and C_C , and these hydraulic coefficients are presented with respect to B/L , D_T/d , H/L for both regular and irregular waves as shown in Figures 7.3 to 7.12. For each figure, the hydraulic contribution by the wave screen, which is quantified by ΔC_i (see Equation (6.1)), is also presented using the graph plotting format in the same way as shown before. The hydraulic responses are discussed from the perspectives of effects of the relative breakwater width, wave steepness and relative breakwater immersion depth in the following sections.

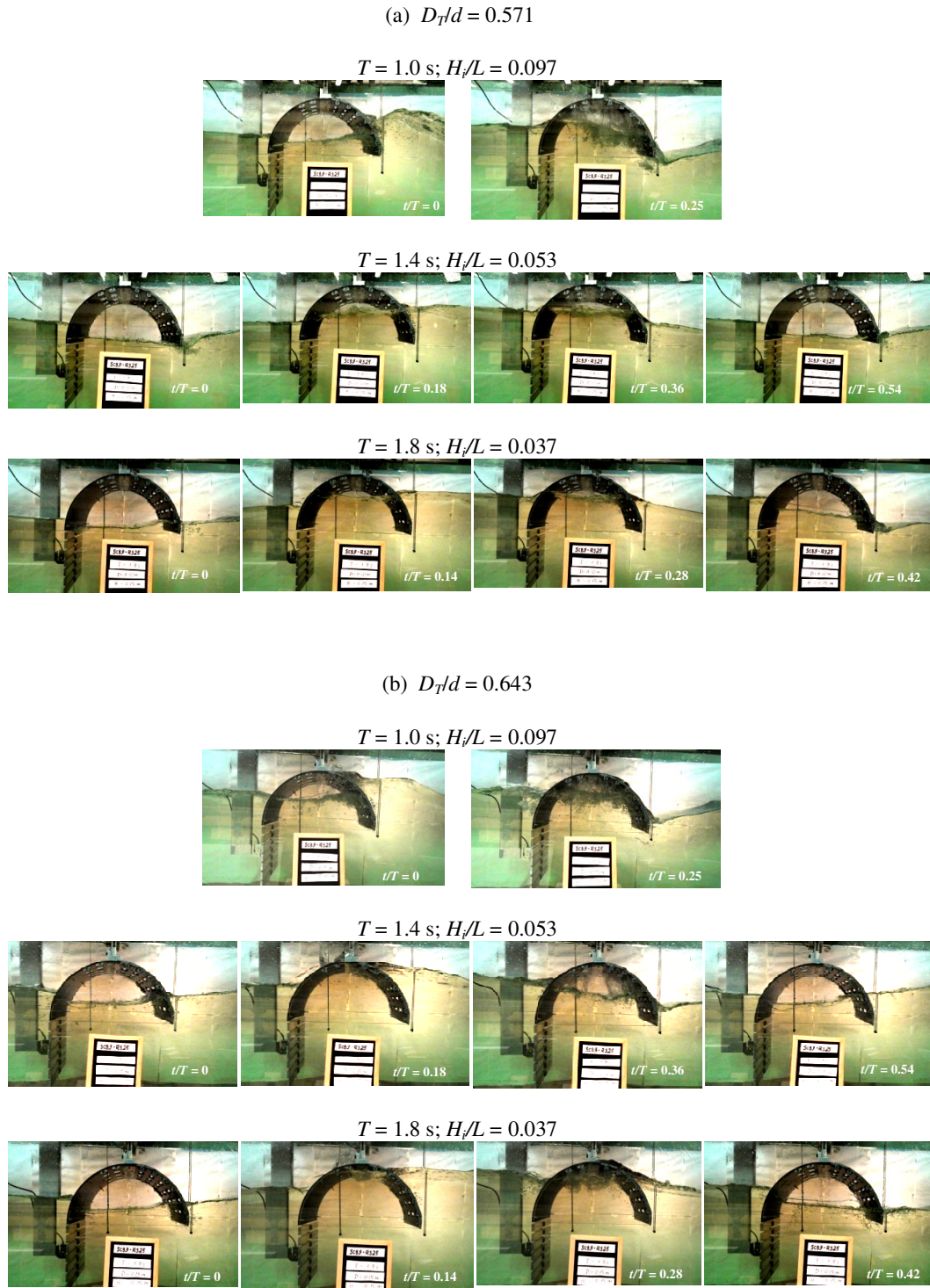


Figure 7.1: Wave interaction with the SCB9-RS25 model at $D_T/d = 0.571$ and 0.643 in regular waves of $H_i = 0.15 \text{ m}$. Note that the incident waves propagated from the left of the test model

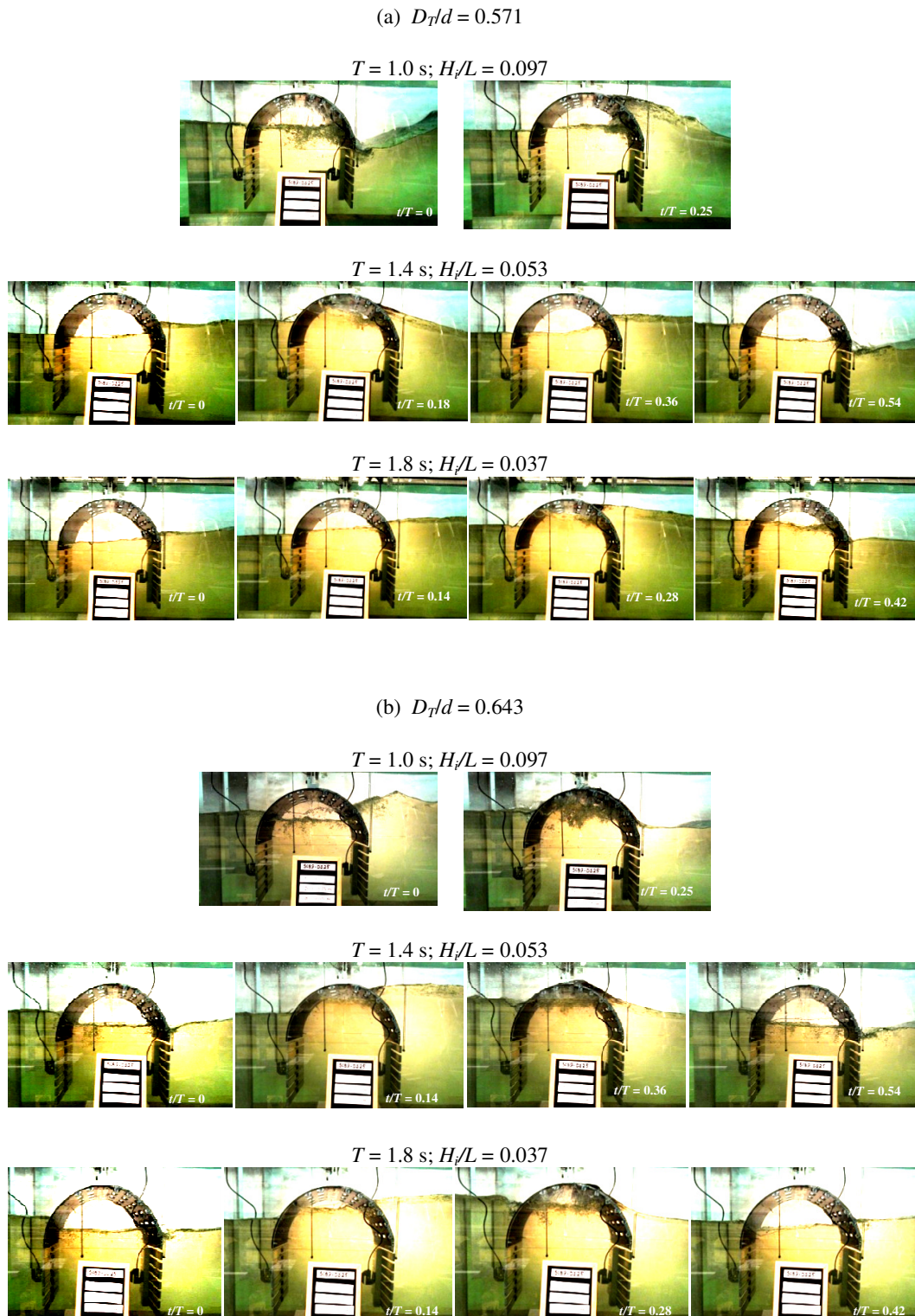


Figure 7.2: Wave interaction with the SCB9-DS25 model at $D_T/d = 0.571$ and 0.643 in regular waves of $H_i = 0.15 \text{ m}$. Note that the incident waves propagated from the left of the test model

7.2.1 Wave Transmission Coefficient – C_T

The wave transmission characteristics of the SCB9-RS25 and SCB9-DS25 models are demonstrated in Figures 7.3 and 7.4, respectively. The C_T values of the models of different D_T/d ratios decrease with the increasing B/L ; however, the decrements become less rapid at $B/L > 0.4$ for both regular and irregular waves. On the contrary, the effect of wave screen on wave attenuation for the test models deteriorates when exposed to shorter period waves, *i.e.* ΔC_T decreases with an increase in B/L . This observation, again, proves that wave screen is most beneficial to the SCB9 model when the structure is subjected to longer period waves irrespective of its submergence level and the screen configuration.

The effect of the relative breakwater immersion depth is clearly seen from Figures 7.3 and 7.4 in that higher D_T/d ratio leads to smaller C_T for both types of model. Also, the efficiency of the wave screen, which is indicated by the variation of ΔC_T , decreases with the increase in D_T/d , entailing that the screen effect on wave attenuation of the SCB9 model at deeper immersion depth is rather small. This can be explained by the fact that the water particle motions decrease exponentially with water depth, and the deeply submerged screen(s) is, therefore, exposed to less interaction with the wave-induced flow. As a result, extending the draft of a deeply immersed SCB9 model using a wave screen(s) may be cost ineffective for a site that is dominated by shorter period waves. It is also found that the influence of wave steepness on C_T of the SCB9-RS25 and SCB9-DS25 models exists in nominal form, *i.e.* waves with larger steepness tend to have better wave attenuation capability. The C_T variation is mainly caused by the SCB9 model as the ΔC_T for the screen remains almost unchanged with the increase in H/L in both sea states.

Table 7.1 summarises the ranges of C_T for the SCB9-RS25 and SCB9-DS25 models corresponding to $D_T/d = 0.500, 0.571$ and 0.643 within the test ranges of $0.12 < B/L < 0.65$ and $0.009 < H/L < 0.12$ for regular waves, and $0.12 < B/L_p < 0.65$ and $0.009 < H_{m0,r}/L_p < 0.10$ for irregular waves. In terms of the breakwater configurations, the SCB9-DS25 model outperforms the SCB9-RS25 model only when the structure is immersed in a modest depth. For larger immersion depths (*i.e.* $D_T/d > 0.571$), the efficiencies of both models are almost analogous; and the rear screen of the SCB9-DS25 model does not seem to contribute to wave attenuation appreciably. Therefore, the SCB9-RS25 model would be an optimum breakwater configuration if the structure is designed to be deeply immersed.

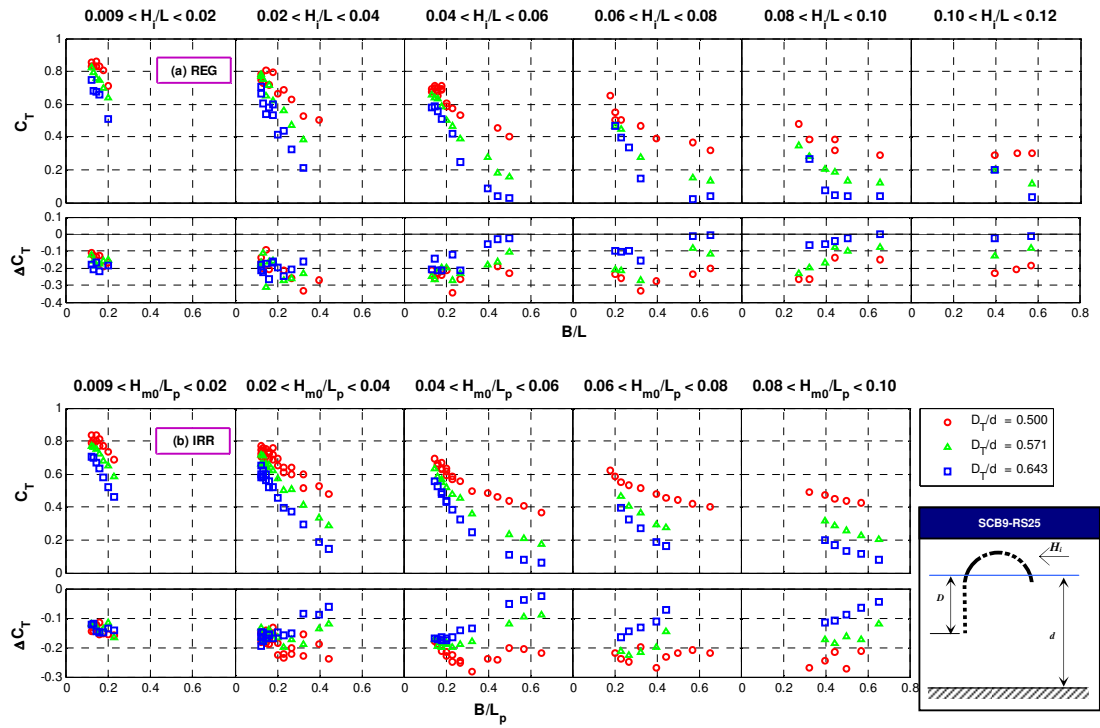


Figure 7.3: C_T and ΔC_T of the SCB9-RS25 model in regular and irregular waves

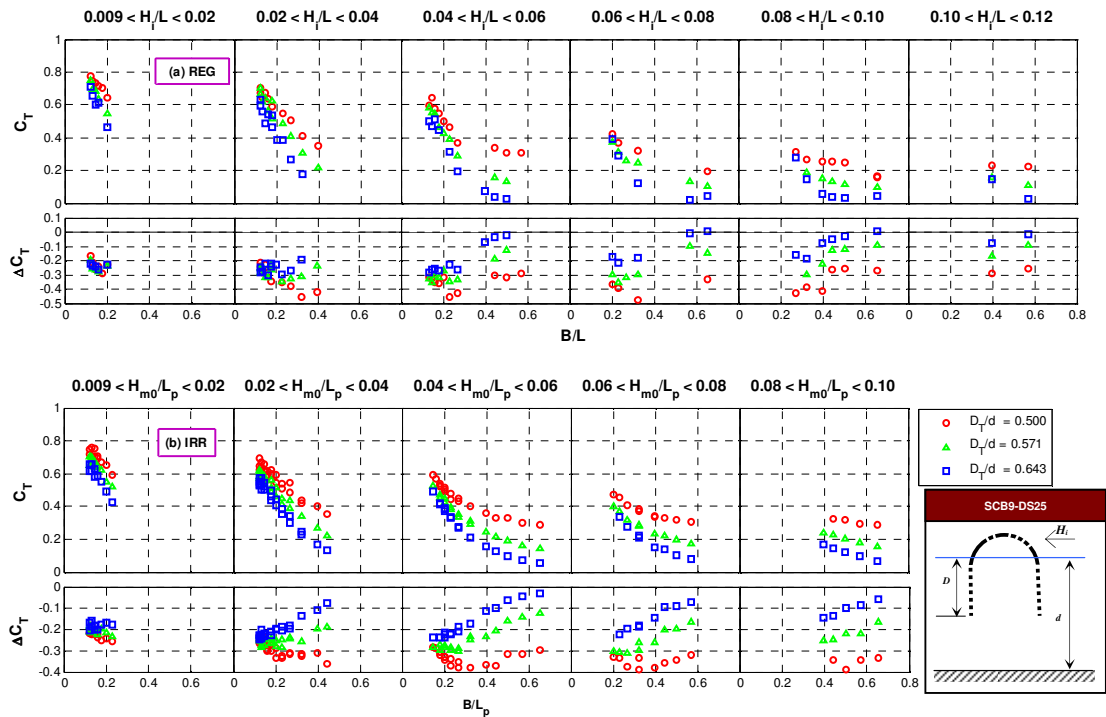


Figure 7.4: C_T and ΔC_T of the SCB9-DS25 model in regular and irregular waves

Table 7.1: Ranges of C_T for the SCB9-RS25 and SCB9-DS25 models

(a) Regular Waves ($0.12 < B/L < 0.65$; $0.009 < H/L < 0.12$)		
D_T/d	SCB9-RS25	SCB9-DS25
0.500	0.29 – 0.86	0.16 – 0.78
0.571	0.12 – 0.82	0.10 – 0.75
0.643	0.02 – 0.75	0.02 – 0.71

(b) Irregular Waves ($0.12 < B/L_p < 0.65$; $0.009 < H_{m0,p}/L_p < 0.10$)		
D_T/d	SCB9-RS25	SCB9-DS25
0.500	0.37 – 0.84	0.29 – 0.76
0.571	0.18 – 0.78	0.16 – 0.71
0.643	0.06 – 0.71	0.06 – 0.66

7.2.2 Wave Reflection Coefficient – C_R

Figures 7.5 to 7.6 demonstrate the reflection characteristics of the SCB9-RS25 and SCB9-DS25 models in regular and irregular waves. For regular waves, the C_R of the models fluctuates over the tested range of B/L , whereby the first peaks of the C_R values mostly occur at $0.15 < B/L < 0.20$; they subsequently drop to minimums at $0.3 < B/L < 0.4$ and rise again at higher range of B/L . For irregular waves, the C_R behaves in the same way as that for regular waves but the fluctuation is much gentler.

The amount of wave reflection incurred by the wave screens is indicated by ΔC_R . The ΔC_R is the largest when the screen is located close to the free surface (*i.e.* $D_T/d = 0.500$) where the energy flux is the greatest. At $D_T/d = 0.643$, the variations of ΔC_R for the single and double screens (indicated by the blue squared markers in Figures 7.5 to 7.6) are insignificant at $B/L > 0.25$; hence, the resulting C_R values for the SCB9-RS25 and SCB9-DS25 models are the least when compared to those C_R values of models with lower D_T/d . The maximum C_R for the SCB9-RS25 model within the test range of B/L is about 0.55 in regular waves and 0.45 in irregular waves, both occurred at $D_T/d = 0.571$ where still water level is positioned close to the mid height of the SCB9 model. Under such conditions, reflection from the SCB9 model is found to be considerable. This finding is agreeable with the maximum C_R of the SCB9 as shown in Figures 5.6 and 5.7. For the SCB9-DS25 model, the highest C_R yielded is about 0.58 in regular waves and 0.48 in irregular waves, both happened at $D_T/d = 0.500$. These amounts of reflection are caused by the joint effects of the SCB9 model and the double screens.

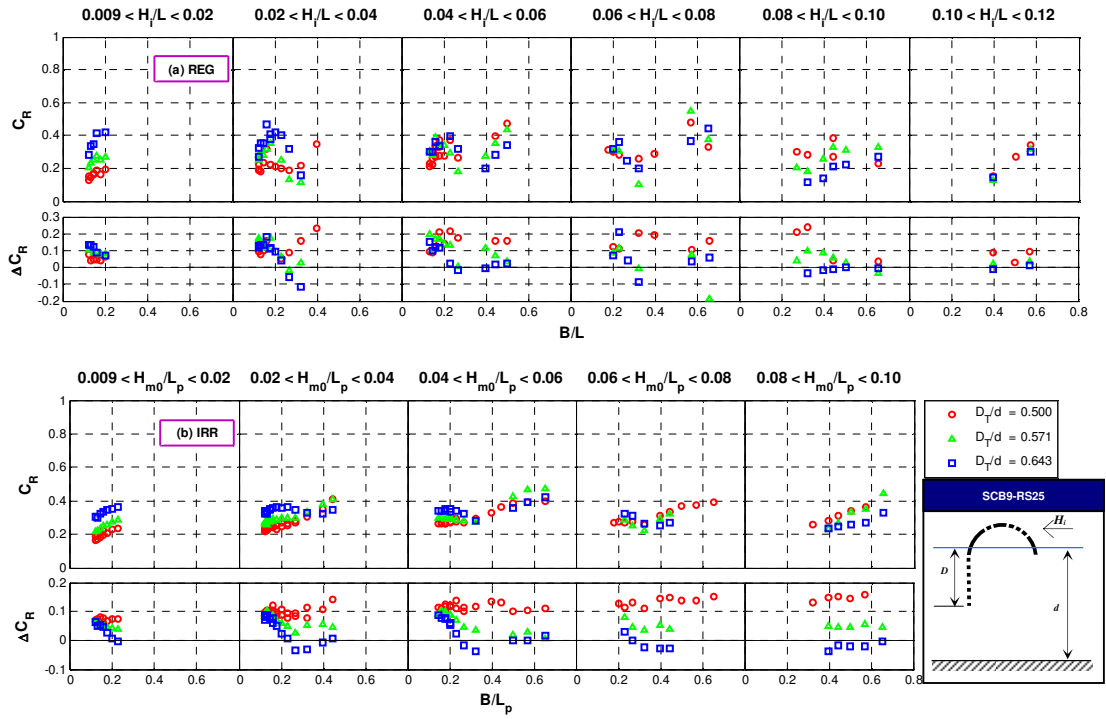


Figure 7.5: C_R and ΔC_R of the SCB9-RS25 model in regular and irregular waves

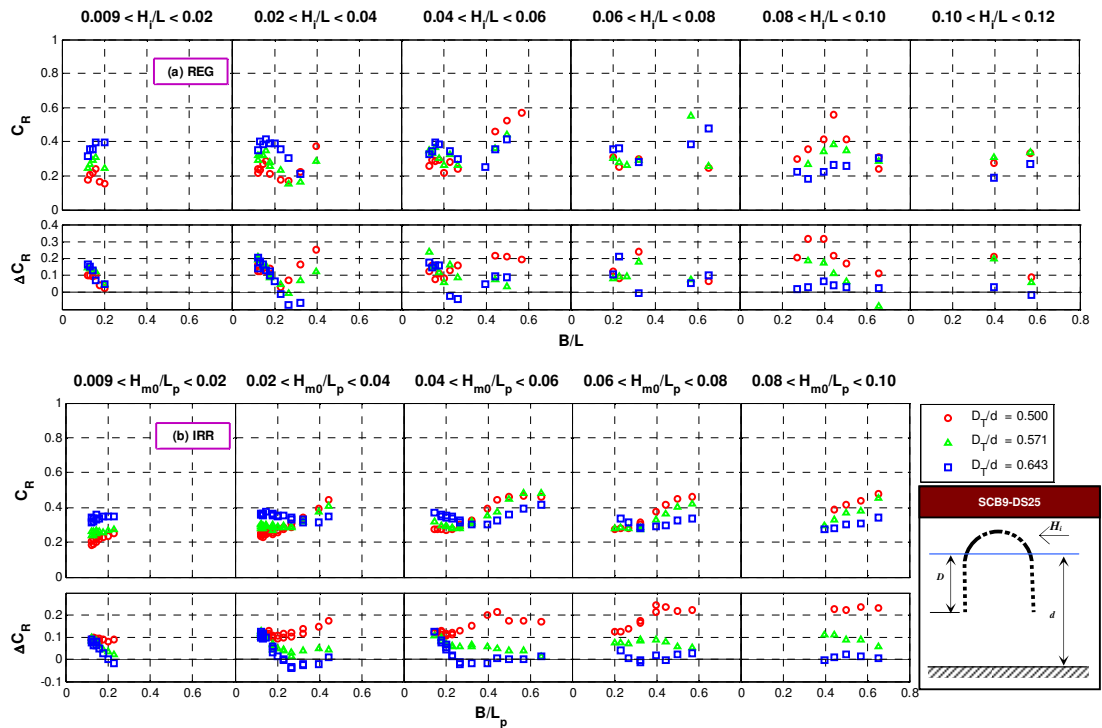


Figure 7.6: C_R and ΔC_R of the SCB9-DS25 model in regular and irregular waves

The overall C_R results reveal that both the SCB9-RS25 and SCB9-DS25 models have similar reflection characteristics at $B/L < 0.4$ whereby C_R values are consistently less than 0.40. At higher B/L range, the SCB9-DS25 model becomes a stronger wave reflector when exposed to very limited period waves, which is uncommon in nature. Wave absorption ability of these models is greatly improved by resonance at $B/L \approx 0.3$ particularly in regular waves. Hence, the relative width ratio can be used as a reference value for designing an effective anti-reflection semicircular breakwater. Table 7.2 summarises the ranges of C_R for the SCB9-RS25 and SCB9-DS25 models corresponding to $D_T/d = 0.500, 0.571$ and 0.643 within the test ranges of $0.12 < B/L < 0.65$ and $0.009 < H/L < 0.12$ for regular waves, and $0.12 < B/L_p < 0.65$ and $0.009 < H_{m0,i}/L_p < 0.10$ for irregular waves.

Table 7.2: Ranges of C_R for the SCB9-RS25 and SCB9-DS25 models

(a) Regular Waves ($0.12 < B/L < 0.65$; $0.009 < H/L < 0.12$)		
D_T/d	SCB9-RS25	SCB9-DS25
0.500	0.13 – 0.48	0.15 – 0.57
0.571	0.11 – 0.55	0.15 – 0.55
0.643	0.12 – 0.47	0.18 – 0.48

(b) Irregular Waves ($0.12 < B/L_p < 0.65$; $0.009 < H_{m0,i}/L_p < 0.10$)		
D_T/d	SCB9-RS25	SCB9-DS25
0.500	0.15 – 0.57	0.19 – 0.48
0.571	0.15 – 0.55	0.24 – 0.48
0.643	0.18 – 0.48	0.27 – 0.42

7.2.3 Energy Dissipation Coefficient – C_L

Energy dissipation coefficients, C_L for the SCB9-RS25 and SCB9-DS25 models are presented in Figure 7.7 and Figure 7.8, respectively. A similar C_L trend can be seen for both models at $B/L < 0.4$ irrespective of sea conditions, in which C_L increases rapidly with B/L , and reaches peak values at $B/L \approx 0.4$. At $B/L > 0.4$, the C_L of regular waves tends to decrease moderately, and the variation of C_L in irregular waves does not seem to change much from the peak values. It is therefore suggested that $B/L \approx 0.4$ could be used as the parameter in designing both SCB9-RS25 and SCB9-DS25 as efficient energy dissipaters. Further, it is found that wave dissipation of the models improves with the increasing wave steepness.

From the results of ΔC_L for both models, it is found that the energy dissipation performance of the RS25 and DS25 models are particularly excellent when (i) subjected to longer period waves; and (ii) the screen is positioned closer to the water surface. It is important to note that these screens do not contribute much to energy dissipation (*i.e.* $\Delta C_L < 0.1$) at $B/L > 0.4$ and $D_T/d > 0.57$ despite the fact that the resulting C_L values are generally high. This shows that the energy dissipation within the test ranges is largely triggered by the SCB9 model alone. Therefore, it is more practical and cost effective to consider the option of extending the draft of the SCB9 model by a screen system for the conditions when (i) $B/L < 0.4$; and (ii) $D_T/d < 0.57$, if the structure is designed to be a good energy dissipater.

A comparison between the SCB9-RS25 and SCB9-DS25 model configurations shows that the SCB9-DS25 model is a better energy dissipater at $B/L < 0.4$, and the performance at higher B/L range is comparable to that of the SCB9-RS25 model. The ΔC_L values of the DS25 are higher than those of the RS25 by about 0.1 within the suggested operating range as mentioned previously due to increased interaction of the double screens with the longer period waves. A summary of the ranges of C_L for the SCB9-RS25 and SCB9-DS25 models corresponding to $D_T/d = 0.500, 0.571$ and 0.643 within the test ranges of $0.12 < B/L < 0.65$ and $0.009 < H/L < 0.12$ for regular waves, and $0.12 < B/L_p < 0.65$ and $0.009 < H_{m0,i}/L_p < 0.10$ for irregular waves is given in Table 7.3.

Table 7.3: Ranges of C_L for the SCB9-RS25 and SCB9-DS25 models

(a) Regular Waves ($0.12 < B/L < 0.65$; $0.009 < H/L < 0.12$)		
D_T/d	SCB9-RS25	SCB9-DS25
0.500	0.23 – 0.89	0.36 – 0.90
0.571	0.28 – 0.94	0.37 – 0.92
0.643	0.36 – 0.97	0.40 – 0.95

(b) Irregular Waves ($0.12 < B/L_p < 0.65$; $0.009 < H_{m0,i}/L_p < 0.10$)		
D_T/d	SCB9-RS25	SCB9-DS25
0.500	0.27 – 0.71	0.39 – 0.77
0.571	0.36 – 0.84	0.44 – 0.85
0.643	0.41 – 0.91	0.47 – 0.90

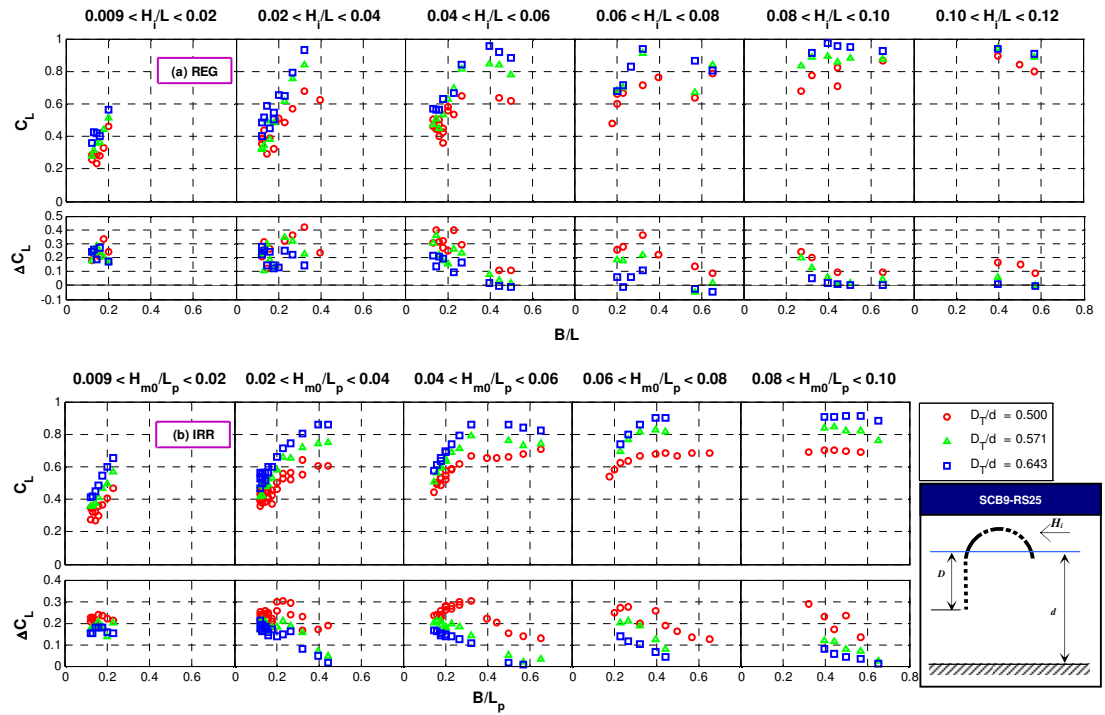


Figure 7.7: C_L and ΔC_L of the SCB9-RS25 model in regular and irregular waves

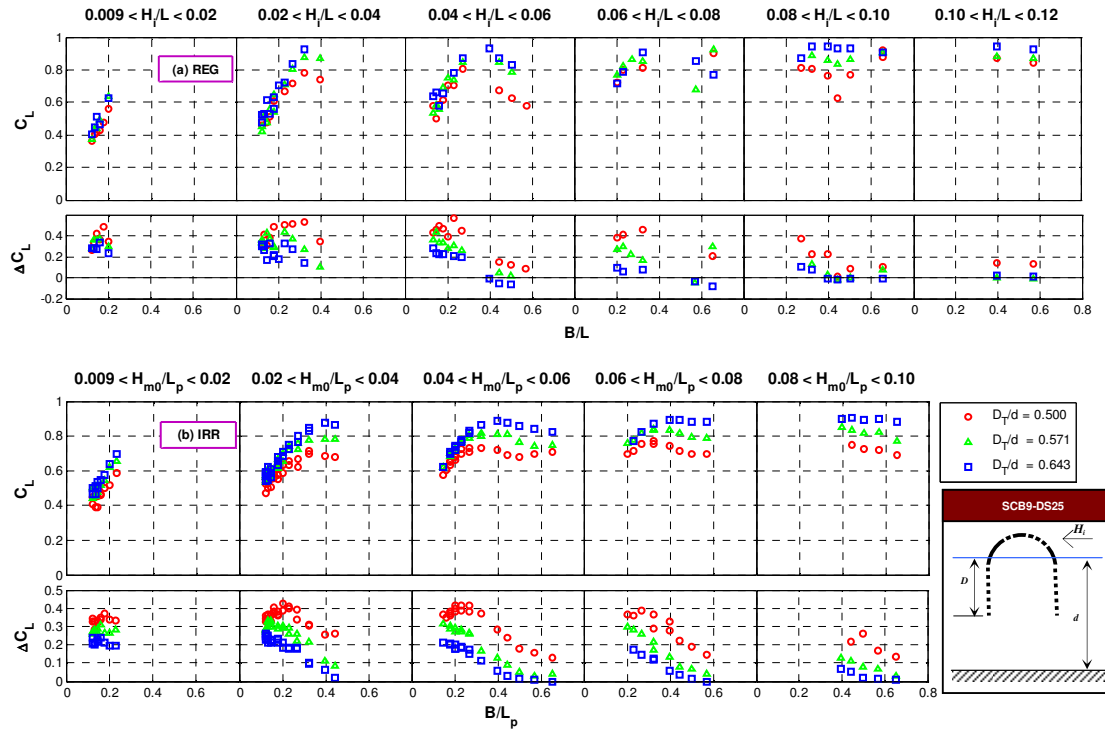


Figure 7.8: C_L and ΔC_L of the SCB9-DS25 model in regular and irregular waves

7.2.4 Wave Disturbance Coefficient in Front of the Breakwater – C_F

The wave climate coefficients in front of the breakwater, C_F for the SCB9-RS25 and SCB9-DS25 models are presented in Figure 7.9 and Figure 7.10, respectively. The figures also exhibit the response of ΔC_F due to influence from RS25 and DS25 models. For both screens, a greater range of ΔC_F can be seen in regular waves, *i.e.* -0.6 – 0.42 for the RS25 models and -0.17 – 0.34 for the DS25 models. This indicates that the screens have raised the level of wave agitation in front of the breakwaters to a certain extent. The highest C_F values attained by the SCB9-RS25 and SCB9-DS25 models are 1.80 and 1.75, respectively, in regular waves and 1.37 and 1.43, respectively, in irregular waves. The proximity of these values for a given sea state implies that the wave climates in front of the SCB9-RS25 and SCB9-DS25 models are rather identical.

For the SCB9-RS25 model (see Figure 7.9), the trends of C_F with respect to B/L for $D_T/d = 0.500$ and 0.571 are rather similar, whereby the dips and peaks of C_F are mostly found at $0.2 < B/L < 0.3$ and $0.4 < B/L < 0.6$, respectively. On the other hand, for $D/d = 0.214$ the behaviour of C_F corresponding to B/L varies largely with wave steepness. The rear screen induces wave amplification in front of the SCB9-RS25 model throughout the test range of B/L except for $0.15 < B/L < 0.30$ regardless of D_T/d . For the SCB9-DS25 model (see Figure 7.10), the C_F behaviour is quite similar to that of the SCB9-RS25 model, particularly for the case of regular waves. The presence of the double screens creates a large excitation of waves in front of the breakwater (indicated by the ΔC_F values) at $D_T/d = 0.500$; and the degree of wave excitation decreases with the immersion depth. It is also found that wave steepness has a varying effect on both C_F and ΔC_F for the SCB9-DS25 model with respect to B/L and D_T/d . The ranges of C_F for the SCB9-RS25 and SCB9-DS25 models corresponding to $D_T/d = 0.500$, 0.571 and 0.643 within the test ranges of $0.12 < B/L < 0.65$ and $0.009 < H_T/L < 0.12$ for regular waves, and $0.12 < B/L_p < 0.65$ and $0.009 < H_{m0,T}/L_p < 0.10$ for irregular waves is given in Table 7.4.

As mentioned before, wave activity directly in front of the SCB9-RS25 and SCB9-DS25 models is a result of a combination of hydraulic phenomena including wave run-up, surging and reflection. This is not an issue if they are designed to be wave overtopping breakwaters. For non-overtopping breakwaters, the SCB9-RS25 and SCB9-DS25 models should be designed to be $0.2 < B/L < 0.3$ for $0.500 \leq D_T/d \leq 0.571$ in regular and irregular waves.

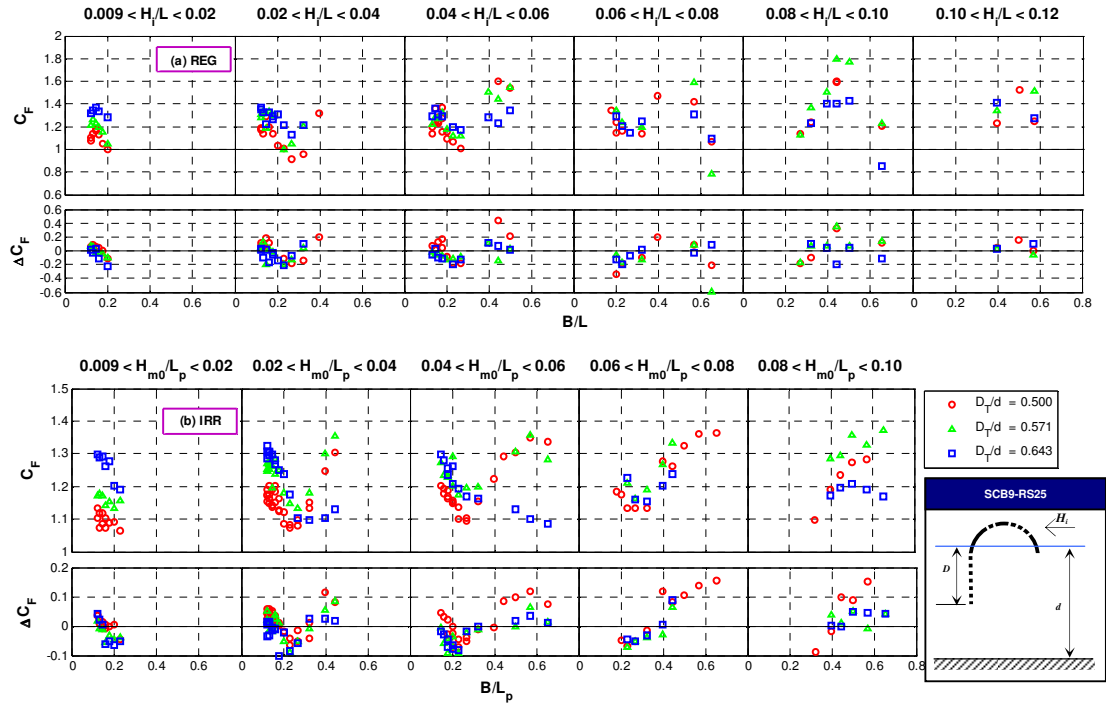


Figure 7.9: C_F and ΔC_F of the SCB9-RS25 model in regular and irregular waves

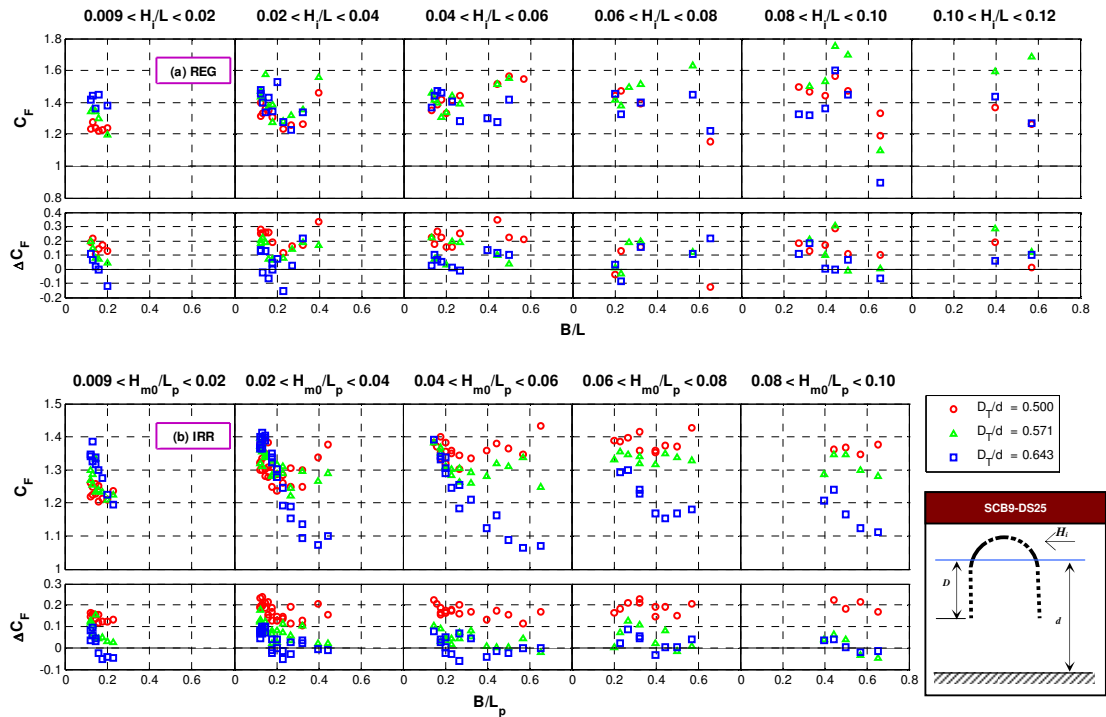


Figure 7.10: C_F and ΔC_F of the SCB9-DS25 model in regular and irregular waves

Table 7.4: Ranges of C_F for the SCB9-RS25 and SCB9-DS25 models

(a) Regular Waves ($0.12 < B/L < 0.65$; $0.009 < H/L < 0.12$)		
D_T/d	SCB9-RS25	SCB9-DS25
0.500	0.91 – 1.60	1.15 – 1.56
0.571	0.79 – 1.80	1.10 – 1.75
0.643	0.85 – 1.43	0.89 – 1.60

(b) Irregular Waves ($0.12 < B/L_p < 0.65$; $0.009 < H_{m0,i}/L_p < 0.10$)		
D_T/d	SCB9-RS25	SCB9-DS25
0.500	1.06 – 1.36	1.20 – 1.43
0.571	1.13 – 1.37	1.21 – 1.36
0.643	1.09 – 1.32	1.06 – 1.41

7.2.5 Wave Disturbance Coefficient in the Breakwater Chamber – C_C

Figures 7.11 to 7.12 display the wave climate coefficients in the interference chamber, C_C for the SCB9-RS25 and SCB9-DS25 models. For the SCB9-RS25 model (see Figure 7.11), the C_C values show a decreasing trend with an increase in B/L for both regular and irregular waves. The C_C values of different D_T/d ratios are greater than unity at $B/L < 0.4$, and are smaller than unity at $B/L > 0.4$. The response of the ΔC_C of the RS25 model is somewhat similar to that of the C_C , whereby an exchange of wave behaviour also occurs at $B/L < 0.4$. The variations of C_C and ΔC_C with respect to D_T/d are found to be less distinctive for the SCB9-RS25 model, particularly at $B/L > 0.4$. The maximum C_C for regular and irregular waves are 1.55 and 1.33, respectively, both measured at $B/L \approx 0.2$. It is also found that wave steepness is a weak affecting parameter for both C_C and ΔC_C of the SCB9-RS25 model.

For the SCB9-DS25 model (see Figure 7.12), a substantial decrease of C_C is observed at $B/L < 0.4$ in both sea conditions. At higher B/L , the reduction of C_C becomes less significant. The wave climate in the interference chamber is much calmer than that of the SCB9-FS25 model due to wave filtering at the frontal barrier of the breakwater. The C_C of the SCB9-DS25 model is also found to decrease with a decrease in D_T/d , which is inversely related to C_F as shown in Figure 7.10. This can be explained by the fact that at smaller immersion depth waves are effectively intercepted by the freeboard of the SCB9 model, resulting in higher wave run-up on the breakwater and lesser amount of wave energy transmitted into the interference chamber; whereas at larger immersion depth waves in front of the breakwater are less aggressive since they are prone to overtop the low-crested SCB9 model and

consequently creating disturbance in the chamber with the infiltrated water. The maximum C_C values for regular and irregular waves are 1.45 and 1.18, respectively, both occurring at $D_T/d = 0.643$ and $B/L \approx 0.2$. Besides, it is also learnt that the wave climate in the chamber of the SCB9-DS25 model is less dependant on the wave steepness.

Table 7.5 summarises the C_L ranges for the SCB9-RS25 and SCB9-DS25 models corresponding to $D_T/d = 0.500, 0.571$ and 0.643 within the test ranges of $0.12 < B/L < 0.65$ and $0.009 < H/L < 0.12$ for regular waves, and $0.12 < B/L_p < 0.65$ and $0.009 < H_{m0,i}/L_p < 0.10$ for irregular waves. The wave properties in the interference chamber are deemed to be crucial in the engineering design of the semicircular caisson. Excessive uplift loadings on the inner circumference of the SCB9 model may eventually lead to structural failure. Careful consideration must be given to the SCB9-RS25 model configuration as the wave activity in the chamber is relatively violent, particularly when exposed to longer period waves.

Table 7.5: Ranges of C_C for the SCB9-RS25 and SCB9-DS25 models

(a) Regular Waves ($0.12 < B/L < 0.65$; $0.009 < H/L < 0.12$)		
D_T/d	SCB9-RS25	SCB9-DS25
0.500	0.42 – 1.42	0.29 – 1.12
0.571	0.67 – 1.46	0.64 – 1.24
0.643	0.68 – 1.53	0.64 – 1.41

(b) Irregular Waves ($0.12 < B/L_p < 0.65$; $0.009 < H_{m0,i}/L_p < 0.10$)		
D_T/d	SCB9-RS25	SCB9-DS25
0.500	0.76 – 1.23	0.56 – 1.04
0.571	0.88 – 1.34	0.73 – 1.14
0.643	0.84 – 1.33	0.73 – 1.17

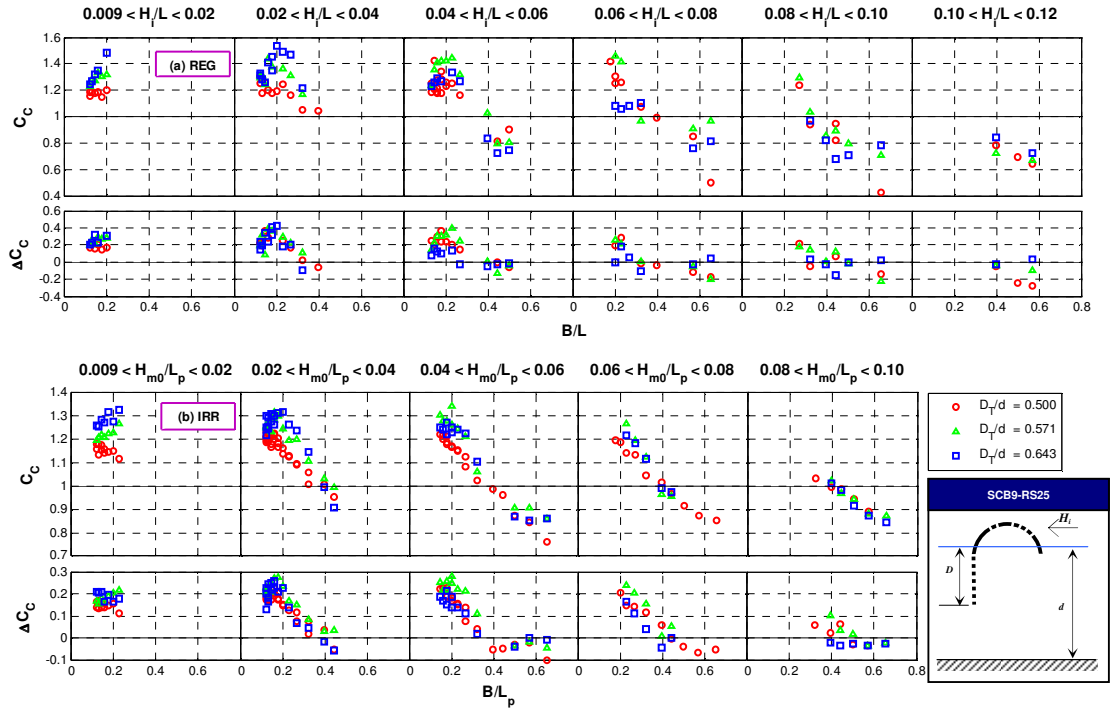


Figure 7.11: C_c and ΔC_c of the SCB9-RS25 model in regular and irregular waves

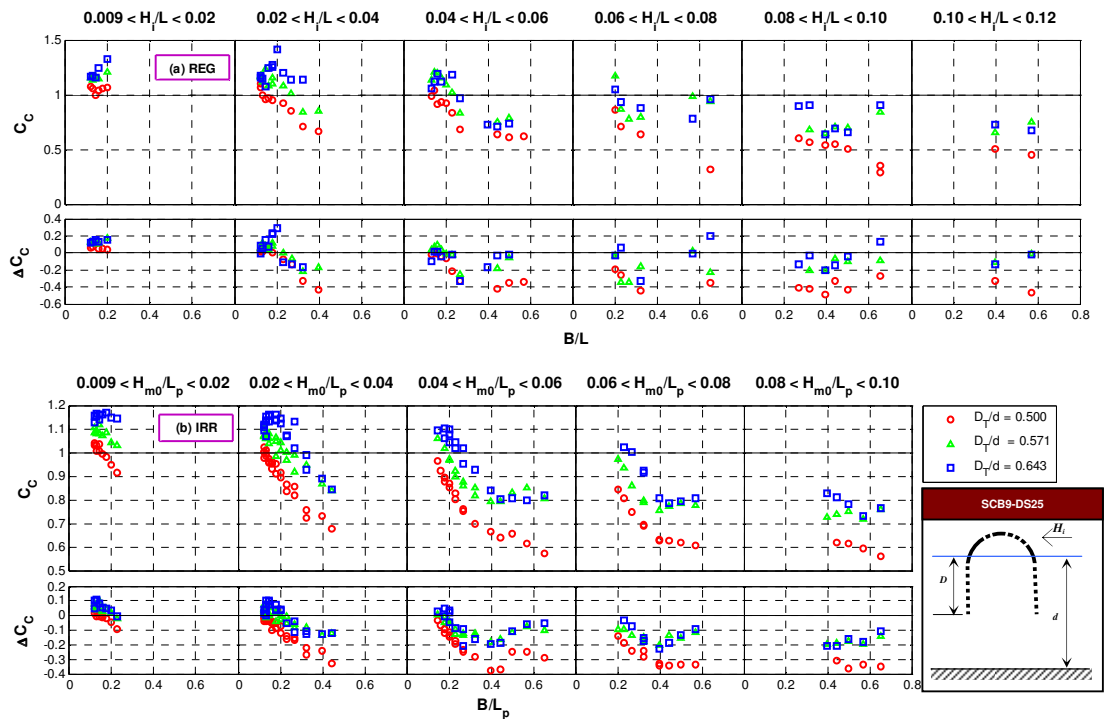


Figure 7.12: C_c and ΔC_c of the SCB9-DS25 model in regular and irregular waves

7.3 Horizontal Loadings on the SCB9-RS25 and SCB9-DS25 Models

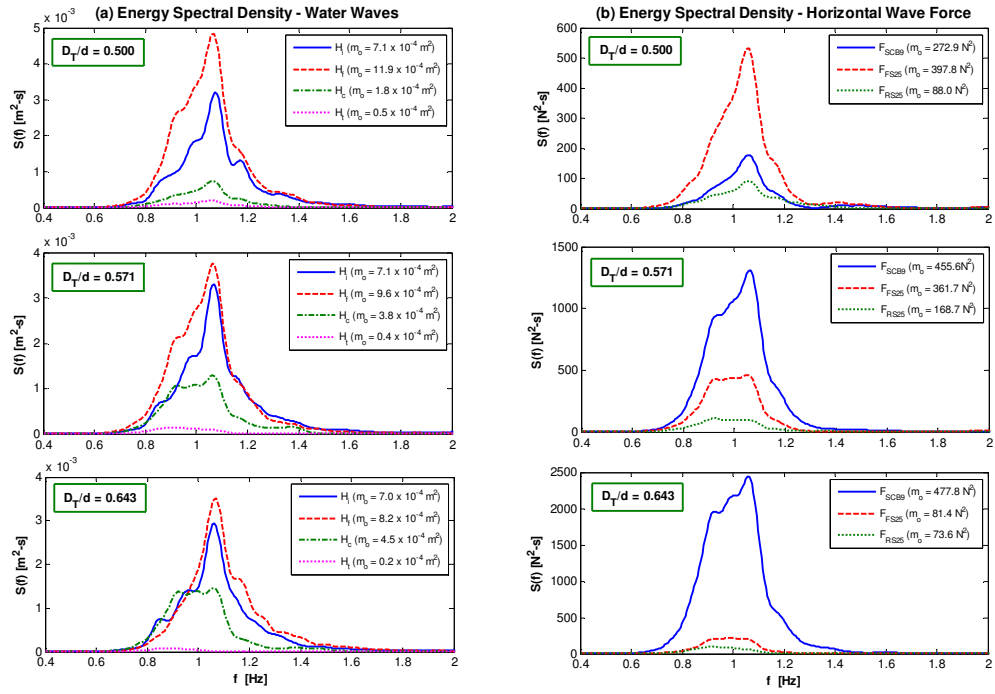
7.3.1 Statistical Distribution

The peak forces under the wave crests (positive forces, F_c) and troughs (negative forces, F_t) acting on the respective elements (*i.e.* SCB9, FS and RS) of the SCB9-DS25 and SCB9-FS25 models were analysed using the Weibull distribution (refer to Section 5.3.5). However, only a sample of the analysis is presented here for demonstration purposes.

Figure 7.13 displays the spectral energy densities for the waves measured around the SCB9-DS25 model, and for the horizontal force responses on (i) SCB9, (ii) FS25 and (iii) RS25, respectively. It is observed that both test cases of $T_p = 0.9$ s and $T_p = 1.4$ s demonstrate the spectral energy of the waves is maximal at the front of the structure and that in the interference chambers is generally smaller than the spectral energy of the incident waves. At $D_T/d = 0.500$, the resulting spectral energy of the horizontal forces acting on the FS25 model for both test cases are found to be considerably larger than those acting on the SCB9 and RS25 models; nonetheless, they reduce in magnitude as D_T/d increases. On the other hand, the force spectra of the SCB9 grow with the increasing D_T/d .

The corresponding Weibull probability plots of F_c and F_t for the SCB9, FS25 and RS25 models are respectively shown in Figure 7.14. The peak forces acting on the model are normalised by their standard deviations, σ_F in the plots, thus giving F/σ_F . It can be seen that the peak forces acting on SCB9, FS25 and RS25 generally follow the Weibull distribution quite well at higher range of F/σ_F . The deviation of the force data at the lower range of F/σ_F resembles that of the incident peak wave crests and troughs as shown in Figure 7.15. This indicates that the peak wave forces are strongly correlated to the peak wave crests and troughs. Although the other test results are not included here, the general trend is found to be similar to the one discussed previously. This implies that the peak wave forces may be adequately predicted by the Weibull distribution, especially at $F/\sigma_F > 0.5$.

(a) $H_{m0} = 0.10$ m, $T_p = 0.9$ s



(b) $H_{m0} = 0.14$ m, $T_p = 1.4$ s

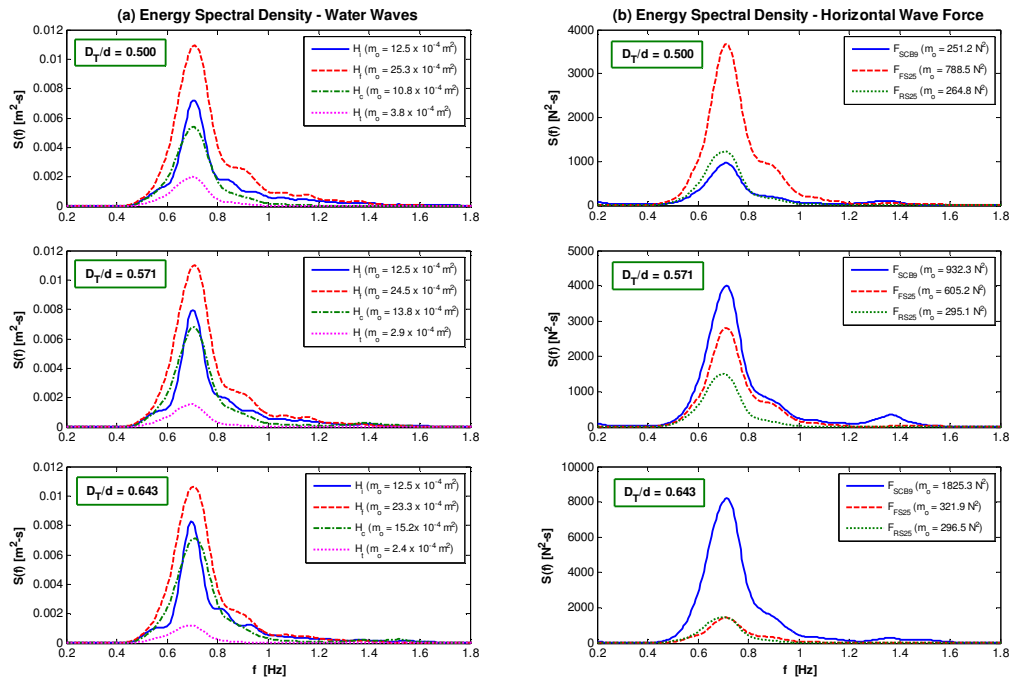
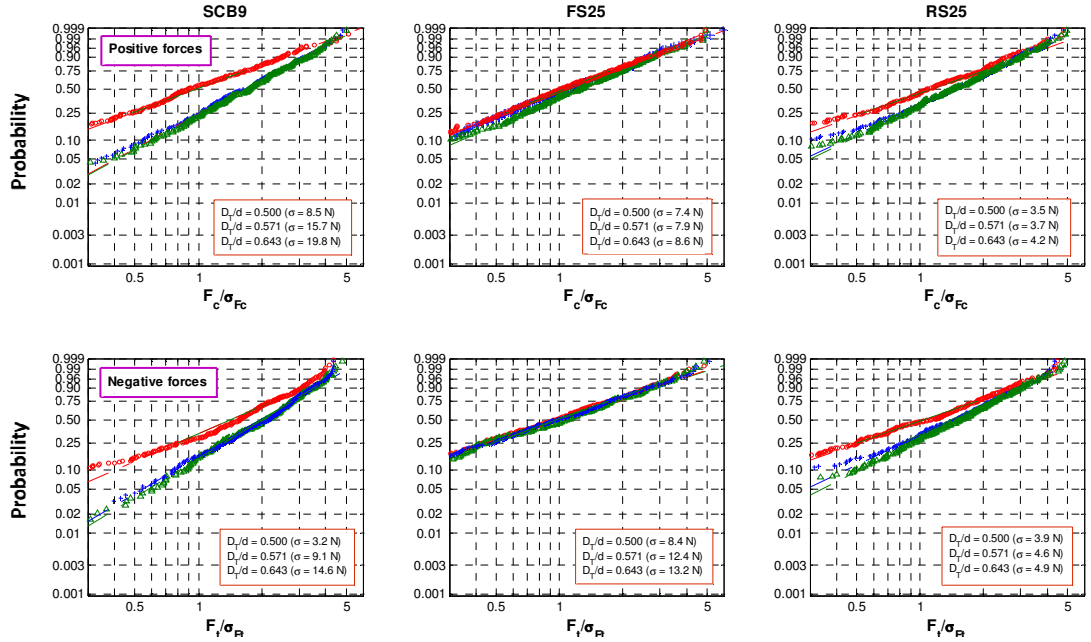


Figure 7.13: Water wave and horizontal wave force spectra for the SCB9-DS25 models at $D_T/d = 0.500, 0.571$ and 0.643

Δ $D_T/d = 0.500$ $+$ $D_T/d = 0.571$ \circ $D_T/d = 0.643$

(a) $H_{m0} = 0.10$ m, $T_p = 0.9$ s



(b) $H_{m0} = 0.14$ m, $T_p = 1.4$ s

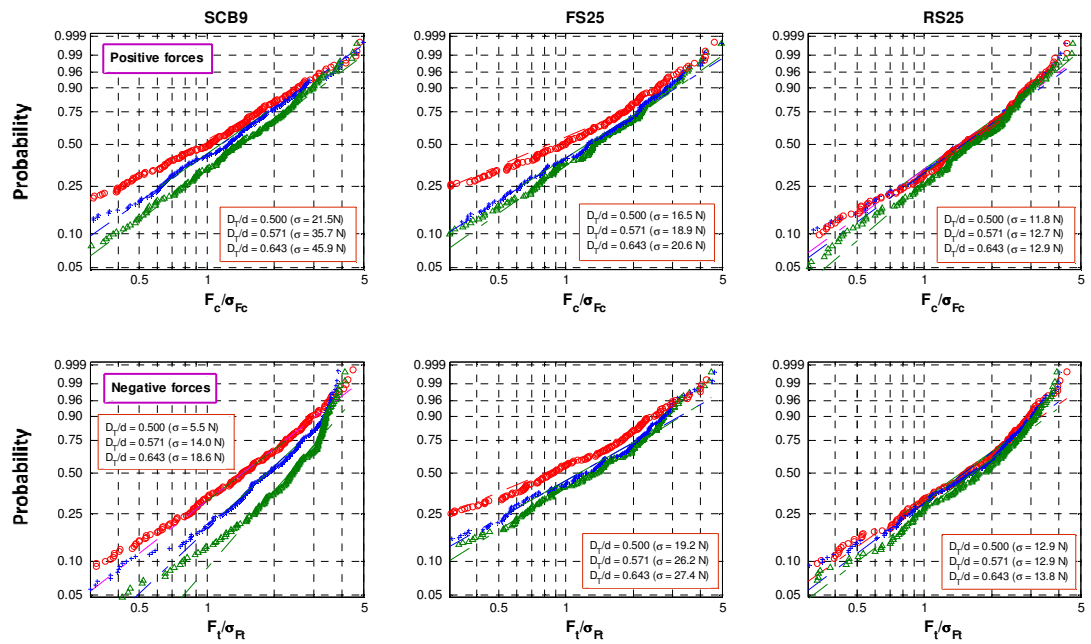


Figure 7.14: Weibull probability plots for the horizontal peak forces acting on the SCB9-DS25 model

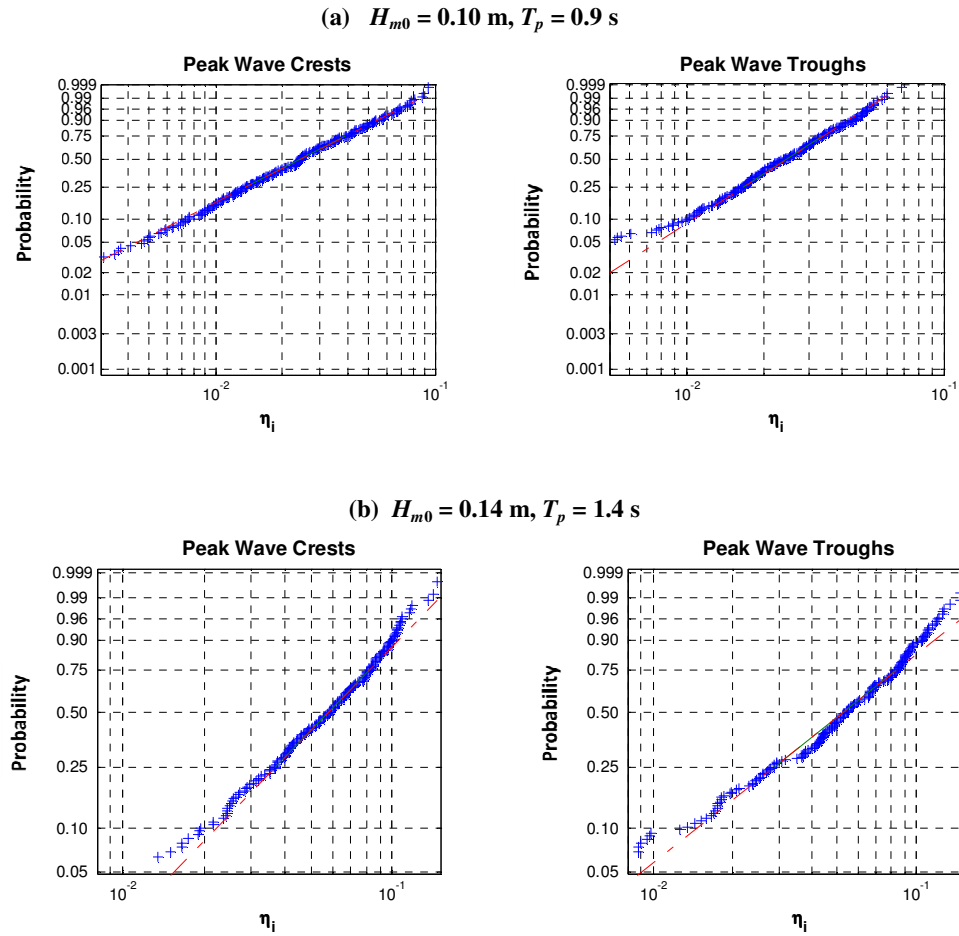


Figure 7.15: Weibull probability plots for the incident peak wave crests and troughs

7.3.2 Parametric Analysis

Parametric analysis for the horizontal wave forces acting on the individual part of the SCB9-RS25 and SCB9-DS25 models is presented in a normalised form, $F_n = F/\rho g H_i D_T$, where F is the horizontal wave force per m length of the test model (F is represented by the mean peak forces in regular waves and the average of the highest one-third of the peak forces in irregular waves), H_i is the significant wave height, and D_T is the total draft of the breakwater (including wave screen). F_n is also termed as the force coefficient and its detailed description is provided in Section 3.6.3. For both models, the force coefficients for the positive and negative forces acting on the individual components (*i.e.* SCB9, FS25 and RS25), which are denoted as $F_{n,c}$ and $F_{n,t}$ respectively, are plotted with respect to wave steepness for different relative wave height, H/d at three relative immersion depths, $D_T/d = 0.500, 0.571$ and 0.643 in Figures 7.16 to 7.19.

7.3.3 SCB9-RS25 Model

Figures 7.16 and 7.17 show the force coefficients for the individual parts of the SCB9-RS25 model (*i.e.* SCB9 and RS25) in regular and irregular waves, respectively. Discussion of the results is made based on the SCB9 and RS25 models:

(a) SCB9

For the SCB9 model exposed to regular waves (see Figure 7.16), the $F_{n,c}$ of different D_T/d and H/d ratios increase initially at the lower range of H/L and subsequently decrease drastically at higher H/L range. The maximum values of $F_{n,c}$ for $H/d = 0.071, 0.143$ and 0.214 occur at $H/L \approx 0.02, 0.04$ and 0.06 , respectively, when $0.500 \leq D_T/d \leq 0.643$. This signifies that wave interception by the SCB9 caisson becomes maximal under such test conditions. Waves of higher steepness tend to dissipate their energy at the SCB9 model and overtop the structure, which in turn reduce the force intensity at the SCB9 model. Nonetheless, this phenomenon is less prominent in irregular waves (see Figure 7.17). For both sea conditions, the $F_{n,c}$ values of the SCB9 model are found to be influenced by H/d and D_T/d , *i.e.* the higher the H/d or the higher the D_T/d , the greater will be the $F_{n,c}$ value. On the other hand, the $F_{n,t}$ values of the SCB9 model are less sensitive to the variation of H/L and H/d but they seem to increase with the increasing D_T/d . The $F_{n,t}$ of the SCB9 model is also found to be smaller than the $F_{n,c}$. This is expected as the negative forces near the free surface are proven to be smaller by Goda and Kakizaki (1967).

(b) RS25

For the RS25 model, the $F_{n,c}$ and $F_{n,t}$ values are relatively small as most of the wave energy has already been intercepted by the SCB9 model. The $F_{n,t}$ values for the RS25 model are consistently higher than the $F_{n,c}$ values for $0.500 \leq D_T/d \leq 0.643$ in both regular and irregular seas. It can also be seen in Figures 7.16 and 7.17 that the force coefficients decrease with the increasing H/L ; and this observation is compatible with the findings of Wang (2006) for an emerged bottom seated semicircular breakwater. The effect of relative wave height on the force coefficients of the RS25 model is also found to be significant, *i.e.* the magnitude of F_n decreases with the decrease in H/d for all tested D_T/d . At $D_T/d \geq 0.571$, the $F_{n,c}$ values of $H/d = 0.071$ in regular waves and those of $H/d = 0.057$ in irregular waves approach zero at larger range of H/L . This is because most of the energy flux was concentrated at the upper column of water, resulting in significant amount of wave response on the SCB9 model; the wave energy at the lower water column, therefore, became so minimal that was hardly detectable in deep waters.

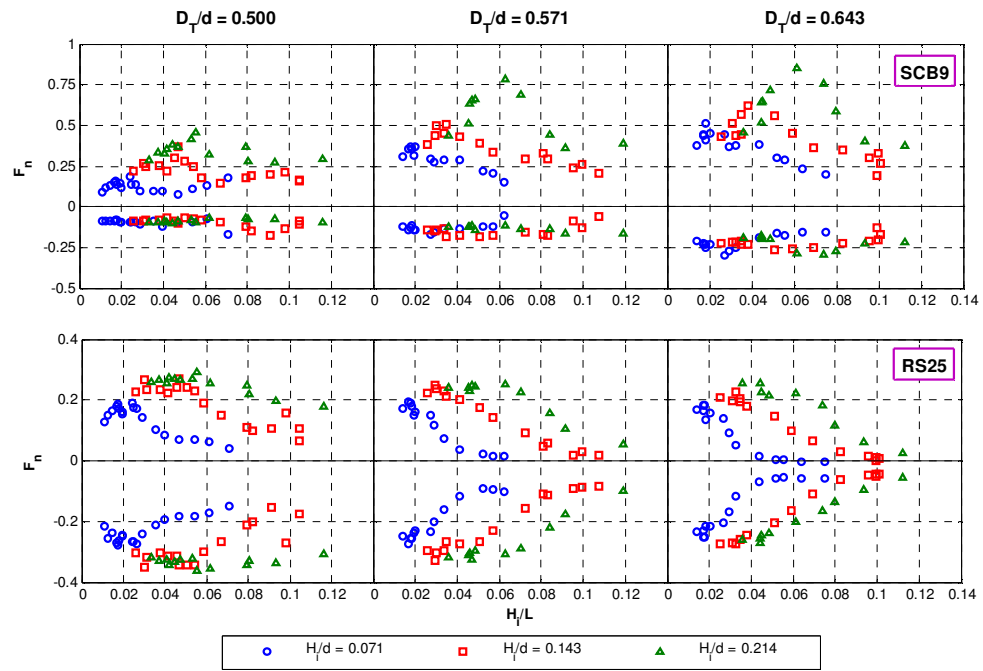


Figure 7.16: Force coefficients for the SCB9-RS25 model at different relative breakwater drafts in regular waves

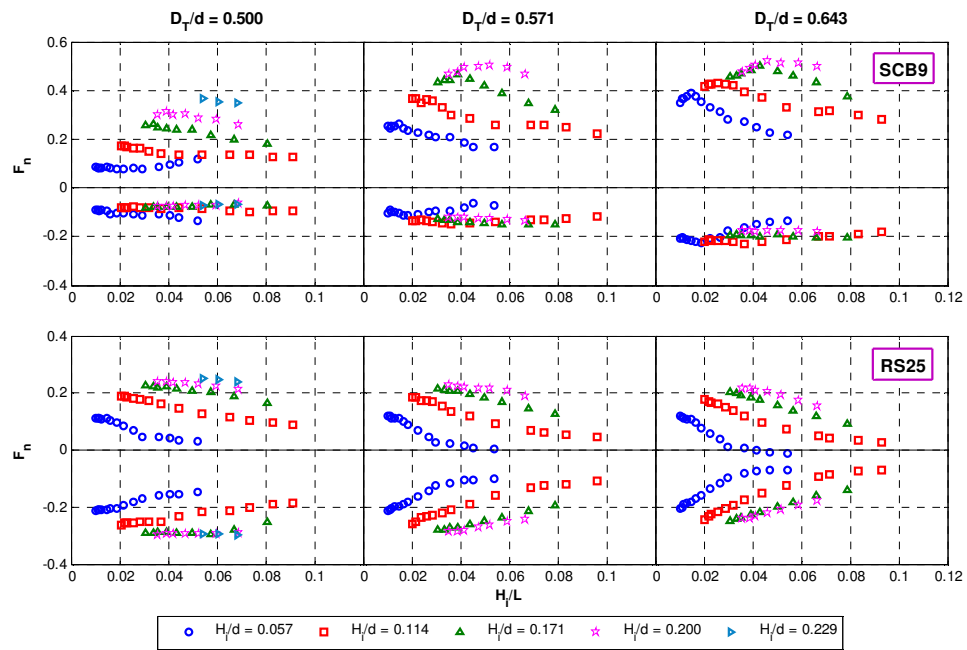


Figure 7.17: Force coefficients for the SCB9-RS25 model at different relative breakwater drafts in irregular waves

7.3.4 SCB9-DS25 Model

The horizontal peak force coefficients for the individual parts of the SCB9-DS25 model (*i.e.* SCB9, FS25 and RS25) in regular and irregular waves are presented in Figures 7.18 and 7.19, respectively. The following discussion is made based on the SCB9 model and the double screens:

(a) SCB9

For the SCB9 model, the $F_{n,c}$ of the respective H/d gradually decreases with the increasing wave steepness; however, the variation of the $F_{n,t}$ with the change of H/L is almost insignificant. The trends of the results are somewhat agreeable to those of the bottom seated semicircular breakwater (Wang, 2006). The contribution of H/d on $F_{n,c}$ is noticeably strong, whereby higher H/d leads to greater $F_{n,c}$; nonetheless, the same effect is not observed for $F_{n,t}$. The variation of $F_{n,t}$ is only seen as the relative breakwater immersion depth increases, *i.e.* the higher the D_T/d the larger will be the $F_{n,t}$. This relationship is also found to be true for $F_{n,c}$. This is reasonable as the SCB9 model with larger immersion provides greater exposure area to wave attack leading to higher horizontal wave forces acting on the structure. Besides, it is also found that the positive forces acting on the SCB9 model are always greater than the negative ones. This is because the positive forces under the wave crests are the highest when close to the free surface (refer to the findings of Goda and Kakizaki in Figure 5.32).

(b) Double Screen – FS25 and RS25

The double screens – FS25 and RS25 have different horizontal wave loading responses depending on the wave climate in front of them. The larger the wave activity the greater will be the wave responses on the screens. The FS25 and RS25 screens also exhibit unique behaviours corresponding to the wave steepness. For the FS25, the F_n of the respective H/d seems to exhibit a parabolic trajectory trend as wave steepness increases; whereas, for the RS25 the measured F_n shows a decrease with wave steepness. The overall trends of the $F_{n,c}$ and $F_{n,t}$ for the FS25 and RS25 screens appear to have mirror symmetry about their imaginary axes that are located at a distance below the principal x -axis, resulting in $|F_{n,t}| > |F_{n,c}|$ for both screens. This phenomenon has also been reported by Goda (1995), McConnell *et al.* (1999) and Wang (2006). Further details are described in Section 6.5. Having said that, the horizontal loadings under the wave troughs becomes a critical design factor to be considered when designing the truncated wave screens.

Other dominant factors affecting the force coefficients of the FS25 and DS25 screens are H/d and D_T/d . The effect of H/d on F_n is apparent from Figures 7.18 and 7.19, *i.e.* the higher the H/d the greater will be the horizontal peak loadings. With regards to the effect of D_T/d , it is interesting to note the decreasing trend of F_n corresponding to the D_T/d , which contradicts with the characteristics of the SCB9 model. Nevertheless, this happens because the screens of lower D_T/d ratio are located closer to the free surface; hence, they are exposed to greater wave loadings. It is also important to highlight the fact that the $F_{n,c}$ values of the screens for smaller range of H/d gradually reduce with H/L and subsequently approach zero at larger range of H/L . The waves at this test range are deepwater waves with small amplitudes whereby the effect is most prominent close to the free surface and it diminishes with water depth and eventually vanishes at a depth that is more than half of the wavelength. Therefore, the forces under the crests of such waves are easily measurable by the SCB9 model located at free surface but are less detectable by the submerged screens, particularly when they are deeply submerged in the water. Since wave activity in the interference chamber is relatively small, the force responses generated by these waves are even more difficult to be captured by the load cells.

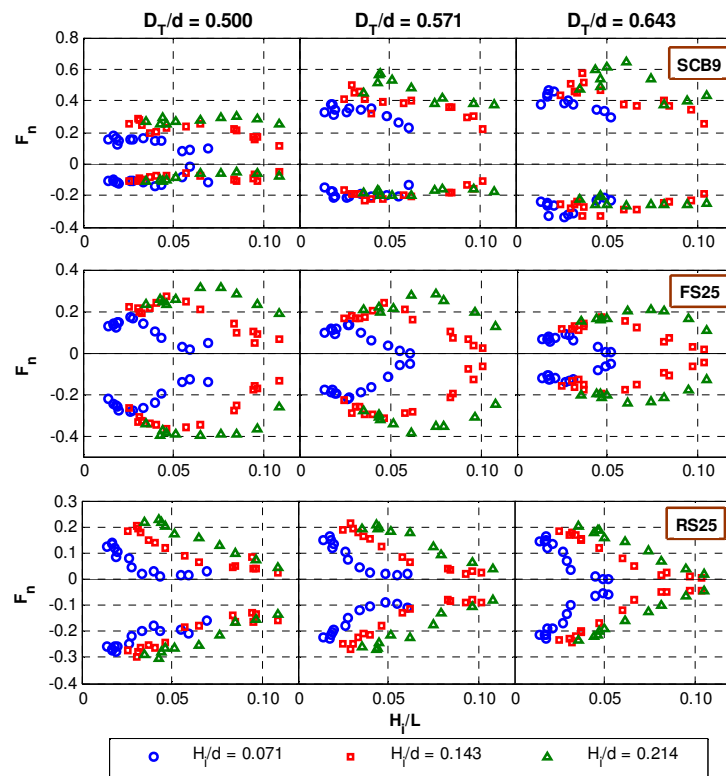


Figure 7.18: Force coefficients for the SCB9-DS25 model at different relative breakwater drafts in regular waves

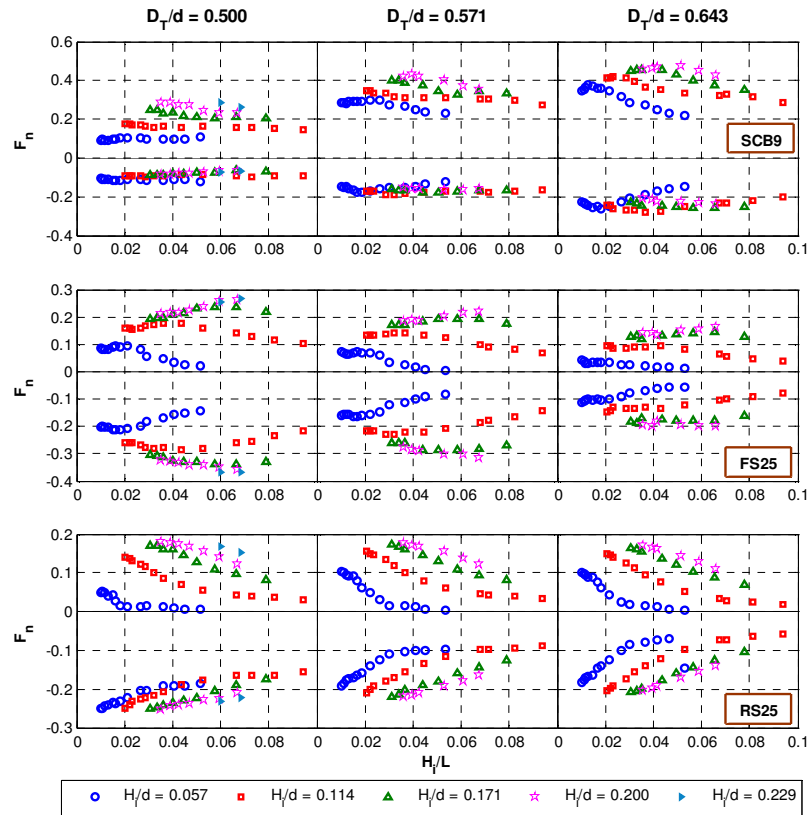
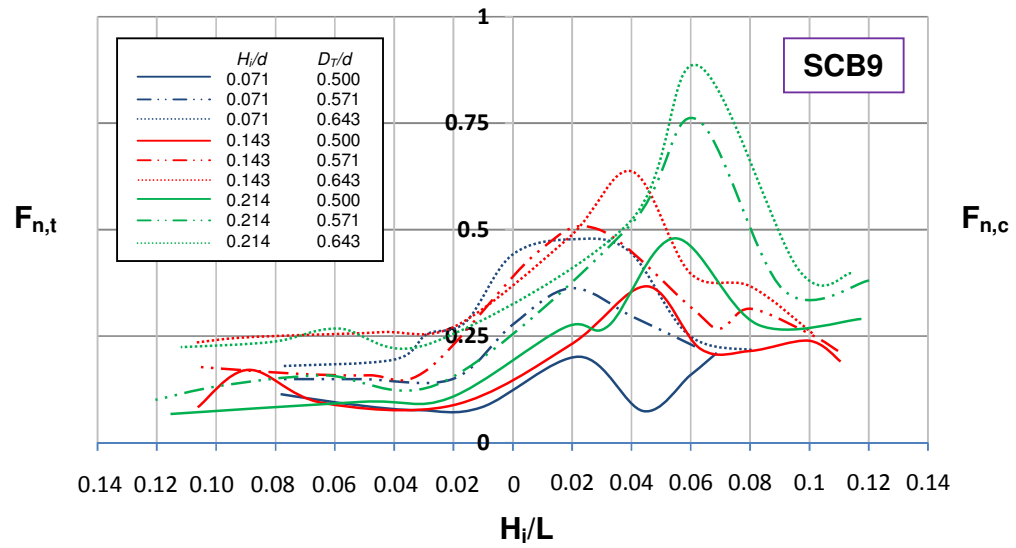


Figure 7.19: Force coefficients for the SCB9-DS25 model at different relative breakwater drafts in irregular waves

7.4 Summary

Hydrodynamic characteristics of two potential breakwater configurations – SCB9-RS25 and SCB9-DS25 have been evaluated with respect to the relative breakwater width, the relative wave height and wave steepness; and their overall performances have been compared and reported in this chapter. The design diagrams for positive and negative horizontal wave forces acting on the SCB9-RS25 and SCB9-DS25 in both regular and irregular waves are presented in Figures 7.20 – 7.23. The choice of the wave screen configuration is largely governed by its design immersion depth. For instance, SCB9 with limited immersion depth performs better when double screens (*i.e.* FS25 and RS25) are installed; however, the contribution of rear screen RS25 on wave attenuation reduces as (i) the relative immersion depth increases; and (ii) the relative breakwater width increases. In this case the use of SCB9-RS25 breakwater would be more realistic. For these reasons, the design of the SCB breakwater with wave screens for a given site should be optimised from the perspectives of the functional creditability and cost effectiveness of the breakwater.

(a) Horizontal wave forces on the SCB9



(b) Horizontal wave forces on the RS25

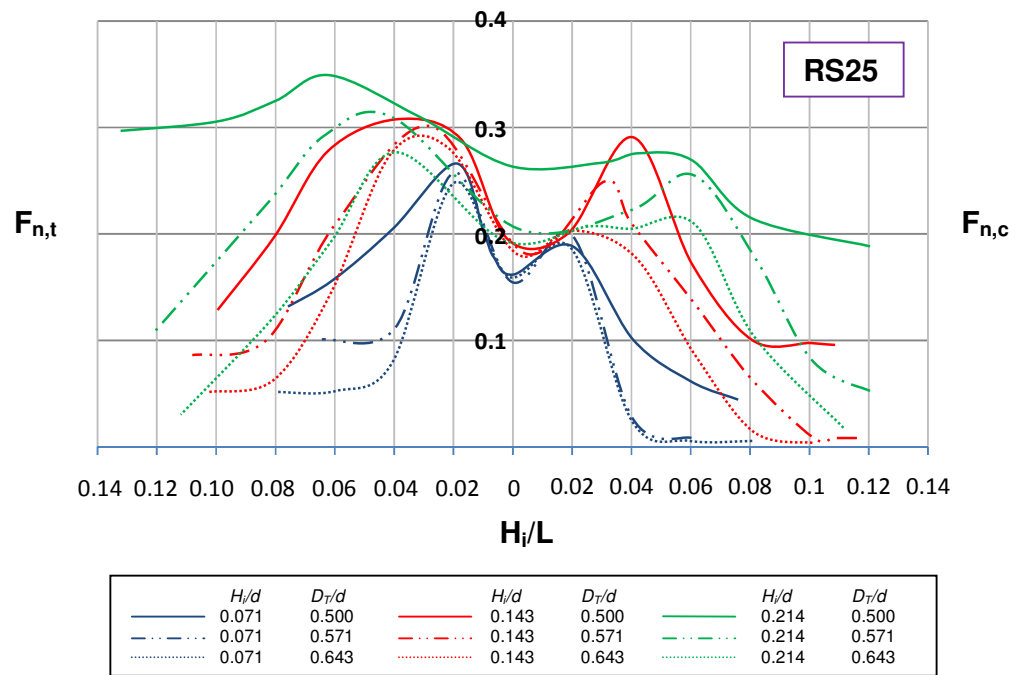


Figure 7.20: Design diagram for positive and negative horizontal wave forces acting on the SCB9-RS25 in regular waves

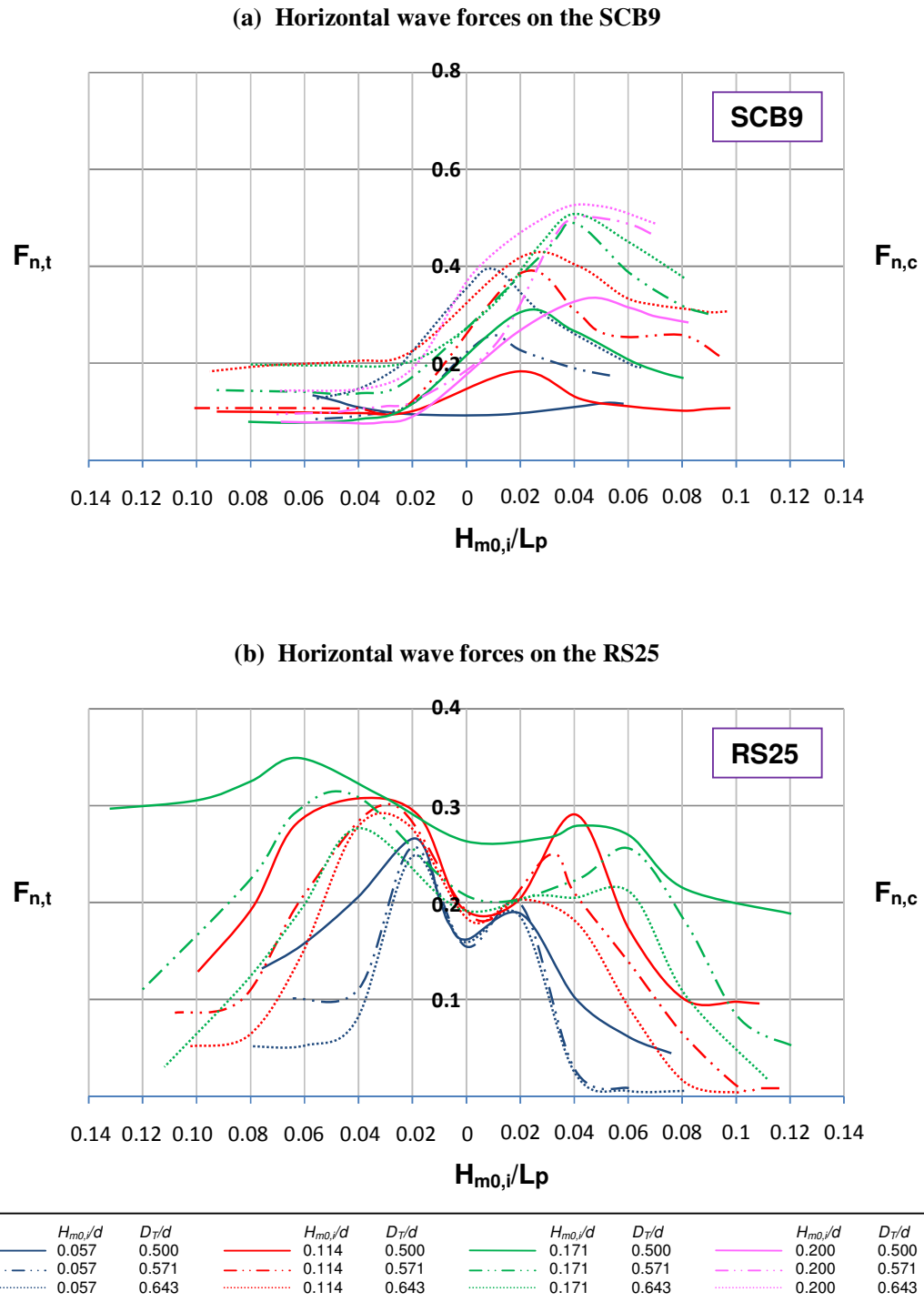


Figure 7.21: Design diagram for positive and negative horizontal wave forces acting on the SCB9-RS25 in irregular waves

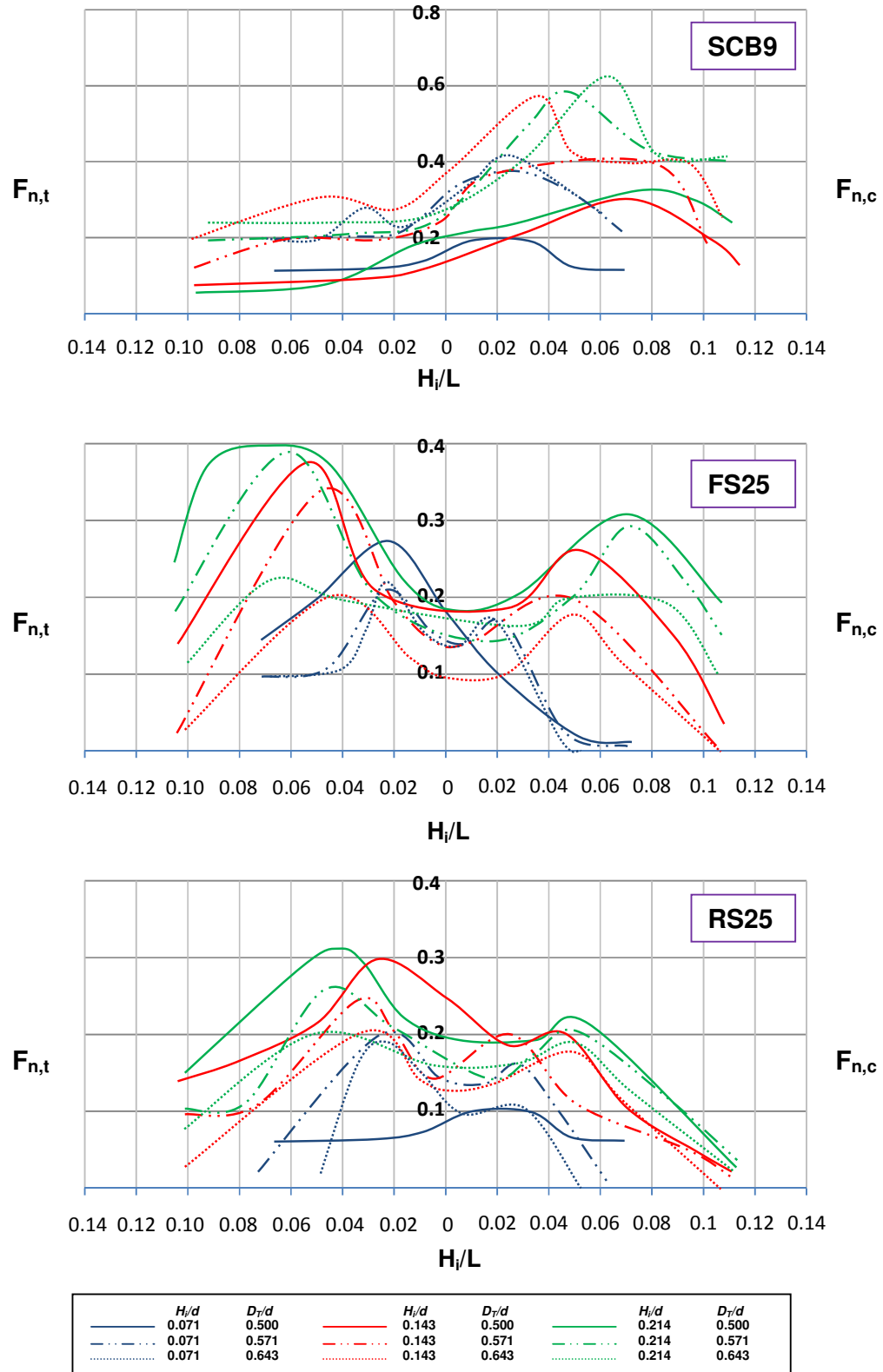
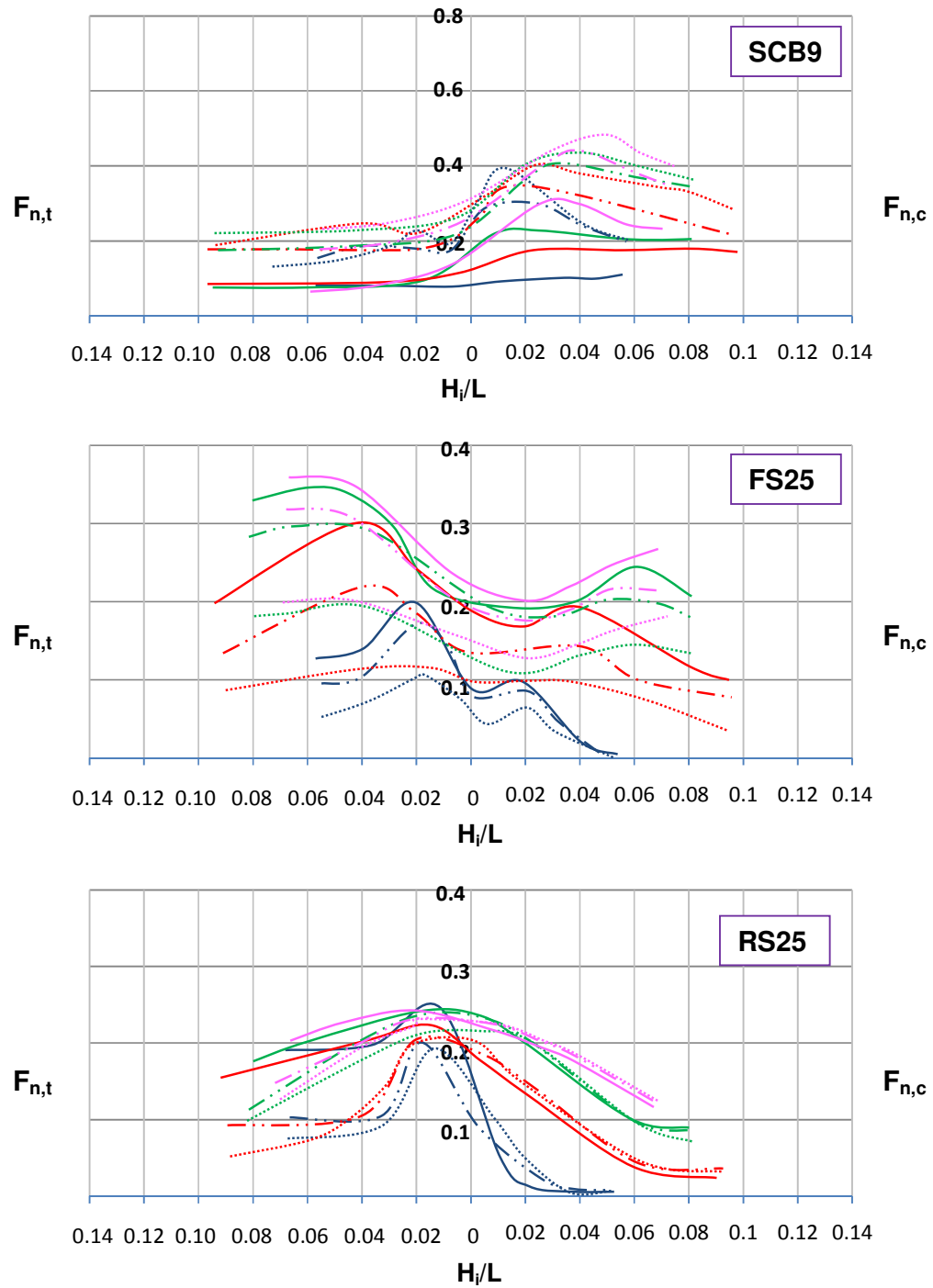


Figure 7.22: Design diagram for positive and negative horizontal wave forces acting on the SCB9-DS25 in regular waves



—	H_{m0}/d	D_T/d	—	H_{m0}/d	D_T/d	—	H_{m0}/d	D_T/d	—	H_{m0}/d	D_T/d
—	0.057	0.500	—	0.114	0.500	—	0.171	0.500	—	0.200	0.500
- - -	0.057	0.571	- - -	0.114	0.571	- - -	0.171	0.571	- - -	0.200	0.571
.....	0.057	0.643	0.114	0.643	0.171	0.643	0.200	0.643

Figure 7.23: Design diagram for positive and negative horizontal wave forces acting on the SCB9-DS25 in irregular waves

8

Engineering Design Tools and Validations

8.1 General

The main purpose of this chapter is to establish empirical equations for the prediction of the hydrodynamic performance of the SCB models. These equations essentially must be robust and easy to use by engineers. A multiple regression technique has been used to develop the predictive equations for the coefficients of transmission, reflection and horizontal wave forces. This chapter also introduces the concept of multiple regression and formation of the empirical equations through the analysis. Accuracy of the empirical models has been validated by a number of statistical parameters. Extra effort has also been put into computing the horizontal wave forces acting on the ‘solid-type’ SCB model using the modified Goda’s method (refer to Section 3.5). Some assumptions have been made to account for the position of the SCB that is fixed at free surface. This proposed method should be further tested and verified by other experimental data sets.

8.2 Multiple Regression Analysis

A multiple regression is a statistical technique that allows the simultaneous testing and modelling of multiple independent variables (*e.g.* x_1, x_2, x_3, \dots) as predictors of a dependent variable, y . In many cases, the dependent and independent variables are termed the “criterion variable” and the “predictor variables” respectively. Here, we consider a least-squares regression, which minimises the sum of squared distances between the data points and the

corresponding predicted values. The model for a multiple linear regression of a criterion variable, y takes the form as follows:

$$y = b_0 + b_1 x_1 + b_2 x_2 + b_3 x_3 + \dots + \varepsilon \quad (8.1)$$

where b_i are the regression coefficients (for $i = 1, 2, 3, \dots$ and b_0 is the intercept) and ε is the error term, which may follow a normal distribution. There are situations in which multiple regression is used to fit models that initially appear to be nonlinear and are subsequently transformed to linear forms by mathematical functions, *e.g.* powers, logarithm, inverse of x , and so on. Transformation of the variables to obtain linear models would make the estimation process much simpler. If this does not help to ‘linearise’ the models, one may use nonlinear regression techniques, including the addition of quadratic and interaction terms, or other models which are more computationally complex.

In this study, a computer program – SPSS/PASW Statistics 17 by IBM (<http://www-01.ibm.com/software/analytics/spss/>) – was used to develop empirical equations for the prediction of the overall hydrodynamic performance of the tested SCB models. SPSS is a powerful software package for data management and advanced statistical analysis, including multiple regression analysis. The software is capable of establishing a linear or nonlinear model of the relationship between the criterion variable and a set of predictor variables. Hence, it is particularly suitable to be used in determining the simplest model that fits an observed relationship associated with the tested SCB models in this study. However, selection of the nonlinear regression model is not readily available in the SPSS software. It is the responsibility of the users (a) to code a nonlinear function that accurately describes the relationship between the criterion and predictor variables; (b) to identify the model parameters and their appropriate starting values; and (c) to check the goodness of fit and residuals of the empirical equations. Failure to set up an appropriate equation would lead to poor estimation of the model.

8.2.1 Multiple Linear Regression

In the present study, empirical analysis was first undertaken using the multiple linear regression (MLR) method with the aim of determining the unique contribution (weightage) of each predictor in affecting the hydrodynamic performance of the SCB test models. Prior to the execution of the MLR, it is important to ensure that the data meet the regression assumptions, *i.e.* linearity, normality of the residuals, homogeneity of variance, lack of

collinearity and absence of outliers (See Appendix K – Part 1 for a discussion of these assumptions). Any violations of these assumptions may lead to misleading results. Validation of the existing data against the assumptions showed that the MLR failed to fit adequately due to violation of some of the regression assumptions. The majority of the data sets showed one or more of these characteristics: a lack of linearity in the relationship, non-normality of the residual and heteroscedasticity of variance (see Appendix K – Part 1). Attempts were made to ‘linearise’ the data through various forms of transformations (an example is presented in Appendix K – Part 2) but these did not improve the quality of the models by much. Therefore, a nonlinear regression method was employed to improve the prediction.

8.2.2 Multiple Polynomial Regressions

Polynomial function is particularly suitable for use in fitting peaks, valleys, ridges and slopes in nonlinear models. In the presence of these nonlinear features, the multiple polynomial regression (MPR) provides good estimation of the arbitrary relationships between criterion and predictor variables. For instance, the second-order polynomial function for a criterion variable that is related to two predictor variables can be formed as:

$$y = b_0 + b_1 x_1^2 + b_2 x_1 x_2 + b_3 x_2^2 + b_4 x_1 + b_5 x_2 + \varepsilon \quad (8.2)$$

The more predictor variables or higher order terms are involved, the more complicated the polynomial function will be. Multiple polynomial regression can be treated as a special case of linear regression by representing Equation (8.2) with:

$$y = b_0 + b_1 X_1 + b_2 X_2 + b_3 X_3 + b_4 x_1 + b_5 x_2 + \varepsilon \quad (8.3)$$

where $X_1 = x_1^2$, $X_2 = x_1 x_2$, and $X_3 = x_2^2$. X_2 is considered to be an interaction term, since x_1 and x_2 interact with each other. If b_2 is significantly different from zero, then the null hypothesis stating that there is no interaction effect can be rejected. The interaction term may sometimes result in multicollinearity, which happens when a high correlation is detected between two or more predictor variables. Strong multicollinearity can cause problems when trying to identify the relative contribution of each predictor in predicting the criterion variable. However, if the “overall” effect of the combined predictors is the only concern of a study, then multicollinearity is not a problem (Draper and Smith, 1981; Neter *et al.*, 1990).

In this study, a stepwise multiple regression was applied in SPSS program. The stepwise method enters the variables into the model one at a time in an order determined by the strength of their correlation with the criterion variable; and at each subsequent step, it adds the variable with the strongest partial correlation. The variable that contributes in the model is retained, but all other variables in the model are then re-tested to assess if they are still contributing to the success of the model. Variables that have less contribution are to be excluded from the model. Thus, this method ensures that the model is made up of the smallest possible set of predictor variables included in the model. A sample of the SPSS outputs using the stepwise method and the description are shown in Appendix L. The model was selected based on two primary criteria: (i) the model account for the highest percentage of variance explained, *i.e.* with the largest adjusted R^2 value, and (ii) for each predictor variable, the p -value for t -test is less than 0.05.

8.2.3 Results

In this study, empirical analyses were undertaken for test cases, namely:

- (a) CASE I : SCB0;
- (b) CASE II : Perforated SCB (SCB9, SCB18 and SCB27);
- (c) CASE III: SCB9 with different B/d ratios;
- (d) CASE IV: SCB9-RS25; and
- (e) CASE V : SCB9-DS25.

The formation of the polynomial functions for the hydrodynamic coefficients of the tested SCB depends on the number of predictor variables concerned:

- (a) 3 predictors (*i.e.* Π_1 , Π_2 and Π_3):

$$C_i \sim \left\{ \begin{array}{l} b_1 \Pi_1^2 + b_2 \Pi_1 \Pi_2 + b_3 \Pi_1 \Pi_3 + b_4 \Pi_2^2 + b_5 \Pi_2 \Pi_3 \\ + b_6 \Pi_3^2 + b_7 \Pi_1 + b_8 \Pi_2 + b_9 \Pi_3 + b_{10} \end{array} \right\} \quad (8.4)$$

(b) 4 predictors (i.e. Π_1, Π_2, Π_3 and Π_4):

$$C_i \sim \left\{ \begin{array}{l} b_1 \Pi_1^2 + b_2 \Pi_1 \Pi_2 + b_3 \Pi_1 \Pi_3 + b_4 \Pi_1 \Pi_4 + b_5 \Pi_2^2 + b_6 \Pi_2 \Pi_3 + b_7 \Pi_2 \Pi_4 \\ + b_8 \Pi_3^2 + b_9 \Pi_3 \Pi_4 + b_{10} \Pi_4^2 + b_{11} \Pi_1 + b_{12} \Pi_2 + b_{13} \Pi_3 + b_{14} \Pi_4 + b_{15} \end{array} \right\} \quad (8.5)$$

The Π 's relate to the dimensionless parameters defined by the Buckingham Pi theorem as discussed in Chapter 3, and b_i 's are the regression coefficients (where $i = 1, 2, 3, \dots$). The empirical equations and the limiting values for the respective types of SCB are tabulated in Table 8.1 and the corresponding regression coefficients are given in Tables 8.2 to 8.6. It must stressed that these empirical relationships are valid only over the test ranges of Π 's covered by the experiments. Outside the range of the experiments, the physical processes may not adhere to the same trend as defined by the mathematical function.

Table 8.1: Summary of notation for the empirical models for the SCB breakwaters

	CASE I	CASE II	CASE III	CASE IV	CASE V
Description	SCB0	Perforated SCB (SCB9/18/27)	SCB9 with different B/d	SCB9-RS25	SCB9-DS25
Emp. Equation	Equation (8.4)	Equation (8.5)	Equation (8.5)	Equation (8.4)	Equation (8.4)
Π_1 (Hydraulic coeff.)	B/L	B/L	B/L	B/L	B/L
Π_1 (Force coeff.)	H/d	H/d	H/d	H/d	H/d
Π_2	D/d	D/d	D/d	D_T/d	D_T/d
Π_3	H/L	H/L	H/L	H/L	H/L
Π_4	<i>n.a.</i>	ϵ_{SCB}	B/d	<i>n.a.</i>	<i>n.a.</i>
Test ranges	$\epsilon_{SCB} = 0\%$ $B/d \approx 0.71$ $0.12 < B/L < 0.50$ $0.07 < D/d < 0.21$ $0.01 < H/L < 0.12$ $0.02 < H/d < 0.30$	$9\% \leq \epsilon_{SCB} \leq 27\%$ $B/d \approx 0.71$ $0.12 < B/L < 0.66$ $0.07 < D/d < 0.21$ $0.01 < H/L < 0.12$ $0.01 < H/d < 0.34$	$\epsilon_{SCB} = 9\%$ $0.71 < B/d < 1.67$ $0.12 < B/L < 0.66$ $0.07 < D/d < 0.50$ $0.01 < H/L < 0.12$ $0.02 < H/d < 0.50$	$\epsilon_{SCB} = 9\%$ $\epsilon_{RS} = 25\%$ $B/d \approx 0.71$ $0.12 < B/L < 0.66$ $0.07 < D/d < 0.21$ $0.50 < D_T/d < 0.64$ $0.01 < H/L < 0.12$ $0.05 < H/d < 0.25$	$\epsilon_{SCB} = 9\%$ $\epsilon_{RS} = \epsilon_{DS} = 25\%$ $B/d \approx 0.71$ $0.12 < B/L < 0.66$ $0.07 < D/d < 0.21$ $0.50 < D_T/d < 0.64$ $0.01 < H/L < 0.12$ $0.05 < H/d < 0.25$

Table 8.2: Regression coefficients of the SCB0 model (CASE I)

(a) Regular waves

	Hydraulic Coefficients				Force Coefficients	
	C_T	C_R	C_F	C_C	$F_{n,t, SCB9}$	$F_{n,c, SCB9}$
b_1	4.618	-3.996	-6.307	3.275	6.714	15.764
b_2	-1.464	–	-3.428	-6.169	21.068	-20.274
b_3	–	3.600	12.077	-20.934	–	–
b_4	–	1.877	–	9.399	-9.748	–
b_5	19.230	-16.006	-27.101	22.193	–	–
b_6	–	-23.903	-126.632	32.037	–	–
b_7	-4.494	3.513	4.908	–	-3.915	–
b_8	-1.344	–	4.377	-3.323	-4.063	–
b_9	-2.706	–	12.354	–	–	–
b_{10}	1.466	0.012	0.194	0.500	0.117	1.365

(b) Irregular waves

	Hydraulic Coefficients				Force Coefficients	
	C_T	C_R	C_F	C_C	$F_{n,t, SCB9}$	$F_{n,c, SCB9}$
b_1	2.754	-2.929	-4.137	0.481	5.584	20.100
b_2	-2.624	2.434	-4.238	-2.117	17.763	-26.274
b_3	–	8.387	–	–	–	-39.447
b_4	-1.646	–	-6.638	1.977	-4.507	16.416
b_5	6.048	-23.672	-7.865	–	–	–
b_6	36.843	-17.718	–	–	80.000	–
b_7	-2.712	2.083	3.807	–	-2.240	1.438
b_8	–	0.526	5.024	-1.473	-4.811	-3.335
b_9	-4.009	-0.993	–	–	-10.035	4.761
b_{10}	1.100	0.206	0.658	0.478	0.233	1.182

Notes:

- Equation (8.4) is used to determine the hydraulic and force coefficients, where $\Pi_1 = B/L$ (for hydraulic coefficients) or $\Pi_1 = H/d$ (for force coefficients), $\Pi_2 = D/d$ and $\Pi_3 = H/L$.
- Limiting values of the test ranges for the empirical model are: $\varepsilon_{SCB} = 0\%$; $B/d \approx 0.71$, $0.12 < B/L < 0.50$, $0.07 < D/d < 0.21$, $0.01 < H/L < 0.12$ and $0.02 < H/d < 0.30$.
- b_{10} is the intercept.

Table 8.3: Regression coefficients of the SCB 9, SCB18 and SCB27 models (CASE II)

(a) Regular waves

	Hydraulic Coefficients				Force Coefficients	
	C_T	C_R	C_F	C_C	$F_{n,t, SCB9}$	$F_{n,c, SCB9}$
b_1	0.761	1.453	<i>n.a.</i>	-0.374	10.295	35.685
b_2	-6.758	1.263	<i>n.a.</i>	–	13.180	-22.388
b_3	2.711	-7.260	<i>n.a.</i>	-6.015	-29.491	–
b_4	–	0.009	<i>n.a.</i>	0.062	0.021	-0.112
b_5	–	-3.817	<i>n.a.</i>	–	19.251	–
b_6	–	-15.509	<i>n.a.</i>	-12.560	9.121	–
b_7	–	–	<i>n.a.</i>	0.065	–	–
b_8	–	-7.730	<i>n.a.</i>	-14.553	42.323	–
b_9	–	-0.038	<i>n.a.</i>	–	-0.128	–
b_{10}	–	–	<i>n.a.</i>	–	0.001	-0.003
b_{11}	-0.842	-0.548	<i>n.a.</i>	-0.555	-4.234	–
b_{12}	-0.270	2.328	<i>n.a.</i>	–	-9.501	2.465
b_{13}	-3.156	5.211	<i>n.a.</i>	4.050	–	–
b_{14}	–	–	<i>n.a.</i>	-0.017	-0.036	0.116
b_{15}	1.224	-0.100	<i>n.a.</i>	1.120	0.721	-0.245

(b) Irregular waves

	Hydraulic Coefficients				Force Coefficients	
	C_T	C_R	C_F	C_C	$F_{n,t, SCB9}$	$F_{n,c, SCB9}$
b_1	0.666	–	0.855	-1.029	12.514	25.605
b_2	-6.274	–	-4.070	–	6.635	–
b_3	3.658	-4.768	–	–	-26.158	33.644
b_4	–	0.004	0.010	0.035	-0.016	-0.037
b_5	–	–	-5.242	–	9.968	–
b_6	–	–	-7.795	–	–	–
b_7	0.006	0.009	-0.021	0.052	0.025	–
b_8	28.557	–	-46.147	–	49.194	-90.883
b_9	0.044	–	-0.071	–	–	–
b_{10}	–	–	–	–	–	–
b_{11}	-0.810	0.624	-0.275	–	-2.981	-4.321
b_{12}	-0.325	0.809	3.454	–	-6.118	–
b_{13}	-4.803	–	7.182	–	-1.946	4.394
b_{14}	–	–	-0.007	-0.011	–	-0.020
b_{15}	1.191	-0.003	0.960	1.057	0.197	1.133

Notes:

- Equation (8.5) is used to determine the hydraulic and force coefficients, where $\Pi_1 = B/L$ (for hydraulic coefficients) or $\Pi_1 = H/d$ (for force coefficients), $\Pi_2 = D/d$, $\Pi_3 = H/L$ and $\Pi_4 = \varepsilon_{SCB}$.
- Limiting values of the test ranges for the empirical model are: $9\% \leq \varepsilon_{SCB} \leq 27\%$; $B/d \approx 0.71$, $0.12 < B/L < 0.66$, $0.07 < D/d < 0.21$, $0.01 < H/L < 0.12$ and $0.01 < H/d < 0.34$.
- b_{15} is the intercept.

Table 8.4: Regression coefficients of the SCB9 model for different B/d ratios (CASE III)

(a) Regular waves

	Hydraulic Coefficients				Force Coefficients	
	C_T	C_R	C_F	C_C	$F_{n,t, SCB9}$	$F_{n,c, SCB9}$
b_1	1.302	1.789	<i>n.a.</i>	<i>n.a.</i>	7.500	5.134
b_2	-3.484	–	<i>n.a.</i>	<i>n.a.</i>	–	-7.043
b_3	1.505	-6.218	<i>n.a.</i>	<i>n.a.</i>	-23.056	–
b_4	0.947	–	<i>n.a.</i>	<i>n.a.</i>	-2.177	-3.292
b_5	1.156	–	<i>n.a.</i>	<i>n.a.</i>	2.177	4.647
b_6	–	-2.862	<i>n.a.</i>	<i>n.a.</i>	17.158	–
b_7	0.976	-0.430	<i>n.a.</i>	<i>n.a.</i>	–	–
b_8	–	17.707	<i>n.a.</i>	<i>n.a.</i>	46.885	-49.883
b_9	–	–	<i>n.a.</i>	<i>n.a.</i>	–	–
b_{10}	-0.274	–	<i>n.a.</i>	<i>n.a.</i>	-0.580	–
b_{11}	-2.356	-0.576	<i>n.a.</i>	<i>n.a.</i>	–	6.980
b_{12}	-2.183	1.337	<i>n.a.</i>	<i>n.a.</i>	-3.383	-1.245
b_{13}	-2.397	–	<i>n.a.</i>	<i>n.a.</i>	-4.055	–
b_{14}	0.355	–	<i>n.a.</i>	<i>n.a.</i>	2.299	–
b_{15}	1.289	0.098	<i>n.a.</i>	<i>n.a.</i>	-1.323	0.728

(b) Irregular waves

	Hydraulic Coefficients				Force Coefficients	
	C_T	C_R	C_F	C_C	$F_{n,t, SCB9}$	$F_{n,c, SCB9}$
b_1	0.715	–	0.562	-0.919	8.585	12.938
b_2	-3.770	-0.770	-2.962	-1.617	0.911	–
b_3	2.846	-1.802	–	–	-19.343	-15.636
b_4	1.073	0.112	0.899	0.432	-2.609	-5.999
b_5	0.724	-0.543	-3.604	0.691	4.552	–
b_6	–	–	–	–	11.797	-6.671
b_7	1.000	-0.226	1.182	-0.477	-0.883	–
b_8	27.372	-18.503	-40.854	–	39.638	-54.862
b_9	0.619	–	0.680	–	–	4.357
b_{10}	-0.126	0.102	0.197	0.316	-0.611	1.315
b_{11}	-1.885	0.519	-0.742	0.274	–	4.749
b_{12}	-1.785	1.406	1.421	0.988	-3.322	–
b_{13}	-4.590	1.056	4.429	–	-3.351	3.597
b_{14}	-0.131	-0.350	-1.222	-0.982	2.657	-2.691
b_{15}	1.424	0.158	1.737	1.439	-1.527	2.002

Notes:

- Equation (8.5) is used to determine the hydraulic and force coefficients, where $\Pi_1 = B/L$ (for hydraulic coefficients) or $\Pi_1 = H/d$ (for force coefficients), $\Pi_2 = D/d$, $\Pi_3 = H/L$ and $\Pi_4 = B/d$.
- Limiting values of the test ranges for the empirical model are: $\varepsilon_{SCB9} = 9\%$; $0.71 < B/d < 1.67$, $0.12 < B/L < 0.66$, $0.07 < D/d < 0.50$, $0.01 < H/L < 0.12$, and $0.02 < H/d < 0.50$.
- b_{15} is the intercept.

Table 8.5: Regression coefficients of the SCB9-RS25 model (CASE IV)

(a) Regular waves

	Hydraulic Coefficients				Force Coefficients			
	C_T	C_R	C_F	C_C	$F_{n,t} SCB9$	$F_{n,c} SCB9$	$F_{n,t} RS25$	$F_{n,c} RS25$
b_1	2.323	0.969	<i>n.a.</i>	–	–	7.061	4.913	-2.398
b_2	-4.737	-0.903	<i>n.a.</i>	–	–	–	–	–
b_3	–	–	<i>n.a.</i>	–	–	–	-7.190	–
b_4	–	1.299	<i>n.a.</i>	-11.461	-3.564	-11.099	–	–
b_5	14.370	-17.700	<i>n.a.</i>	-16.102	–	-14.004	13.384	-7.198
b_6	29.064	-47.804	<i>n.a.</i>	-52.035	–	–	–	13.284
b_7	–	–	<i>n.a.</i>	-1.252	–	–	-2.177	2.072
b_8	-0.871	–	<i>n.a.</i>	14.331	3.196	15.075	–	–
b_9	-13.489	15.207	<i>n.a.</i>	14.222	–	6.083	-4.163	–
b_{10}	1.669	-0.196	<i>n.a.</i>	-3.005	-0.800	-4.662	-0.148	0.080

(b) Irregular waves

	Hydraulic Coefficients				Force Coefficients			
	C_T	C_R	C_F	C_C	$F_{n,t} SCB9$	$F_{n,c} SCB9$	$F_{n,t} RS25$	$F_{n,c} RS25$
b_1	1.185	0.569	1.359	–	–	–	5.592	-4.903
b_2	-3.373	-1.719	-5.528	-1.589	–	1.503	1.393	-0.517
b_3	4.048	-2.773	–	–	–	–	-9.860	3.457
b_4	1.390	–	-7.836	-6.236	-3.700	-9.270	–	–
b_5	2.821	-9.619	3.953	–	–	-11.717	5.713	-4.211
b_6	34.716	-29.740	-13.288	-15.224	–	–	-8.754	15.184
b_7	–	0.987	2.222	–	–	0.824	-2.968	2.830
b_8	-2.276	1.249	10.586	8.033	3.468	12.457	–	–
b_9	-7.812	8.687	–	1.870	–	4.994	1.016	-1.692
b_{10}	1.888	-0.496	-2.194	-1.190	-0.895	-3.903	-0.135	0.025

Notes:

- Equation (8.4) is used to determine the hydraulic and force coefficients, where $\Pi_1 = B/L$ (for hydraulic coefficients) or $\Pi_1 = H/d$ (for force coefficients), $\Pi_2 = D_T/d$ and $\Pi_3 = H/L$.
- Limiting values of the test ranges for the empirical model are: $\varepsilon_{SCB} = 9\%$; $\varepsilon_{RS} = 25\%$; $B/d \approx 0.71$, $0.12 < B/L < 0.65$, $0.07 < D/d < 0.21$, $0.50 < D_T/d < 0.64$, $0.01 < H/L < 0.12$ and $0.05 < H/d < 0.25$.
- b_{10} is the intercept.

Table 8.6: Regression coefficients of the SCB9-DS25 model (CASE V)

(a) Regular waves

	Hydraulic Coefficients				Force Coefficients					
	C_T	C_R	C_F	C_C	$F_{n,t,SCB9}$	$F_{n,c,SCB9}$	$F_{n,t,FS25}$	$F_{n,c,FS25}$	$F_{n,t,RS25}$	$F_{n,c,RS25}$
b_1	2.520	1.435	<i>n.a.</i>	2.054	2.046	–	7.880	-6.888	–	-2.274
b_2	-3.029	-3.683	<i>n.a.</i>	2.190	–	–	1.796	–	-2.341	–
b_3	–	–	<i>n.a.</i>	–	-9.286	–	-30.927	26.369	11.266	-10.575
b_4	–	–	<i>n.a.</i>	-13.872	–	-13.004	3.157	-0.476	-2.570	-1.876
b_5	11.048	-16.693	<i>n.a.</i>	–	–	-9.463	–	–	6.803	-4.395
b_6	44.207	-44.642	<i>n.a.</i>	–	14.542	–	48.017	-30.537	-25.511	27.780
b_7	-0.977	1.439	<i>n.a.</i>	-3.472	–	1.292	-2.921	1.893	–	2.335
b_8	-0.737	2.082	<i>n.a.</i>	16.803	-1.167	16.912	-2.800	–	3.495	2.293
b_9	-13.684	14.314	<i>n.a.</i>	-3.024	–	3.870	–	-1.331	–	-1.713
b_{10}	1.553	-0.922	<i>n.a.</i>	-3.523	0.466	-5.134	0.505	0.153	-1.342	-0.657

(b) Irregular waves

	Hydraulic Coefficients				Force Coefficients					
	C_T	C_R	C_F	C_C	$F_{n,t,SCB9}$	$F_{n,c,SCB9}$	$F_{n,t,FS25}$	$F_{n,c,FS25}$	$F_{n,t,RS25}$	$F_{n,c,RS25}$
b_1	1.522	0.669	1.096	1.788	–	-1.303	5.896	-7.137	-0.917	-2.771
b_2	-2.256	-3.373	-5.556	–	–	1.147	1.567	-1.896	-2.653	-1.296
b_3	–	-2.382	–	-9.673	–	–	-19.322	20.253	4.891	-5.473
b_4	1.788	1.250	-3.088	-4.773	–	-10.280	2.013	-0.217	-4.195	-1.698
b_5	3.890	-6.615	–	4.639	–	-10.915	2.907	–	4.268	-2.365
b_6	67.052	-16.326	-23.971	61.567	–	14.001	14.336	-17.661	-25.842	27.721
b_7	-0.603	1.869	2.065	-1.476	–	0.870	-2.661	3.162	0.876	2.850
b_8	-2.643	–	4.592	6.540	-1.014	13.517	-1.699	–	5.420	2.237
b_9	-10.436	5.904	4.468	-7.154	0.270	3.670	–	-1.372	1.329	-2.593
b_{10}	1.915	-0.162	-0.245	-0.816	0.402	-4.131	0.225	0.044	-1.917	-0.702

Notes:

- Equation (8.4) is used to determine the hydraulic and force coefficients, where $\Pi_1 = B/L$ (for hydraulic coefficients) or $\Pi_1 = H/d$ (for force coefficients), $\Pi_2 = D_T/d$ and $\Pi_3 = H/L$.
- Limiting values of the test ranges for the empirical model are: $\varepsilon_{SCB} = 9\%$; $\varepsilon_{FS} = \varepsilon_{RS} = 25\%$; $B/d \approx 0.71, 0.12 < B/L < 0.65, 0.07 < D/d < 0.21, 0.50 < D_T/d < 0.64, 0.01 < H/L < 0.12$ and $0.05 < H/d < 0.25$.
- b_{10} is the intercept.

8.2.4 Model Validation

8.2.4.1 Validation Tools

Validation of the empirical model with the residuals for the respective hydrodynamic coefficients for each test case is illustrated in Figures 8.1 to 8.10. Note that the predicted coefficient C_L is estimated by Equation (3.16) once the predicted values for C_T and C_R are obtained. These figures show the scatter plots of unstandardized residuals verses the measured values for five cases as mentioned in Section 8.2.3. It can be seen that the majority of the plots show no obvious patterns, thereby confirming that the assumptions of linearity and homogeneity of variance have been met. In order to gain insight on the validation of models and to quantify the variability of the predicted coefficients, several statistical parameters have been selected and described as follows:

(a) *Coefficient of determination, R^2*

R^2 indicates the proportion of the variation in the criterion variable which is accounted for by the model; in other words, it is a measure of the goodness of prediction of the criterion variable by the predictor variables. R^2 is defined by the ratio of the explained variation to the total variation:

$$R^2 = \left[\frac{\sum (Y_m - \bar{Y}_m)(Y_p - \bar{Y}_p)}{\sqrt{\sum (Y_m - \bar{Y}_m)^2 \sum (Y_p - \bar{Y}_p)^2}} \right]^2 \quad (8.6)$$

where Y_p and Y_m are the predicted and measured values of the criterion variable, respectively, and \bar{Y}_p and \bar{Y}_m are the mean values of the predicted and measured variables respectively. Note that R^2 ranges from 0 to 1, with $R^2 = 0$ if there is no linear relation between the criterion and predictor variables, and $R^2 = 1$ if all the observations fall on the regression line.

(b) *Adjusted R squared, R_a^2*

The sample estimate of R^2 tends to overestimate the success of the model especially when adding a large number of variables to the model. To compensate for the optimistic bias of R^2 , an adjusted R squared (R_a^2) which is a function of R^2 adjusted by the number of predictor variables in the model, p and the sample size, N is usually adopted:

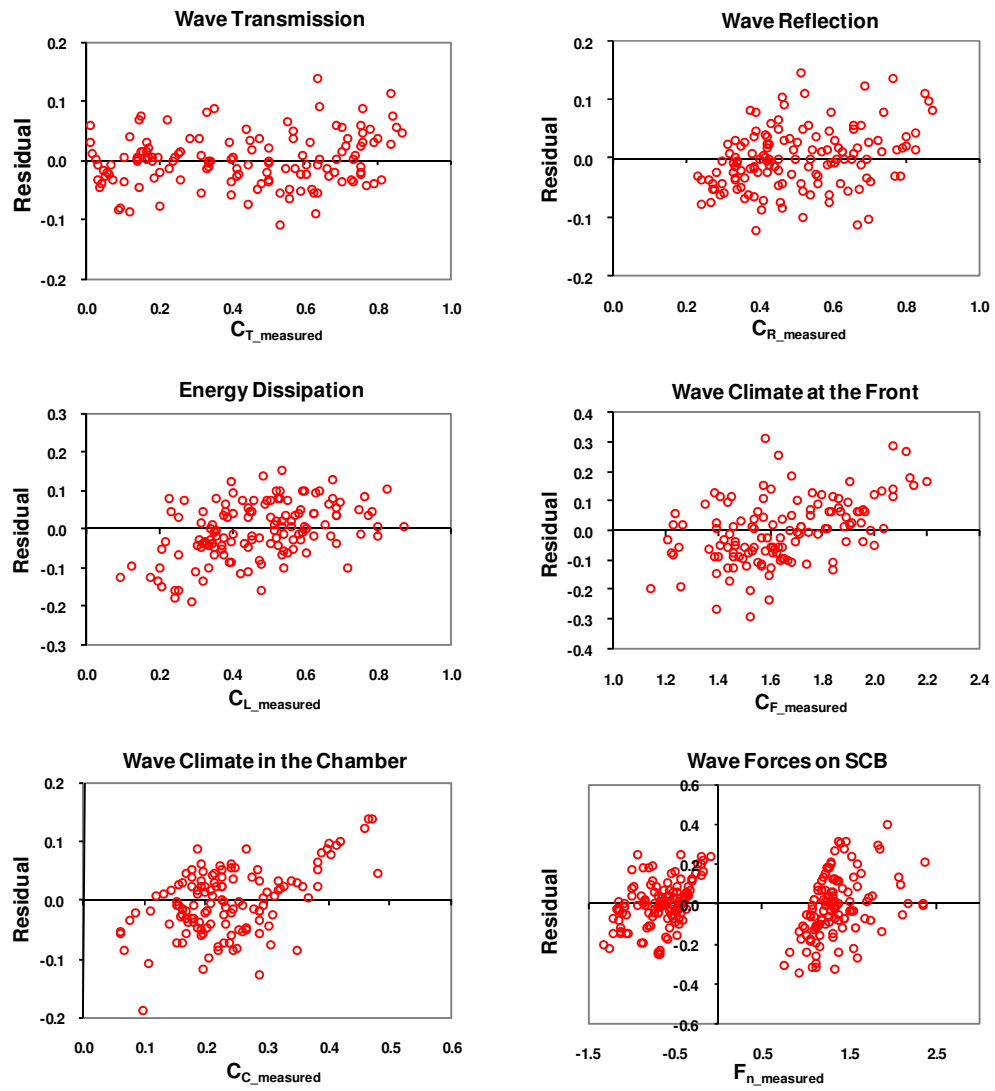


Figure 8.1: Validation of empirical models for SCB0 (CASE I) in regular waves

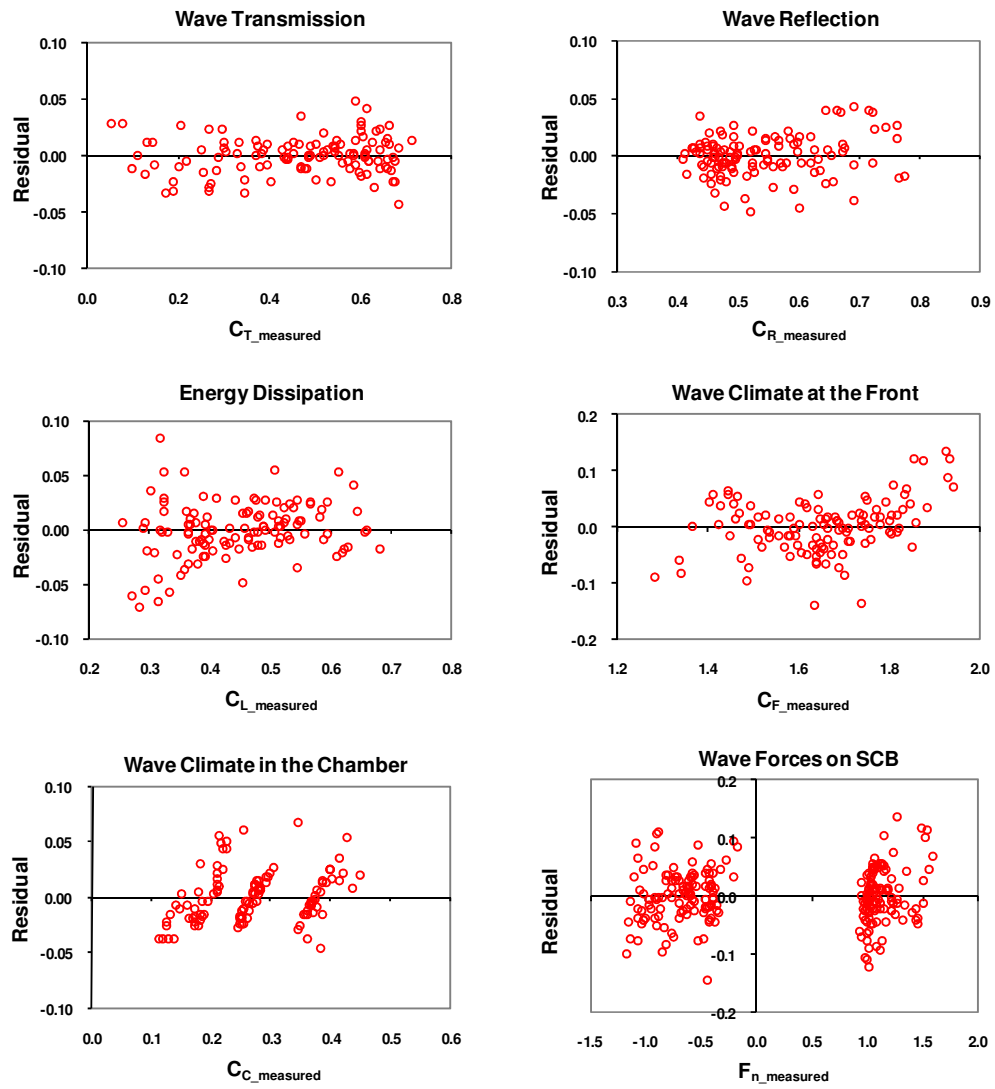


Figure 8.2: Validation of empirical models for SCB0 (CASE I) in irregular waves

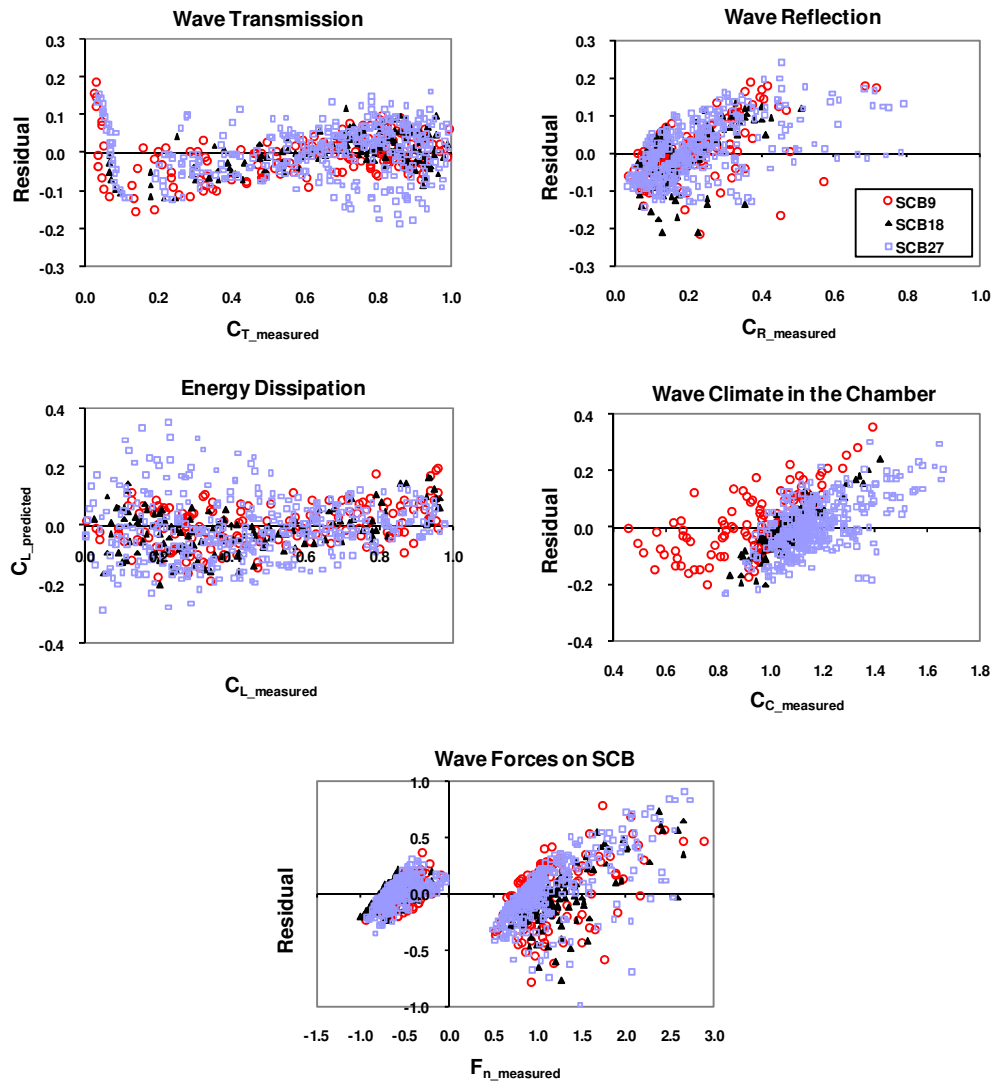


Figure 8.3: Validation of empirical models for the perforated SCB's (CASE II) in regular waves

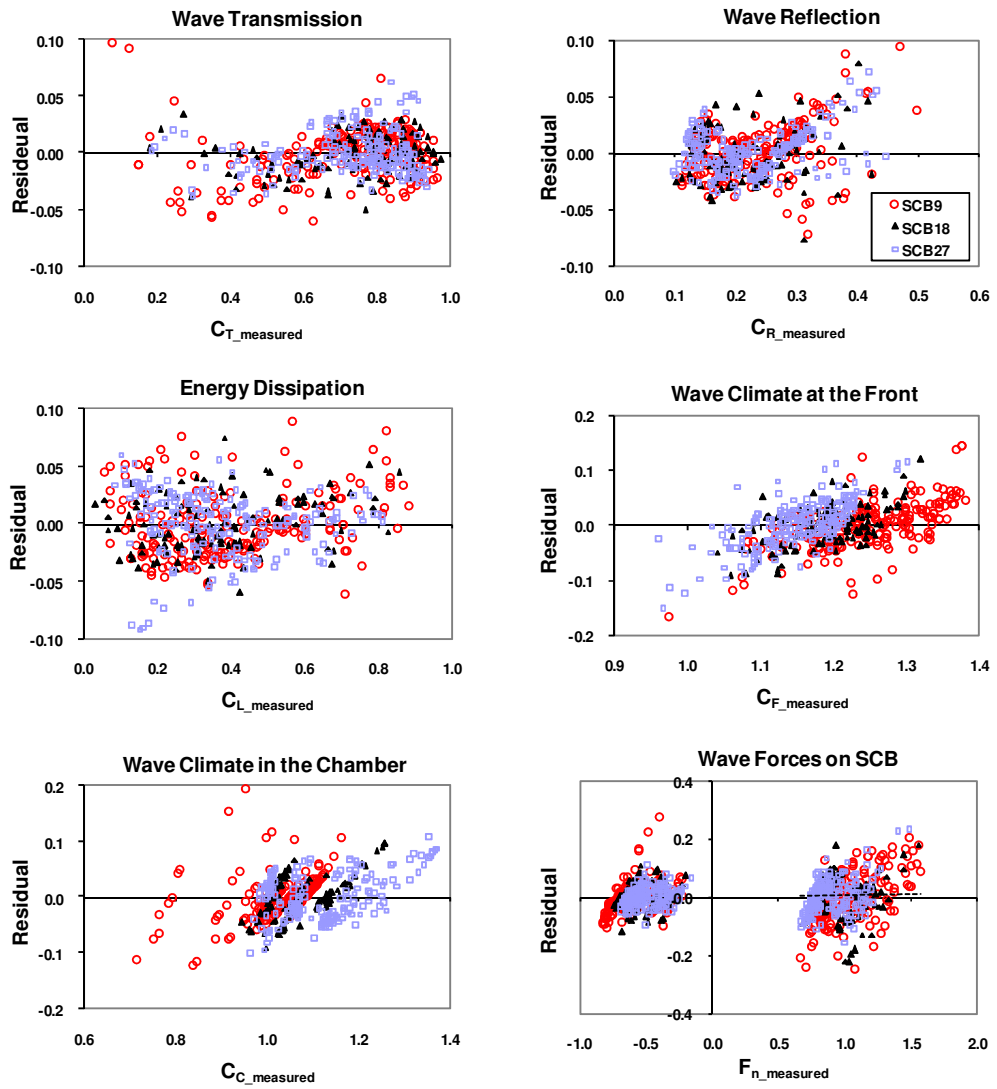


Figure 8.4: Validation of empirical models for the perforated SCB's (CASE II) in irregular waves

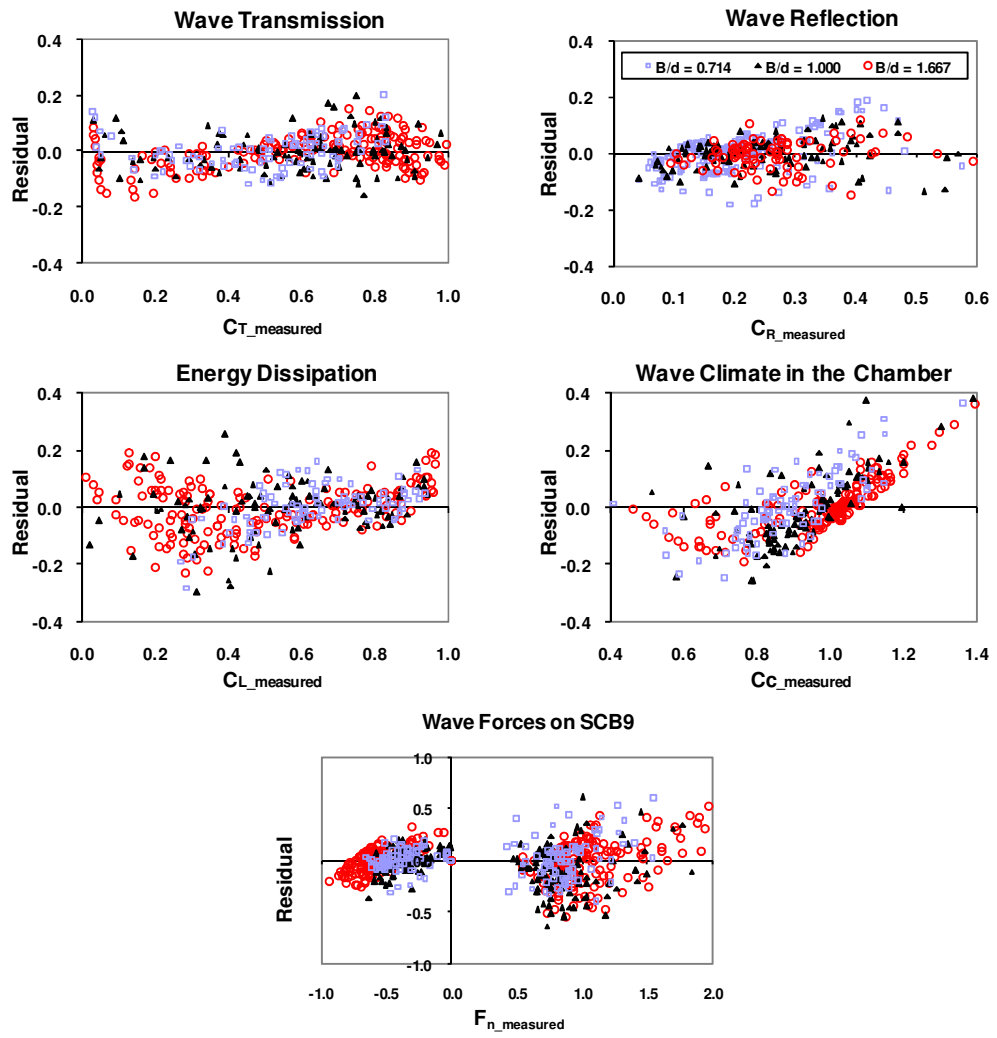


Figure 8.5: Validation of empirical models for the SCB9 with different B/d ratios (CASE III) in regular waves

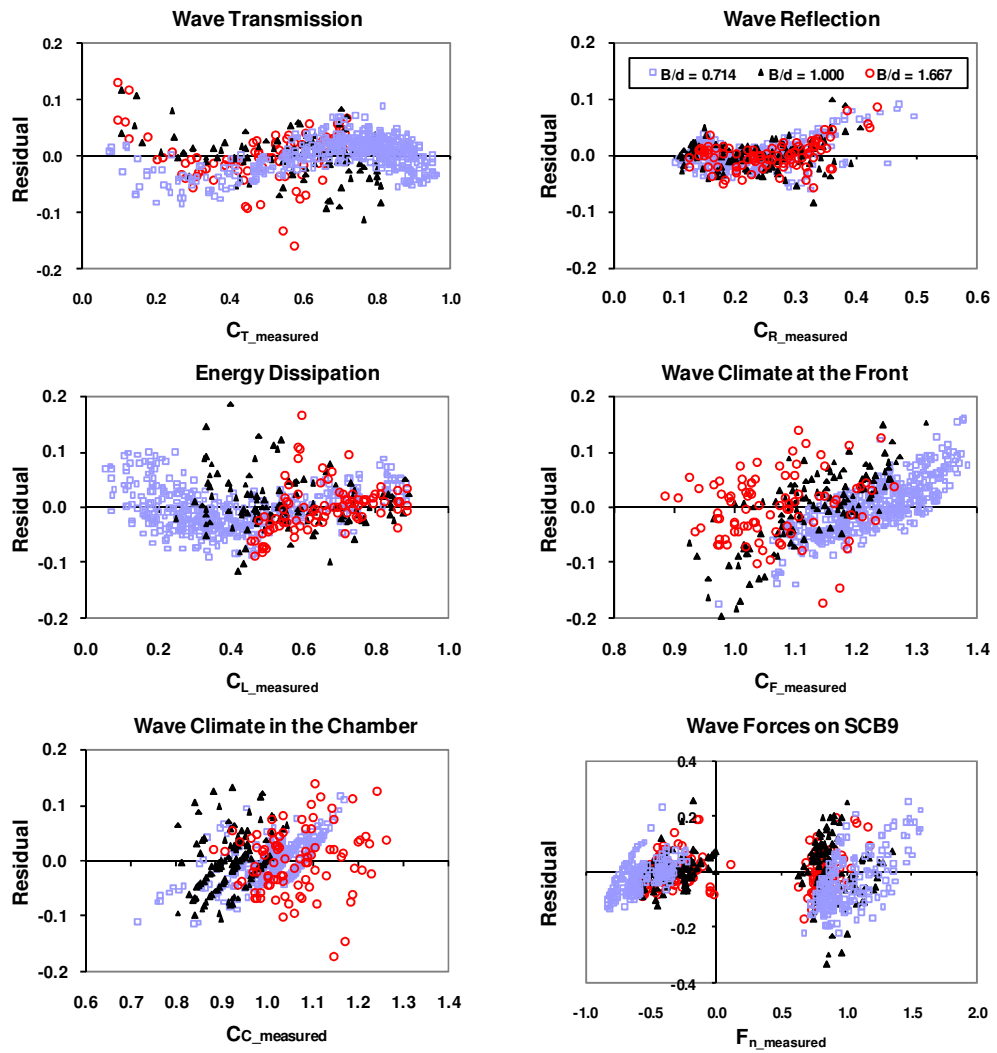


Figure 8.6: Validation of empirical models for the SCB9 with different B/d ratios (CASE III) in irregular waves

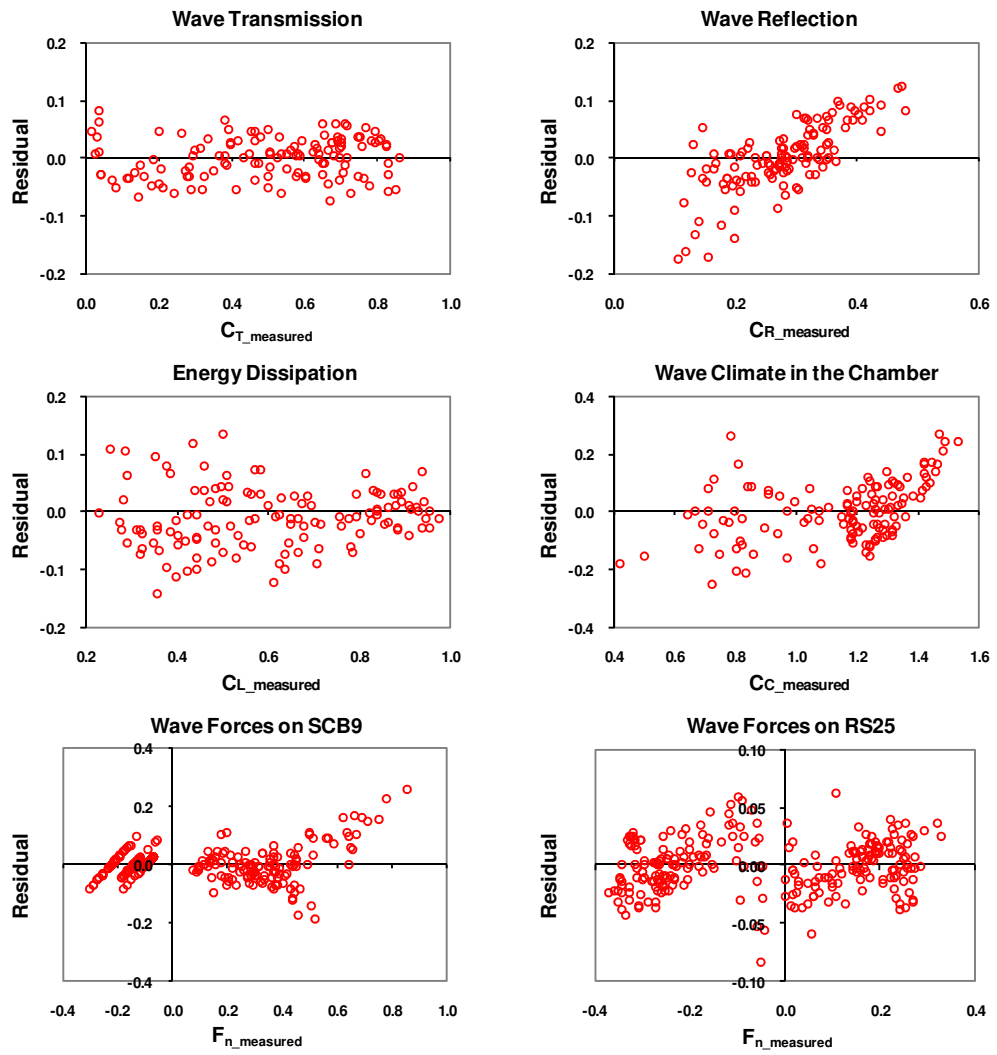


Figure 8.7: Validation of empirical models for SCB9-RS25 (CASE IV) in regular waves

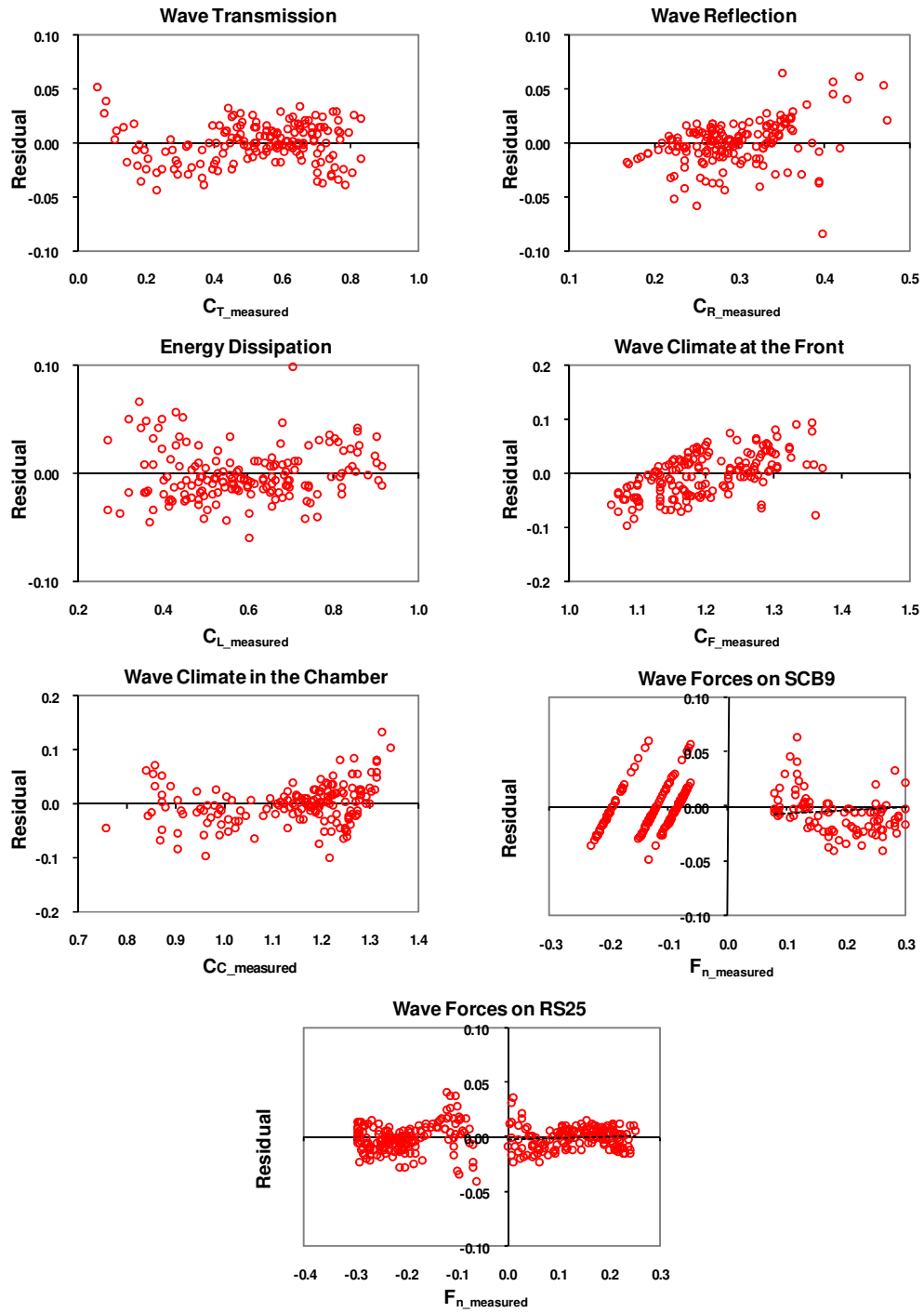


Figure 8.8: Validation of empirical models for SCB9-RS25 (CASE IV) in irregular waves

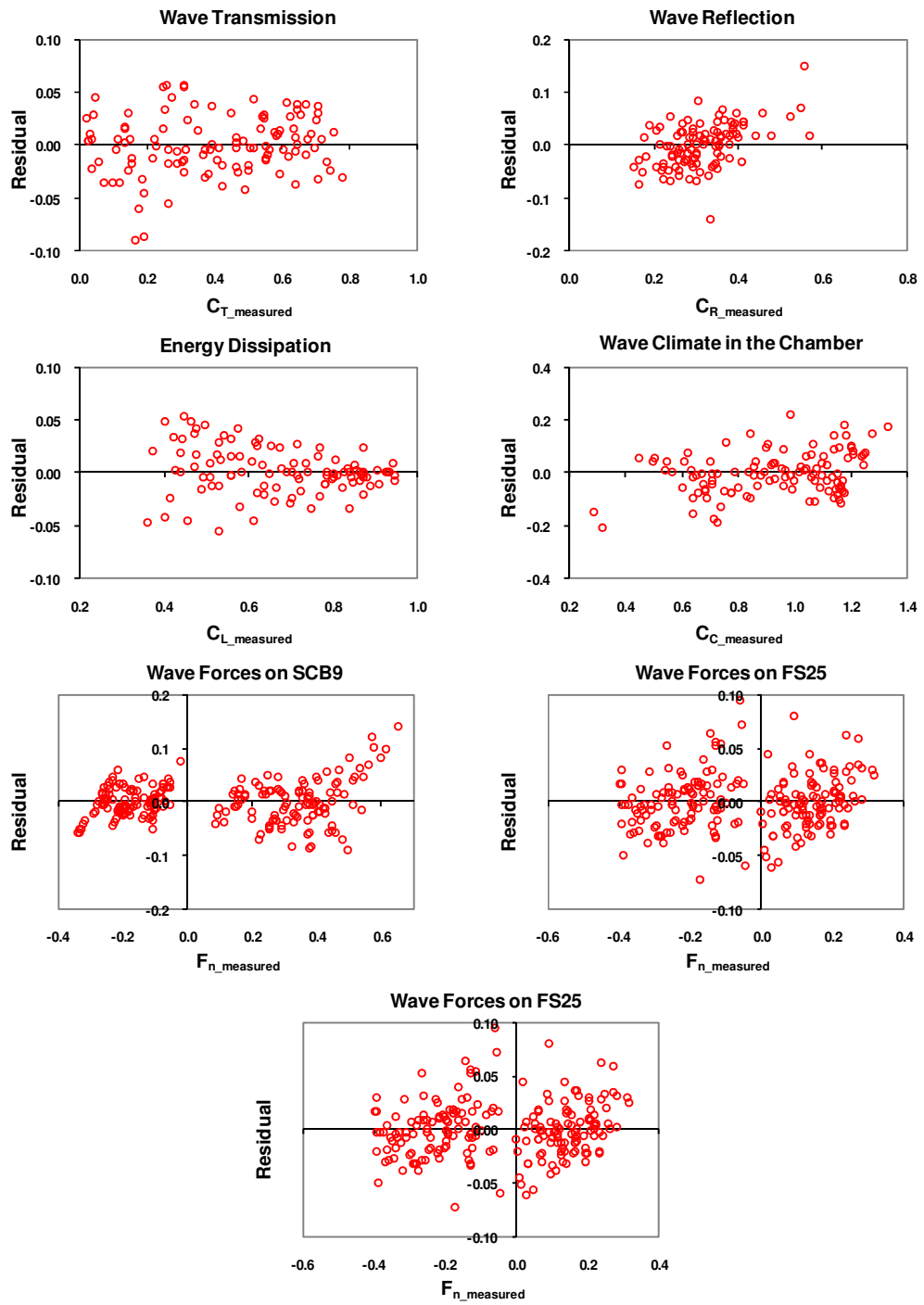


Figure 8.9: Validation of empirical models for SCB9-DS25 (CASE V) in regular waves

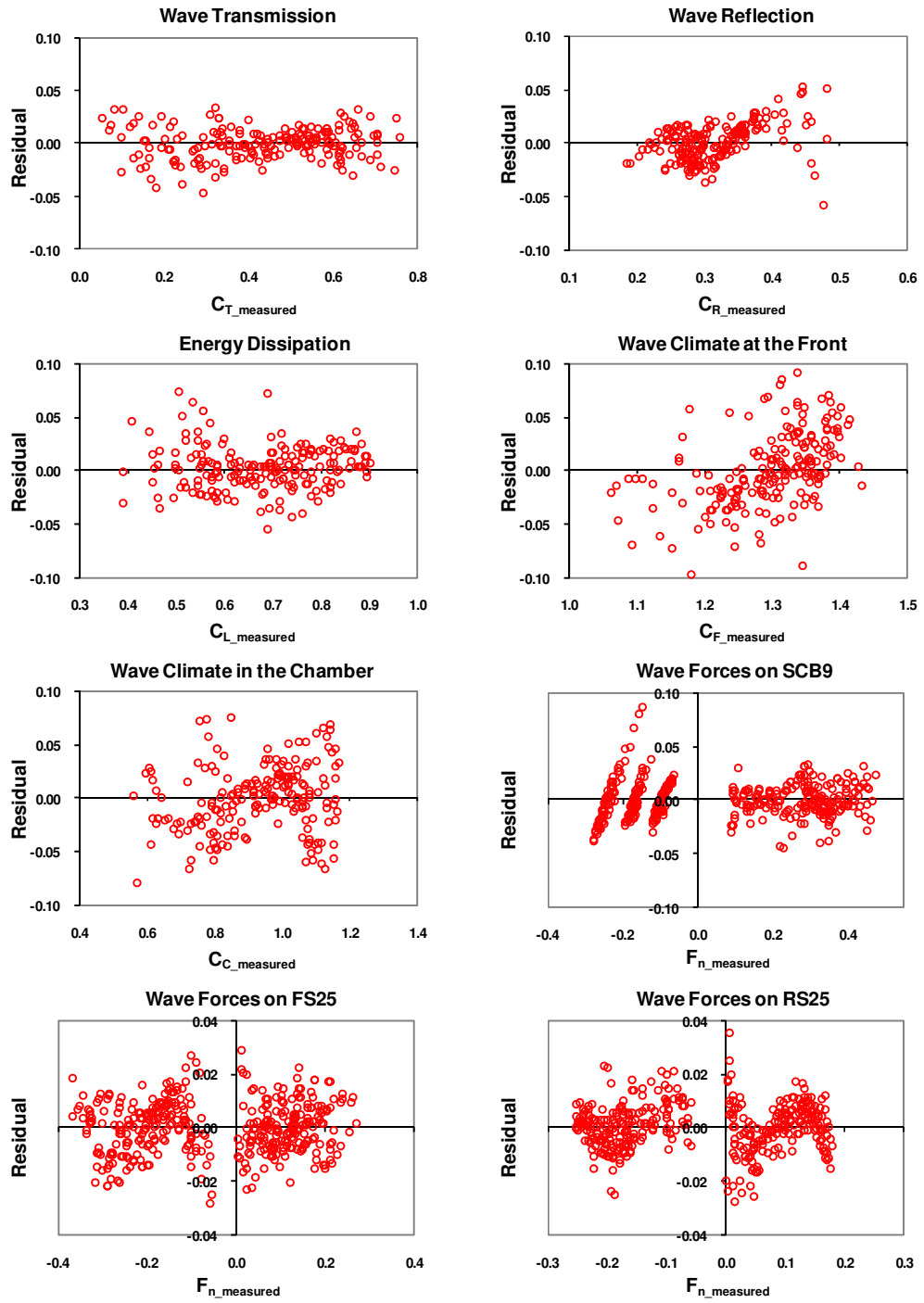


Figure 8.10: Validation of empirical models for SCB9-DS25 (CASE V) in irregular waves

$$R_a^2 = R^2 - \frac{p(1-R^2)}{N-p-1} \quad (8.7)$$

(c) *Root mean squared error, RMSE*

The root mean square error (*RMSE*), also termed as the standard error of the estimate, is a measure to test the repeatability and precision of the model. It measures the spread of the residuals (or errors) about the fitted line. *RMSE* can be expressed as

$$RMSE = \sqrt{\sum \left[\frac{(Y_p - Y_m)^2}{N} \right]} \quad (8.8)$$

RMSE is always positive since it is a measure of the absolute deviation as shown in Equation (8.8). A lower absolute value of *RMSE* indicates a better model.

(d) *Mean of absolute deviation, MAD*

The mean of absolute deviation (*MAD*) provides an insight into the scatter between the predicted and measured results. This is given by

$$MAD = \frac{\sum |Y_p - Y_m|}{N} \quad (8.9)$$

Similar to *RMSE*, *MAD* provides a measure of absolute deviations, whereby it always result in positive values. A lower absolute value of *MAD* indicates a better model with smaller deviations from the predicted values.

(e) *Mean bias error, MBE*

The mean bias error (*MBE*) is an indicator to show the prediction trend of a model. It is given by

$$MBE = \frac{\sum (Y_p - Y_m)}{N} \quad (8.10)$$

Note that within a data set an overestimation of one observation can cancel an underestimation of another. *MBE* remains positive if over-prediction happens, and negative

if under-estimation is the case. $MBE \approx 0$ is desirable as it shows an almost equal spread of positive and negative values along the fitted line.

8.2.4.2 Results

The summary of the statistical evaluation of the test models for five distinct cases is given in Tables 8.7 to 8.11. Overall, the empirical models provide very good estimation of C_T with R_a^2 well beyond 0.93, and with $RMSE$ less than 0.07 in most cases. The C_T model is shown to be adequate with minimal unexplained variations and high repeatability. Even though the prediction for C_R is not as good as that for C_T ($0.683 < R_a^2$ of $C_R < 0.915$), it is still regarded as a good prediction model with relatively low residual errors ($0.019 < RMSE < 0.072$). As a result of the good estimation of both C_T and C_R , the C_L values computed using Equation (3.16) agree with the measured values quite well ($0.800 < R^2$ of $C_L < 0.979$ and $0.024 < RMSE < 0.094$). The prediction models for C_F and C_C are relatively weak in comparison to those for the energy coefficients due to the fact that the models are not robust enough to account for all of the nonlinearities that exist in the data set. In some test cases, the prediction ability of the C_F models is relatively poor with $R_a^2 < 0.5$; hence, the empirical equations are not presented herein.

For the force coefficients, the R_a^2 values vary between 0.639 and 0.982, and the majority of the $RMSE$ values are larger than those of the hydraulic coefficients. These signify that the prediction models for the force coefficients may not be as accurate as those of the C_T and C_R . In addition, it is also observed from Tables 8.7 to 8.11 that the empirical models for the irregular waves are generally better than those for the regular waves due to the fact that the data set for the irregular waves are less scatter.

In summary, the empirical models proposed for the estimation of the hydrodynamic performance of the free surface semicircular breakwaters are generally satisfactory; hence, they can be readily used as a handy tool for quick estimation of the performance of the breakwaters. It is also important to emphasise that sound engineering judgement is necessary when interpreting the results as the input data used for the present analysis were entirely derived from small-scale physical modelling tests that are subjected to laboratory and scale effects.

Table 8.7: Model validation for SCB0 (CASE I)**(a) Regular waves**

	R^2	R_a^2	$RMSE$	MAD	MBE
C_T	0.971	0.970	0.044	0.033	0.000
C_R	0.895	0.890	0.053	0.041	0.000
C_L	0.800	–	0.072	0.059	-0.004
C_F	0.777	0.762	0.113	0.086	0.000
C_C	0.721	0.705	0.072	0.051	0.000
$F_{nt\ SCB9}$	0.821	0.814	0.119	0.084	-0.003
$F_{nc\ SCB9}$	0.701	0.696	0.159	0.127	0.011

(b) Irregular waves

	R^2	R_a^2	$RMSE$	MAD	MBE
C_T	0.991	0.990	0.017	0.013	0.000
C_R	0.964	0.961	0.019	0.014	0.000
C_L	0.938	–	0.025	0.019	0.001
C_F	0.885	0.879	0.049	0.036	0.000
C_C	0.934	0.931	0.023	0.018	0.000
$F_{nt\ SCB9}$	0.968	0.966	0.046	0.034	0.000
$F_{nc\ SCB9}$	0.906	0.900	0.049	0.036	0.000

Table 8.8: Model validation for the perforated SCB's (CASE II)**(a) Regular waves**

	R^2	R_a^2	$RMSE$	MAD	MBE
C_T	0.931	0.930	0.076	0.043	0.005
C_R	0.688	0.683	0.072	0.056	0.000
C_L	0.876	–	0.094	0.072	0.008
C_F	<i>n.a.</i>	<i>n.a.</i>	<i>n.a.</i>	<i>n.a.</i>	<i>n.a.</i>
C_C	0.696	0.692	0.091	0.069	0.000
$F_{nt\ SCB9}$	0.646	0.639	0.108	0.085	0.000
$F_{nc\ SCB9}$	0.672	0.668	0.257	0.109	0.005

(b) Irregular waves

	R^2	R_a^2	$RMSE$	MAD	MBE
C_T	0.987	0.987	0.021	0.016	0.000
C_R	0.916	0.915	0.023	0.018	0.000
C_L	0.979	–	0.028	0.022	0.001
C_F	0.711	0.703	0.043	0.032	0.000
C_C	0.833	0.832	0.039	0.029	0.000
$F_{nt\ SCB9}$	0.915	0.913	0.041	0.030	0.000
$F_{nc\ SCB9}$	0.818	0.815	0.082	0.055	0.003

Table 8.9: Model validation for the SCB9 with different B/d ratios (CASE III)**(a) Regular waves**

	R^2	R_a^2	$RMSE$	MAD	MBE
C_T	0.942	0.940	0.063	0.049	0.000
C_R	0.785	0.779	0.066	0.042	-0.018
C_L	0.859	–	0.091	0.062	0.004
C_F	<i>n.a.</i>	<i>n.a.</i>	<i>n.a.</i>	<i>n.a.</i>	<i>n.a.</i>
C_C	<i>n.a.</i>	<i>n.a.</i>	<i>n.a.</i>	<i>n.a.</i>	<i>n.a.</i>
$F_{n,t} SCB9$	0.712	0.693	0.107	0.084	-0.028
$F_{n,c} SCB9$	0.692	0.680	0.201	0.177	0.093

(b) Irregular waves

	R^2	R_a^2	$RMSE$	MAD	MBE
C_T	0.973	0.972	0.034	0.026	0.000
C_R	0.895	0.894	0.025	0.018	0.000
C_L	0.961	–	0.041	0.031	0.002
C_F	0.718	0.713	0.055	0.042	0.000
C_C	0.821	0.819	0.038	0.029	0.000
$F_{n,t} SCB9$	0.905	0.903	0.054	0.041	0.000
$F_{n,c} SCB9$	0.748	0.744	0.111	0.081	0.001

Table 8.10: Model validation for SCB9-RS25 (CASE IV)**(a) Regular waves**

	R^2	R_a^2	$RMSE$	MAD	MBE
C_T	0.978	0.977	0.036	0.030	0.000
C_R	0.720	0.713	0.064	0.046	0.019
C_L	0.926	–	0.059	0.044	0.013
C_F	<i>n.a.</i>	<i>n.a.</i>	<i>n.a.</i>	<i>n.a.</i>	<i>n.a.</i>
C_C	0.818	0.808	0.105	0.082	0.000
$F_{n,t} SCB9$	0.749	0.745	0.031	0.022	0.000
$F_{n,c} SCB9$	0.818	0.810	0.073	0.051	0.000
$F_{n,t} RS25$	0.928	0.925	0.024	0.019	0.000
$F_{n,c} RS25$	0.941	0.939	0.021	0.017	0.001

(b)**(c) Irregular waves**

	R^2	R_a^2	$RMSE$	MAD	MBE
C_T	0.991	0.990	0.018	0.014	0.000
C_R	0.868	0.861	0.021	0.015	0.000
C_L	0.977	–	0.024	0.019	0.001
C_F	0.696	0.683	0.043	0.033	0.001
C_C	0.927	0.925	0.037	0.028	-0.001
$F_{n,t} SCB9$	0.849	0.847	0.019	0.015	0.000
$F_{n,c} SCB9$	0.970	0.969	0.023	0.017	0.000
$F_{n,t} RS25$	0.961	0.959	0.013	0.010	0.000
$F_{n,c} RS25$	0.982	0.982	0.009	0.008	0.000

Table 8.11: Model validation for SCB9-DS25 (CASE V)**(a) Regular waves**

	R^2	R_a^2	$RMSE$	MAD	MBE
C_T	0.983	0.982	0.029	0.022	0.000
C_R	0.753	0.736	0.043	0.033	0.000
C_L	0.960	–	0.033	0.028	0.002
C_F	<i>n.a.</i>	<i>n.a.</i>	<i>n.a.</i>	<i>n.a.</i>	<i>n.a.</i>
C_C	0.869	0.862	0.087	0.065	0.000
$F_{n,t} SCB9$	0.884	0.880	0.026	0.020	0.000
$F_{n,c} SCB9$	0.885	0.879	0.045	0.034	0.000
$F_{n,t} FS25$	0.923	0.917	0.027	0.020	0.000
$F_{n,c} FS25$	0.887	0.881	0.027	0.018	0.002
$F_{n,t} RS25$	0.941	0.938	0.017	0.013	0.000
$F_{n,c} RS25$	0.955	0.951	0.015	0.011	0.001

(b) Irregular waves

	R^2	R_a^2	$RMSE$	MAD	MBE
C_T	0.991	0.991	0.017	0.016	0.000
C_R	0.900	0.896	0.019	0.014	0.000
C_L	0.922	–	0.035	0.019	0.001
C_F	0.794	0.786	0.035	0.027	0.000
C_C	0.956	0.955	0.033	0.025	0.000
$F_{n,t} SCB9$	0.915	0.914	0.018	0.014	0.000
$F_{n,c} SCB9$	0.978	0.977	0.016	0.011	0.000
$F_{n,t} FS25$	0.983	0.982	0.010	0.008	0.000
$F_{n,c} FS25$	0.978	0.978	0.009	0.007	0.000
$F_{n,t} RS25$	0.956	0.954	0.011	0.006	-0.001
$F_{n,c} RS25$	0.963	0.961	0.011	0.007	0.001

8.3 Prediction of the Horizontal Wave Forces Using Modified Goda's Equations

In this study, the horizontal wave forces under wave crests acting on the 'solid-type' SCB were computed based on the modified Goda's equations as discussed in Section 3.5. It is worthwhile mentioning that Goda's method was first modified by Tanimoto *et al.* (1994) to account for the semicircular shape of the breakwater, and subsequently further modified by the author to address the free surface position of the SCB. Also, it is important to note that the early study of horizontal forces acting on the SCB is conducted with assumptions made based on laboratory observations. There is a need to further validate the accuracy of the model using other similar data sets.

Figure 8.11 shows a comparison between the predicted wave forces, $F_{c_predicted}$ and the measured wave forces, $F_{c_measured}$ for regular and irregular seas, and the corresponding statistical parameters are tabulated in Table 8.12. Prediction of the horizontal forces using the modified Goda's method appears to be surprisingly good even though there is a deviation of $\pm 30\%$ from the measured data. At $D/d = 0.071$, a good agreement is achieved between $F_{c_predicted}$ and $F_{c_measured}$ in regular waves; however, an overestimation of the forces is observed in irregular waves. At higher D/d ratios, the modified Goda's method underestimates the predicted horizontal forces for both regular and irregular seas. This might be due to (i) the simultaneous wave response at the rear curved wall; and (ii) underestimation of the limit of wave run up at the front wall of the solid SCB, η^* as shown in Equation (3.44). Therefore, it is suggested that additional laboratory measurements be made for wave pressure along the external circumference of the SCB and the wave run up at the front curved wall in future experiments to re-validate the proposed model.

8.4 Summary

A number of empirical equations for the prediction of the hydrodynamics of the SCB models have been developed using multiple polynomial regression (see Equations (8.4) – (8.5) and Tables 8.1 – 8.6). They are valid provided the predictor variables are confined within the respective test ranges. These equations are generally simple and user friendly, and can be readily used as a preliminary design or validation model. It is emphasised that the outputs must be interpreted with sound engineering judgement as the input data used for the analysis were derived entirely from small-scale physical modelling tests that are subjected to laboratory and scale effects.

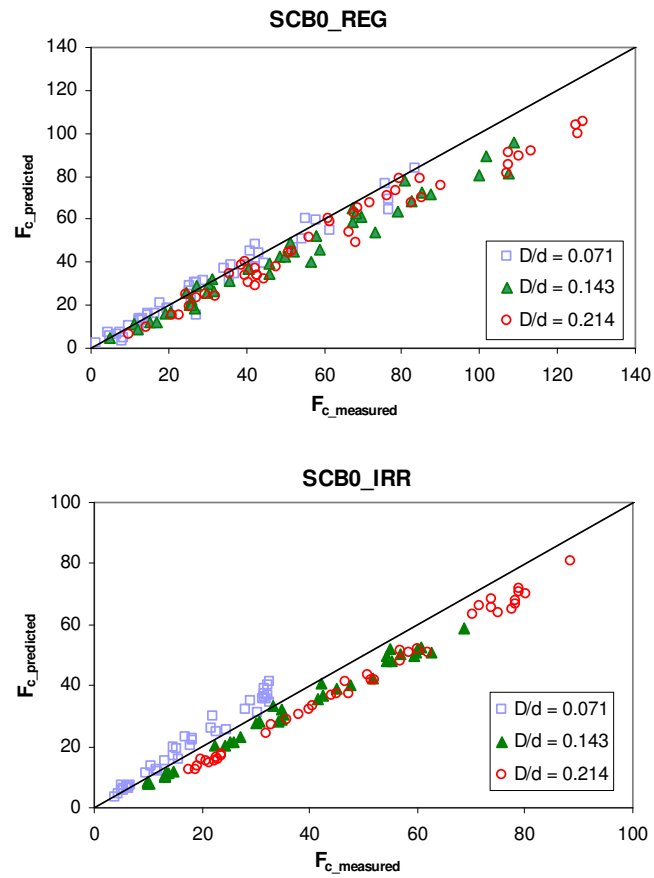


Figure 8.11: Comparison between the measured and predicted horizontal wave forces using the modified Goda’s equations

Table 8.12: Model validation for the measured and predicted horizontal wave forces using the modified Goda’s equations

	R^2	$RMSE$	MAD	MBE
Regular waves	0.966	9.002 N	6.517 N	-5.716 N
Irregular waves	0.969	7.504 N	6.051 N	-4.339 N

9

Conclusions and Recommendations

9.1 General Conclusions

The successful construction of the bottom seated semicircular breakwaters in Japan and China has sparked a great deal of interest among researchers worldwide concerning such breakwaters. However, published literature reveals that very little work has been carried out on the free surface semicircular breakwaters. In order to address this knowledge gap, this research work was undertaken which aimed at investigating the hydrodynamic characteristics of a free surface semicircular breakwater (SCB) and explored strategies to enhance the overall performance of the breakwater through physical modelling.

The research was initiated by empirical tests of a free surface semicircular breakwater constructed without any perforation on the entire curved surface (known as SCB0) in a water wave flume for different depths of immersion. The front curved wall of the model was subsequently perforated with rectangular openings of different dimensions resulting in front wall porosity of 9%, 18% and 27% (denoted as SCB9, SCB18 and SCB27). For the perforated breakwaters, two rows of rectangular openings near the crest of the rear curved wall were provided mainly to allow infiltration of the overtopping waves into the interference chamber. To enhance the performance of the breakwater, the draft was extended by wave screen(s) forming a front screen (denoted as FS), a rear screen (denoted as RS) and double screens (denoted as DS).

In order to study these SCB models, a physical modelling programme was developed to collect the necessary data. The laboratory facilities and measuring devices were checked and calibrated, and careful measures were taken to reduce the potential scale and laboratory effects. The hydrodynamic characteristics of these SCB models were investigated in both regular and irregular seas of varying wave conditions. The wave surface elevations were measured at different locations upstream and downstream of the models to determine the coefficients of wave transmission, C_T , reflection, C_R , and energy dissipation, C_L , as well as the wave disturbance coefficients in front of the breakwater and within its chamber, C_F and C_C . The horizontal wave forces exerted on the SCB model and the wave screen(s) were also measured, and subsequently normalised as a force coefficient, F_n in the analysis. These hydrodynamic coefficients provided a benchmark from which the effectiveness of the test models could be quantified.

A summary of the experimental results pertaining to the free surface SCB, its improved configurations, as well as the associated empirical models is outlined in the following sections.

9.1.1 Free Surface Semicircular Breakwater (SCB)

The primary aim for the experimental study conducted was to identify the SCB configuration that would be the most hydraulically efficient, *i.e.* low wave reflection, high energy dissipation and reasonably low wave transmission. The major findings and corresponding remarks derived from the experimental results (as presented in Chapter 5) are as follows:

- The energy coefficients (*i.e.* C_T , C_R and C_L) of the solid and perforated SCB models were strongly influenced by B/L and D/d , whereas the wave climate coefficients (*i.e.* C_F and C_C) are significantly affected by ε_{SCB} and D/d . For the force coefficient, the positive F_n values are greatly influenced by H/d while the negative force coefficients by D/d .
- The breakwater with impermeable wall – SCB0 model offered higher wave attenuation efficiency (with C_T values as low as 0.01 in regular waves and 0.05 in irregular waves) than the perforated models; nonetheless, it was also highly reflective to incident waves (with C_R values as high as 0.87 in regular waves and 0.78 in irregular waves) posing severe wave climate in front of the breakwater (with C_F values as high as 2.20 in regular waves and 1.94 in irregular waves);

- Even though the perforated SCB models were effective anti-reflection breakwaters, they performed reasonably well only in deeper immersion depth and in seas with limited wave periods. This limited the ability of the breakwaters in different applications;
- The variations of the hydrodynamic performance of the perforated SCB models in all test cases were small in general, except that the breakwater with a front wall of 9% porosity – SCB9 model, promoted less wave activity in the chamber. Other major findings pertaining to the hydrodynamic characteristics of the perforated SCB models are:
 - The effect of ‘Bragg reflection’ in C_R peaked at $0.2 < B/L < 0.3$ and dipped at $0.3 < B/L < 0.4$ in both regular and irregular waves;
 - The energy dissipation mechanisms observed in the experiment included exchange of water jet around the porous wall during the passage of waves, wave run up on the caisson wall, water infiltration into the chamber, development of eddies around the bottom walls, turbulent flow within the chamber and flow instability around the caisson;
 - The perforated SCB models were highly dissipative at $B/L \approx 0.4$ in both regular and irregular waves; and
 - The force coefficients of the perforated SCB models under wave crests, $F_{n,c}$ were larger than those under wave troughs, $F_{n,i}$;
 - The $F_{n,c}$ for the perforated models increased with a decrease of the relative breakwater immersion, D/d or the breakwater placement ratio, B/d ; however, they were less dependent upon the breakwater porosity, ε_{SCB} and wave steepness, H/L .
 - The effects of the rear wall perforation and wave spectra on the force coefficients were insignificant.
- At larger immersion depth, the SCB9 model achieved wave attenuation up to 96% and up to 85% of the incident wave height when exposed to regular and irregular waves, respectively. The maximum energy reflected from the structure was 34% in regular waves and 18% in irregular waves; and the maximum energy loss was 97% in regular waves and 90% in irregular waves. Thus, the SCB9 model was not only an effective anti-reflection breakwater but also an efficient energy dissipater;
- The impact of rear wall perforation of the SCB and the types of spectra used for wave generation on the hydrodynamic performance of the SCB models were insignificant; and
- Based on the analysis of results, the SCB9 model with rear wall perforation was chosen as the most hydraulically effective configuration mainly due to (i) superior wave attenuation ability, (ii) reduced wave activity in the chamber, and (iii) enhancement in

structural stability. However, this model was less effective in controlling wave transmission sufficiently when its immersion depth was limited and exposed to longer period waves.

9.1.2 Effect of Wave Screens

To overcome the shortcomings of the SCB9 model, wave screens of different configurations and porosities were added underneath the SCB9 caisson and these resulted in three types of composite breakwaters: (i) SCB9 with a front screen (denoted as SCB9-FS), SCB9 with a rear screen (denoted as SCB9-RS) and (iii) SCB9 with double screens (denoted as SCB9-DS). The porosity of each screen varied at 25%, 40% and 50%. The main conclusions from Chapter 6, which aimed at determining the most optimum screen configuration and porosity for the SCB9 caisson, are summarised as follows:

- Preliminary tests carried out on the submerged single wave screen of 25% porosity showed poor attenuation ability of the incident wave heights (less than 20%); however, the efficiency was greatly improved when coupled with the SCB9 model. These tests confirmed the role of the wave screen in enhancing the hydraulic performance of the model;
- The SCB9-FS models were weaker wave attenuators compared to the SCB9-RS and SCB9-DS models with identical screen porosities.
- The SCB9-RS models were better energy dissipaters than the SCB9-FS models as the interference chamber was effectively utilised for energy dissipation during interactions with larger waves, producing dissipation of energy up to 90% for regular waves and 80% for irregular waves;
- The SCB9-DS models outperformed other test models by providing the highest wave dampening and energy dissipation capabilities. However, the extension of the screen incurred an increase in wave reflection by about 17%, 12% and 10% for screen porosities of 25%, 40% and 50%, respectively, in both regular and irregular waves; and
- The SCB9 model with double screens of 25% porosity (denoted as SCB9-DS25) was found to provide the highest hydraulic efficiency even though the horizontal forces acting on the breakwater were higher than those models with a single screen. The double screen of the breakwater was particularly helpful in dissipating the energy of the longer period waves and operating in smaller immersion depths.

9.1.3 Optimum Design of SCB

The SCB9-RS25 and SCB9-DS25 models were identified as potential breakwater configurations for maritime applications. These breakwaters were tested in greater range of immersion depths in both regular and irregular waves. The concluding remarks from Chapter 7 are summarised as follows:

- In terms of wave attenuation, the SCB9-DS25 model outperformed the SCB9-RS25 model only when the structure was immersed in a limited depth where $D_T/d < 0.500$. With larger immersion depths ($D_T/d > 0.571$), the use of the SCB9-RS25 model is recommended;
- Both SCB9-RS25 and SCB9-DS25 were found to have similar reflection characteristics (where $C_R < 0.40$) at $B/L < 0.4$. At higher B/L range, the SCB9-DS25 model becomes a stronger wave reflector when exposed to very limited period waves. Wave absorption ability of these models was greatly improved by resonance at $B/L \approx 0.3$; hence, this ratio should be adopted for use in designing a breakwater with low reflection ability;
- The SCB9-DS25 model was a better energy dissipater at $B/L < 0.4$, and its performance at higher range of B/L was comparable to the SCB9-RS25 model;
- Wave activity directly in front of the SCB9-RS25 and SCB9-DS25 models was a result of a combination of various hydraulic phenomena including wave run-up, water build up and reflection. This is not an issue if they are to be designed as wave overtopping breakwaters. For non-overtopping breakwaters, the SCB9-RS25 and SCB9-DS25 models should be designed to be $0.2 < B/L < 0.3$ for $0.500 \leq D_T/d \leq 0.571$ in regular and irregular waves;
- Wave activity in the chamber of the SCB9-RS25 model was relatively violent, particularly when exposed to longer period waves. Careful consideration must be given to the design of the SCB9-RS25 model as excessive uplift loadings on the inner circumference of the SCB9 model may eventually lead to structural failure; and
- The total wave forces acting on the SCB9-DS25 model were greater than those acting on the SCB9-RS25 model due to the use of double screens. The positive forces acting on the SCB9 model were always greater than the negative ones; however, this trend is reversed for the wave screens. The positive forces acting on the rear screen of the SCB9 model were critical due to the increased wave activity in the interference chamber.

9.1.4 Prediction Models

Dimensionless analysis was undertaken to identify the potential affecting parameters for the hydrodynamic coefficients (*i.e.* C_T , C_R , C_L , C_F , C_C and F_n) of the test models. These parameters include the porosity of the front curved wall of the SCB (ϵ_{SCB}), the porosity of the wave screen (ϵ_{screen}), the relative breakwater width (B/L), the relative breakwater immersion depth (D/d), wave steepness (H/L), relative wave height (H/d) and the structure placement ratio (B/d). These affecting parameters were used as a basis in establishing a number of empirical equations for the prediction of the hydrodynamics of the SCB models using multiple polynomial regression.

The predicted results using the empirical models were validated against the measured results, and good agreements are generally achieved, particularly for C_T . The accuracy of the empirical models was also confirmed by a number of statistical parameters, *e.g.* the coefficient of determination (R^2), the adjusted R^2 , root mean squared error ($RMSE$), mean of absolute deviation (MAD) and mean bias error (MBE). These equations are generally simple, user friendly, and readily to be used as design or validation model; nonetheless, they must be used with the condition that all the limiting test ranges are met. The prediction models developed during the course of this research are particularly useful for maritime engineering applications. It must be stressed that the outputs must be interpreted with sound engineering judgement as the input data used for the analysis were obtained entirely from the small-scale physical modelling tests that may be prone to laboratory and scale effects.

9.1.5 Summary

A number of physical models of semicircular breakwaters with various porosity levels were constructed and tested to study the hydrodynamic performance of the breakwaters under various wave conditions. The dominant factors affecting the nature of the hydrodynamic interactions were identified. The SCB9 model was hydraulically more efficient than the other breakwater designs; however, its performance deteriorated in shallow draft condition. Wave screens of various configurations and porosities were proposed as remedies to the problem. Experimental results showed an enhancement in breakwater performance as the SCB9 was coupled with a single rear screen or double screens, both with 25% porosity, underneath the semicircular caisson. Empirical models were developed for quick estimation of the overall hydrodynamic performance of the breakwaters, and their accuracy was validated with the measurements. Overall, the aims of the research have been achieved reasonably well.

9.2 Recommendations for Future Work

Although the objectives set for this research study have generally been met, the scope of the work can be extended and the methodology and results further improved. Future investigations on the free surface semicircular breakwater could focus on the following areas:

- Energy absorption through various hydraulic mechanisms for the SCB models, including wave run-up, turbulence, viscous friction, resonance and vorticity which are poorly described based on observations by the naked eye. A Particle Image Velocimetry (PIV) would be ideal for capturing the disturbed velocity profile and quantifying eddies and turbulence formed around the test models;
- In order to gain deeper insight of the hydrodynamic characteristics of the free surface SCB caisson, extra laboratory measurements should be made for (i) the wave pressures along the external and internal circumferences of the caisson; (ii) the wave run up at the front curved wall; and (iii) the overtopping discharge;
- The length of the wave screen was fixed at 0.30 m in this study. A study on the effect of screen length could be undertaken to determine the most optimum screen length for each breakwater configuration;
- Even though the viscous scale effects were regarded as negligible based on the 'rule-of-thumb' as proposed by Hughes (1993), these effects were not understood well enough to allow quantification of the effects or adoption of empirical correction techniques within the scope of this study. This can only be achieved by repeating the tests for models of the larger scale;
- The present experimental study only focused on the hydrodynamics for a SCB caisson without the supporting structure. The pile-beam supporting system should be further developed and modelled so as to investigate its effect on the overall performance of the breakwater;
- Various SCB models were tested in uni-directional waves in a wave flume. Further experiments are recommended to test the models in a 3-D wave tank under the effect of oblique and multi-directional waves; and
- The empirical models established in this study can be used as a basis or reference for the development of mathematical models. They can also be used to improve the numerical models simulated by commercial CFD packages, *e.g.* STAR-CCM+ and FLUENT.

REFERENCES

- Aburatani, S., Koizuka, T., Sasayama, H., Tanimoto, K. and Namerikawa, N. (1996). Field test on a semi-circular caisson breakwater. *Coastal Engineering Journal in Japan*, 39 (1), 59–78.
- Allsop, N. W. H. (1995). Vertical walls and breakwaters: Optimisation to improve vessel safety and wave disturbance by reducing wave reflections. In *Wave Forces on Inclined and Vertical Wall Structures*, American Society of Civil Engineers: New York, 232–258.
- Allsop, N. W. and Hettiarachchi, S. S. (1988). Reflections from coastal structures. *Proceedings of the 21st International Coastal Engineering Conference*, 1, 782–794.
- Allsop, W. and Kortenhaus, A. (2001). *Probabilistic design tools for vertical breakwaters*. A.A. Balkema Publisher, Chapter 2.
- Allsop, N. W. H. and McBride, M.W. (1993). Reflections from vertical wall: The potentials for improvement in vessel safety and wave disturbance. *Proceedings of the 2nd Monolithic Coastal Structures Workshop*, Madrid.
- Allsop N. W. H., McBride, M.W. and Colombo, D. (1994). The reflection performance of vertical walls and ‘low reflection’ alternatives – results of random wave flume tests. *Proceedings of the 3rd MCS Project Workshop*, Emmelord.
- Allsop, N. W. H., Vicinanza, D. and McKenna, J. E. (1996). Wave forces on vertical and composite breakwaters. *Report SR 443*, HR Wallingford.
- Balaji, R. and Sundar, V. (2002). Hydraulic performance of double screen breakwaters. *Proceedings of the 5th International Conference on Hydro-Science & -Engineering (ICHE-2002)*, Warsaw, Poland.
- Bennett, G. S., McIver, P. and Smallman, J. V. (1992). A mathematical model of a slotted wave screen breakwater. *Coastal Engineering*, 18(3–4), 231–249.
- Brace, N., Kemp, R. and Snelgar, R. (2006). *SPSS for Psychologists*. Palgrave Macmillan, New York, 227 – 244.
- Briggs, M. J. (2001). Performance characteristics of a rapidly installed breakwater system. *Technical Report No. 01-13*. U.S. Army Engineer Research and Development Center, Vicksburg, MS.
- British Standards Institution (1984). *British standard code of practice for maritime structures, Part 1: General criteria. BS 6349: Part 1: 1984*. British Standard Institution, London.
- Brossard, J., Jarno-Druaux, A., Marin, F. and Tabet-Aoul, E. H. (2003). Fixed absorbing semi-immersed breakwater. *Coastal Engineering*, 49(1–2), 25–41.
- Burcharth, H. F. and Hughes, S. A. (2003). Fundamentals of design. In *Coastal Engineering Manual*. U.S. Army Corps of Engineers.
- Chakrabarti, S. K. (1994). Offshore structure modeling. *Advanced Series on Ocean Engineering*, 9 World Scientific, Singapore.
- CIRIA, CUR Centre for Civil Engineering and CETMEF (2007). *The rock manual: C683: The use of rock in hydraulic engineering*. Construction Industry Research and Information Association.
- Coastal Engineering Manual (2003). U.S. Army Corps of Engineers (USACE).

- Dalrymple, R. A. (1985). Introduction to physical models in coastal engineering. In *Physical Modeling in Coastal Engineering*, A. A. Balkema, Rotterdam, The Netherlands, 3–9.
- Dattatri, J., Shanker, N. J., Rahman, H. (1977). Laboratory investigations of submerged platform breakwaters. *Proceedings of the 17th Congress of the IAHR*, Baden, Germany, 4, 89–96.
- Dhinakaran, G., Sundar, V., Sundaravadivelu, R. and Graw, K.U. (2001a). Hydrodynamic characteristics of impermeable and seaside perforated SBW. *Leipzig Annual Civil Engineering Report*, 6, 1–8.
- Dhinakaran, G., Sundar, V., Sundaravadivelu, R. and Graw, K.U. (2001b). Pressure on a seaside perforated semicircular breakwater. *Proceedings of the International Conference in Ocean Engineering*, 84–89.
- Dhinakaran, G., Sundar, V., Sundaravadivelu, R. and Graw, K.U. (2002). Dynamic pressures and forces exerted on impermeable and seaside perforated semicircular breakwaters due to regular waves. *Ocean Engineering*, 29(15), 1981–2004.
- Dhinakaran, G., Sundar, V., Sundaravadivelu, R. and Graw, K. U. (2008). Hydrodynamic characteristics of seaside perforated semicircular breakwaters due to random waves. *Journal of Waterway, Port, Coastal and Ocean Engineering*, 134(4), 237–251.
- Draper, N. R. and Smith, H. (1981). *Applied regression analysis*. Wiley, New York.
- Duclos, G., Josset, C., Clement, A. H., Gentaz, L. and Colmard, C. (2004). Hydrodynamic efficiency of a new design of half-submerged breakwater compared to a rectangular caisson. *Journal of Waterway, Port, Coastal and Ocean Engineering*, 130(3), 127–133.
- Fugazza, M. and Natale, L. (1992). Hydraulic design of perforated breakwaters. *Journal of Waterway, Port, Coastal and Ocean Engineering*, 118 (1), 1–14.
- Gardner, J. D. and Townend, I. H. (1988). Slotted vertical screen breakwaters. *Proceedings of International Conference on Breakwaters*, Eastbourne, 283–297.
- Gilman, J. F. and Kriebel, D. L. (2000). Partial depth pile supported wave barriers: A design procedure. *Proceedings of the International Conference on Coastal Structures '99*, 549–557.
- Goda, Y. (1974). New wave pressure formulae for composite breakwaters. *Proceedings of the 14th Coastal Engineering Conference*, Copenhagen, 1702–1720.
- Goda, Y. (1985). *Random Seas and Design of Maritime Structures*. University of Tokyo Press, Japan.
- Goda, Y. and Kakizaki, S. (1967). Study on finite amplitude standing waves and their pressures upon a vertical wall. *Report of Port and Harbour Research Institute*, 5(10).
- Goda, Y. and Suzuki, Y. (1976). Estimation of incident and reflected waves in random wave experiments. *Proceedings of the 15th Coastal Engineering Conference*, 828–845.
- Graw, K. U., Knapp, S., Sundar, V. and Sundaravadivelu, R. (1998). Dynamic pressures exerted on semicircular breakwater. *Leipzig Annual Civil Engineering Report*, 3, 333–344.
- Gruene, J and Kohlhasse, S. (1974). Wave transmission through vertical slotted walls. *Proceedings of 14th International Conference on Coastal Engineering*, Copenhagen, 1906–1923.
- Günaydın, K. and Kebdaşlı, M. S. (2004). Performance of solid and perforated U-type breakwaters under regular and irregular waves. *Ocean Engineering*, 31(11–12), 1377–1405.

- Günaydin, K. and Kebdaşlı, M. S. (2007). Investigation of Π -type breakwater performance under regular and irregular waves. *Ocean Engineering*, 34(7), 1377–1405.
- Hasselmann, K., Barnett, T. P., Bouws, E., Carlsen, H., Cartwright, D. E., Enkee, K., Ewing, J. A. Gienapp, H., Hasselmann, D. E., Kruseman, P., Meerburg, A., Muller, P., Olbers, D. J., Richter, K., Sell, W. and Walden, H. (1973). Measurement of wind-wave growth and swell decay during the joint North Sea wave project (JONSWAP). *Deutsches Hydrographisches Zeitschrift*, 8(12), 95.
- Hattori, M. (1975). Wave transmissions from horizontal perforated plates. *Proceedings of the 22nd Conference on Coastal Engineering*, Japan, 513–517.
- Heikal, E. M., Salem, T. N. and Koraim, A. S. (2007). Theoretical study for one row of piles used as a breakwater. *Mansoura Engineering Journal*, Egypt.
- Hsiao, S. S., Fang, H. M., Chang, C. M. and Lee, T. S. (2008). Experimental study of the wave energy dissipation due to the porous-piled structure. *Proceedings of the 18th International Offshore and Polar Engineering Conference*, Vancouver, Canada, 592–598.
- Hsu, H. H. and Wu, Y. C. (1999). Scattering of water wave by a submerged horizontal plate and a submerged permeable breakwater. *Ocean Engineering*, 26(4), 325–341.
- Hu, H., Wang, K. H. and Williams, A. N. (2002). Wave motion over a breakwater system of a horizontal plate and a vertical porous wall. *Ocean Engineering*, 29(4), 373–386.
- Huang, Z.H. (2007). Wave interaction with one or two rows of closely spaced rectangular cylinders. *Ocean Engineering*, 34(11–12), 1584–1591.
- Hughes, S. A. (1993). *Physical models and laboratory techniques in coastal engineering*. World Scientific, USA.
- Ikeno, M., Fhimoda, N. and Iwata, K. (1988). A new type of breakwater utilizing air compressibility. *Proceedings of the 21th Coastal Engineering Conference*, 3, 2326–2339.
- Isaacson, M (1991). Measurement of Regular Wave Reflection. *Journal of Waterway, Port, Coastal and Ocean Engineering*, 117(533), 553–569.
- Isaacson, M., Baldwin, J., Premasiri, S. and Yang, G. (1999). Wave interactions with double slotted barriers. *Applied Ocean Research*, 21(2), 81–91.
- Isaacson, M., Premasiri, S. and Yang, G. (1998). Wave interaction with vertical slotted barrier. *Journal of Waterway, Port, Coastal and Ocean Engineering*, 124(3), 118–126.
- Isaacson, M., Whiteside, N., Gardiner, R. and Hay, D. (1995). Modelling of a circular-section floating breakwater. *Canadian Journal of Civil Engineering*, 22, 714–722.
- Jamieson, W. W. and Mansard, E. P. D. (1987). An efficient upright wave absorber. *Proceedings of the ASCE Specialty Conference on Coastal Hydrodynamics*, University of Delaware, Newark, Delaware, 124–139.
- Jarlan, G. E. (1961). *A perforated vertical wall breakwater*. Dock and Harbour Authority, 41(486), 394–398.
- Jeon, C. H. and Cho, Y. S. (2006). Bragg reflection of sinusoidal waves due to trapezoidal submerged breakwaters. *Ocean Engineering*, 33(14–15), 2067–2082.

- Ji, C. H. and Suh, K. D. (2008). Reflection and transmission of irregular waves by multiple-row curtainwall-pile breakwaters. *Proceedings of the 18th International Offshore and Polar Engineering Conference*, Vancouver, Canada, 656–663.
- Jia, D. H. (1999). Numerical model for the semicircular breakwater. *Technical Report of the First Design Institute of Navigation Engineering*, Ministry of Communication of China (in Chinese).
- Kamphuis, J. W. (1991). Physical modeling. In editor, *Handbook of Coastal and Ocean Engineering*, J. B. Herbich, Ed., 2, Gulf Publishing Company, Houston, Texas.
- Keulegan, G. H. (1950a). Wave motion. In *Engineering Hydraulics*, H. Rouse, Ed., John Wiley and Sons, New York, 711–768.
- Keulegan, G. H. (1950b). The gradual damping of a progressive oscillatory wave with distance in a prismatic rectangular channel. *National Bureau of Standards*, Washington, DC.
- Koiftis, T. and Prinos, P. (2005a). On the hydrodynamic efficiency of floating breakwaters. *Proceedings of the Conference of Arabian Coast*, Dubai.
- Koiftis, T. and Prinos, P. (2005b). 2DV hydrodynamics of a catamaran-shaped floating structure. *IASME Transactions*, 7(2), 1180–1189.
- Kondo, H. (1979). Analysis of breakwater having two porous walls. *Proceedings of the International Conference of Coastal Structure' 79*, 2, 962–977.
- Koraim, A. S. (2007). Efficiency of double rows of piles used as a breakwater. *Mansora Engineering Journal*, Egypt.
- Koutandos, E. V. (2007). Hydrodynamic analysis of a skirt breakwater. *Proceedings of the ICE: Maritime Engineering*, 160, 121–133.
- Koutandos, E. V. (2009). Hydrodynamics of vertical semi-immersed slotted barrier. *WSEAS Transaction on Fluid Mechanics*, 3(4), 85–96.
- Koutandos, E. and Prinos, P. (2005). Design formulae for wave transmission behind floating breakwaters. *Proceedings of the IAHR XXXI Congress*, Seoul, Korea, 4081 – 4089.
- Koutandos, E. V. and Prinos, P. E. (2011). Hydrodynamic characteristics of semi-immersed breakwater with an attached porous plate. *Ocean Engineering*, 38(1), 34–48.
- Kriebel, D. L. (2000). Performance of vertical wave barriers in random seas. *Proceedings of International Conference on Coastal Structures '99*, Rotterdam, 525–532.
- Kriebel, D. and Bollmann, C. (1996). Wave transmission past vertical wave barriers. *Proceedings of 25th International Conference on Coastal Engineering*, Orlando, 2470–2483.
- Krishnakumar, C., Sundar, V. and Sannasiraj, S. A. (2010). Hydrodynamic performance of Single- and Double-Wave Screens. *Journal of Waterway, Port, Coastal and Ocean Engineering*, 136(59), 59–65.
- Le Méhauté, B. (1976). Similitude in coastal engineering. *Journal of the Waterways, Harbours and Coastal Engineering*, 102(3), 317–335.
- Le Méhauté, B. (1990). Similitude. In *Ocean Engineering Science*, B. Le Méhauté, Ed., 9, Part B in the series *The Sea*, John Wiley and Sons, New York, 955–980.

- Li, D., Panchang, V., Tang, Z., Demirebilek, Z., and Ramsden, J. (2005). Evaluation of an approximate method for incorporating floating docks in harbor wave prediction models. *Canadian Journal of Civil Engineering*, 32, 1082 – 1092.
- Liu, C. G. and Tao, J. H. (2004). Modeling the interaction of solitary waves and semi-circular breakwaters by using Unsteady Reynolds Equations. *Journal of Applied Mathematics and Mechanics*, 25 (10), Shanghai University, 1118–1129.
- Liu, P. L. F. and Abbaspour, M. (1982). Wave scattering by a rigid thin barrier. *Journal of Waterway, Port, Coastal and Ocean Engineering*, 108, 479–491.
- Liu, Y, Li Y. C. and Teng, B. (2007). Wave interaction with a perforated wall breakwater with a submerged horizontal porous plate. *Ocean Engineering*, 34(17–18), 2364–2373.
- Liu, Y, Li Y. C., Teng, B., Jiang, J. and Ma, B. (2008). Total horizontal and vertical forces of irregular waves on partially perforated caisson breakwater. *Coastal Engineering*, 55(6), 537–552.
- Losada, I., Losada, M. and Losada, R. (1994). Wave spectrum scattering by vertical thin barriers. *Applied Ocean Research*, 14(3), 191–199.
- Mansard, E. P. D. and Funke, E. R. (1980). The measurement of incident and reflected spectra using a least squares method. *Proceedings of the 17th Coastal Engineering Conference*, 154–172.
- McBride, M. W., Smallman, J. V. and Allsop, N. W. H. (1994). Numerical model of absorbing wave screens. *Report IT400*, HR Wallingford.
- McCartney (1985). Floating breakwater design. *Journal of Waterway, Port, Coastal and Ocean Engineering*, 111(2), 304–319.
- McConnell, K. J., Allsop, N. W. H. and Flohr, H. (1999). Seaward wave loading on vertical coastal structures. *Proceedings of the International Conference on Coastal Structure '99*, 1, Santander, Spain.
- Michel, B., Marc, R.J. and Guillaume, C. (2003). Perforated breakwaters, Dieppe Harbour Jarlan Caisson: General schedule and acquired experience. *Proceedings of the 13th International Offshore and Polar Engineering Conference*, Honolulu, Hawaii, USA.
- Nallayarasu, S., Cheong, H. F. and Jothi Shankar, N. (1995). Estimation of Incident and Reflected Waves in Regular Wave Experiment. In *Ocean Engineering*, 22, Elsevier, UK, 77–86.
- Neelamani, S. and Gayathri (2006). Wave interaction with twin plate wave barrier. *Ocean Engineering*, 33(3–4), 495–516.
- Neelamani, S. and Rajendran, R. (2002a). Wave interaction with T-type breakwaters. *Ocean Engineering*, 29(2), 151–175.
- Neelamani, S. and Rajendran, R. (2002b). Wave interaction with ‘⊥’-type breakwaters. *Ocean Engineering*, 29(5), 561–589.
- Neelamani, S. and Reddy, M.S. (1992). Wave transmission and reflection characteristics of a rigid surface and submerged horizontal plate. *Ocean Engineering*, 19(4), 327–341.
- Neelamani, S. and Vedagiri, M. (2002). Wave interaction with partially immersed twin vertical barriers. *Ocean Engineering*, 29(2), 215–238.
- Neter, J., Wasserman, W. and Kutner, M. H. (1990). *Applied linear statistical models: Regression, analysis of variance and experimental designs*. McGraw-Hill.

- Oumeraci, H. (1984). Scale effects in coastal hydraulic models. *Proceedings in the Symposium on Scale Effects in Modeling Hydraulic Structures*, H. Kobus, Ed., International Association for Hydraulic Research, 7.10.1–7.10.7.
- Patarapanich, M. (1984). Maximum and zero reflection from submerged plate. *Journal of Waterway, Harbors, Coast and Ocean Engineering*, 110(2), 171–181.
- Patarapanich, M and Cheong, H. F. (1989). Reflection and transmission characteristics of regular and random waves from a submerged horizontal plate. *Coastal Engineering*, 13(2), 161–182.
- Payne, G. (2008). Guidance for the experimental tank testing for wave energy converters. Supergen Marine.
- Pierson, W. J. and Moskowitz, L. (1964). A proposed spectral form for fully developed wind seas based on the similarity theory of S. A. Kitaigorodskii. *Journal Geophys. Res.*, 69, 5181–5190.
- Rageh, O. S. and Koraim, A. S. (2009). The use of vertical walls with horizontal slots as breakwaters. *The 13th International Water Technology Conference*, Hurghada, Egypt.
- Rageh, O. S. and Koraim, A. S. (2010). Hydraulic performance of vertical walls with horizontal slots used as breakwater. *Coastal Engineering*, 57(8), 745–756.
- Reddy, M.S. and Neelamani, S. (1992). Wave transmission and reflection characteristics of partially immersed rigid vertical barrier. *Ocean Engineering*, 19 (3), 313–325.
- Reeve, D., Chadwick, A. and Fleming, C. (2004). *Coastal engineering – Processes, theory and design practice*. Spon Press, UK.
- Rogers, D. and Bolton King, G. (1997). *Wave generation using OCEAN and WAVE - Version 3.61*. Edinburgh Design Ltd.
- Sahoo, T., Chan, A. T., and Chwang, A. T. (2000). Scattering of oblique surface waves by permeable barrier. *Journal of Waterway, Port, Coastal and Ocean Engineering*, 126(4), 196–205.
- Sasajima, H., Koizuka, T. and Sasayama, H. (1994). Field demonstration test of a semicircular breakwater. *Proceedings of HYDROPORT'94*, Yokosuko, Japan, 1, 593–610.
- Sharp, J. J. (1981). *Hydraulic modeling*. Butterworth, London, England.
- Sorensen, R. M. (1978). *Basic Coastal Engineering*. John Wiley and Sons.
- Sri Krishna Priya, M., Roop Sekhar, K. A., Sundar, V., Sundaravadivelu, R., Graw, K. U. and Knapp, S. (2000a). Hydrodynamic pressure on semicircular breakwaters. *Proceedings of the 4th International Conference on Hydrosience and Engineering*, Seoul, South Korea.
- Sri Krishna Priya, M., Roop Sekhar, K.A., Sundar, V., Sundaravadivelu, R. and Graw, K. U. (2000b). Pressure exerted on submerged semicircular breakwaters. *Leipzig Annual Civil Engineering Report*, 5, 551–560.
- Subba Rao, K. G., Rao, N. B. S. and Sathyanarayana (1999). Laboratory investigation on wave transmission through two rows of perforated hollow piles. *Ocean Engineering*, 26(7), 675–699.
- Subba Rao, K. G., Shirlal, Varghese, R. V. and Govindaraja, K. R. (2009). Physical model studies on wave transmission of a submerged inclined plate breakwater. *Ocean Engineering*, 36(15–16), 1199–1207.

- Suh, K. D. and Ji, C. H. (2006). Reflection and transmission of regular waves by multiple-row curtainwall-pile breakwaters. *Proceedings of the International Conference of Coastal Engineering*, 1303–4313.
- Suh, K. D., Jung, H. Y. and Pyun, C. K. (2007). Wave reflection and transmission by curtainwall-pile breakwaters using circular piles. *Ocean Engineering*, 34(14–15), 2100–2106.
- Suh, K. D., Shin, S. and Cox, D. T. (2006). Hydrodynamic characteristics of pile-supported vertical wall breakwaters. *Journal of Waterway, Port, Coastal and Ocean Engineering*, 132 (2), 83–96.
- Sundar, V. and Raghu, D. (1997a). Wave induced pressure on semicircular breakwaters. *Proceeding of 2nd Indian National Conference on Harbour Engineering*, Thiruvananthapuram, India.
- Sundar, V. and Ragu, V. (1997b). Dynamic pressures and run-up on semicircular breakwaters due to random waves. *Ocean Engineering*, 25(4–5), 221–241.
- Sundar, V. and Subba Rao, B. V. V. (2002). Hydrodynamic pressure and forces on quadrant front face pile supported breakwater. *Ocean Engineering*, 29(2), 193–214.
- Sundar, V. and Subba Rao, B. V. V. (2003). Hydrodynamic performance characteristics of quadrant front-face pile-supported breakwater. *Journal of Waterway, Port, Coastal and Ocean Engineering*, 129(1), 22–33.
- Takahashi, S., Kotake, Y., Fujiwara, R. and Isobe, M. (2002). Performance evaluation of perforated-wall caissons by VOF numerical simulations. *Proceeding of the 28th International Conference on Coastal Engineering*, 1364–1376.
- Takahashi, S., and Shimosako, K. (1994). Wave pressure on a perforated wall. *Proceedings International Conference on Hydro-Technical Engineering for Port and Harbour Construction (Hydro-Port)*, Yokosuku, Japan. (In Japanese)
- Takahashi, S., Tanimoto, K. and Shimosako, K. (1994). A proposal of impulsive pressure coefficient for the design of composite breakwaters. *Proceedings International Conference on Hydro-Technical Engineering for Port and Harbour Construction (Hydro-Port)*, Yokosuku, Japan, 1(1), 489–504. (In Japanese)
- Tanimoto, K. and Goda, Y. (1992). Historical development of breakwater structures in the world. *Proceeding of the Conference on Coastal Structures and Breakwaters*. Thomas Telford, London, 193 – 206. (In Japanese)
- Tanimoto, K., Y., Namerikawa, N. and Sekimoto, T. (1988). Hydraulic characteristics and design wave forces of semi-circular caisson breakwaters (No.2). *Proceedings of Coastal Engineering*, JSCE, 35, 662–666. (In Japanese)
- Tanimoto, K., Namerikawa, N., Ishimaru, Y. and Sekimoto, T. (1989). A hydraulic experimental study on semi-circular caisson breakwaters. *Report of the Port and Harbour Research Institute.*, 28(2), 3–32. (in Japanese)
- Tanimono, K. and Takahashi, S. (1994a). Japanese experiences on composite breakwaters. *Proceedings of International Workshop on Wave Barriers in Deepwaters*, Yokosuka, Japan, 1–22.
- Tanimono, K. and Takahashi, S. (1994b). Design and construction of caisson breakwaters – the Japanese experience. *Coastal Engineering*, 22(1–2), 57–77.

- Tanimoto, K and Yoshimoto, Y. (1982). Theoretical and experimental study of reflection coefficient for wave dissipating caisson with a permeable front wall. *Rept. of Port and Harbour Research Institute*, 21(3), 43–77. (In Japanese)
- Tanimoto, K., Yoshimoto, Y., Namerikawa, N. and Ishimaru, Y. (1987). Hydraulic characteristics and design wave forces of semi-circular caisson breakwaters. *Proceedings of Coastal Engineering*, JSCE, 34, 551–555. (In Japanese)
- Teh, H. M., Venugopal, V. and Bruce, T. (2010). Hydrodynamic performance of a free surface semicircular perforated breakwater. *Proceedings of the 32nd International Conference on Coastal Engineering*, Shanghai, China.
- Teh, H. M., Venugopal, V. and Bruce, T. (2011). Performance analysis of a semicircular free surface breakwater. *Proceedings of the 30th International Conference on Ocean, Offshore and Arctic Engineering*, Rotterdam, The Netherlands.
- Teh, H. M., Venugopal, V. and Bruce, T. (2012). Hydrodynamic characteristics of a free surface semicircular breakwater exposed to irregular waves. *Journal of Waterway, Port, Coastal and Ocean Engineering*, 138(2), ASCE, 149-163.
- Tobiasson, B. O. and Kollmeter, R. C. (1991). *Marinas and small craft harbors*. Van Nostrand Reinhold, New York.
- Tsay, T. K., and Liu, P. L. F. (1983). A finite element model for wave refraction and diffraction. *Applied Ocean Research*, 5(1), 30–37.
- Usha, R. and Gayathri, T. (2005). Wave motion over a twin-plate breakwater. *Ocean Engineering*, 32(8–9), 1054–1072.
- Van der Meer, J. W. (1988). *Rock slopes and gravel beaches under wave attack*. PhD Dissertation, Delft Hydraulic Communication No. 396, Delft Hydraulic Laboratory, Emmeloord, The Netherlands.
- Wang, L. Q. (2006). *The study of 2-d and 3-d random waves acting on a semicircular breakwater*. PhD thesis. Dalian University of Technology, China. (in Chinese)
- Wang, Y., Wang, G and Li, G.(2006). Experimental study on the performance of the multiple-layer breakwater. *Ocean Engineering*, 33(13), 1829–1839.
- Wang, L. Q., Zhang, N. C., Yu, Y. X. and Liu, M. (2005). Interaction between oblique waves and semicircular breakwater. *China Ocean Engineering*, 123 (11), 33–40. (in Chinese)
- Wiegel, R. L. (1960). Transmission of waves past a rigid vertical barriers. *Journal of Waterways and Harbour*, 86(1), 1–12.
- World Meteorological Organization (1998). Guide to wave analysis and forecasting. *WMO-No. 702*. Secretariat of the World Meteorological Organization, Geneva, Switzerland.
- Xie, S. L. (1999). Wave forces on submerged semi-circular breakwater and similar structures. *China Ocean Engineering*, 13 (1), 63–72.
- Xie, S. L. (2001). Design of semi-circular breakwaters and estuary jetties. *Proceedings of XXIX IAHR Congress*, Beijing, 90–95.
- Yagci, O., Kirca, V. S. O., Kabdasli, M. S., Celik, A. O., Unal, N. E. and Aydingakko, A. (2006). An experimental model application of wave screen: Dynamic pressure, water particle velocity, and wave measurements. *Ocean Engineering*, 33(10), 1299–1321.

- Yu, Y. X., Zhang, N. C. & Rao, Y. H. (1999). Hydraulic experimental study on semi-circular breakwater. *China Ocean Engineering*, 17(4), 39–48. (in Chinese)
- Yuan, D. K. and Tao, J. H. (2002). Calculation of wave forces on semicircular breakwater. *Technical report of China Port and Harbour Construction*, 2, 11–15. (in Chinese)
- Yuan, D. K. and Tao, J. H. (2003). Wave forces on submerged, alternatively submerged, and emerged semicircular breakwaters. *Coastal Engineering*, 48(2), 75–93.
- Yueh, C. Y., Chuang, S. H. and Wu, M. T. (2008). Wave reflection from absorbing-type breakwaters. *Proceedings of the 18th International Offshore and Polar Engineering Conference*, Vancouver.
- Zhang, N. C., Wang, L. Q., and Yu, Y. X. (2005). Oblique irregular waves load on semicircular breakwater. *Coastal Engineering*, 47 (4), 183–104.

APPENDIX A: Wave decay due to internal friction

Task: To determine how long it takes for internal shearing stresses to reduce the height of linear wave to 99.8% of its original height using Keulegan's model (1950a)

Water temperature θ	=	10 °C
Density of water ρ	=	999.63 kg/m ³
Dynamic viscosity of water μ	=	0.001308 kg/m.s
Kinematic viscosity ν	=	1.308×10^{-6} m ² /s
Wave decay ratio H_t/H_i	=	0.998

T (s)	L (m)	Ψ	t (s)	Travel Distance (m)
0.7	0.765	0.0001766	11.34	12.39
0.8	0.999	0.0001035	19.33	24.14
0.9	1.262	0.0000649	30.85	43.26
1	1.551	0.0000430	46.60	72.28
1.1	1.856	0.0000300	66.73	112.60
1.2	2.171	0.0000219	91.31	165.19
1.3	2.489	0.0000167	120.02	229.79
1.4	2.805	0.0000131	152.43	305.40
1.5	3.118	0.0000106	188.34	391.50
1.6	3.427	0.0000088	227.52	487.32
1.7	3.731	0.0000074	269.68	591.86
1.8	4.032	0.0000064	314.95	705.48

Keulegan's model (1950a):

$$\frac{H_t}{H_i} = e^{-\left(\frac{8\pi^2\nu}{L^2}\right)t}$$

$$\frac{H_t}{H_i} = e^{-\Psi t}$$

$$-\ln\left(\frac{H_t}{H_i}\right) = \Psi t$$

$$t = \frac{-\ln\left(\frac{H_t}{H_i}\right)}{\Psi}$$

$$Dis\ tan\ ce = \frac{Lt}{T}$$

APPENDIX B: Wave decay due to viscous friction

Task: To determine the percentage of wave decay due to viscous friction using Keulegan's model (1950b)

Water temperature θ	=	10 °C
Density of water ρ	=	999.63 kg/m ³
Dynamic viscosity of water μ	=	0.001308 kg/m.s
Kinematic viscosity ν	=	1.308×10^{-6} m ² /s
Wave tank width B	=	0.4 m
Horizontal distance x_p	=	2.5 m
Undamped wave height H_1	=	0.20 m

T (s)	L (m)	C (m)	$4\pi d/L$	Φ_1	Φ_2	Ω	H_2	%
0.7	0.765	1.093	11.500	49367.624	49375.838	0.01109	0.195	2.7
0.8	0.999	1.249	8.806	3340.957	3347.247	0.00906	0.196	2.2
0.9	1.262	1.402	6.971	534.719	539.698	0.00755	0.196	1.9
1	1.551	1.551	5.672	146.957	151.009	0.00636	0.197	1.6
1.1	1.856	1.687	4.740	58.572	61.958	0.00542	0.197	1.3
1.2	2.171	1.809	4.052	29.915	32.809	0.00466	0.198	1.2
1.3	2.489	1.915	3.535	18.136	20.661	0.00408	0.198	1.0
1.4	2.805	2.004	3.136	12.385	14.625	0.00362	0.198	0.9
1.5	3.118	2.079	2.822	9.178	11.193	0.00327	0.198	0.8
1.6	3.427	2.142	2.567	7.209	9.043	0.00298	0.199	0.7
1.7	3.731	2.195	2.358	5.911	7.595	0.00276	0.199	0.7
1.8	4.032	2.240	2.182	4.999	6.557	0.00257	0.199	0.6

Keulegan's model (1950b):

$$\frac{H_2}{H_1} = e^{-\Omega x_p}$$

$$\Omega = \frac{2}{BC} \sqrt{\frac{\pi\nu}{T}} \left[\frac{\sinh\left(\frac{4\pi d}{L}\right) + \frac{2\pi B}{L}}{\sinh\left(\frac{4\pi d}{L}\right) + \frac{4\pi d}{L}} \right]$$

$$\Omega = \frac{2}{BC} \sqrt{\frac{\pi\nu}{T}} \left[\frac{\Phi_1}{\Phi_2} \right]$$

APPENDIX C: Wave probe separations for the measurement of incident and reflected wave heights using Mansard and Funke's method (1980)

(a) Regular waves

T (s)	f (Hz)	d (m)	L (m)	B/L	d/L	Water Condition	X_{12} (mm)	X_{23} (mm)
0.7	1.43	0.7	0.765	0.654	0.915	Deep	77	130
0.75	1.33	0.7	0.878	0.569	0.797	Deep	88	130
0.8	1.25	0.7	0.999	0.501	0.701	Deep	100	130
0.85	1.18	0.7	1.127	0.444	0.621	Deep	113	130
0.9	1.11	0.7	1.262	0.396	0.555	Deep	126	280
1.0	1.00	0.7	1.551	0.322	0.451	Transitional	155	280
1.1	0.91	0.7	1.856	0.269	0.377	Transitional	186	280
1.2	0.83	0.7	2.171	0.230	0.322	Transitional	200	280
1.3	0.77	0.7	2.489	0.201	0.281	Transitional	217	280
1.4	0.71	0.7	2.805	0.178	0.250	Transitional	249	400
1.5	0.67	0.7	3.118	0.160	0.225	Transitional	281	400
1.6	0.63	0.7	3.427	0.146	0.204	Transitional	312	400
1.7	0.59	0.7	3.731	0.134	0.188	Transitional	343	400
1.8	0.56	0.7	4.032	0.124	0.174	Transitional	373	500
1.9	0.53	0.7	4.329	0.116	0.162	Transitional	403	500

(b) Irregular waves

T_p (s)	f_p (Hz)	d (m)	L_p (m)	B/L_p	d/L_p	Water Condition	X_{12} (mm)	X_{23} (mm)
0.7	1.43	0.7	0.765	0.654	0.915	Deep	77	130
0.75	1.33	0.7	0.878	0.569	0.797	Deep	88	130
0.8	1.25	0.7	0.999	0.501	0.701	Deep	100	130
0.85	1.18	0.7	1.127	0.444	0.621	Deep	113	130
0.9	1.11	0.7	1.262	0.396	0.555	Deep	126	280
1.0	1.00	0.7	1.551	0.322	0.451	Transitional	155	280
1.1	0.91	0.7	1.856	0.269	0.377	Transitional	186	280
1.2	0.83	0.7	2.171	0.230	0.322	Transitional	200	280
1.3	0.77	0.7	2.489	0.201	0.281	Transitional	217	280
1.4	0.71	0.7	2.805	0.178	0.250	Transitional	249	400
1.5	0.67	0.7	3.118	0.160	0.225	Transitional	281	400
1.6	0.63	0.7	3.427	0.146	0.204	Transitional	312	400
1.7	0.59	0.7	3.731	0.134	0.188	Transitional	343	400
1.8	0.56	0.7	4.032	0.124	0.174	Transitional	373	500
1.9	0.53	0.7	4.329	0.116	0.162	Transitional	403	500

APPENDIX D: Test parameters for Experiment *Series A1*

SCB0

			Wave Steepness, H/L (REG)											
T	L	B/L	0.01	0.02	0.03	0.04	0.05	0.06	0.07	0.08	0.09	0.1	0.11	0.12
0.7	0.765	0.654												
0.8	0.999	0.501		0.020		0.040		0.060		0.080		0.100		0.120
0.9	1.262	0.396		0.025		0.050		0.076		0.101		0.126		0.151
1	1.551	0.322		0.031		0.062		0.093		0.124		0.155		
1.1	1.856	0.269		0.037		0.074		0.111		0.148				
1.2	2.171	0.230		0.043		0.087		0.130		0.174				
1.3	2.489	0.201		0.050		0.100		0.149		0.199				
1.4	2.805	0.178		0.056		0.112		0.168						
1.5	3.118	0.160		0.062		0.125		0.187						
1.6	3.427	0.146		0.069	0.103	0.137	0.171	0.206				Wave height, H_i (m)		
1.7	3.731	0.134		0.075	0.112	0.149	0.187							
1.8	4.032	0.124		0.081	0.121	0.161	0.202							

			Wave Steepness, H_{m0}/L_p (JONS)											
T_p	L_p	B/L_p	0.01	0.02	0.03	0.04	0.05	0.06	0.07	0.08	0.09	0.1	0.11	0.12
0.7	0.765	0.654												
0.8	0.999	0.501				0.040		0.060		0.080				
0.9	1.262	0.396			0.038		0.063	0.076		0.101				
1	1.551	0.322			0.047		0.078	0.093		0.124				
1.1	1.856	0.269		0.037		0.074		0.111						
1.2	2.171	0.230		0.043		0.087		0.130						
1.3	2.489	0.201		0.050		0.100	0.124	0.149						
1.4	2.805	0.178	0.028	0.056	0.084	0.112	0.140							
1.5	3.118	0.160	0.031	0.062	0.094	0.125								
1.6	3.427	0.146	0.034	0.069	0.103	0.137						Wave height, H_{m0i} (m)		
1.7	3.731	0.134	0.037	0.075	0.112	0.149								
1.8	4.032	0.124	0.040	0.081	0.121									

SCB9

			Wave Steepness, H/L (REG)											
T	L	B/L	0.01	0.02	0.03	0.04	0.05	0.06	0.07	0.08	0.09	0.1	0.11	0.12
0.7	0.765	0.654		0.015		0.031		0.046		0.061		0.077		0.092
0.8	0.999	0.501		0.020		0.040		0.060		0.080		0.100		0.120
0.9	1.262	0.396		0.025		0.050		0.076		0.101		0.126		0.151
1	1.551	0.322		0.031		0.062		0.093		0.124		0.155		
1.1	1.856	0.269		0.037		0.074		0.111		0.148				
1.2	2.171	0.230		0.043		0.087		0.130		0.174				
1.3	2.489	0.201		0.050		0.100		0.149		0.199				
1.4	2.805	0.178		0.056	0.084	0.112	0.140	0.168						
1.5	3.118	0.160		0.062	0.094	0.125	0.156	0.187						
1.6	3.427	0.146		0.069	0.103	0.137	0.171					Wave height, H_i (m)		
1.7	3.731	0.134		0.075	0.112	0.149	0.187							
1.8	4.032	0.124		0.081	0.121	0.161	0.202							

			Wave Steepness, H_{m0}/L_p (JONS)											
T_p	L_p	B/L_p	0.01	0.02	0.03	0.04	0.05	0.06	0.07	0.08	0.09	0.1	0.11	0.12
0.7	0.765	0.654		0.015		0.031		0.046		0.061				
0.8	0.999	0.501		0.020		0.040		0.060		0.080				
0.9	1.262	0.396		0.025		0.050		0.076		0.101				
1	1.551	0.322		0.031	0.047	0.062	0.078	0.093		0.124				
1.1	1.856	0.269		0.037	0.056	0.074	0.093	0.111		0.148				
1.2	2.171	0.230		0.043	0.065	0.087	0.109	0.130		0.174				
1.3	2.489	0.201		0.050	0.075	0.100	0.124	0.149						
1.4	2.805	0.178	0.028	0.056	0.084	0.112	0.140							
1.5	3.118	0.160	0.031	0.062	0.094	0.125	0.156							
1.6	3.427	0.146	0.034	0.069	0.103	0.137						Wave height, H_{m0i} (m)		
1.7	3.731	0.134	0.037	0.075	0.112	0.149								
1.8	4.032	0.124	0.040	0.081	0.121									

APPENDIX D: Test parameters for Experiment *Series A1*

SCB18

			Wave Steepness, H/L (REG)											
T	L	B/L	0.01	0.02	0.03	0.04	0.05	0.06	0.07	0.08	0.09	0.1	0.11	0.12
0.7	0.765	0.654		0.015		0.031		0.046		0.061		0.077		0.092
0.8	0.999	0.501		0.020		0.040		0.060		0.080		0.100		0.120
0.9	1.262	0.396		0.025		0.050		0.076		0.101		0.126		
1	1.551	0.322		0.031		0.062		0.093		0.124		0.155		
1.1	1.856	0.269		0.037		0.074		0.111		0.148				
1.2	2.171	0.230		0.043		0.087		0.130		0.174				
1.3	2.489	0.201		0.050		0.100		0.149		0.199				
1.4	2.805	0.178		0.056		0.112		0.168						
1.5	3.118	0.160		0.062		0.125		0.187						
1.6	3.427	0.146		0.069	0.103	0.137	0.171				Wave height, H_i (m)			
1.7	3.731	0.134		0.075	0.112	0.149	0.187							
1.8	4.032	0.124		0.081	0.121	0.161	0.202							

			Wave Steepness, H_{rms}/L_p (JONS)											
T_p	L_p	B/L_p	0.01	0.02	0.03	0.04	0.05	0.06	0.07	0.08	0.09	0.1	0.11	0.12
0.7	0.765	0.654												
0.8	0.999	0.501				0.040		0.060		0.080				
0.9	1.262	0.396				0.050		0.076		0.101				
1	1.551	0.322			0.047	0.062	0.078	0.093		0.124				
1.1	1.856	0.269		0.037	0.056	0.074	0.093	0.111						
1.2	2.171	0.230		0.043	0.065	0.087	0.109	0.130						
1.3	2.489	0.201		0.050	0.075	0.100	0.124	0.149						
1.4	2.805	0.178	0.028	0.056	0.084	0.112	0.140							
1.5	3.118	0.160	0.031	0.062	0.094	0.125								
1.6	3.427	0.146	0.034	0.069	0.103	0.137					Wave height, H_{rms} (m)			
1.7	3.731	0.134	0.037	0.075	0.112	0.149								
1.8	4.032	0.124	0.040	0.081	0.121									

SCB27

			Wave Steepness, H/L (REG)											
T	L	B/L	0.01	0.02	0.03	0.04	0.05	0.06	0.07	0.08	0.09	0.1	0.11	0.12
0.7	0.765	0.654			0.023	0.031	0.038	0.046	0.054	0.061	0.069	0.077	0.084	0.092
0.8	0.999	0.501		0.020	0.030	0.040	0.050	0.060	0.070	0.080	0.090	0.100	0.110	0.120
0.9	1.262	0.396		0.025	0.038	0.050	0.063	0.076	0.088	0.101	0.114	0.126	0.139	0.151
1	1.551	0.322		0.031	0.047	0.062	0.078	0.093	0.109	0.124	0.140	0.155	0.171	0.186
1.1	1.856	0.269		0.037	0.056	0.074	0.093	0.111	0.130	0.148	0.167	0.186	0.204	0.223
1.2	2.171	0.230	0.022	0.043	0.065	0.087	0.109	0.130	0.152	0.174	0.195	0.217		
1.3	2.489	0.201	0.025	0.050	0.075	0.100	0.124	0.149	0.174	0.199	0.224			
1.4	2.805	0.178	0.028	0.056	0.084	0.112	0.140	0.168	0.196					
1.5	3.118	0.160	0.031	0.062	0.094	0.125	0.156	0.187	0.218					
1.6	3.427	0.146	0.034	0.069	0.103	0.137	0.171	0.206						
1.7	3.731	0.134	0.037	0.075	0.112	0.149	0.187				Wave height, H_i (m)			
1.8	4.032	0.124	0.040	0.081	0.121	0.161	0.202							
1.9	4.329	0.116	0.043	0.087	0.130	0.173								

			Wave Steepness, H_{rms}/L_p (JONS)											
T_p	L_p	B/L_p	0.01	0.02	0.03	0.04	0.05	0.06	0.07	0.08	0.09	0.1	0.11	0.12
0.7	0.765	0.654												
0.8	0.999	0.501				0.040	0.050	0.060	0.070	0.080				
0.9	1.262	0.396			0.038	0.050	0.063	0.076		0.101	0.114			
1	1.551	0.322			0.047	0.062	0.078	0.093		0.124				
1.1	1.856	0.269		0.037	0.056	0.074	0.093	0.111		0.148				
1.2	2.171	0.230		0.043	0.065	0.087	0.109	0.130						
1.3	2.489	0.201		0.050	0.075	0.100	0.124	0.149						
1.4	2.805	0.178	0.028	0.056	0.084	0.112	0.140							
1.5	3.118	0.160	0.031	0.062	0.094	0.125								
1.6	3.427	0.146	0.034	0.069	0.103	0.137								
1.7	3.731	0.134	0.037	0.075	0.112	0.149					Wave height, H_{rms} (m)			
1.8	4.032	0.124	0.040	0.081	0.121									
1.9	4.329	0.116	0.043	0.087	0.130									

APPENDIX E: Test parameters for Experiment Series A2

 $d = 0.30 \text{ m}$

T	L	B/L	Wave Steepness, H_i/L (REG)		
			$H_i = 0.05 \text{ m}$	$H_i = 0.10 \text{ m}$	$H_i = 0.15 \text{ m}$
0.7	0.754	0.663	0.066	0.106	
0.75	0.856	0.584	0.058	0.093	
0.8	0.96	0.521	0.052	0.104	
0.9	1.168	0.428	0.043	0.086	
1	1.372	0.364	0.036	0.073	0.087
1.1	1.573	0.318	0.032	0.064	0.095
1.2	1.77	0.282	0.028	0.056	0.085
1.3	1.963	0.255	0.025	0.051	0.076
1.4	2.153	0.232	0.023	0.046	0.070
1.5	2.341	0.214	0.021	0.043	0.064
1.6	3.527	0.142	0.014	0.028	0.043

T_p	L_p	B/L_p	Wave Steepness, $H_{m0,i}/L_p$ (JONS)		
			$H_{m0,i} = 0.04 \text{ m}$	$H_{m0,i} = 0.08 \text{ m}$	$H_{m0,i} = 0.12 \text{ m}$
0.7	0.754	0.663	0.053	0.080	
0.75	0.856	0.584	0.047	0.070	
0.8	0.96	0.521	0.042	0.083	
0.9	1.168	0.428	0.034	0.068	0.086
1	1.372	0.364	0.029	0.058	0.087
1.1	1.573	0.318	0.025	0.051	0.076
1.2	1.77	0.282	0.023	0.045	0.068
1.3	1.963	0.255	0.020	0.041	0.061
1.4	2.153	0.232	0.019	0.037	0.056
1.5	2.341	0.214	0.017	0.034	0.051
1.6	3.527	0.142	0.011	0.023	0.034

 $d = 0.50 \text{ m}$

T	L	B/L	Wave Steepness, H_i/L (REG)		
			$H_i = 0.05 \text{ m}$	$H_i = 0.10 \text{ m}$	$H_i = 0.15 \text{ m}$
0.7	0.764	0.654	0.065	0.105	
0.75	0.876	0.571	0.057	0.091	
0.8	0.995	0.503	0.050	0.101	
0.85	1.119	0.447	0.045	0.089	
0.9	1.248	0.401	0.040	0.080	
1.0	1.512	0.331	0.033	0.066	0.079
1.1	1.780	0.281	0.028	0.056	0.084
1.2	2.047	0.244	0.024	0.049	0.073
1.3	2.311	0.216	0.022	0.043	0.065
1.4	2.57	0.195	0.019	0.039	0.058
1.5	2.825	0.177	0.018	0.035	0.053
1.6	3.077	0.162	0.016	0.032	0.049
1.7	3.325	0.150	0.015	0.030	0.045

T_p	L_p	B/L_p	Wave Steepness, $H_{m0,i}/L_p$ (JONS)			
			$H_{m0,i} = 0.04 \text{ m}$	$H_{m0,i} = 0.08 \text{ m}$	$H_{m0,i} = 0.12 \text{ m}$	$H_{m0,i} = 0.14 \text{ m}$
0.7	0.764	0.654	0.052	0.079		
0.75	0.876	0.571	0.046	0.068		
0.8	0.995	0.503	0.040	0.080		
0.85	1.119	0.447	0.036	0.071		
0.9	1.248	0.401	0.032	0.064	0.080	
1.0	1.512	0.331	0.026	0.053	0.079	
1.1	1.780	0.281	0.022	0.045	0.067	
1.2	2.047	0.244	0.020	0.039	0.059	0.573
1.3	2.311	0.216	0.017	0.035	0.052	0.647
1.4	2.57	0.195	0.016	0.031	0.047	0.720
1.5	2.825	0.177	0.014	0.028	0.042	0.791
1.6	3.077	0.162	0.013	0.026	0.039	0.862
1.7	3.325	0.150	0.012	0.024	0.036	0.931

APPENDIX F: Test parameters for Experiment Series A3

The effect of wave spectra

			Wave Steepness, H_{m0}/L_p (PM & JONS)							
T_p	L_p	B/L_p	0.01	0.02	0.03	0.04	0.05	0.06	0.07	0.08
0.8	0.999	0.501				0.040	0.050	0.060	0.070	
0.9	1.262	0.396			0.038	0.050	0.063	0.076		0.101
1	1.551	0.322			0.047	0.062	0.078	0.093		0.124
1.1	1.856	0.269		0.037	0.056	0.074	0.093	0.111		
1.2	2.171	0.230		0.043	0.065	0.087	0.109	0.130		
1.3	2.489	0.201		0.050	0.075	0.100	0.124			

APPENDIX G: Test parameters for Experiment Series A4

SCB9 vs. SCB9X

			Wave Steepness, H/L (REG)											
T	L	B/L	0.01	0.02	0.03	0.04	0.05	0.06	0.07	0.08	0.09	0.1	0.11	0.12
0.7	0.765	0.654		0.015		0.031		0.046		0.061		0.077		0.092
0.8	0.999	0.501		0.020		0.040		0.060		0.080		0.100		0.120
0.9	1.262	0.396		0.025		0.050		0.076		0.101		0.126		0.151
1	1.551	0.322		0.031		0.062		0.093		0.124		0.155		
1.1	1.856	0.269		0.037		0.074		0.111		0.148				
1.2	2.171	0.230		0.043		0.087		0.130		0.174				
1.3	2.489	0.201		0.050		0.100		0.149		0.199				
1.4	2.805	0.178		0.056	0.084	0.112	0.140	0.168						
1.5	3.118	0.160		0.062	0.094	0.125	0.156	0.187						
1.6	3.427	0.146		0.069	0.103	0.137	0.171					Wave height, H_i (m)		
1.7	3.731	0.134		0.075	0.112	0.149	0.187							
1.8	4.032	0.124		0.081	0.121	0.161	0.202							

			Wave Steepness, H_{m0}/L_p (JONS)											
T_p	L_p	B/L_p	0.01	0.02	0.03	0.04	0.05	0.06	0.07	0.08	0.09	0.1	0.11	0.12
0.7	0.765	0.654												
0.8	0.999	0.501				0.040		0.060		0.080				
0.9	1.262	0.396				0.050		0.076		0.101				
1	1.551	0.322				0.062		0.093		0.124				
1.1	1.856	0.269		0.037		0.074		0.111						
1.2	2.171	0.230		0.043		0.087		0.130						
1.3	2.489	0.201		0.050	0.075	0.100								
1.4	2.805	0.178	0.028	0.056	0.084	0.112								
1.5	3.118	0.160	0.031	0.062	0.094	0.125								
1.6	3.427	0.146	0.034	0.069	0.103	0.137						Wave height, $H_{m0,j}$ (m)		
1.7	3.731	0.134	0.037	0.075	0.112									
1.8	4.032	0.124	0.040	0.081	0.121									

APPENDIX H: Test parameters for Experiment *Series B1*

Test model: SS25, SCB9-FS25

T	L	B/L	Wave Steepness, H_i/L (REG)		
			$H_i = 0.05$ m	$H_i = 0.10$ m	$H_i = 0.15$ m
0.8	0.999	0.501	0.050	0.100	0.097
1	1.551	0.322	0.032	0.064	0.069
1.2	2.171	0.230	0.023	0.046	0.053
1.4	2.805	0.178	0.018	0.036	0.044
1.6	3.427	0.146	0.015	0.029	0.037
1.8	3.731	0.134	0.013	0.027	

T_p	L_p	B/L_p	Wave Steepness, $H_{m0,i}/L_p$ (JONS)		
			$H_{m0,i} = 0.04$ m	$H_{m0,i} = 0.08$ m	$H_{m0,i} = 0.12$ m
0.8	0.999	0.501	0.040	0.080	0.077
1	1.551	0.322	0.026	0.052	0.055
1.2	2.171	0.230	0.018	0.037	0.043
1.4	2.805	0.178	0.014	0.029	0.035
1.6	3.427	0.146	0.012	0.023	0.032
1.8	3.731	0.134	0.011	0.021	

APPENDIX I: Test parameters for Experiment *Series B2*

Regular waves

Test models: SCB9, SCB9-FS25/40/50, SCB9-RS25/40/50, SCB9-DS25/40/50

T	L	B/L	Wave Steepness, H_i/L (REG)		
			$H_i = 0.05$ m	$H_i = 0.10$ m	$H_i = 0.15$ m
0.7	0.765	0.654	0.065	0.131	
0.75	0.878	0.569	0.057	0.114	
0.8	0.999	0.501	0.050	0.100	
0.85	1.127	0.444	0.044	0.089	
0.9	1.262	0.396	0.040	0.079	0.119
1	1.551	0.322	0.032	0.064	0.097
1.1	1.856	0.269	0.027	0.054	0.081
1.2	2.171	0.230	0.023	0.046	0.069
1.3	2.489	0.201	0.020	0.040	0.060
1.4	2.805	0.178	0.018	0.036	0.053
1.5	3.118	0.160	0.016	0.032	0.048
1.6	3.427	0.146	0.015	0.029	0.044
1.7	3.731	0.134	0.013	0.027	0.040
1.8	4.032	0.124	0.012	0.025	0.037

APPENDIX I: Test parameters for Experiment Series B2 (Cont'd)

Irregular waves

Test models: SCB9, SCB9-FS25

T_p	L_p	B/L_p	Wave Steepness, $H_{m,0}/L$ (JONS)							
			$H_i = 0.02$ m	0.04 m	0.06 m	0.08 m	0.10 m	0.12 m	0.14 m	0.16 m
0.7	0.765	0.654	0.013	0.052	0.078					
0.75	0.878	0.569	0.011	0.046	0.068	0.091				
0.8	0.999	0.501	0.010	0.040	0.060	0.080				
0.85	1.127	0.444	0.009	0.035	0.053	0.071	0.089			
0.9	1.262	0.396	0.008	0.032	0.048	0.063	0.079			
1	1.551	0.322	0.006	0.026	0.039	0.052	0.064	0.077		
1.1	1.856	0.269	0.005	0.022	0.032	0.043	0.054	0.065		
1.2	2.171	0.230	0.005	0.018	0.028	0.037	0.046	0.055	0.064	
1.3	2.489	0.201		0.016	0.024	0.032	0.040	0.048	0.056	0.064
1.4	2.805	0.178		0.014	0.021	0.029	0.036	0.043	0.050	0.057
1.5	3.118	0.160		0.013	0.019	0.026	0.032	0.038	0.045	0.051
1.6	3.427	0.146		0.012	0.018	0.023	0.029	0.035	0.041	0.047
1.8	3.731	0.134		0.011	0.016	0.021	0.027	0.032	0.038	
1.9	4.032	0.124		0.010	0.015	0.020	0.025	0.030	0.035	

Test models: SCB9-RS25, SCB9-DS25

T_p	L_p	B/L_p	Wave Steepness, $H_{m,0}/L$ (JONS)							
			$H_i = 0.02$ m	0.04 m	0.06 m	0.08 m	0.10 m	0.12 m	0.14 m	0.16 m
0.7	0.765	0.654		0.052	0.078					
0.75	0.878	0.569		0.046	0.068	0.091				
0.8	0.999	0.501		0.040	0.060	0.080				
0.85	1.127	0.444		0.035	0.053	0.071	0.089			
0.9	1.262	0.396		0.032	0.048	0.063	0.079			
1	1.551	0.322		0.026	0.039	0.052	0.064	0.077		
1.1	1.856	0.269		0.022	0.032	0.043	0.054	0.065		
1.2	2.171	0.230		0.018	0.028	0.037	0.046	0.055	0.064	
1.3	2.489	0.201		0.016	0.024	0.032	0.040	0.048	0.056	0.064
1.4	2.805	0.178		0.014	0.021	0.029	0.036	0.043	0.050	0.057
1.5	3.118	0.160		0.013	0.019	0.026	0.032	0.038	0.045	0.051
1.6	3.427	0.146		0.012	0.018	0.023	0.029	0.035	0.041	0.047
1.8	3.731	0.134		0.011	0.016	0.021	0.027	0.032	0.038	
1.9	4.032	0.124		0.010	0.015	0.020	0.025	0.030	0.035	

Test models: SCB9-FS40/50, SCB9-RS40/50, SCB9-DS40/50

T_p	L_p	B/L_p	Wave Steepness, $H_{m,0}/L$ (JONS)							
			$H_i = 0.02$ m	0.04 m	0.06 m	0.08 m	0.10 m	0.12 m	0.14 m	0.16 m
0.7	0.765	0.654		0.052	0.078					
0.75	0.878	0.569		0.046		0.091				
0.8	0.999	0.501		0.040		0.080				
0.85	1.127	0.444		0.035		0.071	0.089			
0.9	1.262	0.396		0.032		0.063	0.079			
1	1.551	0.322		0.026		0.052		0.077		
1.1	1.856	0.269		0.022		0.043		0.065		
1.2	2.171	0.230		0.018		0.037		0.055	0.064	
1.3	2.489	0.201		0.016		0.032		0.048		0.064
1.4	2.805	0.178		0.014		0.029		0.043		0.057
1.5	3.118	0.160		0.013		0.026		0.038	0.045	
1.6	3.427	0.146		0.012		0.023		0.035	0.041	
1.8	3.731	0.134		0.011		0.021		0.032	0.038	
1.9	4.032	0.124		0.010		0.020		0.030	0.035	

APPENDIX J: Test parameters for Experiment Series B3

Test models: SCB9, SCB9-RS25, SCB9-DS25

<i>T</i>	<i>L</i>	<i>B/L</i>	Wave Steepness, <i>H_i/L</i> (REG)		
			<i>H_i</i> = 0.05 m	<i>H_i</i> = 0.10 m	<i>H_i</i> = 0.15 m
0.7	0.765	0.654	0.065	0.131	
0.75	0.878	0.569	0.057	0.114	
0.8	0.999	0.501	0.050	0.100	
0.85	1.127	0.444	0.044	0.089	
0.9	1.262	0.396	0.040	0.079	0.119
1	1.551	0.322	0.032	0.064	0.097
1.1	1.856	0.269	0.027	0.054	0.081
1.2	2.171	0.230	0.023	0.046	0.069
1.3	2.489	0.201	0.020	0.040	0.060
1.4	2.805	0.178	0.018	0.036	0.053
1.5	3.118	0.160	0.016	0.032	0.048
1.6	3.427	0.146	0.015	0.029	0.044
1.7	3.731	0.134	0.013	0.027	0.040
1.8	4.032	0.124	0.012	0.025	0.037

Test models: SCB9, SCB9-DS25

<i>T_p</i>	<i>L_p</i>	<i>B/L_p</i>	Wave Steepness, <i>H_{m0,i}/L_p</i> (JONS)							
			<i>H_i</i> = 0.02 m	0.04 m	0.06 m	0.08 m	0.10 m	0.12 m	0.14 m	0.16 m
0.7	0.765	0.654		0.052	0.078					
0.75	0.878	0.569		0.046	0.068	0.091				
0.8	0.999	0.501		0.040	0.060	0.080				
0.85	1.127	0.444		0.035	0.053	0.071	0.089			
0.9	1.262	0.396		0.032	0.048	0.063	0.079			
1	1.551	0.322		0.026	0.039	0.052	0.064	0.077		
1.1	1.856	0.269		0.022	0.032	0.043	0.054	0.065		
1.2	2.171	0.230		0.018	0.028	0.037	0.046	0.055	0.064	
1.3	2.489	0.201		0.016	0.024	0.032	0.040	0.048	0.056	
1.4	2.805	0.178		0.014	0.021	0.029	0.036	0.043	0.050	
1.5	3.118	0.160		0.013	0.019	0.026	0.032	0.038	0.045	
1.6	3.427	0.146		0.012	0.018	0.023	0.029	0.035	0.041	
1.8	3.731	0.134		0.011	0.016	0.021	0.027	0.032	0.038	
1.9	4.032	0.124		0.010	0.015	0.020	0.025	0.030	0.035	

Test models: SCB9-RS25

<i>T_p</i>	<i>L_p</i>	<i>B/L_p</i>	Wave Steepness, <i>H_{m0,i}/L_p</i> (JONS)							
			<i>H_i</i> = 0.02 m	0.04 m	0.06 m	0.08 m	0.10 m	0.12 m	0.14 m	0.16 m
0.7	0.765	0.654		0.052	0.078					
0.75	0.878	0.569		0.046		0.091				
0.8	0.999	0.501		0.040		0.080				
0.85	1.127	0.444		0.035		0.071	0.089			
0.9	1.262	0.396		0.032		0.063	0.079			
1	1.551	0.322		0.026		0.052		0.077		
1.1	1.856	0.269		0.022		0.043		0.065		
1.2	2.171	0.230		0.018		0.037		0.055	0.064	
1.3	2.489	0.201		0.016		0.032		0.048		
1.4	2.805	0.178		0.014		0.029		0.043		
1.5	3.118	0.160		0.013		0.026		0.038	0.045	
1.6	3.427	0.146		0.012		0.023		0.035	0.041	
1.8	3.731	0.134		0.011		0.021		0.032	0.038	
1.9	4.032	0.124		0.010		0.020		0.030	0.035	

APPENDIX K: Multiple linear regression**PART 1: Regression diagnostics - Assumptions of linear regression**

- (a) *Linearity*: The relationship between the predictors and criterion variables should be linear.
- (b) *Normality of the residuals*: The errors should be normally distributed. Normality of residuals can be evaluated by a histogram on residuals with superimposed normal curve or a P-P plot of regression standardised residual (see Figure K1).
- (c) *Homogeneity of variance (homoscedasticity)*: The error variance should be constant. This can be tested by a plot of standardised residuals by predicted values. The scatter of the data points in the plot shows that the data meet the requirement of homoscedasticity (Figure K2a). Contrary, a regular trend of the data implies that the data is heteroscedastic (Figure K2b) which, in turn, precludes generalisation and distorts the significance tests.
- (d) *Independence*: It is important to choose a predictor variable that might be correlated with the criterion variable, but is not strongly correlated with the other predictor variables. Multicollinearity happens when a high correlation is detected between two or more predictor variables. Statistical parameters, such as tolerance and variance inflation factor (VIF) are the useful tools used to assess the multicollinearity problem in SPSS software. A tolerance < 1 or VIF > 10 indicates high inter-correlation among the predictor variables and this suggests that multicollinearity may happen.
- (e) *Absence of outliers*: A more reliable regression model can be obtained by removing outliers from the data set. Outlier distortion may bias the results, and the effect is particularly large when the sample size is small. SPSS software is capable of diagnosing the outliers and eliminating them from the data set.

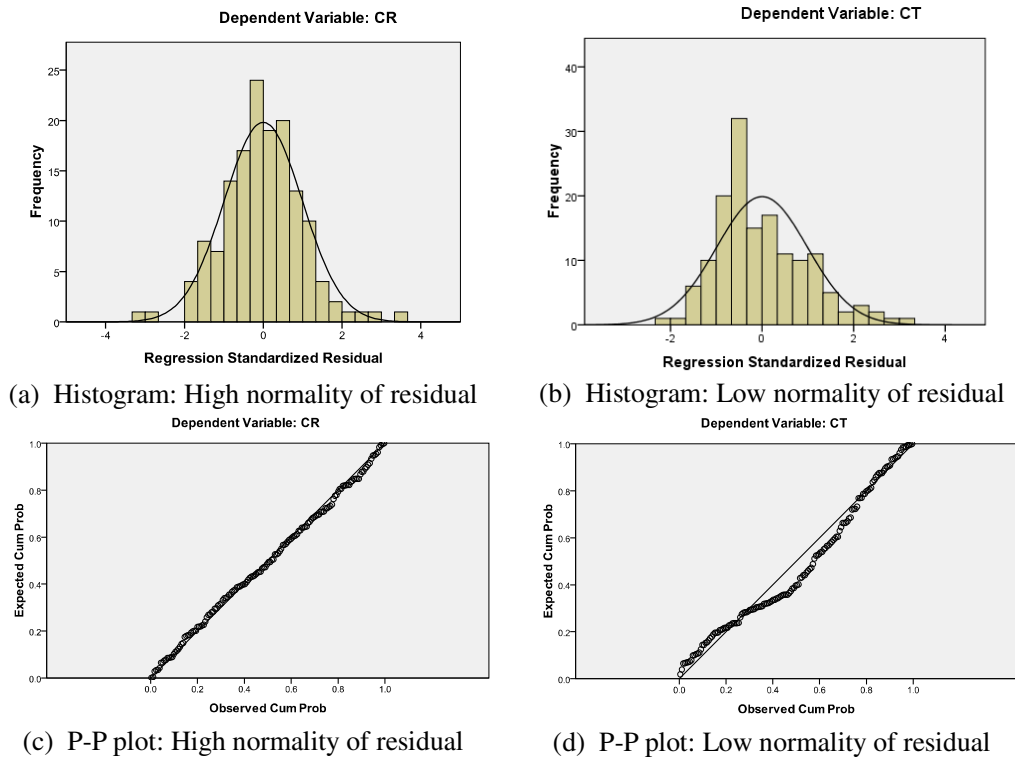


Figure K1: Test of normality: SCB9-DS25 in irregular waves ($0.11 < B/L < 0.35$)

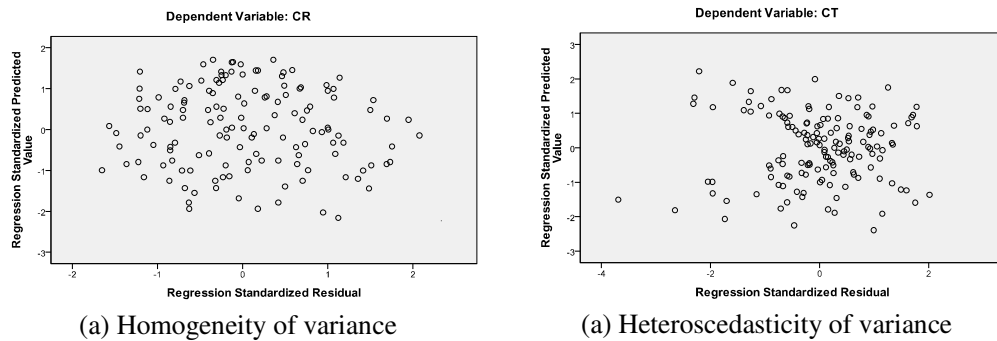


Figure K2: Plots of standardised residuals by predicted values: SCB9-DS25 in irregular waves ($0.11 < B/L < 0.35$)

APPENDIX K: Multiple linear regression

PART 2: SPSS outputs: Multiple linear regression

Multiple linear regression analysis for C_R of the SCB9-DS25 model in irregular waves ($0.11 < B/L < 0.35$)

Variables Entered/Removed^a

Model	Variables Entered	Variables Removed	Method
1	LnH_L, LnD_d, LnB_L ^a	.	Enter

a. All requested variables entered.

b. Dependent Variable: CR

Model Summary

Model	R	R Square	Adjusted R Square	Std. Error of the Estimate
1	.819 ^a	.671	.664	.02461

a. Predictors: (Constant), LnH_L, LnD_d, LnB_L

ANOVA^b

Model		Sum of Squares	df	Mean Square	F	Sig.
1	Regression	.178	3	.059	97.987	.000 ^a
	Residual	.087	144	.001		
	Total	.265	147			

a. Predictors: (Constant), LnH_L, LnD_d, LnB_L

b. Dependent Variable: CR

Coefficients^a

Model		Unstandardized Coefficients		Standardized Coefficients	t	Sig.	Collinearity Statistics	
		B	Std. Error	Beta			Tolerance	VIF
1	(Constant)	.551	.018		29.888	.000		
	LnB_L	.001	.008	.010	.171	.864	.714	1.400
	LnD_d	.320	.020	.786	16.428	.000	.998	1.002
	LnH_L	.020	.005	.248	4.384	.000	.714	1.401

a. Dependent Variable: CR

(a) Variable Entered/Removed

Three predictor variables (*i.e.* $Ln B/L$, $Ln D_T/d$ and $Ln H/L$) were selected to test the respective influences on the criterion variable (C_R). The relative contribution of each predictor variable can be assessed by several statistical methods. The most advanced is the Stepwise method, in which each predictor variable is entered in sequence to the model and the contribution is assessed. If adding the predictor variable contributes significantly to the model then it is retained. With the inclusion of this new variable, all other variables, which have been added at an early stage, are subsequently retested to see if they are still contributing to the success of the model. Any variables with small or insignificant contribution will be automatically removed from the model. This method eventually minimise the possible set of predictor variables included in the model. On the other hand, the “simultaneous” method, which SPSS calls the “Enter” method, retains all of the predictor variables regardless of the level of their contribution to the model. This method the safest to use if the theoretical model is unavailable and the number of cases is relatively low (Brace *et al.*, 2006).

(b) *Model Summary*

The ‘model summary’ evaluates the goodness of prediction of the criterion variable by knowing the predictor variables, using a number of statistical parameters, *i.e.* R , R^2 , adjusted R^2 , and the p -value resulted from the F -statistics. In brief, the Pearson correlation, R is a measure of the correlation between the measured and the predicted values. The coefficient of determination, R^2 indicates the proportion of the variation in the criterion variable which is accounted for by the predictor variables. The adjusted R^2 provides the most useful measure of the success of the model and to reflect how well the model fits the criterion variables. The standard error of the estimate measures the spread of the residuals (or errors) about the fitted line. In this example, an adjusted R^2 of 0.664 implies that the model has accounted for almost 66% of the variance in the criterion variables. The model is rather weak even though the standard error of the estimate for the model is relatively small ($RMSE = 0.025$).

(c) *ANOVA*

Analysis of variance (ANOVA) tests for a linear relationship between the variables and determines how much the variance is account for by the independent variables. In another words, ANOVA tests how well the independent variables predict the score on the dependent variable. F statistics is the ratio of the mean square for regression to the residual mean square. F is large when the predictor variables help to explain the variation of the criterion variable. The p -values (significant value of the null hypothesis) associated with the F -statistics must be less than 5% for the predictor variable to be statistically significant. In this example, F (97.987) indicates that the predictor variables may adequately explain the variation in C_R , and the linear relation is shown to be significant as a whole (p value < 0.0005).

(d) *Coefficients*

The constant and regression coefficients for determining the regression equation are specified by the unstandardised constants B . The “Std. Error” is the standard error of the regression coefficient B . The standardised regression coefficient (beta), which is measured in units of standard deviation, is used to assess how strongly each predictor variable affects the criterion variable. The predictor with the largest beta coefficient has the largest correlation with the criterion variable; thereby playing major part in the regression. The t -tests are the tests of significance for each parameter estimate, *i.e.* the predictor variables are tested by the null hypothesis that there is no linear relationship between the criterion and predictor variables, and this hypothesis has to be rejected in order to become statistically significant. “Sig” is the p -value of t -statistics, in which “Sig” has to be less than 5% to be significant. In this example, $Ln D_T/d$ gives the greatest contribution because a change of one standard deviation on $Ln D_T/d$ produces a change of 0.786 standard deviations in the C_R provided that all other predictor variables are held constant. The t -statistics provide another indication regarding the relative importance of each variable in the model, in which $Ln D_T/d$ is clearly the stronger predictor than $Ln B/L$ and $Ln H/L$. It is also realised that $Ln B/L$ is statistically insignificant (Sig > 0.0005) and is, therefore, recommended to be excluded from the model. Collinearity statistics show that VIF of the predictor variables are well below 10, signifying that multicollinearity problem does not exist in the model.

APPENDIX L: SPSS output for a multiple polynomial regression

Multiple polynomial regression analysis for C_T of the SCB9-DS25 model in regular waves

Variables Entered/Removed^a

Model	Variables Entered	Variables Removed	Method
1	B_LXD_D	.	Stepwise (Criteria: Probability-of-F-to-enter <= .050, Probability-of-F-to-remove >= .100).
2	B_LXB_L	.	Stepwise (Criteria: Probability-of-F-to-enter <= .050, Probability-of-F-to-remove >= .100).
3	H_L	.	Stepwise (Criteria: Probability-of-F-to-enter <= .050, Probability-of-F-to-remove >= .100).
4	H_LXH_L	.	Stepwise (Criteria: Probability-of-F-to-enter <= .050, Probability-of-F-to-remove >= .100).
5	D_DXH_L	.	Stepwise (Criteria: Probability-of-F-to-enter <= .050, Probability-of-F-to-remove >= .100).
6	D_D	.	Stepwise (Criteria: Probability-of-F-to-enter <= .050, Probability-of-F-to-remove >= .100).
7	B_L	.	Stepwise (Criteria: Probability-of-F-to-enter <= .050, Probability-of-F-to-remove >= .100).

a. Dependent Variable: CT

Stepwise method is chosen for the regression analysis for C_T of the SCB9-DS25 model in regular waves. This table demonstrate the order in which the variables entered and removed. In this case, seven variables were added with no removal. A new model number is assigned in the leftmost column whenever a new variable is added to the model.

Model Summary^a

Model	R	R Square	Adjusted R Square	Std. Error of the Estimate
1	.896 ^a	.803	.801	.09616
2	.945 ^b	.893	.891	.07110
3	.973 ^c	.946	.945	.05077
4	.984 ^d	.967	.966	.03972
5	.987 ^e	.975	.974	.03506
6	.990 ^f	.981	.980	.03066
7	.992 ^g	.983	.982	.02880

- a. Predictors: (Constant), B_LXD_D
 b. Predictors: (Constant), B_LXD_D, B_LXB_L
 c. Predictors: (Constant), B_LXD_D, B_LXB_L, H_L
 d. Predictors: (Constant), B_LXD_D, B_LXB_L, H_L, H_LXH_L
 e. Predictors: (Constant), B_LXD_D, B_LXB_L, H_L, H_LXH_L, D_DXH_L
 f. Predictors: (Constant), B_LXD_D, B_LXB_L, H_L, H_LXH_L, D_DXH_L, D_D
 g. Predictors: (Constant), B_LXD_D, B_LXB_L, H_L, H_LXH_L, D_DXH_L, D_D, B_L
 h. Dependent Variable: CT

Model 1 accounted for 80.1% of the variance (Adjusted $R^2 = 0.801$). The inclusion of $(B/L)^2$ resulted in additional 9% of the variance being explained (Adjusted $R^2 = 0.891$). The percentage of the explained variance increases with an increase of the variables added to the model. The final model (Model 7) included B/L which accounted for 98.2% of the variance (Adjusted $R^2 = 0.982$).

APPENDIX L: SPSS output for a multiple polynomial regression (Cont'd)

ANOVA^a

Model		Sum of Squares	df	Mean Square	F	Sig.
1	Regression	4.190	1	4.190	453.176	.000 ^a
	Residual	1.026	111	.009		
	Total	5.216	112			
2	Regression	4.660	2	2.330	460.931	.000 ^b
	Residual	.556	110	.005		
	Total	5.216	112			
3	Regression	4.935	3	1.645	638.334	.000 ^c
	Residual	.281	109	.003		
	Total	5.216	112			
4	Regression	5.046	4	1.261	799.580	.000 ^d
	Residual	.170	108	.002		
	Total	5.216	112			
5	Regression	5.085	5	1.017	827.126	.000 ^e
	Residual	.132	107	.001		
	Total	5.216	112			
6	Regression	5.117	6	.853	907.189	.000 ^f
	Residual	.100	106	.001		
	Total	5.216	112			
7	Regression	5.129	7	.733	883.516	.000 ^g
	Residual	.087	105	.001		
	Total	5.216	112			

- a. Predictors: (Constant), B_LXD_D
- b. Predictors: (Constant), B_LXD_D, B_LXB_L
- c. Predictors: (Constant), B_LXD_D, B_LXB_L, H_L
- d. Predictors: (Constant), B_LXD_D, B_LXB_L, H_L, H_LXH_L
- e. Predictors: (Constant), B_LXD_D, B_LXB_L, H_L, H_LXH_L, D_DXH_L
- f. Predictors: (Constant), B_LXD_D, B_LXB_L, H_L, H_LXH_L, D_DXH_L, D_D
- g. Predictors: (Constant), B_LXD_D, B_LXB_L, H_L, H_LXH_L, D_DXH_L, D_D, B_L
- h. Dependent Variable: CT

This table summarizes the ANOVA result for the seven models whereby all of them are considered significant with $p < 0.05$.

Coefficients^a

Model		Unstandardized Coefficients		Standardized Coefficients	t	Sig.
		B	Std. Error	Beta		
1	(Constant)	.745	.019		40.170	.000
	B_LXD_D	-2.144	.101	-.896	-21.288	.000
2	(Constant)	.922	.023		40.224	.000
	B_LXD_D	-4.542	.260	-1.899	-17.498	.000
	B_LXB_L	2.027	.210	1.047	9.644	.000
3	(Constant)	.963	.017		57.194	.000
	B_LXD_D	-3.972	.193	-1.661	-20.542	.000
	B_LXB_L	1.971	.150	1.018	13.129	.000
	H_L	-2.487	.241	-.312	-10.333	.000
4	(Constant)	1.074	.019		57.381	.000
	B_LXD_D	-3.800	.153	-1.589	-24.888	.000
	B_LXB_L	1.848	.118	.954	15.603	.000
	H_L	-7.985	.683	-1.001	-11.686	.000
	H_LXH_L	46.277	5.529	.697	8.370	.000
5	(Constant)	1.122	.019		60.269	.000
	B_LXD_D	-4.595	.195	-1.921	-23.514	.000
	B_LXB_L	2.418	.146	1.248	16.596	.000
	H_L	-11.975	.932	-1.501	-12.854	.000
	H_LXH_L	44.205	4.895	.666	9.031	.000
	D_DXH_L	7.945	1.414	.581	5.620	.000
6	(Constant)	1.469	.062		23.789	.000
	B_LXD_D	-4.471	.172	-1.869	-25.969	.000
	B_LXB_L	2.327	.128	1.202	18.134	.000
	H_L	-17.178	1.209	-2.153	-14.212	.000
	H_LXH_L	45.362	4.285	.683	10.587	.000
	D_DXH_L	16.766	1.955	1.225	8.578	.000
	D_D	-.618	.106	-.169	-5.827	.000
7	(Constant)	1.553	.062		25.107	.000
	B_LXD_D	-3.029	.404	-1.266	-7.491	.000
	B_LXB_L	2.520	.130	1.301	19.335	.000
	H_L	-13.684	1.447	-1.715	-9.454	.000
	H_LXH_L	44.207	4.035	.666	10.955	.000
	D_DXH_L	11.048	2.351	.808	4.698	.000
	D_D	-.737	.104	-.201	-7.071	.000
	B_L	-.977	.251	-.699	-3.892	.000

a. Dependent Variable: CT

The table report unstandardized coefficient B , standardized coefficient $Beta$ and the t and Sig (p) values. Explanation for these parameters was given in Appendix K.

APPENDIX L: SPSS output for a multiple polynomial regression (Cont'd)

Excluded Variables^a

Model		Beta In	t	Sig.	Partial Correlation	Collinearity Statistics Tolerance	
1	B_L	.463 ^a	2.383	.019	.222	.045	
	D_D	-.123 ^a	-2.970	.004	-.272	.965	
	H_L	-.326 ^a	-6.759	.000	-.542	.543	
	B_LXB_L	1.047 ^a	9.644	.000	.677	.082	
	B_LXH_L	-.090 ^a	-.971	.334	-.092	.207	
	D_DXD_D	-.122 ^a	-2.953	.004	-.271	.965	
	D_DXH_L	-.378 ^a	-7.982	.000	-.606	.504	
	H_LXH_L	-.238 ^a	-4.674	.000	-.407	.574	
2	B_L	-1.185 ^b	-6.531	.000	-.530	.021	
	D_D	.116 ^b	2.943	.004	.271	.581	
	H_L	-.312 ^b	-10.333	.000	-.703	.542	
	B_LXB_L	-.390 ^b	-6.089	.000	-.504	.178	
	D_DXD_D	.116 ^b	2.949	.004	.272	.582	
	D_DXH_L	-.295 ^b	-8.308	.000	-.623	.476	
	H_LXH_L	-.238 ^b	-6.935	.000	-.553	.574	
	3	B_L	-.734 ^c	-5.020	.000	-.435	.019
D_D		.041 ^c	1.357	.178	.129	.542	
B_LXB_L		.857 ^c	7.284	.000	.574	.024	
D_DXD_D		.041 ^c	1.367	.174	.130	.543	
D_DXH_L		.651 ^c	4.782	.000	.418	.022	
H_LXH_L		.697 ^c	8.370	.000	.627	.044	
4		B_L	-.627 ^d	-5.568	.000	-.474	.019
		D_D	.024 ^d	.999	.320	.096	.537
	B_LXB_L	.197 ^d	.896	.372	.086	.006	
	D_DXD_D	.024 ^d	1.014	.313	.098	.539	
	D_DXH_L	.581 ^d	5.620	.000	.477	.022	
	5	B_L	-.327 ^e	-1.575	.118	-.151	.005
		D_D	-.169 ^e	-5.827	.000	-.493	.215
		B_LXB_L	.081 ^e	.412	.681	.040	.006
D_DXD_D		-.167 ^e	-5.764	.000	-.489	.216	
6		B_L	-.699 ^f	-3.892	.000	-.355	.005
		B_LXB_L	.080 ^f	.466	.642	.045	.006
		D_DXD_D	.148 ^f	.392	.696	.038	.001
		7	B_LXB_L	.067 ^g	.417	.678	.041
	D_DXD_D		.131 ^g	.370	.712	.036	.001

a. Predictors in the Model: (Constant), B_LXD_D

b. Predictors in the Model: (Constant), B_LXD_D, B_LXB_L

c. Predictors in the Model: (Constant), B_LXD_D, B_LXB_L, H_L

d. Predictors in the Model: (Constant), B_LXD_D, B_LXB_L, H_L, H_LXH_L

e. Predictors in the Model: (Constant), B_LXD_D, B_LXB_L, H_L, H_LXH_L, D_DXH_L

f. Predictors in the Model: (Constant), B_LXD_D, B_LXB_L, H_L, H_LXH_L, D_DXH_L, D_D

g. Predictors in the Model: (Constant), B_LXD_D, B_LXB_L, H_L, H_LXH_L, D_DXH_L, D_D, B_L

h. Dependent Variable: CT

The table lists the statistics for the variables that were excluded from each model. *Beta In* is the standardized regression coefficient that would result if the variable were entered into the equation at the next step. The *t*-test is the significance test for the regression coefficient. The Partial Correlation is the correlation of each criterion variable with the predictor variables after removing the linear effect of variables already in the equation. Collinearity exists as a result of strong correlations among the predictor variables.

APPENDIX M: Relative contribution of the breakwater placement ratio, B/d on the hydraulic coefficients in regular waves

Transmission coefficient, C_T

Model		Unstandardized Coefficients		Standardized Coefficients	t	Sig.
		B	Std. Error	Beta		
1	(Constant)	1.421	.020		72.329	.000
	B/d	-0.078	.012	-.116	-6.446	.000
	B/L	-1.008	.033	-.620	-30.105	.000
	D/d	-2.339	.079	-.529	-29.630	.000
	H/L	-2.096	.187	-.230	-11.217	.000

Reflection coefficient, C_R

Model		Unstandardized Coefficients		Standardized Coefficients	t	Sig.
		B	Std. Error	Beta		
1	(Constant)	-.018	.017		-1.066	.287
	B/d	.003	.011	.010	.287	.774
	B/L	.504	.030	.672	16.589	.000
	D/d	.991	.069	.498	14.312	.000
	H/L	-1.124	.165	-.275	-6.807	.000

Dissipation coefficient, C_L

Model		Unstandardized Coefficients		Standardized Coefficients	t	Sig.
		B	Std. Error	Beta		
1	(Constant)	-.241	.027		-8.769	.000
	B/d	.118	.017	.186	7.048	.000
	B/L	.696	.048	.445	14.372	.000
	D/d	1.936	.109	.467	17.758	.000
	H/L	3.107	.263	.365	11.828	.000

Wave climate coefficient in front of the breakwater, C_F

Model		Unstandardized Coefficients		Standardized Coefficients	t	Sig.
		B	Std. Error	Beta		
1	(Constant)	1.279	.031		41.224	.000
	B_d	-.191	.019	-.464	-9.996	.000
	B_L	.046	.053	.046	.858	.391
	D_d	.502	.124	.187	4.046	.000
	H_L	.317	.296	.057	1.072	.284

Wave climate coefficient in the breakwater's chamber, C_C

Model		Unstandardized Coefficients		Standardized Coefficients	t	Sig.
		B	Std. Error	Beta		
1	(Constant)	1.196	.028		42.246	.000
	B_d	-.067	.017	-.160	-3.833	.000
	B_L	-.405	.049	-.397	-8.254	.000
	D_d	.134	.114	.049	1.178	.239
	H_L	-1.607	.270	-.285	-5.953	.000

APPENDIX N: Relative contribution of the breakwater placement ratio, B/d on the hydraulic coefficients in irregular waves

Transmission coefficient, C_T

Model		Unstandardized Coefficients		Standardized Coefficients	t	Sig.
		B	Std. Error	Beta		
1	(Constant)	1.041	.010		103.922	.000
	B_d	.161	.012	.260	13.546	.000
	B_L	-.879	.025	-.628	-35.396	.000
	D_d	-1.410	.037	-.713	-37.703	.000
	H_L	-1.066	.177	-.105	-6.010	.000

Reflection coefficient, C_R

Model		Unstandardized Coefficients		Standardized Coefficients	t	Sig.
		B	Std. Error	Beta		
1	(Constant)	.184	.005		39.415	.000
	B_d	-.135	.006	-.583	-24.419	.000
	B_L	.386	.012	.736	33.317	.000
	D_d	.648	.017	.876	37.198	.000
	H_L	-1.168	.083	-.307	-14.115	.000

Dissipation coefficient, C_L

Model		Unstandardized Coefficients		Standardized Coefficients	t	Sig.
		B	Std. Error	Beta		
1	(Constant)	.028	.011		2.490	.013
	B_d	.084	.014	.135	6.211	.000
	B_L	.709	.028	.500	24.975	.000
	D_d	1.276	.043	.638	29.865	.000
	H_L	2.465	.203	.240	12.160	.000

Wave climate coefficient in front of the breakwater, C_F

Model		Unstandardized Coefficients		Standardized Coefficients	t	Sig.
		B	Std. Error	Beta		
1	(Constant)	1.325	.011		124.780	.000
	B_d	-.231	.013	-.750	-18.277	.000
	B_L	-.051	.026	-.073	-1.930	.054
	D_d	.218	.040	.223	5.505	.000
	H_L	1.067	.188	.212	5.671	.000

Wave climate coefficient in the breakwater's chamber, C_c

Model		Unstandardized Coefficients		Standardized Coefficients	t	Sig.
		B	Std. Error	Beta		
1	(Constant)	1.188	.007		170.120	.000
	B_d	-.195	.008	-.722	-23.498	.000
	B_L	-.294	.017	-.482	-16.979	.000
	D_d	.257	.026	.299	9.872	.000
	H_L	.013	.124	.003	.108	.914